

DESIGN AND CONTROL OF PWM CONVERTER WITH LCL TYPE FILTER
FOR GRID INTERFACE OF RENEWABLE ENERGY SYSTEMS

A THESIS SUBMITTED TO
THE GRADUATE SCHOOL OF NATURAL AND APPLIED SCIENCES
OF
MIDDLE EAST TECHNICAL UNIVERSITY

BY
EMRE KANTAR

IN PARTIAL FULFILLMENT OF THE REQUIREMENTS
FOR
THE DEGREE OF MASTER OF SCIENCE
IN
ELECTRICAL AND ELECTRONICS ENGINEERING

JULY 2014

Approval of the thesis:

**DESIGN AND CONTROL OF PWM CONVERTER WITH LCL TYPE
FILTER FOR GRID INTERFACE OF RENEWABLE ENERGY SYSTEMS**

submitted by **EMRE KANTAR** in partial fulfillment of the requirements for the degree of **Master of Science in Electrical and Electronics Engineering Department, Middle East Technical University** by,

Prof. Dr. Canan Özgen
Dean, Graduate School of **Natural and Applied Sciences**

Prof. Dr. Gönül Turhan Sayan
Head of Department, **Electrical and Electronics Engineering**

Assoc. Prof. Dr. Ahmet M. Hava
Supervisor, **Electrical and Electronics Eng. Dept., METU**

Examining Committee Members:

Prof. Dr. Muammer Ermiş
Electrical and Electronics Engineering Dept., METU

Assoc. Prof. Dr. Ahmet M. Hava
Electrical and Electronics Engineering Dept., METU

Prof. Dr. Kemal Leblebicioğlu
Electrical and Electronics Engineering Dept., METU

Assoc. Prof. Dr. Umut ORGUNER
Electrical and Electronics Engineering Dept., METU

Eyyup Demirkutlu, M.Sc.
ADULARYA Energy Electric Gen. and Mining Inc.

Date: 18/07/2014

I hereby declare that all information in this document has been obtained and presented in accordance with academic rules and ethical conduct. I also declare that, as required by these rules and conduct, I have fully cited and referenced all material and results that are not original to this work.

Name, Last name : Emre Kantar

Signature :

ABSTRACT

DESIGN AND CONTROL OF PWM CONVERTER WITH LCL TYPE FILTER FOR GRID INTERFACE OF RENEWABLE ENERGY SYSTEMS

Kantar, Emre

M.Sc., Department of Electrical and Electronics Engineering
Supervisor : Assoc. Prof. Dr. Ahmet M. Hava

July 2014, 349 Pages

This thesis involves the PWM and control unit design and simulation for three-phase PWM converter widely used for grid-interface of renewable energy systems, motor drives, etc. The study involves selecting the LCL filter parameters, switching frequency, the PWM method, the cost-effective feedback controlled algorithm, etc. for the converter. The design is verified by means of detailed computer simulations. The study considers the normal and unbalanced grid conditions, which may occur in the grid operating conditions. Several power ratings and operating conditions are considered to provide a thorough performance evaluation of the designed system.

Keywords: Active damping, back to back converter, capacity factor, control, converter, DC/AC, design, filter design, full-scale power converter, grid code, grid-connected, inverter, LCL filter, passive damping, PI controller, PWM, resonance, resonance frequency, sampling, space vector, THD, three-level NPC, three-level T, two-level, wind power, wind turbine, voltage source converter.

ÖZ

YENİLENEBİLİR ENERJİ SİSTEMLERİNİN ŞEBEKE ARAYÜZÜ İÇİN LCL TİPİ SÜZGEÇLİ PWM ÇEVİRİCİ TASARIM VE DENETİMİ

Kantar, Emre

Yüksek Lisans, Elektrik ve Elektronik Mühendisliği Bölümü

Tez Yöneticisi : Doç. Dr. Ahmet M. Hava

Temmuz 2014, 349 Sayfa

Bu tez, üç fazlı PWM çeviricinin sıklıkla kullanıldığı yenilenebilir enerji sistemlerinin şebeke arayüzü, motor sürücü devreleri vb. uygulamalar için PWM ve denetim birimlerinin tasarımını, ve sistemin ayrıntılı benzetimini içerir. Bu çalışma, çevirici için LCL süzgeç parametrelerinin, anahtarlama frekansının, PWM yönteminin, uygun maliyetli geri besleme denetimli algoritmaların seçimini vb. içerir. Tasarım, ayrıntılı bilgisayar benzetimleri aracıyla doğrulanacaktır. Bu çalışmada dengeli ve dengesiz şebeke koşulları uygulamada karşılaşılabilecek durumlar ışığında göz önünde bulundurulacaktır. Bu çalışmada, tasarımı yapılan sistemin, tam anlamıyla eksiksiz ve kapsamlı bir başarımlı değerlendirilmesini sunabilmek amacıyla birkaç güç değeri ve farklı çalışma koşulları göz önünde bulundurulacaktır.

Anahtar Kelimeler: Aktif sönümlendirme, çevirici, çnlama, çnlama sıklığı, DA/AA, darbe genişlik modülasyonu (DGM), denetim, edilgen (pasif) sönümlendirme, evirici, gerilim kaynaklı evirici (GKE), kapasite faktörü, LCL süzgeç, örnekleme, PI denetleyici, rüzgar türbini, süzgeç tasarımı, şebeke kodu, süzgeç tasarımı, şebeke bağlantılı, tasarım, THB, uzay vektörü.

*To the people who died in Gezi Park protests
and
To the coal miners who died in Soma Disaster*

ACKNOWLEDGEMENTS

I would like to thank my supervisor, Assoc. Prof. Dr. Ahmet M. Hava for his support, encouragement, guidance and critiques on this study throughout my graduate education. I have gained an engineering insight owing to his supervision.

I would like to express my deepest gratitude to my dearest love Cansu Birgen for her endless love, support, and encouragements in all aspects of my life. Without her support, I would not be able to finish this work.

I express my deepest gratitude to my family for their patience and support throughout my life. They have always been on my side in all of my decisions.

I would like to thank my closest friends Anıl Civil, Yasin Çevik, Yeti Gürbüz and Gürkan Yıldırım for their wonderful company and support throughout this work.

I would like to thank my friends S. Nadir Usluer and Barış Çiftçi for their help and support.

I wish to thank the Department of Electrical and Electronics Engineering faculty and staff and Graduate School of Natural and Applied Sciences for their help throughout my graduate study.

I wish to thank to Middle East Technical University Department of Electrical and Electronics Engineering faculty and staff for their help throughout my graduate studies.

TABLE OF CONTENTS

ABSTRACT	v
ÖZ	vi
ACKNOWLEDGEMENTS	viii
TABLE OF CONTENTS	ix
LIST OF TABLES	xvi
LIST OF FIGURES	xviii
LIST OF ABBREVIATIONS.....	xxvi
CHAPTERS	
1. INTRODUCTION	1
1.1. Background and Motivation	1
1.2. Typical Wind Turbine Configurations	5
1.2.1. Wind Turbine System with Full-Scale Power Converter	6
1.2.2. Three-Phase Grid-Side DC/AC PWM-VSC (Two/Three-Level)	7
1.2.3. <i>LCL</i> -Type Filter Configuration in Grid-Connected Systems	10
1.2.4. Design Challenges	12
1.3. Scope of the Thesis.....	13
2. WIND ENERGY SYSTEMS	17
2.1. Introduction.....	18
2.2. Wind Power Plants	21
2.2.1. Differences between Wind Plant and Conventional Power Plant.....	22

2.2.2.	Differences between Onshore and Offshore Wind Power Plants	23
2.2.3.	Different Levels of Connection	25
2.2.4.	Step-Up Transformer Structure	28
2.2.4.1.	Transformer Type.....	29
2.2.4.2.	Winding Connection.....	29
2.3.	General Structure of Individual Wind Turbines.....	30
2.3.1.	Recent Wind Turbine Configurations.....	32
2.3.2.	Back-to-Back PWM-VSC for Partial-Scale and Full-Scale Converters.....	34
2.3.3.	Grid-Side DC/AC Converter of the Back-to-Back PWM-VSC for Full-Scale Converters.....	35
2.4.	Capacity Factor and Operational Efficiency Definitions as the Performance Indicator of Individual Wind Turbines.....	37
2.4.1.	Definition of Capacity Factor.....	38
2.4.2.	Novel Operational Efficiency Definition for Wind Turbines.....	41
2.5.	Grid Codes Overview.....	42
2.5.1.	Active Power Control.....	43
2.5.2.	Reactive Power and Voltage Control	46
2.5.3.	Frequency and Voltage Operating Ranges.....	48
2.5.4.	Fault Ride Through Capability	49
2.5.5.	Overview of International Standards Concerning Power Quality Inserted by Wind Farms into the Grid.....	52
2.5.5.1.	Current and Voltage Harmonic Standards Considered in the Design Phase.....	54
2.5.5.1.1.	Harmonic Voltage Injection Limits Set by EN 50160	54
2.5.5.2.	The Impact of Injected Harmonics According to Stiffness of the Grid	58

2.5.5.2.1. The Impact of Grid Stiffness on Harmonic Current Injection Limits Set by VDEW	60
2.6. Conclusions.....	61
3. DETERMINATION OF SWITCHING FREQUENCY CONSTRAINT REGARDING EFFICIENCY TARGET OF THE DESIGN.....	63
3.1. A Brief Survey on Recent Converter Properties	64
3.1.1. Features of Low-Voltage and Medium Voltage Wind Turbine Converters	64
3.1.2. Types of Power Semiconductors According to Power Rating	66
3.1.3. Modulation Strategies of Wind Turbine Converters	67
3.2. Determination of Switching Frequency Constraint Regarding Efficiency Target of the Design.....	68
3.3. Illustration through a Numerical Design	70
3.4. Summary and Conclusions	72
4. A COMPREHENSIVE <i>LCL</i> -FILTER STUDY REGARDING CONTROL AND STABILITY ANALYSES	73
4.1. Improvements Provided by <i>LCL</i> -Filters.....	74
4.2. System Description and Modeling	76
4.3. Control Overview and Controller Design.....	78
4.3.1. Control Overview	78
4.3.1.1. Three Phase <i>abc</i> -frame to Two Phase <i>dq</i> -frame Conversion	80
4.3.1.2. Mathematical Model of the <i>LCL</i> -Filter for Controller Design	84
4.3.1.3. Frequency Characteristic of the <i>LCL</i> -Filter for Controller Design	85
4.3.1.4. Controller Design Regarding the Rotating <i>dq</i> -Frame.....	87
4.3.2. Current Control Loop Design (Inner Loop Design).....	89
4.3.2.1. Impacts of Sampling Mode in Current Control Loop.....	92
4.3.3. DC Link Voltage Control Loop Design (Outer Loop Design).....	95

4.4.	Stability Analysis.....	97
4.4.1.	Filter Modeling for Stability Analysis.....	98
4.4.2.	Overview of Resonance Damping Techniques.....	102
4.4.3.	Passive Damping Technique	104
4.4.4.	Active Damping Technique using Filter Capacitor Current Feedback.....	107
4.4.4.1.	Active Damping under Grid-Current Feedback.....	109
4.4.4.2.	Active Damping under Converter-Current Feedback.....	112
4.4.5.	Controller and Active Damping Gain Determination.....	116
4.4.6.	Identification of Active Damping Regions for <i>LCL</i> -Filters	130
4.4.6.1.	<i>LCL</i> Resonance Frequency above Critical Resonance Frequency	133
4.4.6.2.	<i>LCL</i> Resonance Frequency below Critical Resonance Frequency.....	134
4.5.	Case Studies.....	135
4.5.1.	Simulation Results via SIMPLORER® for GCF Control	135
4.5.1.1.	Case I– GCF with AD in Low-Resonant Frequency Region	137
4.5.1.2.	Case II– GCF without AD in High-Resonant Frequency Region ($C_f=20\ \mu\text{F}$)...	138
4.5.1.3.	Case III– GCF without AD in High-Resonant Frequency Region ($C_f=30\ \mu\text{F}$)	139
4.5.1.4.	Stability Analysis of the Simulated System via MATLAB®	141
4.5.1.5.	FFT Analysis of the Simulated System.....	143
4.5.2.	Simulation Results via SIMPLORER® for CCF Control.....	144
4.5.2.1.	Case I-CCF without AD in Low-Resonant Frequency Region.....	145
4.5.2.2.	Case II– CCF without AD in High-Resonant Frequency Region	146
4.5.2.3.	Case III– CCF with AD in High-Resonant Frequency Region	147
4.5.2.4.	Stability Analysis of the Simulated System via MATLAB®	149
4.5.2.5.	FFT Analysis of the Simulated System.....	150

4.5.3. Dynamic and Resonance Damping Performance Comparison between GCF and CCF	151
4.6. Summary and Conclusions	157
5. <i>LCL</i> -FILTER DESIGN METHODOLOGY FOR GRID CONNECTED VOLTAGE SOURCE CONVERTERS	161
5.1. Overview of Control Methods and Damping Techniques.....	162
5.2. Conventional <i>LCL</i> -Filter Design Algorithm.....	164
5.2.1. <i>LCL</i> -Filter Design Case-Study	169
5.2.2. Assessment of the Designed <i>LCL</i> -Filter through Simulations	176
5.2.2.1. Grid Code Compatibility.....	182
5.2.2.2. The Assessment of Efficiency vs. PWM Method	183
5.2.2.3. Damping Loss Comparison against PWM Method.....	184
5.3. Proposed <i>LCL</i> -Filter Design Algorithm Including Controllability Issues.....	188
5.3.1. Case-Studies.....	197
5.3.1.1. Case-Study I: 250 kVA System	197
5.3.1.2. Case-Study II: 1 MVA System	204
5.3.1.3. Case-Study III: 3 MVA System.....	210
5.3.2. Tuning of Control Parameters	211
5.3.2.1. Detailed Analysis for 1 MVA Case under GCF Method	213
5.3.2.2. Detailed Analysis for 1 MVA Case under CCF Method	222
5.4. Summary and Conclusions	230
6. SEMICONDUCTOR MODULE AND MAGNETIC CIRCUIT LOSS CHARACTERIZATION CONSIDERING CONVERTER TOPOLOGIES AND PWM METHODS.....	235
6.1. Introduction.....	235
6.2. Overview of Proposed VSC Topologies	237

6.2.1. Commutation Configuration.....	238
6.2.2. A General Scheme for Calculation of Switching and Conduction Losses of Power Semiconductors in Computer Simulations	241
6.2.2.1. Conduction Losses.....	241
6.2.2.2. Switching Losses.....	242
6.3. Topological Loss Comparison	243
6.3.1. Semiconductor Loss Calculated with Computer Simulation Loss Calculator.....	244
6.3.2. <i>LCL</i> -Filter Loss Model	247
6.4. Efficiency Comparison between Two-level and Three-level Topologies	250
6.5. Converter Current Ripple Estimation of Two-level and Three-level Topologies	254
6.6. Impact of PWM Pattern on Output Performance of 2L and 3L Topologies.....	257
6.7. Summary and Conclusions	264
7. DESIGN OF GRID CONNECTED PWM CONVERTERS CONSIDERING TOPOLOGY AND PWM METHODS FOR LOW-VOLTAGE WIND TURBINES	267
7.1. Converter Design Methodology	270
7.1.1. Optimum Switching Frequency Designation	273
7.1.2. <i>LCL</i> -Filter Design	274
7.1.3. Grid Requirements Compatibility Test.....	275
7.1.4. Achieving Identical Output	280
7.1.5. Figure of Merit: Operational Efficiency	283
7.1.6. Operational Cost Evaluation	287
7.1.6.1. Initial Cost Analysis	288
7.1.6.2. Accumulated Cost Savings Using Capacity Factor	289
7.2. Case Study: 3 MVA VSC Design.....	293
7.3. Conclusions.....	296

8. THE PERFORMANCE ANALYSIS OF THREE-PHASE TWO-LEVEL VIA COMPUTER SIMULATIONS.....	299
8.1. Phase Locked Loop.....	300
8.2. Simulation Studies.....	301
8.2.1. Modeled Wind Energy Characteristics.....	305
8.2.2. Simulation Results under Balanced Grid Conditions.....	306
8.2.2.1. Input Characteristics.....	306
8.2.2.2. Output Characteristics.....	307
8.2.2.3. Steady-state measurements.....	309
8.2.2.4. Dynamic Response under Rapidly Changing Conditions.....	310
8.2.3. Simulation Results under Distorted Grid Conditions.....	311
8.2.3.1. Input Characteristics.....	311
8.2.3.2. Output Characteristics.....	312
8.2.3.3. Steady-state measurements.....	315
8.2.3.4. Dynamic Response under Rapidly Changing Conditions.....	315
8.2.4. Simulation Results under Unbalanced Grid Conditions.....	316
8.2.4.1. Input Characteristics.....	317
8.2.4.2. Output Characteristics.....	317
8.2.4.3. Steady-state measurements.....	321
8.2.4.4. Dynamic Response under Rapidly Changing Conditions.....	322
8.3. Summary.....	323
9. CONCLUSION.....	325
REFERENCES.....	335
APPENDIX A.....	349

LIST OF TABLES

TABLES

Table 2.1 Wind power installed in European countries by the end of 2013 (MW).....	19
Table 2.2 General differences between onshore and offshore wind turbines [30].	25
Table 2.3 Transmittable power and connection of wind turbines to different levels of the electrical network [32].	28
Table 2.4 Wind speed classification.	41
Table 2.5 Values of individual harmonic voltages at the supply terminals for orders up to 25, given in percent of nominal voltage U_n [49].....	55
Table 2.6 Values of individual harmonic currents at the supply terminals, given in percent of fundamental rated current I_r [51].....	57
Table 2.7 Specification of exponents according to IEC 61000-3-6.....	57
Table 2.8 Allowed rated harmonic currents (VDEW [53]).	61
Table 3.1 ACS800 low-voltage wind turbine converters [105].	65
Table 3.2 Transistors overview [108].	67
Table 4.1 System parameters used for simulation.....	117
Table 4.2 Regions of effective AD control under CCF and GCF.	131
Table 4.3. System parameters used in case-studies.	135
Table 4.4 Selection of C_f below and above critical region.	136
Table 4.5. Differences between GCF and CCF control.	156
Table 5.1 <i>LCL</i> -filter design specifications.	170
Table 5.2 Designed filter and controller parameters.....	176
Table 5.3 Comparison between GCF and CCF.....	181
Table 5.4 Input parameters for case-studies.	197
Table 5.5 Performance analysis for $C_f=150\mu\text{F}$ (3%).....	203
Table 5.6 Performance analysis for $C_f=332\mu\text{F}$ (5%).....	206

Table 5.7 Performance analysis for $C_f=1000\mu\text{F}$ (5%).	210
Table 5.8 Parameters to be used in case-studies.	212
Table 5.9 K_p tuning regarding PM and BW (GCF).	215
Table 5.10 Dynamic performance outputs (GCF– $\zeta=0.707$).	218
Table 5.11 Dynamic performance outputs (GCF– $\zeta=0.5$).	221
Table 5.12 PM and BW tuning for ID.	223
Table 5.13 K_p tuning regarding PM and BW for ID control with AD.	226
Table 6.1 Simulation parameters for topological comparison analysis.	236
Table 6.2 Switching states for 2L-VSC.	239
Table 6.3 Switching states for 3L-VSC	239
Table 6.4 Switching loss energies.	240
Table 6.5 Selected semiconductors for topological comparison analysis.	243
Table 7.1 Simulation parameters to illustrate design steps.	273
Table 7.2 Designed <i>LCL</i> -filter parameters.	275
Table 7.3 Wind speed classification.	286
Table 7.4 Comparison of η_{op} (%) under <i>C.F.</i>	287
Table 7.5 TCO of PSMU.	288
Table 7.6 s_θ vs. operation time in Japan, France and the USA.	290
Table 7.7 Comparison of η_{op} (%) under <i>C.F.</i>	292
Table 7.8 Differential TCO comparison between NPC and $T_{RB-IGBT}$.	292
Table 7.9 Simulation parameters for 3 MVA system.	293
Table 7.10 Comparison of η_{op} (%) under <i>C.F.</i> (3 MVA).	295
Table 7.11 Differential TCO comparison between NPC and $T_{RB-IGBT}$ (3 MVA).	295
Table 8.1 2L-VSC simulation parameters.	305
Table 8.2 2L-VSC steady-state measurements.	310
Table 8.3 2L-VSC steady-state measurements (distorted grid).	315
Table 8.4 2L-VSC steady-state measurements (unbalanced grid).	321

LIST OF FIGURES

FIGURES

Figure 1.1 Global cumulative installed wind capacity [2].	2
Figure 1.2 Estimated LCOE for wind between 1980-2009 for US and Europe [4].	3
Figure 1.3 Total number of publications about wind turbines and wind farms [5].	3
Figure 1.4 Typical configurations for wind turbine system.	5
Figure 1.5 Standard three-phase two-level VSC topology.	9
Figure 1.6 One converter leg (a) 2L (b) 3L-NPC (c) 3L-T.	9
Figure 1.7 Grid connected three-phase 2L-VSC system with <i>LCL</i> -filter.	10
Figure 2.1 Global cumulative and annual installed wind capacity [22].	18
Figure 2.2 Global market forecast 2014-2018 [22].	20
Figure 2.3 Turkey Wind Resource Map at 50 m [24].	20
Figure 2.4 General structure of offshore wind farms [30].	24
Figure 2.5 Collector system for wind farm [29].	26
Figure 2.6 Connection at different voltage levels according to power [29].	28
Figure 2.7 Typical wind farm network- single line diagram (only a few turbines are shown) [40].	29
Figure 2.8 Typical wind turbine configuration [30].	31
Figure 2.9 Block diagram of a typical wind turbine [29].	31
Figure 2.10 Wind turbine configurations [25].	33
Figure 2.11 Back-to-back PWM-VSC for wind turbine system with full-scale converter.	36
Figure 2.12 Grid-connected DC/AC converter cascaded with <i>LCL</i> -filter.	36
Figure 2.13 MWT62/1.0 (a) Power curve (b) Energy output.	39
Figure 2.14 Modified MWT62/1.0 power curve.	40
Figure 2.15 Active power control requirements	44

Figure 2.16 Typical power vs. frequency response [33].	45
Figure 2.17 P-Q dependencies of three variants [36].	46
Figure 2.18 V-Q dependency [36].	47
Figure 2.19 Typical requirements for power factor variation range in relation to the voltage [33].	47
Figure 2.20 Voltage/Frequency operating ranges [36].	48
Figure 2.21 Comparison of the operating frequency limits in European countries [33].	49
Figure 2.22 Limiting voltage curves at PCC [36].	51
Figure 2.23 Principle of voltage support during a grid fault [36].	52
Figure 2.24 Suggested harmonic standards for grid-connected wind turbines.	54
Figure 2.25 (a) U_{PCC} at power injection of SWT = 1 p.u. (b) Outline of a process of grid instabilization fora weak grid with a low SCR [50].	59
Figure 3.1 Power semiconductors [108].	66
Figure 3.2 Determination of f_{sw} constraint regarding efficiency target of the design.	69
Figure 3.3 η (%) vs. f_{sw} plot of three VSC topologies under SVPWM.	71
Figure 3.4. η (%) vs. f_{sw} (SVPWM and DPWM1).	71
Figure 4.1 Grid connected three-phase VSC with control block.	76
Figure 4.2 Current control structure.	79
Figure 4.3 Stationary abc -frame and stationary $\alpha\beta$ - frame.	80
Figure 4.4 Vector diagram of PWM-VSC control structure.	82
Figure 4.5 Equivalent circuit of LCL network under dq -synchronous frame.	85
Figure 4.6 The magnitude responses of L -filter and LCL -filter.	86
Figure 4.7 Decomposition of vectors in dq -frame.	86
Figure 4.8 Block diagram of voltage oriented current control loop.	88
Figure 4.9 Current controller block diagram (a) Converter-side current feedback.	90
Figure 4.10 Block diagram of current control loop.	91
Figure 4.11 Block diagram of simplified current control loop.	91
Figure 4.12 (a) Single-update PWM method (sampling at start) (b) Single-update PWM method (sampling at middle).	93
Figure 4.13 Double-update PWM method.	94
Figure 4.14 Block diagram of outer voltage control loop.	96

Figure 4.15 Undamped per phase (a) equivalent circuit (b) equivalent block diagram of <i>LCL</i> -network for stability analysis.	99
Figure 4.16 Bode plot of the open-loop VSC system with <i>LCL</i> -filter.	100
Figure 4.17 Line voltage/current of undamped vs. damped system.	101
Figure 4.18 Position of poles in undamped to damped cases.	101
Figure 4.19 Modified current control loop with the addition of resonance damping.	102
Figure 4.20 Attenuation capability of <i>LCL</i> -filter under distinct damping methods.	103
Figure 4.21 <i>LCL</i> -filter with PD per phase circuit (a) equivalent circuit (b) equivalent block diagram of <i>LCL</i> -network.	106
Figure 4.22 Block diagram of inner control loop with AD.	107
Figure 4.23 Current controller block diagram with AD.	108
Figure 4.24 Impact of AD block in resonance damping.	109
Figure 4.25 Block diagram of GCF control.	109
Figure 4.26 Block diagram of GCF with AD control.	111
Figure 4.27 Block diagram of CCF control.	112
Figure 4.28 Block diagram of equivalent CCF control.	113
Figure 4.29 Pole locations under GCF and CCF without AD.	114
Figure 4.30 Block diagram of equivalent CCF control with AD.	115
Figure 4.31 Magnitude and phase response of <i>LCL</i> -filters under distinct damping factors.	118
Figure 4.32 Phase lag of <i>LCL</i> -filter as a function of damping factor and the ratio of crossover frequency to resonant frequency.	119
Figure 4.33 Impact of PI-controller on magnitude and phase response.	121
Figure 4.34 Impact of decreasing damping factor shown by pole-zero map.	123
Figure 4.35 Step responses of $G_p(s)$ and $G_s(s)$	124
Figure 4.36 Impact of damping factor on phase margin (CCF).	125
Figure 4.37 Impact of K_p change on open-loop bode plot (CCF).	126
Figure 4.38 Root locus under K_p change (CCF).	127
Figure 4.39 Impact of K_p change on open-loop bode plot (GCF).	128
Figure 4.40 Root locus under K_p change (GCF).	129
Figure 4.41 Impact of K_p change on phase response (CCF) – detailed.	129

Figure 4.42 Root loci (a) GCF in high f_{res} (b) GCF in low f_{res} (c) CCF in high f_{res} (d) CCF in low f_{res}	133
Figure 4.43 Simulation outputs GCF with AD (low f_{res}).	137
Figure 4.44 Simulation outputs under GCF without AD (high f_{res} , $C_f=20\mu\text{F}$).....	138
Figure 4.45 Outputs under GCF and enabled/disabled AD (high f_{res} , $C_f=30\mu\text{F}$).	139
Figure 4.46 Various root-loci for Case I-II-III under GCF.	142
Figure 4.47 FFT of I_g and I_c ($C_f=20\mu\text{F}$) under GCF (a) w/o AD (b) with AD.....	143
Figure 4.48 FFT of I_g and I_c ($C_f=30\mu\text{F}$) under GCF (a) w/o AD (b) with AD.....	144
Figure 4.49 Simulation outputs under CCF without AD (low f_{res}).....	145
Figure 4.50 Simulation outputs under CCF without AD (high f_{res} , $C_f=20\mu\text{F}$).....	146
Figure 4.51 Simulation outputs under CCF with AD (high f_{res} , $C_f=20\mu\text{F}$).....	147
Figure 4.52 Dampening the resonance effect in CCF by AD (low f_{res}).	148
Figure 4.53 Various root-loci for Case I-II-III under CCF.	150
Figure 4.54 I_g harmonics (%) with CCF method for $C_f=20\mu\text{F}$ (a) I_g and I_c (b) I_g and I_c (AD).	151
Figure 4.55 Pole locations (Red CCF, blue GCF).....	152
Figure 4.56 Step response of I_g under GCF: $K_p=1.07$ ($\zeta=0.3$).	154
Figure 4.57 Step response of I_g under GCF: $K_p=1.07$ ($\zeta=0.707$).....	154
Figure 4.58 Step response of I_g under CCF: $K_p=1.07$ (Matched bandwidth with GCF).....	155
Figure 4.59 Step response of CCF: $K_p=1.51$ (Matched resonance damping with GCF).	155
Figure 5.1 LCL -filter design algorithm for passively damped resonance.	165
Figure 5.2 Harmonic attenuation against r	171
Figure 5.3 Magnitude and phase response of LCL -filter under various R_d	172
Figure 5.4 Open-loop pole-zero map under GCF ($\zeta_{ol} = 0.5$).....	173
Figure 5.5 Closed-loop pole-zero map under GCF ($\zeta_{cl} = 0.332$).....	173
Figure 5.6 Open-loop pole-zero map under CCF ($\zeta_{ol} = 0.5$).....	175
Figure 5.7 Closed-loop pole-zero map under CCF ($\zeta_{cl}=0.329$)	175
Figure 5.8 Simulation results of LCL -filter based VSC using $R_d=0.27\ \Omega$ under GCF.	178
Figure 5.9 Simulation results of LCL -filter based VSC using $R_d=0.82\ \Omega$ under GCF.	179
Figure 5.10 Simulation results of LCL -filter based VSC using $R_d=0.4\ \Omega$ under CCF.	180
Figure 5.11 Dynamic response of grid-current in dq -frame (a) GCF and (b) CCF.....	181

Figure 5.12 THD _i (%) vs. frequency (Hz).....	183
Figure 5.13 Efficiency change vs. load percentage under GCF.....	184
Figure 5.14 Harmonic content of I_{cf} against PWM methods under GCF.....	185
Figure 5.15 Harmonic content of I_{cf} against PWM methods under CCF.....	187
Figure 5.16 Determination of ω_c tuning zone.....	191
Figure 5.17 Proposed <i>LCL</i> -filter design algorithm.....	196
Figure 5.18 Proposed <i>LCL</i> -filter design algorithm (updated).....	200
Figure 5.19 Set of λ vs. α	202
Figure 5.20 Set of solutions for f_{sw} : [2-2.5] kHz, C_f : [0.01-0.05] p.u.....	204
Figure 5.21 Closed-loop bode plot for CCF ($\alpha=0.22$, $L_c=145\mu\text{H}$).....	207
Figure 5.22 Closed-loop bode plot for GCF ($\alpha=0.22$, $L_c=135\mu\text{H}$).....	208
Figure 5.23 Dynamic response for $\alpha=0.22$ (a) CCF, $L_c=145\mu\text{H}$ (b) GCF, $L_c=135\mu\text{H}$	209
Figure 5.24 Proposed controller tuning methodology for GCF technique.....	212
Figure 5.25 Designating ω_c zone for controller tuning.....	214
Figure 5.26 Pole-zero movements under GCF for (a) $\zeta=0.707$ (b) $\zeta=0.5$	217
Figure 5.27 Step responses under GCF for $\zeta=0.707$ (a) $K_p=[0.3:0.6]$ (b) $K_p=[0.35, 1]$	219
Figure 5.28 Bode plots for $\zeta=0.707$ (a) Open-loop (PM: 55.2°, 36.1°) (b) Closed-loop (PM: 110°, 12.5°).....	220
Figure 5.29 Step response under GCF at $\zeta=0.5$ for $K_p=[0.35,1]$	221
Figure 5.30 Proposed control algorithm for inherent damping (ID).....	222
Figure 5.31 Closed-loop bode plot under CCF control ($L_c=145\mu\text{H}$, $\alpha=0.22$).....	224
Figure 5.32 Closed-loop bode plots (a) $K_d=0$ (b) $K_d=0.93$	225
Figure 5.33 Pole movements under CCF control for $L_c=145\mu\text{H}$ (without AD).....	226
Figure 5.34 Pole movements under CCF control for $L_c=145\mu\text{H}$ (with AD, $K_d=0.32$).....	227
Figure 5.35 Step response under CCF control for $L_c=145\mu\text{H}$ (with AD, $K_d=0.93$).....	227
Figure 5.36 Bode plots under GCF control for $K_p=0.36$ (a) Open-loop (b) Closed-loop....	229
Figure 5.37 Bode plots under CCF control for $K_p=0.82$ (a) Open-loop (b) Closed-loop....	229
Figure 5.38 Step response comparison between CCF and GCF control.....	232
Figure 6.1 One converter leg (a) 2L (b) 3L-NPC (c) 3L-T.....	238
Figure 6.2 Brand new diode-less bidirectional switch for 3L-T.....	241
Figure 6.3 Conduction loss calculation block.....	242

Figure 6.4 Switching loss calculation block.....	243
Figure 6.5 Semiconductor losses (W) vs. time (ms) at $f_{sw}=2$ kHz: (a) 2L-VSC	244
Figure 6.6 Junction temperature ($T_j(C^\circ)$) vs. time (ms) at $f_{sw}=2$ kHz:(a) 2L-VSC (b) 3L-NPC (c) 3L-T.....	245
Figure 6.7 Semiconductor losses (W) at $f_{sw}=2$ kHz: (a) 2L (b) 3L-NPC (c) 3L-T	245
Figure 6.8 IGBT Loss (kW) vs. f_{sw} (kHz) plot of three VSC topologies under SVPWM...	246
Figure 6.9 Assumed total filter loss vs. rated MVA (for full-load).....	247
Figure 6.10 Core loss modeling against switching frequency (kHz).....	249
Figure 6.11 <i>LCL</i> -filter loss vs. load (%) characteristic.	250
Figure 6.12. η (%) vs. f_{sw} plot of three VSC topologies under SVPWM.	251
Figure 6.13 With the inclusion of <i>LCL</i> -filter loss, η (%) vs. load (%) characteristic (a) 2L- VSC ($f_{sw}=2$ kHz) (b) All topologies under $P_{fe}=25\%$	253
Figure 6.14 2L-VSC voltage vectors.....	255
Figure 6.15 Δi_{max} (%) vs. m_i plot under SVPWM and DPWM1 (a) 2L-VSC (b) 3L-VSC. 256	
Figure 6.16. η (%) vs. f_{sw} (SVPWM and DPWM1).....	258
Figure 6.17. THD _i (%) vs. $L_c(\%)$ under SVPWM and DPWM1 (a) 2L (b) 3L (c) 2L&3L (Full load i.e. THD=TDD).	259
Figure 6.18 THD _i (%) vs. L_c and f_{sw} : (a) 2L-SVPWM (b) 2L-DPWM1	260
Figure 6.19 Δi_{max} (%) vs. m_i plot under SVPWM and DPWM1 (a) 2L-VSC (b) 3L-VSC ($f_{sw}=2$ kHz for SVPWM, $f_{sw}=3$ kHz for DPWM1).	261
Figure 6.20 Δi_{max} (%) vs. m_i plot of 3L-VSC under SVPWM and DPWM1.....	262
Figure 6.21 WTHD vs. m_i plot under SVPWM and DPWM1 ($f_{sw}=2$ kHz for SVPWM, $f_{sw}=3$ kHz for DPWM1).....	263
Figure 7.1 Simplification to topological comparison.	271
Figure 7.2 Simplified PSMU topologies.....	271
Figure 7.3 Complete design flow diagram (dashed boxes provide supplementary information for the related step).....	272
Figure 7.4 η (%) vs. f_{sw} plot of three VSC topologies under SVPWM.....	274
Figure 7.5 Proposed <i>LCL</i> -filter design algorithm	277
Figure 7.6 (a) Ripple (%) vs. L_c (%) (b) THD _i (%) vs. L_c (%).....	278
Figure 7.7 Harmonic attenuation vs. r	279

Figure 7.8 Achieving identical output	280
Figure 7.9 THD _i (%) vs. L_c under SVPWM (a) $f_{sw-2L}=2$ kHz, $f_{sw-3L}=0.25f_{sw-2L} \div 1.5f_{sw-2L}$ (b) $f_{sw-2L}=2$ kHz, $f_{sw-3L}=0.95$ kHz.	281
Figure 7.10 Ripple (%) vs. L_c under SVPWM	282
Figure 7.11 Power curve of MWT62/1.0	283
Figure 7.12 Modified MWT62/1.0 power curve.	284
Figure 7.13 η (%) vs. load (%) characteristic for all topologies.	287
Figure 7.14 Improvement brought by 3L-T _{RB} -IGBT in η (%) vs. load (%) characteristic under $P_{fe}=25\%$	292
Figure 8.1 PLL structures for three phase grid synchronization.	301
Figure 8.2 Simulation screen for three-phase 2L-VSC (Main body).....	302
Figure 8.3 The circuit model of the control loops.	303
Figure 8.4 The circuit model of the PWM signal generation unit.....	303
Figure 8.5 The circuit model of the PLL implementation.	303
Figure 8.6 The circuit model of the distorted grid voltage.	304
Figure 8.7 Implementation of the semiconductor loss calculator block.	304
Figure 8.8 Modeled wind power (green) and I-V (red-blue) characteristics.	306
Figure 8.9 DC bus voltage ripple.	307
Figure 8.10 Grid-side currents (blue I_{ga} , red I_{gb} , green I_{gc}).	307
Figure 8.11 Capacitor currents (blue I_{cfa} , red I_{cfb} , green I_{cfc}).	308
Figure 8.12 Phase a grid-side voltage and current (blue I_{ga} , orange V_{ga}).	308
Figure 8.13 Phase a grid-side voltage and PLL output (blue V_{ga} , red $V_g * \cos\theta$).	308
Figure 8.14 PLL vs. time.	309
Figure 8.15 α vs. β frame components of grid-side current.	309
Figure 8.16 Dynamic response of DC-link voltage (blue), input power (green).	310
Figure 8.17 Dynamic response of DC-link voltage (purple) and grid currents (blue I_{ga} , red I_{gb} , green I_{gc}).	311
Figure 8.18 DC bus voltage ripple.	312
Figure 8.19 Grid-side currents (blue I_{ga} , red I_{gb} , green I_{gc}).	312
Figure 8.20 Capacitor currents (blue I_{cfa} , red I_{cfb} , green I_{cfc}).	313
Figure 8.21 Phase a grid-side voltage and current (blue I_{ga} , orange V_{ga}).	313

Figure 8.22 Phase a grid-side voltage and PLL output (blue V_{ga} , red $V_g \cdot \cos\theta$).	314
Figure 8.23 PLL vs. time (s).	314
Figure 8.24 α vs. β frame components of grid-side current.	314
Figure 8.25 Dynamic response of DC-link voltage (blue), input power (green).	316
Figure 8.26 Dynamic response of DC-link voltage (purple) and grid currents (blue I_{ga} , red I_{gb} , green I_{gc}).	316
Figure 8.27 DC bus voltage ripple.	317
Figure 8.28 Grid voltages (blue V_{ga} , red V_{gb} , green V_{gc}).	317
Figure 8.29 Grid-side currents (blue I_{ga} , red I_{gb} , green I_{gc}).	318
Figure 8.30 Capacitor currents (blue I_{cfa} , red I_{cfb} , green I_{cfc}).	318
Figure 8.31 Phase a grid-side voltage and current (blue I_{ga} , orange V_{ga}).	319
Figure 8.32 Phase a grid-side voltage and PLL output (blue V_{ga} , red $V_g \cdot \cos\theta$).	319
Figure 8.33 PLL vs. time.	319
Figure 8.34 α vs. β frame components of grid-side current.	320
Figure 8.35 FFT analysis of I_g (Graph).	320
Figure 8.36 FFT analysis of I_g (Table).	321
Figure 8.37 Dynamic response of DC-link voltage (blue), input power (green).	322
Figure 8.38 Dynamic response of DC-link voltage (purple) and grid currents (blue I_{ga} , red I_{gb} , green I_{gc}).	322
Figure 9.1 Overview of the study together with the favored methods under considered topologies.	333

LIST OF ABBREVIATIONS

2L-VSC	Two-level Voltage Source Converter
3L-VSC	Three-level Voltage Source Converter
AD	Active Damping
BW	Bandwidth
C.F	Capacity Factor
CCF	Converter Current Feedback
CEC	California Energy Commission
DPWM1	Discontinuous Pulse Width Modulation 1
DSP	Digital Signal Processor
ESR	Equivalent Series Resistance
GCF	Grid Current Feedback
HAWT	Horizontal Axis Wind Turbine
IGBT	Insulated Gate Bipolar Transistor
MOSFET	Metal Oxide Semiconductor Field Effect Transistor
PD	Passive Damping
PLL	Phase Locked Loop
PM	Phase Margin
PV	Photovoltaic
PWM	Pulse Width Modulation
SCC	Short Circuit Power
SCR	Short Circuit Ratio
SVPWM	Space Vector Pulse Width Modulation
TDD	Total Demand Distortion
THD	Total Harmonic Distortion

TSO	Transmission System Operator
WPP	Wind Power Plants
WT	Wind Turbine

CHAPTER 1

INTRODUCTION

1.1. Background and Motivation

Electrical energy is the main artery of modern life. It is widely utilized almost every aspect in daily life in order to provide life functioning. Electrical heaters, electric lamps, electric motors widely employed in domestic and industrial applications, home appliances, industrial applications, and so on create a vast demand on electricity.

Nevertheless, recent industrial developments, developing technology and the excessive growth of human population not only increase the demand on energy but also compel the mankind to find alternative energy sources due to the declining fuel based energy sources. If the energy demand grows in this pace, overall energy consumption of the world is expected to be increased by 42.7% by the end of 2035 [1]. Nowadays, fossil fuels meet a great proportion of the energy need of the world, increasing CO₂ emission in a great extent and its footprint on nature is unrecoverable. Owing to this threat, countries are heading towards renewable energy sources in order not to jeopardy the lives of future generations. Thus, popularity of the renewable energy sources such as hydro, wind, and photovoltaic (PV) energy is rising day by day.

By the end of 2013, global cumulative installed wind capacity is around 318.1GW based on the data provided by Global Wind Energy Council, GWEC [2] in Figure 1.1. It is evident from this figure that wind capacity has grown substantially in recent years. In the light of the numbers, the annual wind energy capacity has grown by 12.5% in 2013 [2]-[3]. Besides, it is expected that total installations should nearly

double from today's numbers by the end of the period, going from just over 300 GW today to just about 600 GW by the end of 2018 [3]. Furthermore, governments make new policies to incite the installations of renewable energy systems, particularly wind energy systems. They supply grants and reduce taxes for entrepreneurs to attract their attention into this field. Therefore, it may further accelerate the growth this expected growth rate.

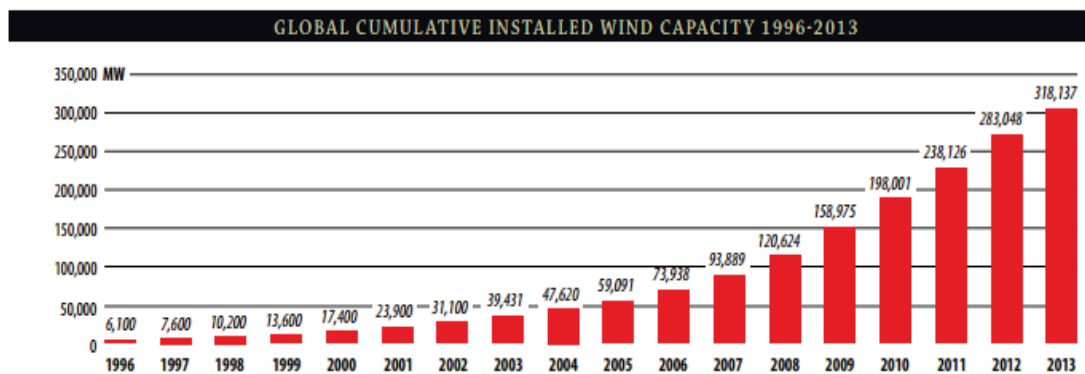


Figure 1.1 Global cumulative installed wind capacity [2].

According to Siemens internal forecasts, global generation capacity of electricity is expected to nearly double from today's 6,500 GW to 10,500 GW by 2030. And by 2035, renewables will already be generating more than 25% of world's electricity, with a quarter of this coming from wind, being the second largest renewable energy source after hydro power according to the International Energy Agency (IEA) [2].

Another great impact that appeals the installation of wind turbine systems is simply, the decline of wind turbine installation costs while the other means of energy production cost is increasing continuously. Between 1980 and the early 2000s, significant reductions in capital cost and increases in performance had the combined effect of dramatically reducing the levelized cost of energy (LCOE) for onshore wind energy [4]. Data from three different historical evaluations, as highlighted in Figure 1.2, illustrate that the LCOE of wind power declined by a factor of more than

three, from more than \$150/MWh to approximately \$50/MWh between 1980s and the early 2000s (Figure 1.2). However, beginning in about 2003 and continuing through the latter half of the past decade, wind power capital costs increased—driven by rising commodity and raw materials prices, increased labor costs, improved manufacturer profitability, and turbine upscaling—thus pushing wind’s LCOE upward in spite of continued performance improvements (Figure 1.2) [4].

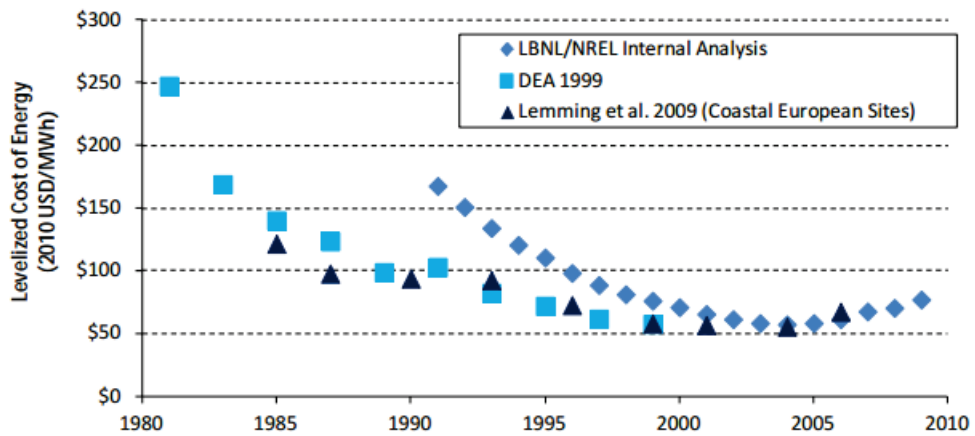


Figure 1.2 Estimated LCOE for wind between 1980-2009 for US and Europe [4].

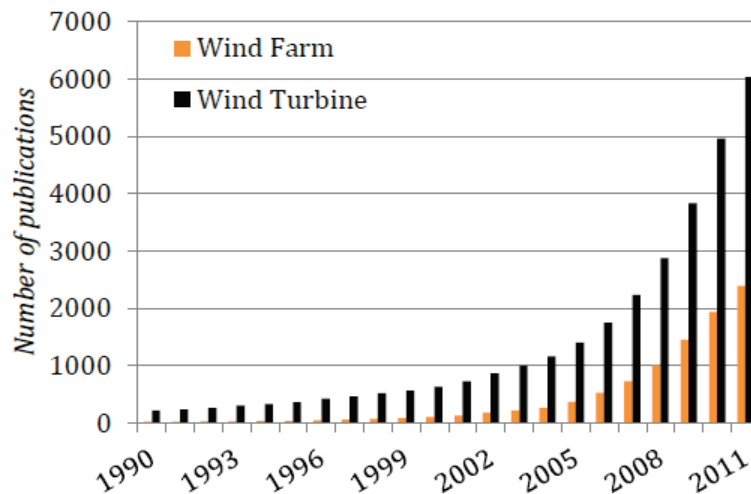


Figure 1.3 Total number of publications about wind turbines and wind farms [5].

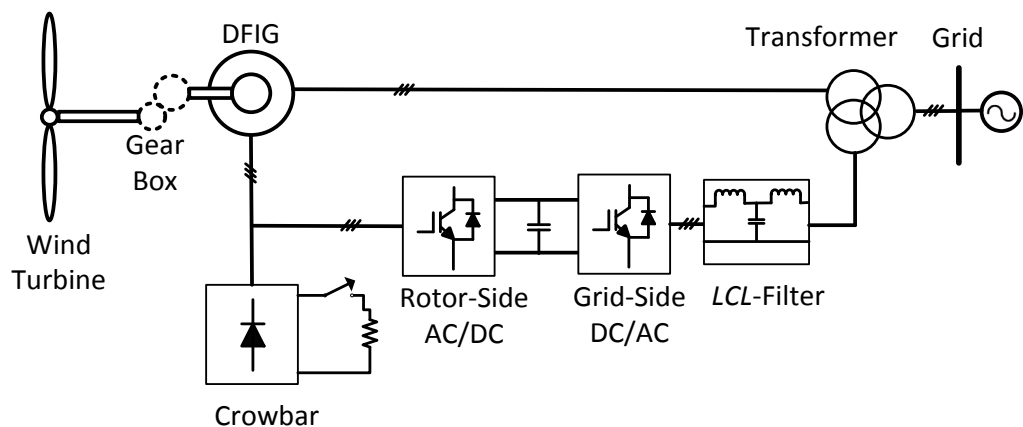
Lastly, in agreement with the increase in cumulative wind turbine installations shown in Figure 1.1, the researches on this topic have escalated extensively [5]. The general interest in wind power can be easily seen in the increasing number of publications by years as depicted in Figure 1.3.

Apart from the benefits, advantages and innovations brought by wind energy systems; there are also drawbacks and challenges in this branch naturally. First of all, wind energy sources may be geographically far away from the settlements and installations where the energy is needed. Thus, circulating the current along a long distance through the power system not only degrades the effectiveness but also make the production vulnerable against natural and man-made hazards [4]. Secondly, flicker problems may arise at the point of common coupling (PCC) due to the unpredictable and intermittent nature of the wind [2][3]. Besides, the instantaneous real and reactive power of the source and the grid should be matched to continue nominal voltage and frequency of the grid, which is a hard task to achieve in the case of wind energy due to the difficulties in estimating the wind speed nearly instantaneously. Nowadays, the wind energy interface to the grid has reached very large amounts, making disconnection of wind farms during any fault condition impossible. For this reason, there are a number of international grid codes and standards that the individual wind turbines and wind farms should comply with during both balanced and unbalanced situations [3][6]. All of these specific constraints will be considered in much detail in Chapter 2.

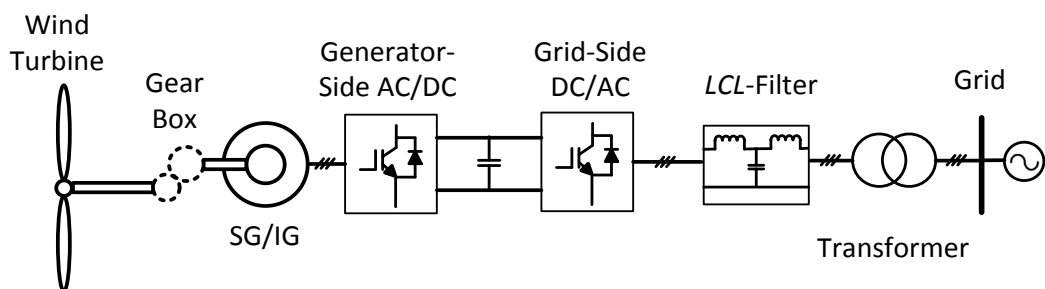
The majority of installed wind turbines are connected to the bulk power system. They are rarely installed singly, instead being installed in groups of tens or hundreds of similar turbines (wind farms) which group the generated power and supply it to the power system through an interfacing network known as the collector system [6]. All in all, wind turbine applications are grouped as wind farms (hundreds of MW) and individual turbines (500kW-4MW, for special wind generator topologies max. 7MW nowadays) that are connected to the grid through PCC. Further details about the voltage levels and so on will be provided in Chapter 2.

1.2. Typical Wind Turbine Configurations

The utilization of the power electronics in recent wind turbine system can be divided into two categories, namely: a wind turbine system with partial-scale power converter and a wind turbine system with full-scale power converter, which both are illustrated in Figure 1.4 (DFIG: Doubly-Fed Induction Generator, SG: Synchronous Generator, IG: Induction Generator). There are also different types of wind turbine topologies in the literature but these two structures are favored in most of the applications [8].



(a) Back-to-back PWM-VSC for wind turbine system with partial-scale converter.



(b) Back-to-back PWM-VSC for wind turbine system with full-scale converter.

Figure 1.4 Typical configurations for wind turbine system.

As the most widespread configurations for wind turbine systems are introduced, it is evident that back-to-back PWM-VSC cascaded with *LCL*-filter configuration is mutual in both systems. Thus in this chapter, as descending into particulars of wind turbine systems step by step, back-to-back converter topology will be the next topic to be focused in the following section. Then, further specialization in the power converters aspect will be made.

1.2.1. Wind Turbine System with Full-Scale Power Converter

As shown in Figure 1.4(b), the full-scale power converter configuration equipped with synchronous generator (SG) or induction generator (IG) is considered as a promising technology for multi-MW wind turbine system [6] [8]. The generator stator winding is connected to the grid through a full-scale power converter, which performs the reactive power compensation and also a smooth grid connection for the entire operating speed. Some variable speed wind turbine system may become gearless by introducing the multi-pole generator [6]. The elimination of the slip rings, simpler gearbox and full power controllability during the grid faults are the main advantages. However, in order to satisfy the power rating, the widely used approach nowadays is to implement several converter modules or power devices in parallel, which of course are challenging the complexity and reliability of the whole wind turbine system [8].

In this dissertation, wind turbine system with full-scale converter will be the focus. Due to the extensive and well-established knowledge, as well as the simpler circuit structure and fewer components, the back-to-back VSC is the most attractive solution in the commercial market of wind turbines [8]. Back-to-back VSC configuration is simply a cascaded topology of AC/DC and DC/AC VSCs as evident in Figure 1.4. In this configuration, dynamic circulation of energy back and forth through the switches can be achieved.

As agreed in Figure 1.4, wind energy is transferred to the generator through gear box and converted into AC power. Then, generator-side AC/DC converter produces DC power that is the input of grid-side DC/AC converter. In this thesis, the design of the

grid-side DC/AC converter is of particular interest and will be the primary focus. Its comprehensive design procedure in conjunction with the low-pass *LCL*-type filter design will be the framework of this dissertation. Grid-side DC/AC VSC is the most critical part of the wind turbine system since the produced AC power injected to the grid must comply with stringent grid codes. For this reason, design process requires special attention and deep knowledge beyond know how design approaches.

1.2.2. Three-Phase Grid-Side DC/AC PWM-VSC (Two/Three-Level)

Three-phase pulse width modulation voltage source converter (PWM-VSC) is one of the most favorable interface devices to the power grid for many applications, particularly in renewable energy systems. As renewable energy projects are spreading all over the world rapidly, three-phase PWM-VSCs are getting more popular due to enhanced controllability, high efficiency, reliable performance with long life and simplicity. Also, they possess superior advantages over conventional converters such as adjustable power factor, high efficiency and flexibility.

Power range of grid connected three-phase PWM-VSC based renewable energy systems covers 100kW-7MW and such systems are classified according to the power levels of an application. For instance, solar energy (PV) applications (of solar farms, involving central inverters) are effective for the power ranges starting from typically 100 kW up to 1 MW whereas; wind power converters are generally designed for 500 kW-7 MW power scale nowadays [6].

Existing VSC topologies used in physical power system operations can be classified as the conventional three-phase two-level converter and the three-phase three-level converter based on the neutral-point-clamped (NPC-type) and T-type converter [5] [6][8][9]. There are also other VSC topologies based on different combinations of the NPC-type and multilevel converters. Minimization of the switching frequency of the semiconductors employed in VSC and production of a high-quality sinusoidal voltage waveform with minimum or no filtering requirement are the mutual objectives of these topologies.

Three-phase two-level (2L) VSC is the most appealing solution owing to its popularity, simplicity and well-established information in the literature. However, particularly for high power wind turbine designs the two-level (2L) VSC topology reaches the design limits due to the restricted technology of power semiconductors that can be switched up to only a few kHz. For this reason, the maximum rated output power can reach at most a few MW in modern wind turbines utilizing 2L-VSC as the grid-side converter. For larger power capacity wind turbine designs that 2L-VSC is not feasible; utilization of higher level VSC is favored. In the literature, three-level (3L) topologies and multi-level topologies are widely used beyond the power levels that the utilization of 2L-VSC is not viable [7]. In Chapter 6, utilization of three-level (3L) VSC topologies (NPC and T-type) as alternatives to 2L-VSC in low-voltage high power applications will be examined under several power levels and operating conditions. Then, the most lucrative and optimal topology among 2L, 3L-NPC and 3L-T is highlighted with respect to the financial aspect of the power electronics [7].

To sum up, this thesis will focus on three-phase two-level and three-phase three-level PWM-VSC (NPC and T-type) design particular for individual wind turbine applications within 500 kW-7 MW power scale [6]. Certainly, smaller power levels will also be provided throughout the analysis in the following chapters to represent individual low power scale wind turbines (Chapter 4-5).

The conventional three-phase 2L-VSC topology using six IGBT switches is depicted in Figure 1.5. It consists of three legs, with two IGBTs mounted on each leg [7][15]-[20]. Additionally, each IGBT has an anti-parallel diode to allow bidirectional current flow. A bulky dc-link capacitor is placed on the DC side to supply a source of reactive power when needed [15]-[20].

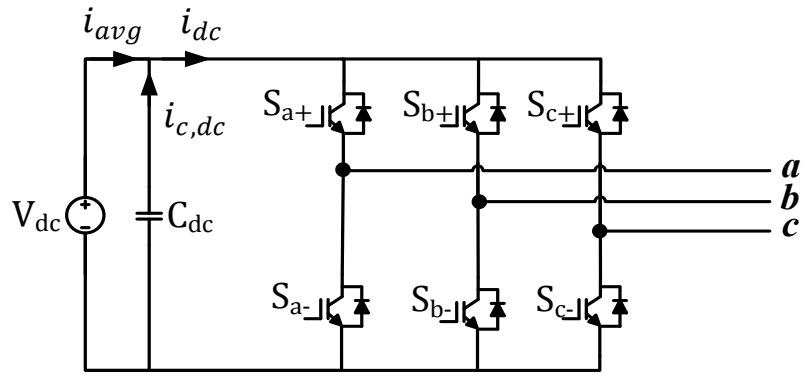


Figure 1.5 Standard three-phase two-level VSC topology.

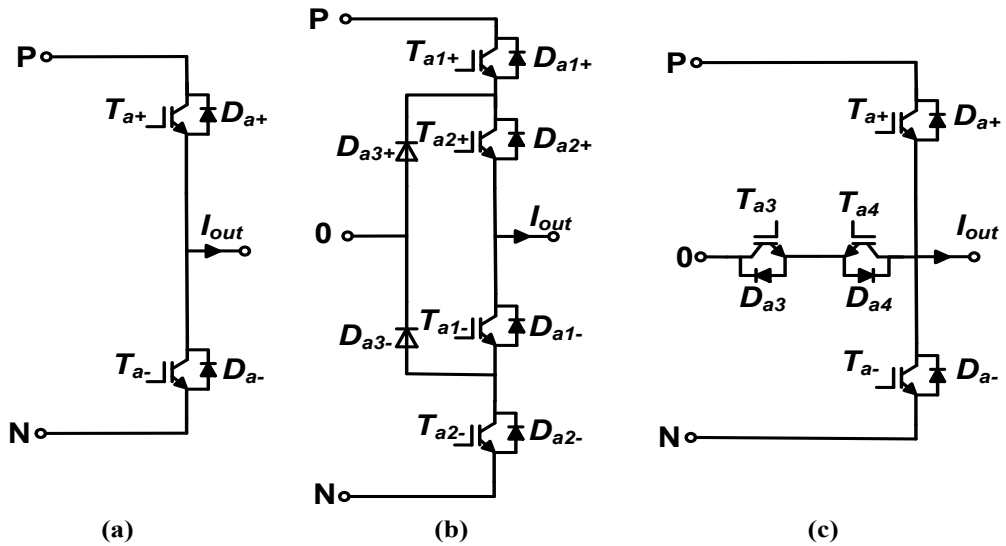


Figure 1.6 One converter leg (a) 2L (b) 3L-NPC (c) 3L-T.

Figure 1.6 introduces one leg diagrams of 2L-VSC, 3L-NPC and 3L-T VSC topologies in (a), (b) and (c) respectively. All three converter legs of Figure 1.5 shall be replaced with the 3L leg modules of Figure 1.6, to obtain the full schemes of 3L-NPC and 3L-T type VSCs [7].

In order to generate proper switching sequence of the gate signals, there is a switching control block, which is an essential part of the VSC. The aim of this control block is to produce an output voltage waveform as close as possible to a pure

sinusoidal waveform, with high power controllability and minimum switching loss. For this purpose, PWM techniques are widely used in VSC switching strategies [9]. In PWM methods, the switches are forced to be turned on and off at a rate considerably higher than the fundamental frequency. The output wave is chopped and the width of the resulting pulse is modulated. Undesirable harmonics in the output waveform are shifted to the higher frequencies, and filtering requirements are much reduced [9]. Further details concerning different PWM patterns will be provided in Chapter 4, 5 and 6.

1.2.3. *LCL*-Type Filter Configuration in Grid-Connected Systems

The connection to the electric utility is provided through low-pass filters, particularly via *LCL*-line filters in modern PWM VSCs ensuring a more compact system and better harmonic attenuation compared to the conventional *L*-filters and *LC*-filters. In this dissertation, *LCL*-type filter is preferred. Figure 1.7 demonstrates a three-phase 2L-VSC connected to the grid through an *LCL*-filter. *LCL* components in each phase in Figure 1.7 shall be replaced with either *L*-filter or *LC*-filter, to obtain the full schemes of grid connected three-phase 2L-VSC system with *L*-filter and *LC*-filter, respectively.

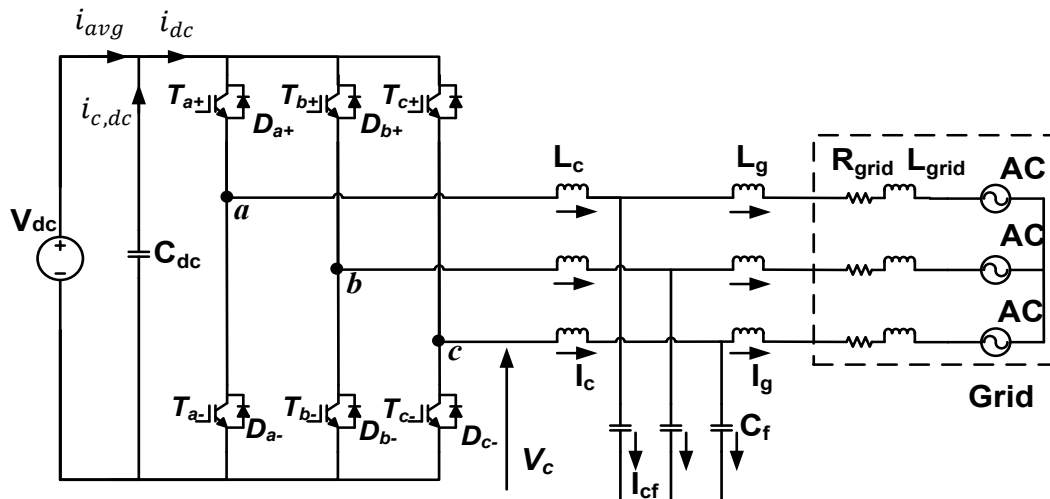


Figure 1.7 Grid connected three-phase 2L-VSC system with *LCL*-filter.

Before discussing the benefits introduced by the *LCL*-filter; low-pass filter configurations in grid connected applications are mentioned briefly as follows.

For *L*-Filter as a first order filter, ordinary inductor filter attenuation is -20 dB / decade over the entire frequency range. In the applications where this filter is used, the frequency of VSCs switching has to be high enough for sufficient attenuation of the VSC harmonics [10].

LC-filter is a second order filter and it achieves -40 dB / decade attenuation. For further attenuation of the switching components, a shunt element is required, because *L*-filter already provides low attenuation of the inverter switching components. As a shunt element, a capacitor is applied for this purpose. For *LC*-filter the load impedance across *C* becomes comparatively high for the values at and above the switching frequency. The cost and the active power consumption of the *LC*-filter are higher compared to the *L*-filter due to the additional shunt element.

The last but the not least filter configuration is *LCL*-filter. *LCL*-filter is beneficial since its attenuation is better in terms of inverter switching harmonics compared to *L* and *LC*-filters. Its area of utilization grows day-by-day particularly in renewable energy projects. The crucial benefits brought by *LCL*-filter configuration are summarized below:

- i. Production of reactive power and distortion of low grid current;
- ii. -60 dB/decade attenuation for frequency values which are excessive of the resonance frequency;
- iii. Opportunity of applying a relatively low switching frequency for a given harmonic attenuation.

If inductance value on the converter side is low, complying with stringent grid standards is difficult without using a *LCL*-filter. Achievements of lower levels of harmonic distortion with lower switching frequencies and with less overall stored energy are possible if *LCL*-filter is used. However, *LCL*-filter cause dynamic and steady state input current distortion owing to resonance.

According to the vast number of articles and publications regarding *LCL*-filters in the literature, it is proven that *LCL*-line filters are useful on PWM switching harmonic attenuation [11]-[14]. Moreover, it is favorable over ordinary *L*-filters in terms of size and weight. Single *L* filters are relatively bulky and costly for particularly in high power applications in which switching frequency is bounded with a few kHz. All in all, *LCL*-line filters provide a more compact size and dynamic response.

A thorough study concerning *LCL*-filters is provided in Chapter 4 and Chapter 5. Chapter 4 consists of stability and controllability issues with an extensive theoretical background supported well by simulation results and MATLAB[®] tools whereas Chapter 5 addresses the comprehensive design procedure for *LCL*-filters employed in VSCs.

1.2.4. Design Challenges

For the mentioned high power range of wind power VSC design (500 kW-7MW), size, cost, cooling, weight, efficiency, maintenance, etc. start to become severe constraints of the design. For instance, for an optimum efficiency expectation, switching frequency must be kept low. Low switching frequencies not only degrade the filtering performance but also force extensive increase in the size of the filters. Due to the high power rating, semiconductor switches become more expensive, bulkier and cooling turns into a harder issue, making the system even more bulky and costly due to the presence of large heat sinks and/or more complex cooling hardware. Since the electrical equipment reside in a box on top of the tower that the turbine blades connected to the electrical system via a gear box, all of these components must be carried on top of the tower. This situation rather obstructs the maintenance. Besides, increased power levels has also raised the overall weight of the converter substantially, in return requiring a much stiffer tower and leading to a harder hoisting of the operation.

1.3. Scope of the Thesis

The framework of the thesis is design of three-phase PWM-VSC widely used for grid-interface of renewable energy systems, particularly of wind turbine systems. The design procedure also involves devising the optimal *LCL*-filter parameters, determining the switching frequency, the PWM method, the VSC topology (two-level, three-level NPC, three-level T), the cost-effective feedback controlled algorithm, etc. for the VSC. Then, the design is verified by means of detailed computer simulations and computer based mathematical tool outputs. The study takes into account the balanced and unbalanced grid conditions, which may occur in the grid operating conditions. Several power ratings, operating conditions and financial aspects are considered to provide a thorough performance evaluation of the designed system.

The primary contribution of this thesis is to provide a top to bottom design methodology that can span a wide power scale of grid connected PWM converters employed in wind turbine systems (under different PWM methods, VSC topologies, load conditions, modulation indices and switching frequencies) and yield the optimum;

- i. Filtering including the design of *LCL*-parameters and control scheme,
- ii. Topology among two-level (2L), three-level NPC (3L-NPC) and three-level T (3L-T) VSCs,
- iii. PWM method;

that provide the lowest cost solution while fulfilling the design requirements.

In the literature [8]-[10], [11]-[14], proposed design methods consider only the preferred methodology (topology, PWM method, set of filter parameters, current control technique, etc.) under the specified working conditions (rated power, switching frequency, full load, etc.). For this reason, as the primary contribution of this thesis work, the novel design algorithm can span a wide range of power levels under different PWM methods, VSC topologies, load conditions, modulation indices, switching frequencies, and set of filter parameters. Thus, design results for

different systems with different performances can be evaluated and compared, allowing a better determination of a suitable system.

The second main contribution of this thesis is the novel *LCL*-filter design algorithm. In the literature [11]-[14], proposed filter design algorithms are more or less superficial since they do not put much emphasis on the stability concern throughout the *LCL*-design phase apart from implementing several conventional know-how design tips. However, this dissertation descends in the particulars of *LCL*-design phase by involving the location of the resonance frequency as well as the impact of the different current feedback methods (grid-side, converter-side) on the *LCL*-design phase. In this aspect, novel control block diagrams, optimum damping hints and more are contributed to the literature.

The third main contribution of this dissertation is the figure of merit called operational efficiency. Literature lacks an operational efficiency definition that involves large scale of power converters employed in large scale wind turbine generators. Thereby, a simple procedure is proposed which takes into account the wind characteristics and capacity factor and yields coefficients for the operational efficiency formula for the specific application based on the capacity factor and wind speed. Hence, a fair calculation of the operational efficiency of a unit is achieved.

This dissertation consists of nine chapters.

Chapter 2 elaborates the types of wind energy systems according to their output power level and intermittency characteristics. A number of statistical data concerning the proportion that wind turbine (WT) applications constitute in the total installed capacity both in domestic and worldwide aspects are provided. Additionally, the insights on WT applications are broadened in terms of capacity factor, power quality i.e. grid code requirements regarding the type and location (country, geographical conditions, etc.) of the application, fault conditions and transformer structures on PCC connection in the light of individual and farm applications.

Chapter 3 states determination of switching frequency constraint of the converter design using efficiency constraint by taking the type of VSC topology and PWM pattern into account.

Chapter 4 provides the extensive control background of the grid-connected PWM VSCs utilizing *LCL*-type filters. Optimum damping hints are provided regarding active damping, passive damping and inherent damping techniques. The importance of the location of resonant frequency is also studied and exemplified via comprehensive case studies. Additionally, the main differences between grid-side feedback and converter-side feedback, which are not mentioned in the literature in such a clear way, are well-explained based on thorough MATLAB[®] and simulation outputs.

Chapter 5 discusses the *LCL*-filter design methods by comparing the conventional methods presented in literature with the novel design algorithm intrinsic to this thesis work. The design algorithm puts special emphasis on the controllability and stability issues of *LCL*-filters and involves them into the design phase. Thereby, optimum filter components in terms of size, cost, filtering performance and reliability are delivered. In the final part, a novel fine tuning methodology for controller and active damping gain constants are provided for each of grid-side current control and converter-side current control.

Chapter 6 affords a brief topological comparison of two-level and three-level VSC regarding differences in hardware components and semiconductor losses. Besides, a general scheme for calculation of switching and conduction losses of power semiconductors in computer simulations is provided. By merging these two, a detailed comparative study between 2L-VSC and 3L-VSC is conducted considering semiconductor loss, *LCL*-filter loss model, converter efficiency, converter-side current ripple and PWM pattern. Prominent differences between 3L-NPC and 3L-T are also mentioned.

Chapter 7 merges the content studied in the previous chapters and uses it as background and input to the analyses conducted in this chapter. In this chapter, an

extended top to bottom converter design algorithm is constructed such that it enables various system designs operating under distinct PWM method, *LCL*-filter parameter set, load, modulation index, and switching frequency. The design methodology starts with the determination of switching frequency constraint. Next, *LCL*-filter design and its stability analysis are completed. Then, investigation on finding optimum topological solution amongst VSC topologies of 2L, 3L-NPC, and 3L-T and optimal PWM method is provided by regarding the efficiency and grid-code requirements of the application. With the proposed design method, selection criterion for the best combination (VSC topology and PWM pattern) is reduced to economic assessment. For each combination, the pay-off time of the total initial cost is calculated and the one providing the shortest time period i.e. shortest pay-off time is highlighted as the optimum solution. Thus, a straightforward top to bottom converter design method becomes possible.

In Chapter 8, detailed performance analysis of three-phase 2L -VSC is conducted via the computer simulation software Ansoft – Simplorer[®][21]. For a selected power level, extended performance analyses including both transient and steady-state responses are provided under balanced and unbalanced grid conditions.

Finally, the dissertation concludes with a summary of information and experience gained throughout the study. Developments and future work are also addressed.

CHAPTER 2

WIND ENERGY SYSTEMS

This chapter is provided so as to clarify the requirements and restrictions dictated by recent international grid codes and standards particular for wind energy systems. Grid codes not only state the grid-connection properties regarding real power, reactive power, voltage and frequency but also assess the quality of the power injected into the grid. The optimal design of power electronics converters present in each wind turbine could only be achieved by taking those restrictions, limits, and specifications into account.

This chapter starts with recent developments in wind energy area and scope of the chapter is specialized step-by-step adopting the ‘general to particular’ approach. Firstly, wind power plants (WPPs) are elaborated after the introduction section. Secondly, as being one of the elements of WPPs, the general structure of individual wind turbines (WT) are considered. As the performance inspection criterion of the established WTs, “capacity factor ($C.F$)” definition is provided. Then, as the primary focus of this thesis, one of the power electronics converters of the full-scale individual wind turbines namely; grid-side DC/AC converter of the back-to-back PWM-VSC is regarded. As a remark, $C.F$ discloses the power rating that the grid-side DC/AC VSC operates. Thus, $C.F$ definition is an essential input for the grid-side VSC design phase. Finally, international grid codes and harmonic standards that the designed grid-side PWM-VSC should comply with are examined in quite detail. The flow of this chapter can be denoted simply: WPP→WT→grid-side VSC→capacity factor of WT and VSC →grid codes and harmonic standards.

2.1. Introduction

Renewable energy has gained a great attention in all over the world and its use is growing fast. Wind is an outstanding renewable energy source among others (geothermal, hydro, wave, tidal, biomass, solar). Wind energy has benefited from technical developments and subsidies which resulted in the higher penetration of wind power into the grid [22]. The fast growth of the wind energy stimulated many research and study in this field focusing on the integration of wind power to the conventional grid. Besides, governmental bodies have provided grants and funds for research supporting renewable energies [22]. Wind energy has many advantages such as carbon free energy production (no CO₂ emission), lower operational cost (no fuel requirement) and added capacity value to the power production system (contribution to meet peak demands) [22][23]. In Figure 2.1, increasing wind power installation worldwide can be observed for years 1996 to 2013 [22]. As can be seen, global annual installed wind capacity has been exponentially increasing recently.

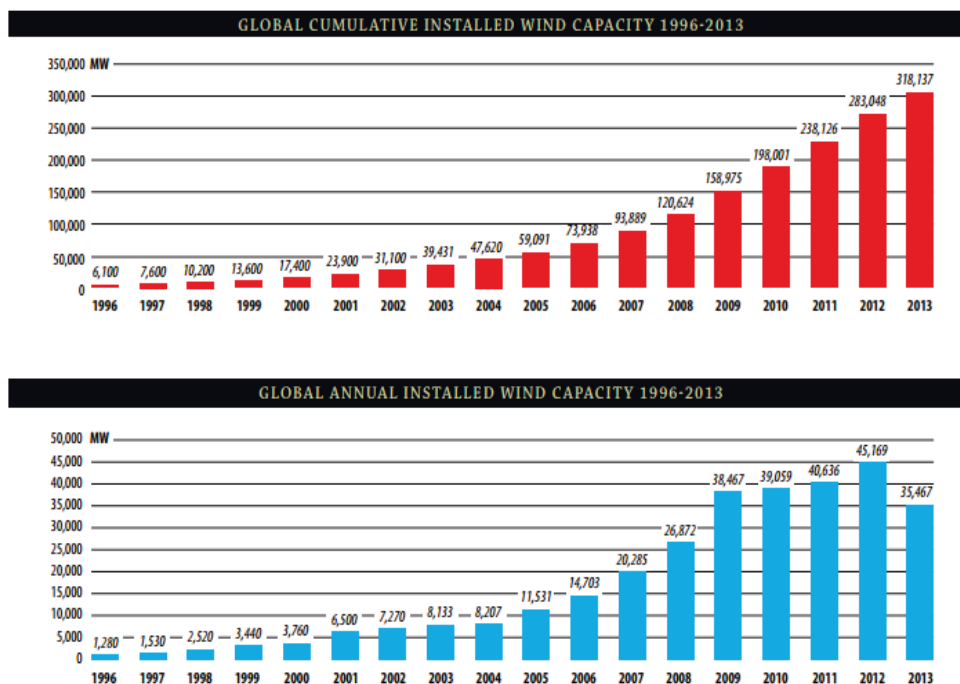


Figure 2.1 Global cumulative and annual installed wind capacity [22].

In Table 2.1, the installed wind power in Europe has shown for 2012, the capacity installed in 2013 and the total installed capacity in 2013. Germany is in the leading position with the highest installed wind power capacity. Spain has the second highest capacity after Germany. Denmark has also a good installed capacity with the largest domestic wind penetration (20%) and is expected to reach 50% level with the help of great connections to the ENTSO-E, Norway and Sweden [23].

Table 2.1 Wind power installed in European countries by the end of 2013 (MW).

	End of 2012	New on 2013	Total End of 2013
Germany	31270	3238	34250
Spain	22784	175	22959
United Kingdom	8649	1883	10531
Italy	8118	444	8552
France	7623	631	8254
Denmark	4162	657	4772
Portugal	4529	196	4724
Sweden	3746	724	4470
Poland	2496	894	3390
Turkey	2312	646	2959
Netherlands	2391	303	2693
Romania	1905	695	2600
Ireland	1749	288	2037
Greece	1749	116	1865
Austria	1378	308	1684
Rest of Europe	4956	832	5737
Total Europe	109817	12031	121474

It is expected that total installations should nearly double from today's numbers by the end of the period, going from just over 300 GW today to just about 600 GW by the end of 2018 as revealed in Figure 2.2 [22]. As can be seen in Table 2.1, Turkey is in the early stage of wind power utilization. However, there is well-known wind energy potential in Turkey which can be seen in Figure 2.3. Moreover, future projections for expansion of wind power in Turkey show that up to 20% penetration level of the total installed capacity is expected [24]. High penetration levels steer the

power system operators for revision of grid codes and investigation of the compatibility level for wind turbine grid connection. These integration studies are held by Turkish Electricity Transmission Company (TEIAS) and Energy Market Regulatory Authority (EMRA), since predicted impacts of wind power will be offset regarding grid regulations and codes [24].

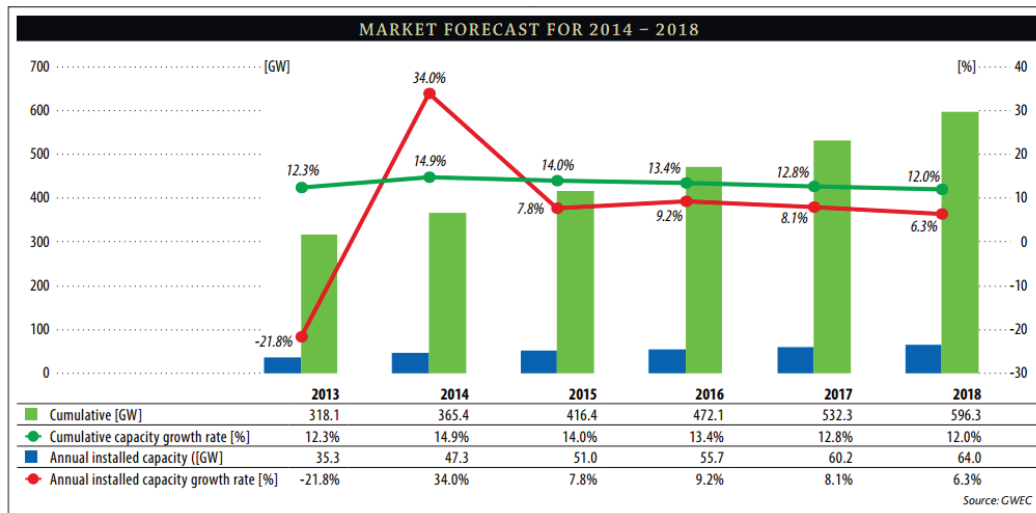


Figure 2.2 Global market forecast 2014-2018 [22].

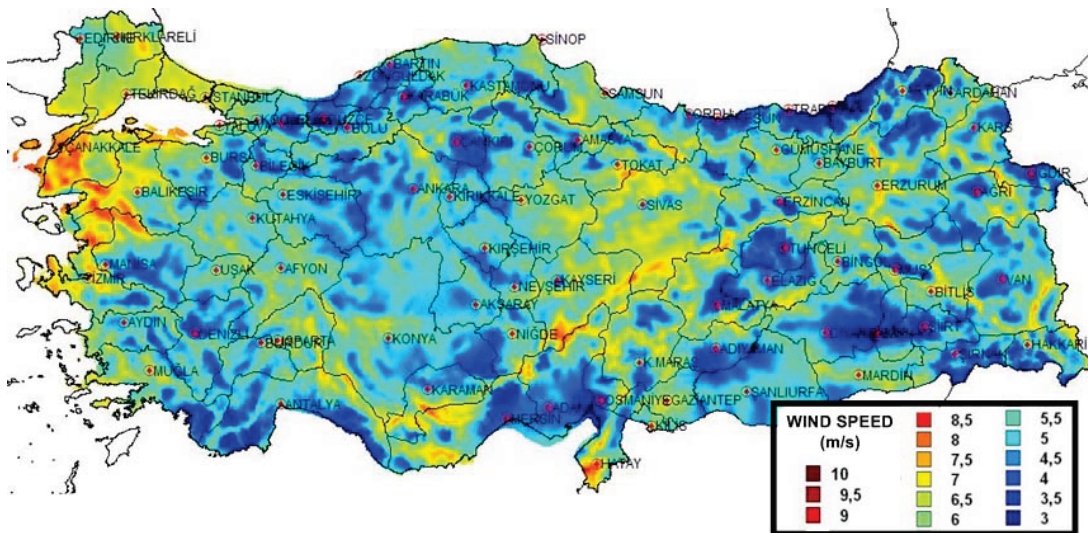


Figure 2.3 Turkey wind resource map at 50 m [24].

2.2. Wind Power Plants

Abovementioned progress and developments in wind energy has caused changes in conventional power system. Considering the circumstances, wind power is only advantageous if it is compatible with the existing regulations of power system operators. Wind farms should operate according to the current system condition for system reliability and stability as well as for further developments in wind energy. Before the wide expansion of wind energy, wind power had been utilized in medium and low voltage power distribution systems. Wind turbines were not suitable for participation in power system control responding to voltage or frequency disturbances [25]. In case of a system disturbance, wind turbines were disconnected and reconnected after fixing the fault as a common practice for handling the situation. Yet, this way of problem handling the problem has changed owing to high wind power penetration and recent technological developments in wind turbines [29]. Moreover, Transmission System Operators (TSOs), wind turbine producers and Wind Power Plant (WPP) developers would collaborate for integration of future wind installations and stability in power system operations.

Wind power integration studies can be summarized with categories shown below:

- i. Revising grid codes held by power system operators with developers of WPP for definition of WPP connection, planning and operation.
- ii. Technological developments in wind turbines held by wind turbine manufacturers.
- iii. WPP connection studies regarding the WPP infrastructure and controller, performed by WPP developers to meet requirements in grid code or following technical regulations.

Conventional power plants mostly consist of synchronous generators. Therefore, they are capable of supporting the power system by providing inertia response, re-synchronizing torque, oscillation damping, short circuit capability and voltage recovery when system faults occur [26]. Thus, conventional power plants are able to comply with the grid codes owing to these features. Hence, existing power system operators show stability and reliability in grid operations. However, WPPs have

completely different properties and conditions which introduce extra considerations to the control systems. Control structure of WPPs is not straightforward as in conventional power plants as described above. Aspects of the WPPs can be summarized as below [26]:

- i. Wind turbines produce power in WPPs. They have a converter-based grid interface technology (permanent magnet synchronous generators with full-scale converters or doubly-fed induction generators with partial scale converters).
- ii. Changing wind speed causes variation in generator speed of the wind turbines and fluctuation (variable wind speed turbines). Thus, rotor speed of wind turbines is consequently decoupled with the frequency of the transmission system due to the use of full-scale converters.
- iii. Typical capacity of wind turbines is much smaller compared to conventional power plants (from hundreds kW to 7 MW).
- iv. WPPs do not only consist of individual wind turbines but also collector systems and other devices (energy storage, FACTS devices, etc.) together with controllers. In other words, every individual wind turbine terminal is exposed to different operating conditions from the point of connection in steady-state and transient conditions.
- v. Every individual wind turbine has its own electrical and mechanical control systems.
- vi. Converter-based wind turbines have decoupled active and reactive power controls.

2.2.1. Differences between Wind Plant and Conventional Power Plant

In modern WPPs, wind turbines with power converters such as DFIG and full-scale converter turbines are employed. In a conventional (synchronous) generator, rotor flux is attached to rotor pole with no slip so that any oscillation at generator shaft occurs as grid and generator shaft oscillations. Large generator oscillation appears as a great power oscillation on grid and it might have an impact on other generators

which are connected to the same line [29]. However, in a WPP, the rotor does not have to synchronous rotation with flux. Flux might glide on rotor surface at an adjustable speed with control of the power converter which is connected to the winding. If an oscillation occurs at any of the turbines, mechanical rotor oscillations do not have to be translated to the grid, since the rotor flux can be controlled separately from the rotational rotor speed with a flux orientation controller using the power converter [29]. Furthermore, diversity within the WPP enables each individual turbine to operate independently at its own operating point. Therefore, the response of an individual turbine in the entire WPP might appear as distributed responses from numerous turbines instead of a one single great response as it happens in conventional power plants [29].

2.2.2. Differences between Onshore and Offshore Wind Power Plants

Only consideration was onshore WPPs in the early phases of the technology development. However, offshore wind technology is more in center of current studies after exploration of great potential of offshore wind production (50 GW for US only) [29]. Good wind input as resource, short distance and easy access to transmission line, short distance to load center, accessibility to main transportation highway, available land at a reasonable price and environmental suitability are the main properties of location for a good WPP [29].

Most of the good locations for a WPP having abovementioned attributes are already reserved by early wind energy developers. Therefore, there are more opportunities and options for future planning of offshore WPP locations. Not only plant location but also easy transportability of wind energy equipment is advantageous for offshore WPPs. Size of wind turbines are getting larger with increasing weight due to developments in this technology. For instance, for wind turbines with capacities of 5 MW, size of wind turbine blades get considerably long and road transportation can be a very challenging situation [29]. If they are transported by ships as in offshore case, the road transport challenge can be prevented. Despite the advantages, there are drawbacks in offshore WPPs, especially the higher costs. To elaborate, there are

certain extra costs related to transportation, foundation, equipment installation and power transmission as well as operation and maintenance costs of offshore WPPs. For WPPs installed in deep water, the cost would be even higher compared shallow water WPPs since they can use AC transmission especially when located near the shore [29]. However, for offshore WPPs located far from the shore (35 miles limit), AC transmission may not be suitable. Because, excessive reactive power generated by submarine cables might cause over voltage at several buses. Thus, inductive compensation has to be involved. When DC transmission is used, there may be additional costs since power converters must be installed to interface with grid at onshore substation and at WPP substation (Figure 2.4).

Figure 2.4 reveals that array cabling (AC) connects rows of wind turbines to the offshore transformer station. The offshore sea cable (AC or DC) connects the offshore transformer station to the onshore grid. For larger distances from shore, high voltage DC (HVDC) transformer stations are used to transmit the electricity via DC cable to the shore. For safe operations, offshore cables are buried up to three meters deep into the seabed [30]. Finally, Table 2.2 summarizes prominent differences between onshore and offshore WTs.

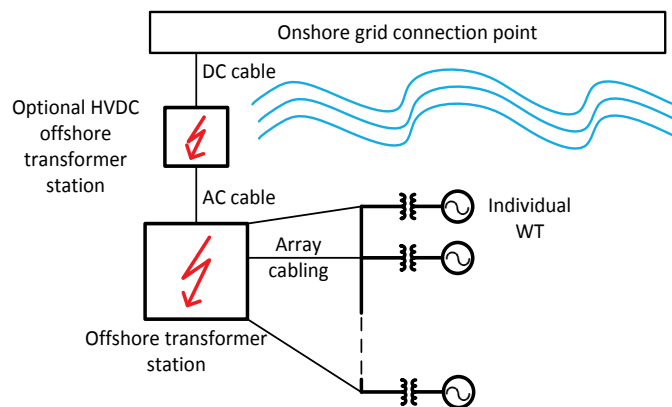


Figure 2.4 General structure of offshore wind farms [30].

Table 2.2 General differences between onshore and offshore wind turbines [30].

	Onshore Wind	Offshore Wind
Resources	<ul style="list-style-type: none"> • Wind potential for 2,000 full load hours • Limited sites available 	<ul style="list-style-type: none"> • Wind potential for 4,000 full load hours • Large sites still available
Dimensions	<ul style="list-style-type: none"> • 1 – 3 MW wind turbines • Wind farms of 10 – 50 MW installed capacity • Investment of €30 – €70 million per wind farm • At full load, one wind turbine produces a household’s annual consumption* in 200 minutes 	<ul style="list-style-type: none"> • 3 – 7 MW wind turbines • Wind farms of 50 – 1,000 MW installed capacity • Investment of €1 – €3 billion per wind farm • At full load, one wind turbine produces a household’s annual consumption* in 40 minutes
Environment	<ul style="list-style-type: none"> • Land-based conditions • Unrestricted access (24 hours / 7 days a week) 	<ul style="list-style-type: none"> • Rough marine conditions • Distance to shore 1 – 70 km • Access limited by high waves and storms
Foundations	<ul style="list-style-type: none"> • Built on solid ground • Standard concrete foundations cast on site 	<ul style="list-style-type: none"> • Differing soil conditions (sand, clay, rock) and erosion • Foundation type depends on water depth and soil consistency (e.g. monopiles, gravity, tripod)

*based on average annual electricity consumption of 3,500 KWh

2.2.3. Different Levels of Connection

Most of installed wind turbines have connection to power system. Seldom, they are installed individually. Instead, their installation is usually in groups of several turbines consisting wind farms which combine generated power and supply it to power system via an interfacing network (collector system) [31]. A typical collector system composed of the passive elements is written below:

- i. Individual generator transformers (mostly pad-mounted at base of every wind turbine) increase voltage from the sub-1 kV level at the generator to medium-voltage (MV) levels (typically 34.5 kV).
- ii. Medium-voltage underground cables which connect the turbine rows.
- iii. Medium-voltage overhead lines from the turbine rows to the main substation.
- iv. Step-up transformer(s) at the main substation which increase the voltage to transmission levels.

The abovementioned step-by-step connections are highlighted in Figure 2.5. It summarizes the entire procedure of wind power insertion into the mains.

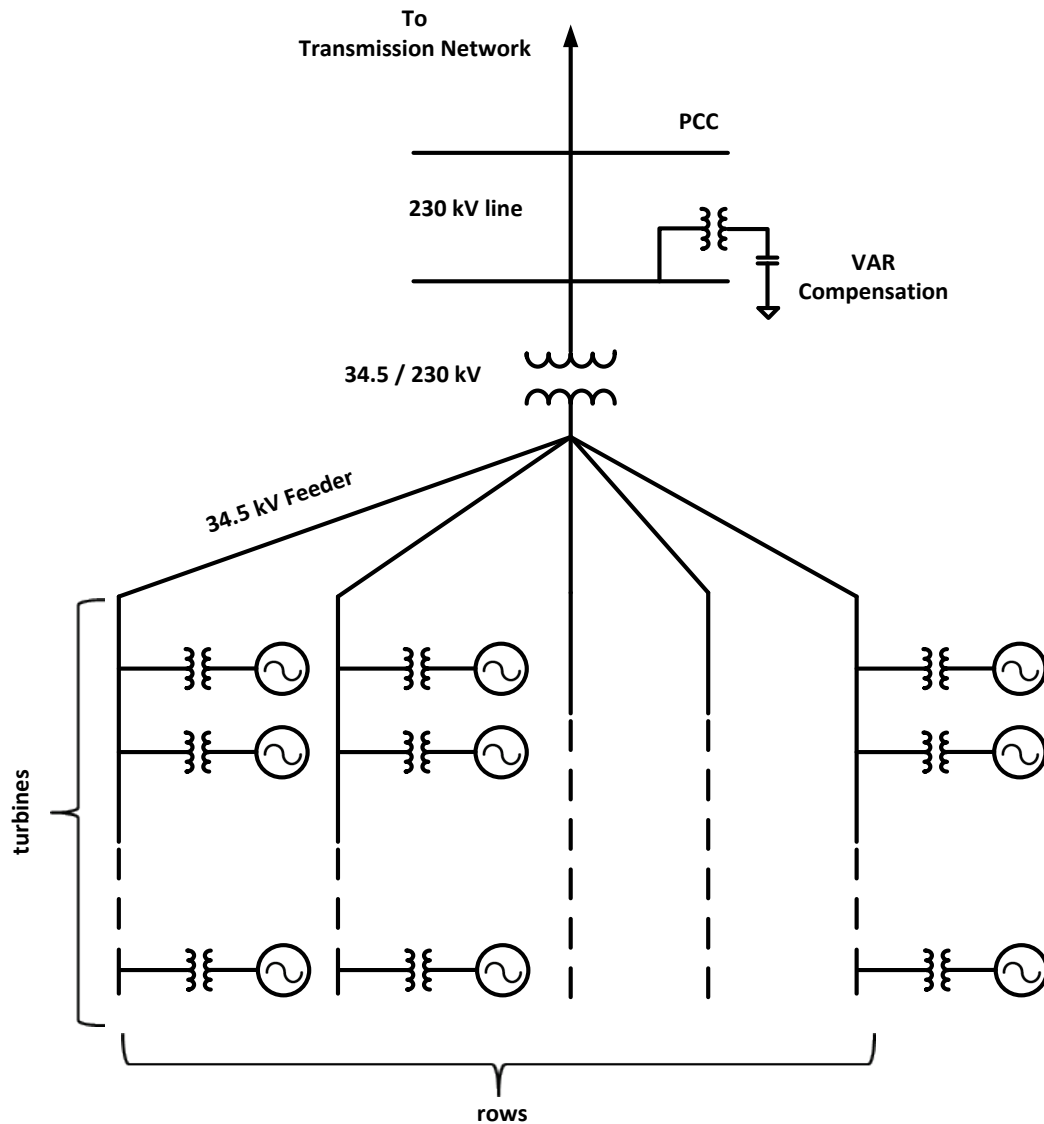


Figure 2.5 Collector system for wind farm [29].

A typical WPP composed of several individual wind turbine generators (WTGs) are connected to a medium voltage collector system, and they are tied to a transmission system at the interconnection point [31]. WTGs in utility-scale have nameplate

ratings in a range of 500 kW to 7 MW. A typical terminal voltage is in range of 575 to 690 V [32]. A step-up transformer, usually pad-mounted, connects every WTG to a medium voltage collector system which operates at 12–34.5 kV (Figure 2.5). A typical collector system composed of one or more feeders connected in a collector system station. One or more station transformers at the collector system station are utilized to obtain transmission system voltage. If collector system station is not adjacent to interconnection point, an interconnection transmission line is necessary.

Mechanically switched capacitors as reactive compensation and continuously variable devices (STATCOM or static VAR system) can be installed at collector system station [29]. Shunt reactive compensation at the WTG terminals can be installed to correct power factor regarding type of WTG. Amount and characteristic of reactive compensation are defined by requirements of interconnection and design considerations of collector system regarding voltage regulation and losses.

Voltage level at which the collector system interconnects with the power system affects wind turbines and wind farms on the bulk power system. WPP location and size affect voltage level of interconnection. Grid codes define the standards for acceptable values for wind farms interconnected to power system [25][33]–[37]. Common concerns are reactive power compensation and voltage control. Stability level of voltage might be the limiting factor when making decision on the maximum size of a wind plant suitable for interconnection at a particular node. These concerns are considerably severe in situations where wind farms are far from load centers or connected to power system via a weak network [29]. Also, wind turbines can also be connected separately as individual or in smaller groups to distribution networks. However, power quality is a bigger concern compared to stability (Figure 2.6).

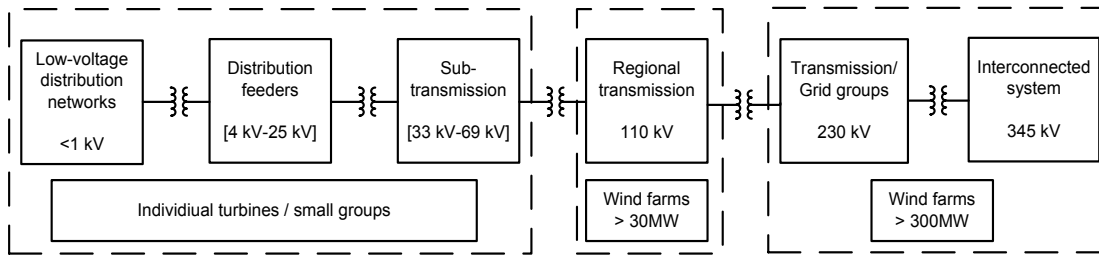


Figure 2.6 Connection at different voltage levels according to power [29].

In the light of Figure 2.6, Table 2.3 elaborates and summarizes the relationship between transmittable power and connection of wind turbines to different levels of the electrical network [32].

Table 2.3 Transmittable power and connection of wind turbines to different levels of the electrical network [32].

Voltage system	Size of wind turbine or wind farm	Transmittable power
Low voltage system	For small to medium turbines	up to = 300 kW
Feeder of the medium voltage system	For medium to large wind turbines and small wind farms	up to = 2-5 MW
Medium voltage system, at transformer substation to high voltage	For medium to large onshore wind farms	Up to = 10-40 MW
High voltage system	Clusters of large onshore wind farms	Up to = 100 MW
Extra high voltage system	Large offshore wind farms	>0.5 GW

2.2.4. Step-Up Transformer Structure

Dedicated step-up transformer is employed for each turbine for wind turbines in MW rating category [38].

2.2.4.1. Transformer Type

Pad-mounted three-phase distribution transformers are employed where WTG step-up transformers are used [38]. These transformers are commodities which fulfill the required duty at a low cost. WTGs with transformers in the nacelle or on platforms of the tower are not in the scope of this study.

2.2.4.2. Winding Connection

Most of the WTG producers specify delta (MV) – grounded-wye (LV) winding connections for step-up transformers of the wind turbines as revealed in Figure 2.7. Reasons for this connection are to enhance isolation of the WTG from the zero-sequence behavior of the collector feeder (unfaulted phase voltage increase when ground faults occur) and to exhibit a solid ground source for the LV side connected to the WTG. Besides, delta-wye connection is favorable over wye-wye connection because it not only isolates the triplen harmonics but also provides higher line-to-line voltage ratio with the same winding turn ratio, reducing the cost potentially [39]. Nevertheless, delta-wye configuration, particularly delta side causes $\pi/6$ phase shift between the primary and the secondary voltages/currents. Also, it creates a strong coupling between dq -stationary frame variables in the current control loop.

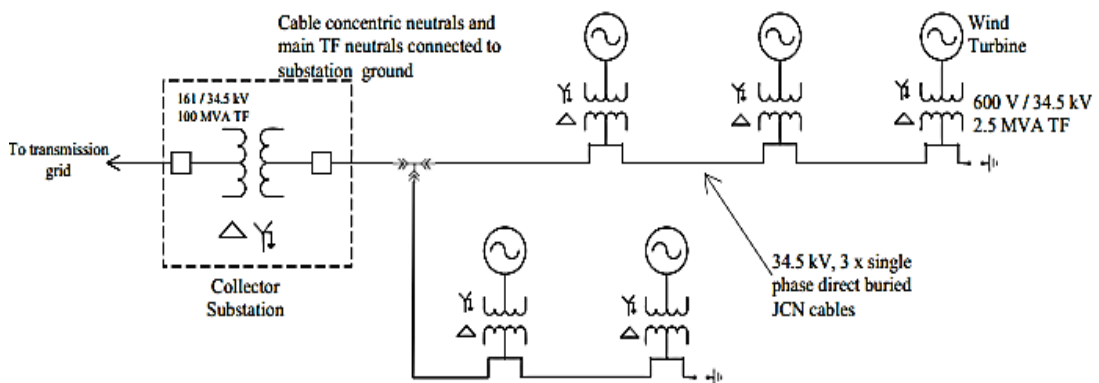


Figure 2.7 Typical wind farm network- single line diagram (only a few turbines are shown) [40].

Grounded wye-wye transformers are employed frequently in utility load-serving applications [40]. They are available widely as well. There is a common misunderstanding that this connection supplies a ground source to the collector feeder when the feeder becomes isolated from the collection substation. This concept is only true if the WTG is a grounded source, which is generally not the case [40].

2.3. General Structure of Individual Wind Turbines

Today, wind turbine technologies are being used in a great variety [27][28]. Typically, WPPs compose of numerous (hundreds) of turbines mostly having the same technology. Wind turbine technologies vary largely in terms of cost, complexity, efficiency in wind energy extraction and use of extra utility/equipment. Horizontal axis wind turbine (HAWT) is the most common technology in utility-scale applications [28]. Axis of rotation of the HAWT blades is parallel to the ground. Vertical axis wind turbine (VAWTs) is a developing technology; however, the technology is not mature yet for use in utility-scale applications. Power ratings for HAWTs are typically in the range of 500 kW to 7 MW [29]. The power output of VAWTs is inherently fluctuating and non-dispatchable which must be considered.

There is a common HAWT classification done according to number of blades; they are single bladed, two bladed, three bladed and multi bladed. They can also be further classified as upwind and downwind turbines according to input wind direction [25]. Figure 2.8 shows a typical HAWT configuration which employs a blade and hub rotor assembly for extraction of power from wind, a gear-train for stepping up the shaft speed at the slowly spinning rotor to the higher speeds necessary for driving the generator, and an induction machine or synchronous machine for electromechanical energy conversion. Lastly, step-up transformers are employed for injection of the produced electrical energy to the grid [30].

Induction machines are commonly used units for generation owing to their asynchronous nature. Maintenance of a constant synchronous speed for synchronous generator is difficult since wind speed varies. Yet, full-scale converter turbines are capable of employing high pole count permanent magnet synchronous generators, as

the generator and the grid frequency are perfectly decoupled [29]. Power electronic converters are employed for regulation of real and reactive power output of turbines.

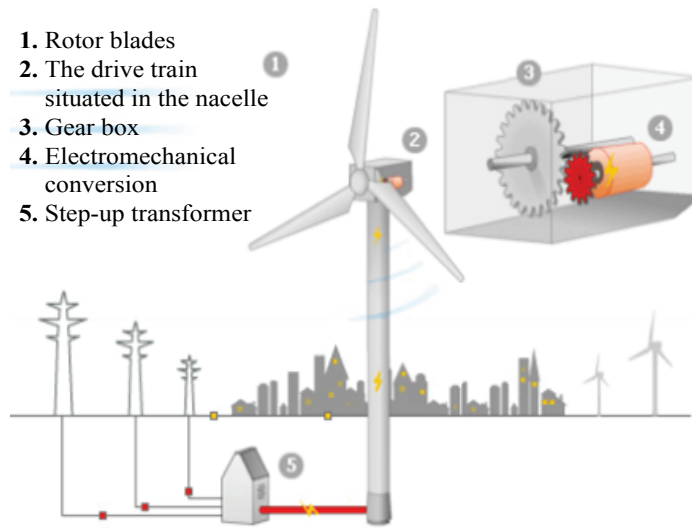


Figure 2.8 Typical wind turbine configuration [30].

In Figure 2.9, a typical framework for representation of commonly used wind turbine technologies can be seen. Different types of wind turbines are described further in the following subsection.

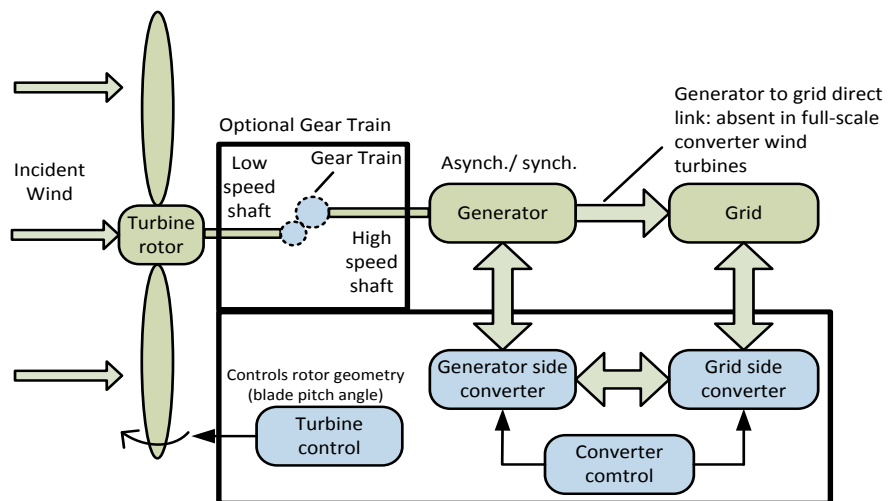


Figure 2.9 Block diagram of a typical wind turbine [29].

2.3.1. Recent Wind Turbine Configurations

Wind turbines are classified into four main configurations due to differences in production technology [25]:

1. Early and relatively simple wind turbine configuration indicates the turbines directly connected to the grid and equipped with an asynchronous squirrel cage induction generator (SCIG). This configuration requires capacitor banks to compensate reactive power. The configuration can be improved further with addition of blade-angle control (pitch control) to the wind turbine.
2. Wound rotor induction generator (WRIG) equipped with variable rotor resistor circuit is another configuration. Mechanical construction of the configuration is analogue to the SCIG concept. However, there is an extra rotor circuit to be able to control the active power and speed of the rotor by changing the rotor resistance. Capacitor banks are employed to compensate the reactive power.
3. Variable speed wind turbine (VSWT) with partial scale frequency converter configuration, also known as doubly fed induction generator (DFIG), indicates a WRIG including a converter circuit in the rotor. The converter which equals to %30 of rated generator power achieves compensation of the reactive power and provides smoother grid connection.
4. VSWTs are able to connect to the power system via full-scale frequency converter owing to recent technological developments. Full-scale converter achieves decoupled active and reactive power control with a better and smoother grid connection, and operation as in partial converter case. Two types of generators are applied in this configuration; wound rotor synchronous generators (excited electrically) and permanent magnet synchronous generators (PMSG).

The configurations which are described above can be seen in Figure 2.10. Regarding these classifications, numerous combinations of wind turbines are available in the market. Yet, the scope of this study will be limited to the VSWTs with partial and full-scale converter concepts (3rd and 4th configurations) as they are the state of the

art turbine technologies. VSWT configurations have already been introduced in Figure 1.4 in Chapter 1.

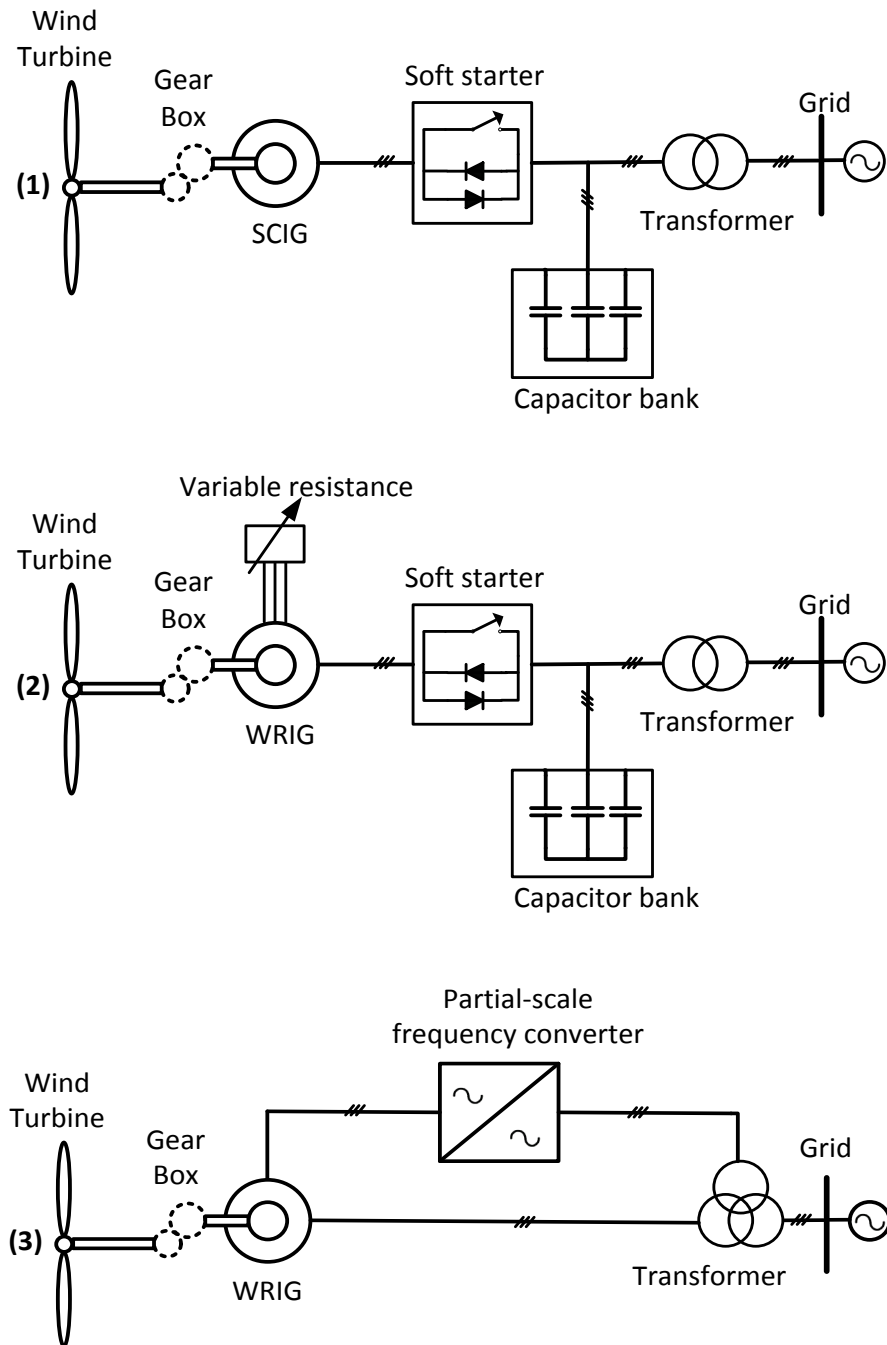


Figure 2.10 Wind turbine configurations [25].

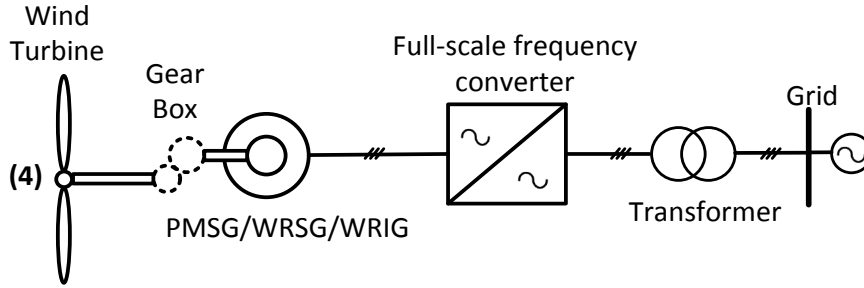


Figure 2.10 (continued) Wind turbine configurations [25].

2.3.2. Back-to-Back PWM-VSC for Partial-Scale and Full-Scale Converters

Induction machine stator is directly connected to the grid (see Figure 1.4 & Figure 2.10) in DFIG configuration (3rd configuration). Rotor circuit consists of a controlled AC/ DC converter including six IGBTs (three legs with two IGBTs each as described in Chapter 1) for controlling AC currents in the rotor circuit, a DC link capacitor acting as energy storage, filter for DC link voltage, and an identical DC/AC converter to interface with grid. Each converter is a voltage-source converter (VSC) switched using PWM.

Back-to-back PWM-VSC configuration is the most commonly employed three-phase frequency converter configuration. For a typical DFIG turbine, this configuration is needed to be rated at about 30% of total power rating of the induction generator, and will enable approximately 30% speed variation for the values higher than synchronous speed. Grid side converter is usually used for keeping the DC link voltage constant and providing limited reactive power support to the grid, meantime the rotor side-converter controls the active and reactive power output of the induction generator [29].

However, a converter is the only path for power flow from wind turbine to the grid in full-scale converter turbines. Converter has to be rated accordingly to be able to handle the overall power output of wind turbine. These turbines mostly use high pole

count permanent magnet synchronous generators, in addition employment of induction generators is also possible [25][29].

2.3.3. Grid-Side DC/AC Converter of the Back-to-Back PWM-VSC for Full-Scale Converters

As mentioned in previous sections, recently produced individual wind turbines are in the range of 500 kW- 7 MW. Moreover, VSC is the one and only power flow path for full-scale configurations. For these reasons, the grid-side converter of the back-to-back PWM-VSC (Figure 2.11), which is the focus of the thesis work, should be designed according to the power levels in the specified range.

Figure 2.11 elaborates the configuration for a full-scale converter wind turbine depicted in Figure 1.4 whereas Figure 2.12 further elaborates the grid-side VSC by modeling the DC output of generator-side converter as a DC current source to the grid-side VSC. This configuration is similar to DFIG configuration; however, with the important distinction that the rotor is not accessed, and the stator is not directly connected to the grid. Instead, the stator interfaces with generator-side PWM-VSC. DC link capacitor is used for smoothing the DC link voltage as in DFIG turbines. The grid-side VSC does power transfer to the grid. It also controls the amount of active and reactive power injected to the grid [29]. Although back-to-back PWM VSC configuration occurs similar to DFIG configuration, the generator-side VSC and DFIG rotors-side VSC perform different functions in fact, as does the grid-side VSC for each case. This configuration is commonly preferred for permanent magnet synchronous generator (PMSG) machines; however, it can also be used for other types of generators. It is a four-quadrant converter, and both real and reactive power can be moved in both directions.

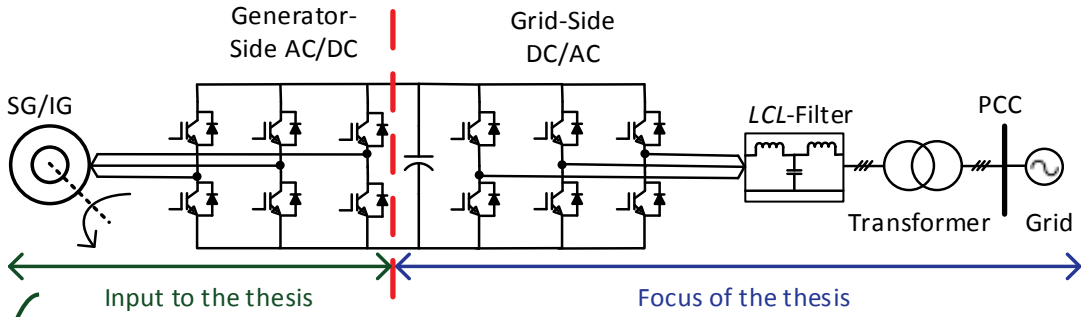


Figure 2.11 Back-to-back PWM-VSC for wind turbine system with full-scale converter.

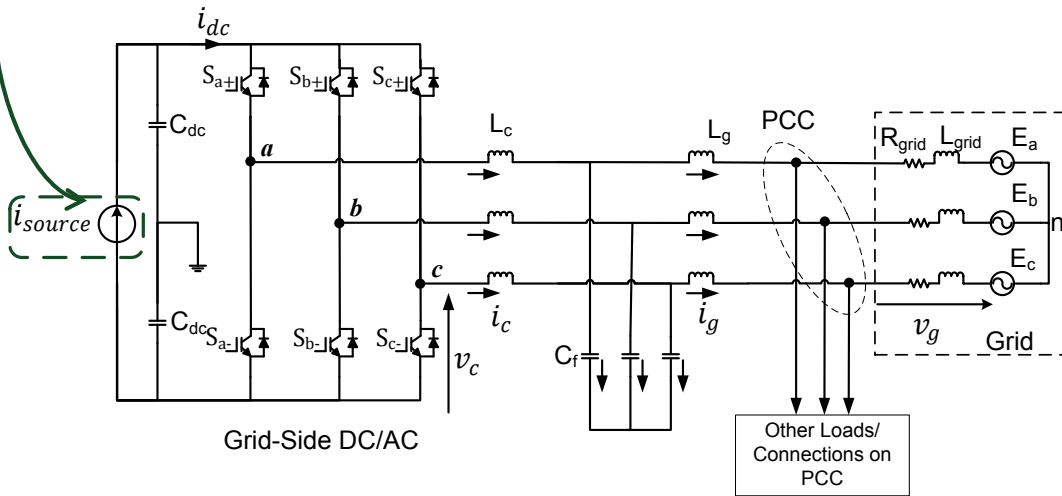


Figure 2.12 Grid-connected DC/AC converter cascaded with *LCL*-filter.

Up to this point, the scope of the thesis is narrowed down by adopting the ‘general to particular’ approach. For this purpose; firstly WPPs are regarded. Secondly, as being one of the elements of WPPs, the general structure of individual wind turbines (WT) are taken into consideration. And finally, the special power electronics part of the individual wind turbines, grid-side DC/AC converter of the back-to-back PWM-VSC for full-scale wind turbine is considered (WPP→WT→VSC). Details and summary of the concepts are as below:

- i. WPPs are elaborated in terms of:
 - a. Power scale of wind farms and their corresponding voltage-level connections,

- b. Types and winding properties of the grid interface step-up transformers.
 - c. Comparison between onshore and offshore wind farms,
 - d. Comparison between wind plants and conventional power plants,
- ii. Individual wind turbines are expanded in terms of:
 - a. Types of recent wind turbine configurations,
 - b. Special emphasis on partial-scale and full-scale converters.
- iii. Back-to-back PWM-VSC for full-scale converters (Figure 2.11) are particularized in terms of:
 - a. Grid-connected DC/AC converter together with *LCL*-filter (Figure 2.12).

As of this point, capacity factor definition will be given in order to define a figure of merit called operational efficiency to assess the performance of a wind turbine and hence the performance of the grid-side DC/AC converter. Then, the grid codes concerning the control of active power, reactive power, voltage, and frequency under normal and faulty conditions together with the quality of inserted power to grid by wind turbines/farms will be investigated.

2.4. Capacity Factor and Operational Efficiency Definitions as the Performance Indicator of Individual Wind Turbines

Converters operating in renewable energy systems do not always perform at rated load due to intermittent characteristic of nature. Energy derived from the sun and wind varies with time, day of the week, season, weather and similar natural factors. Particularly, wind turbines usually operate 40% of the time annually. They generate small amount or no power about 60% of the time [29]. Due this intermittent source characteristic of wind, mean output power of an individual wind turbine cannot be anticipated easily. Besides, the peak demand does not usually overlap with the maximum energy production of turbines. Therefore, energy storage in grid has been a hot topic recently. When the energy produced by the wind turbine (or PV/other

renewables) exceeds the demand, energy is stored by numerous means presented in literature and once the demand exceeds the production, the stored energy is utilized. Hence, the necessity of coinciding peak production with peak demand has been eliminated.

Consequently, performance (efficiency) analysis of an individual wind turbine regarding only rated power production is not a fair assessment. In the literature, there are several operational efficiency definitions such as ‘EURO Efficiency’ and ‘CEC Efficiency’ [101][102] weighing several partial power generation with predetermined coefficients as depicted in (2.1) and (2.2).

$$\eta_{\text{EURO}} = 0.03 \cdot \eta_{5\%} + 0.06 \cdot \eta_{10\%} + 0.13 \cdot \eta_{20\%} + 0.1 \cdot \eta_{30\%} + 0.48 \cdot \eta_{50\%} + 0.2 \cdot \eta_{100\%} \quad (2.1)$$

$$\eta_{\text{CEC}} = 0.04 \cdot \eta_{10\%} + 0.05 \cdot \eta_{20\%} + 0.12 \cdot \eta_{30\%} + 0.21 \cdot \eta_{50\%} + 0.53 \cdot \eta_{75\%} + 0.05 \cdot \eta_{100\%} \quad (2.2)$$

However, these criteria are more suitable to evaluate PV applications or small scale wind turbines. Yet, a novel operational efficiency definition including large power scale wind turbine applications is needed to be developed in this section. To develop an operational efficiency definition for wind turbines including all possible rated powers, power output vs. wind speed characteristic is required. This type of attributes can be obtained in manufacturer datasheets. MWT62/1.0 (Mitsubishi Wind Turbine Generator) [84] is selected as the reference wind turbine generator to illustrate the methodology. Its rated power is 1 MW and the grid-side DC/AC converter is designed considering connection to the low-voltage grid at 690 V line-to-line. Before deriving the novel operational efficiency definition, definition of capacity factor widely used in industry is given in the following section.

2.4.1. Definition of Capacity Factor

Wind turbine manufacturers assess their products regarding widely used term ‘capacity factor’ (*C.F*). Capacity factor is a measure of a wind turbine’s actual

output, which varies with the wind speed over a period of time. Thus, capacity factor is the actual output over a period of time as proportion of a wind turbine or plant's maximum capacity [99]:

$$\text{Capacity Factor (\%)} = \frac{\text{Power output (W)}}{\text{Rated (Max.) power (W)}} * 100 \quad (2.3)$$

Several capacity factors (i.e. percent power output) versus wind speed characteristic provided in MWT62/1.0 datasheet are emphasized in Figure 2.13(a) and ideal annual energy output in MWh vs. annual average wind speed attribute is also depicted in Figure 2.13(b). Plus, several illustrative *C.F.* cases are pointed. To highlight the power attributes of the selected wind generator, the first curve is elaborated as revealed in Figure 2.14 and then converted into rectangular boxes without changing the area under the curve to ease the numerical calculations. The rectangular form assumes that the capacity factor is constant within the corresponding wind speed intervals.

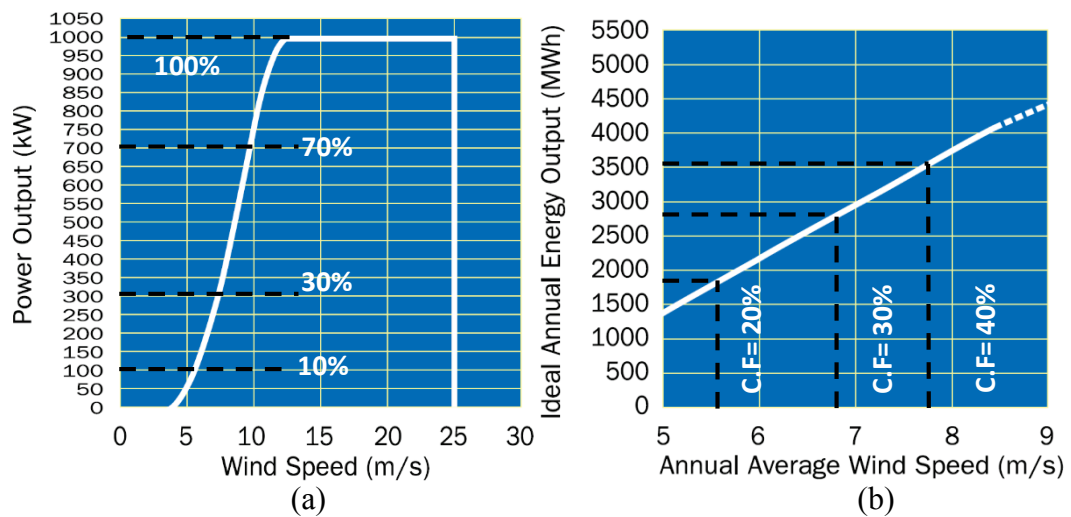


Figure 2.13 MWT62/1.0 (a) Power curve (b) Energy output.

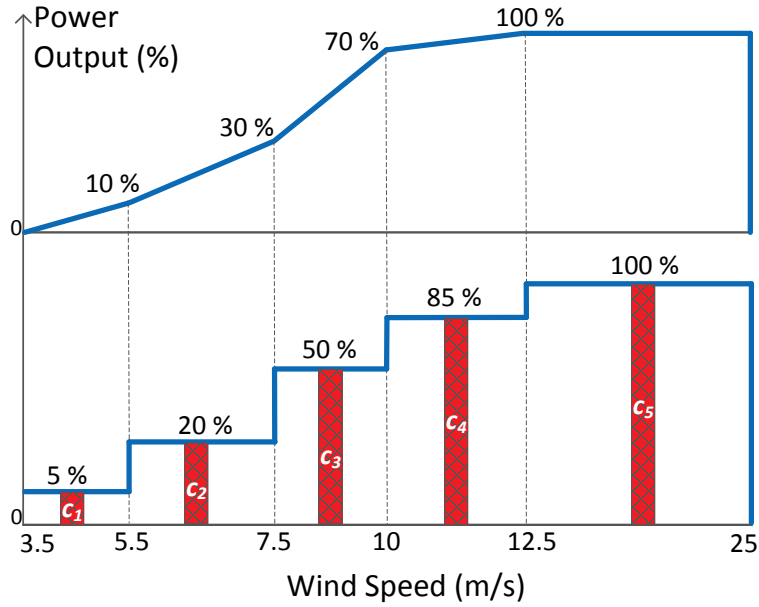


Figure 2.14 Modified MWT62/1.0 power curve.

As evident in the power curve in Figure 2.14, wind speed is split into regions through which power output (P_{out}) is assumed as constant. The red-hatched slices referenced from c_1 to c_5 in Figure 2.14 depict the portions of each wind strength benefited throughout the operation time (i.e. when wind speed is between 3.5-25 m/s). Depending on the width of these slices, the mean capacity factor (mean P_{out}) is determined by weighing 5%, 20%, 50%, 85%, and 100% power outputs correspondingly as given in (2.4). As a remark, by following the same procedure any kind of P_{out} vs. wind speed characteristics can be modeled as shown above. Thus, it is quite convenient to model different types of wind generators in this aspect.

The active operation time of a wind turbine per annum can be represented with σ as revealed in (2.5). Since the power curve in Figure 2.14 represents the duration of active power generation, summation of weighing constants should be equal to the fraction σ as depicted in (2.6).

$$C.F(\%) = c_1 * 5 + c_2 * 20 + c_3 * 50 + c_4 * 85 + c_5 * 100 \quad (2.4)$$

$$\sigma = \frac{\text{Duration of active power generation per annum [hour]}}{\text{One year [hour]}} \quad (2.5)$$

$$\sum_{m=1}^5 c_m = \sigma \quad (2.6)$$

To illustrate the methodology, three distinct capacity factors, 20%, 30%, and 40% will be considered while deriving the operational efficiency definition.

2.4.2. Novel Operational Efficiency Definition for Wind Turbines

The classified wind speed intervals according to possible wind strengths in Figure 2.14 are tabulated in Table 2.4. Then, occurrence frequency of each wind strength is weighed so that corresponding 5%, 20%, 50%, 85% and 100% power outputs provide the mean capacity factors depicted in the first column of Table 2.4. The wind data provided in [99] was benefited to determine ϕ_1 - ϕ_5 in Table 2.4. ϕ_1 - ϕ_5 coefficients represent the weight of each wind strength benefited during $\sigma\%$ operation time. The sum of the wind speed coefficients is unity as revealed in (2.7). Thus, c_1 - c_5 and ϕ_1 - ϕ_5 represent the coefficients of the same weigh function; however, $\sum c_m = \sigma$ whereas $\sum \phi_n = 1$. Thus, in order to reflect idle time period (no power generation) c_1 - c_5 constants should be normalized by multiplying ϕ_1 - ϕ_5 with σ as shown in (2.8). Consequently, equivalent capacity factor per annum is embodied.

Table 2.4 Wind speed classification.

<i>C.F</i> (%)	Wind Speed Coefficients (ϕ_n)				
	ϕ_1	ϕ_2	ϕ_3	ϕ_4	ϕ_5
	3.5-5.5 m/s <i>P_{out}</i> =5%	5.5-7.5 m/s <i>P_{out}</i> =20%	7.5-10 m/s <i>P_{out}</i> =50%	10-12.5 m/s <i>P_{out}</i> =85%	12.5-25 m/s <i>P_{out}</i> =100%
20 %	0.30	0.30	0.20	0.10	0.10
30 %	0.20	0.25	0.15	0.15	0.25
40 %	0.10	0.10	0.20	0.25	0.35

$$\sum_{n=1}^5 \phi_n = 1 \quad (2.7)$$

$$\sum_{m=1}^5 c_m = \sigma * \sum_{n=1}^5 \phi_n \quad (2.8)$$

Operational efficiency η_{op} can be calculated using (2.9):

$$\eta_{op} = \phi_1 \cdot \eta_{5\%} + \phi_2 \cdot \eta_{20\%} + \phi_3 \cdot \eta_{50\%} + \phi_4 \cdot \eta_{85\%} + \phi_5 \cdot \eta_{100\%} \quad (2.9)$$

where $\eta_{5\%}$, $\eta_{20\%}$, $\eta_{50\%}$, $\eta_{85\%}$, and $\eta_{100\%}$ are the efficiencies at 5%, 20%, 50%, 85%, and 100% load (power output), respectively. As a remark, η_{op} definition uses coefficients ϕ_1 - ϕ_5 since efficiency can be discussed only when power is generated. Wind speed classification as given in Table 2.4, and an efficiency curve against output power percentage to calculate necessary efficiency values ($\eta_{5\%}$, $\eta_{20\%}$, $\eta_{50\%}$, $\eta_{85\%}$, $\eta_{100\%}$) are necessary to compute the operational efficiency (η_{op}) of the wind turbine.

To sum up, the novel operational efficiency definition provided in this chapter is a more flexible definition compared to EURO and CEC definitions since it has variable weigh coefficients that takes into account *C.F* of corresponding wind turbine. Hence, operational efficiency is obtained in a fairer manner regarding the intermittent attributes of the wind.

2.5. Grid Codes Overview

In Chapter 1, due to the high wind power penetration in power system the necessity of grid codes to monitor the quality and sustainability of the wind energy injected into the grid was briefly stated. Additionally, recent wind turbine technologies were also described. In this section, widely used grid connection requirements determined by international codes dedicated for wind turbine applications, fault ride-through

capabilities of different wind turbine technologies and the impact of grid stiffness on the quality limits of the injected power to the grid will be explained in detail. Since, grid-side VSC design is made according to the restrictions and boundaries determined by these special grid codes.

Connection and operational requirements are defined by grid codes for all parties involved such as power plant owners, large consumers and service providers related to transmission system. Specifications of original grid codes for power plants were held regarding synchronous machines. Yet, wind turbines are designed based on different technologies having considerable impacts on conventional transmission system [44]. TSOs have done the revision of the grid codes to be able to sustain reliable and stable power production to the loads, meantime they enable large scale wind power production [36][41]-[43]. Although the requirements are dependent on the characteristics of each individual transmission system, structural harmonization study for the grid codes was meant establishing a general common grid code scheme in which generic layout and specifications are fixed and agreed upon by all the TSOs, developers of WPP, and wind turbine manufacturers [45]. With this approach, WPPs, regardless of any specific grid codes, should meet the common requirements. The most common requirements consist of:

- i. Control of active power,
- ii. Control of reactive power and voltage,
- iii. Operating ranges of frequency and voltage,
- iv. Capability of fault ride through (FRT).

Requirements mentioned above and further discussions can be seen in the literature [23][33]-[35][44]-[46]. A brief review of these common requirements is included for the investigations performed in this thesis.

2.5.1. Active Power Control

Dynamic participation of wind turbines is necessary in the grid operation control in terms of regulation of their active power output. Regulation of active power in grid

codes cover active power control modes limiting the maximum active power, balancing the active power output, and defining the ramp rates either in upward or downward direction. Examples of mentioned control modes can be seen in Figure 2.15.

Control modes enable TSOs managing wind turbines in a predictable way to decrease the uncertainties due to the wind behavior. They could also provide supervision for integration of wind turbines into current transmission plans and market operations. In addition, maintaining power reserve can be achieved via employment of these modes to control frequency. Update rate of active power reference (from TSOs), rate of start-up ramp, rate of shut down ramp, and functions of system protection are the extra requirements which are specified in the active power control title in grid codes [33]-[35].

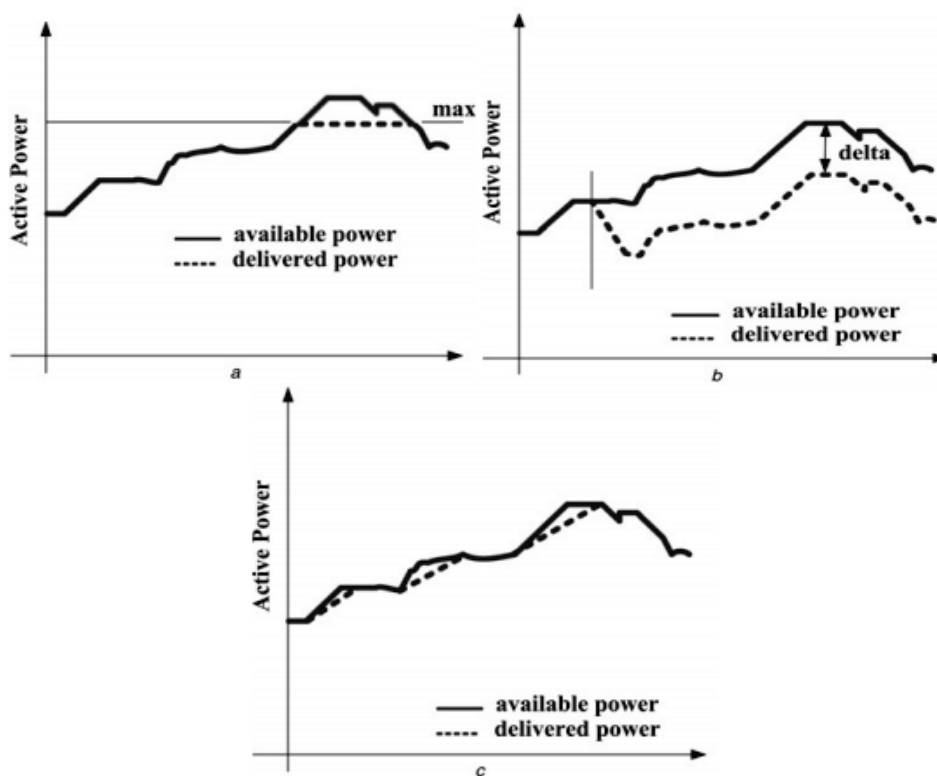


Figure 2.15 Active power control requirements

- (a) Absolute power constraint (b) Delta production constraint (active power reserve)
- (c) Power gradient constraint [33].

Active participation of wind power plants is possible for grid operation and control done regulating the output power. Currently, all of the grid codes regulate the requirements on regulation capabilities of the active power of wind power plants by taking the form of several different modes of control into account. This situation is illustrated in Figure 2.15. Considering the primarily available active power (i.e. prevailing wind properties), output power can be adjusted to a specific amount of power (Figure 2.15(a)) or to endure a stable relationship with the available power such as maintenance of a specified reserve, the value either in MW or in a percentage value of the available power (Figure 2.15(b)). There may be some extra requirements such as limitation of the change rate of the output power (Figure 2.15(c)). Increase in power is possible by ramp rate; however, system operation with a power reserve is required to become effective while the output power is decreasing.

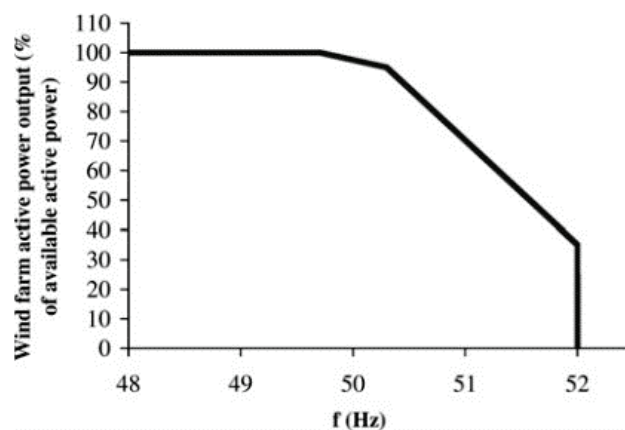


Figure 2.16 Typical power vs. frequency response [33].

Provision of related services from wind power plants such as participatory frequency control and spinning reserve provision as a consequence of active power control are already mentioned previously. As can be seen in Figure 2.16, frequency response request is possible within the over-frequency region (reduction of active power related to deviation of positive frequency) as well as under frequency. In the latter,

the wind power plant should be in operation with a power reserve if frequency is in the normal operating range. This situation inevitably has economic aspects.

2.5.2. Reactive Power and Voltage Control

Reactive power output of a wind turbine is regulated in response to changes in voltage at grid connection point as well as reactive power references which are sent by TSOs. Requirements of reactive power are dependent on the properties of grid connection point such as short-circuit power of the connection point, X/R ratio, and penetration level of wind power. In grid operation, three different options are possible for reactive power references which are defined by TSO; reactive power, power factor and voltage references. Grid codes indicate these operating conditions of reactive power such as P/Q and V/Q curves as shown in Figure 2.17 and Figure 2.18, respectively. In addition, rate of reactive power ramp, control of reactive power and accuracy of measurement, settling and rise times for reactive power change are set in grid codes.

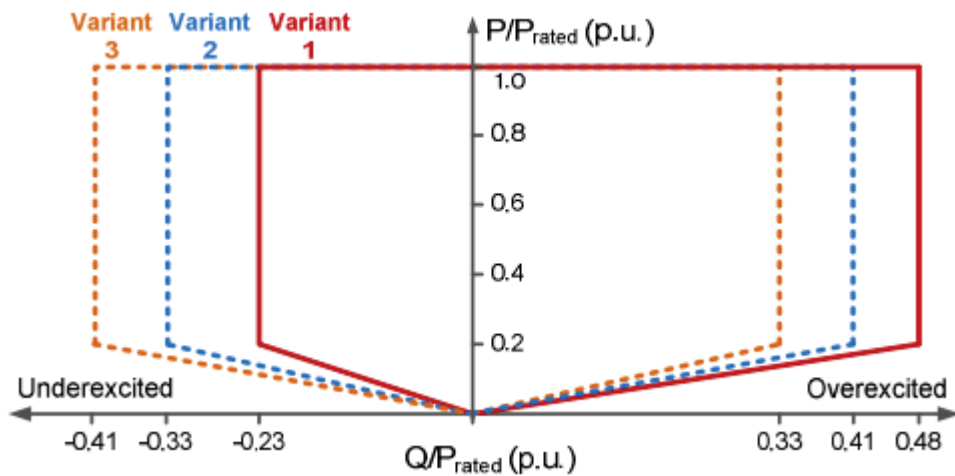


Figure 2.17 P-Q dependencies of three variants [36].

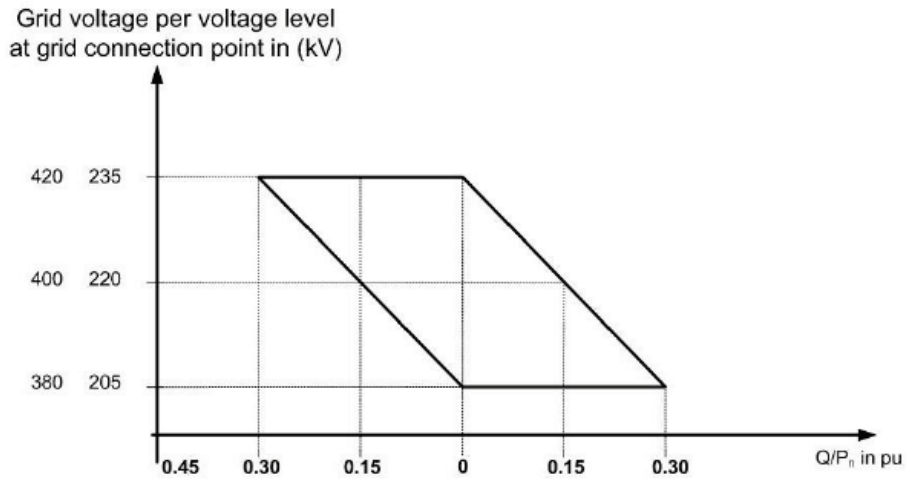


Figure 2.18 V-Q dependency [36].

Capabilities of reactive power regulations are demanded by several grid codes. This requirement is affected by external provision of a specific reactive power value or by a specific power factor. Furthermore, capability of reactive power regulation might be exploited for voltage control purposes in the wind power plant connection point, or in a relatively distant node. Figure 2.19 shows typical requirements for the power factor regulation range which depends on the terminal voltage and the active output power of the wind farm, respectively.

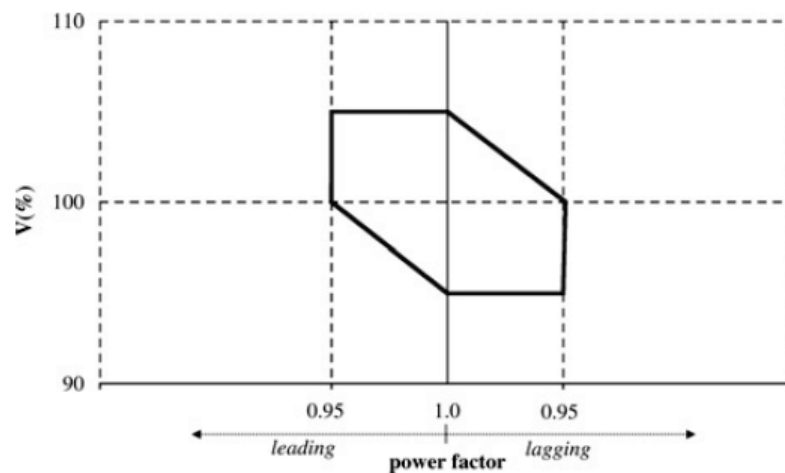


Figure 2.19 Typical requirements for power factor variation range in relation to the voltage [33].

2.5.3. Frequency and Voltage Operating Ranges

Wind turbines have to be able to operate in a range of the rated voltage and frequency values of the point of common coupling (PCC) in order to avoid instable operation caused by the disturbances in the grid. This requirement can be defined as the frequency/voltage operation zones shown below:

- i. Continuous operation in a defined range below and above the nominal point.
- ii. Time limited operation with possible reduced output in extended ranges.
- iii. Immediate disconnection.

In grid codes, voltage-frequency operational range window is graphically represented in Figure 2.20. These ranges rely on the characteristics of the transmission system.

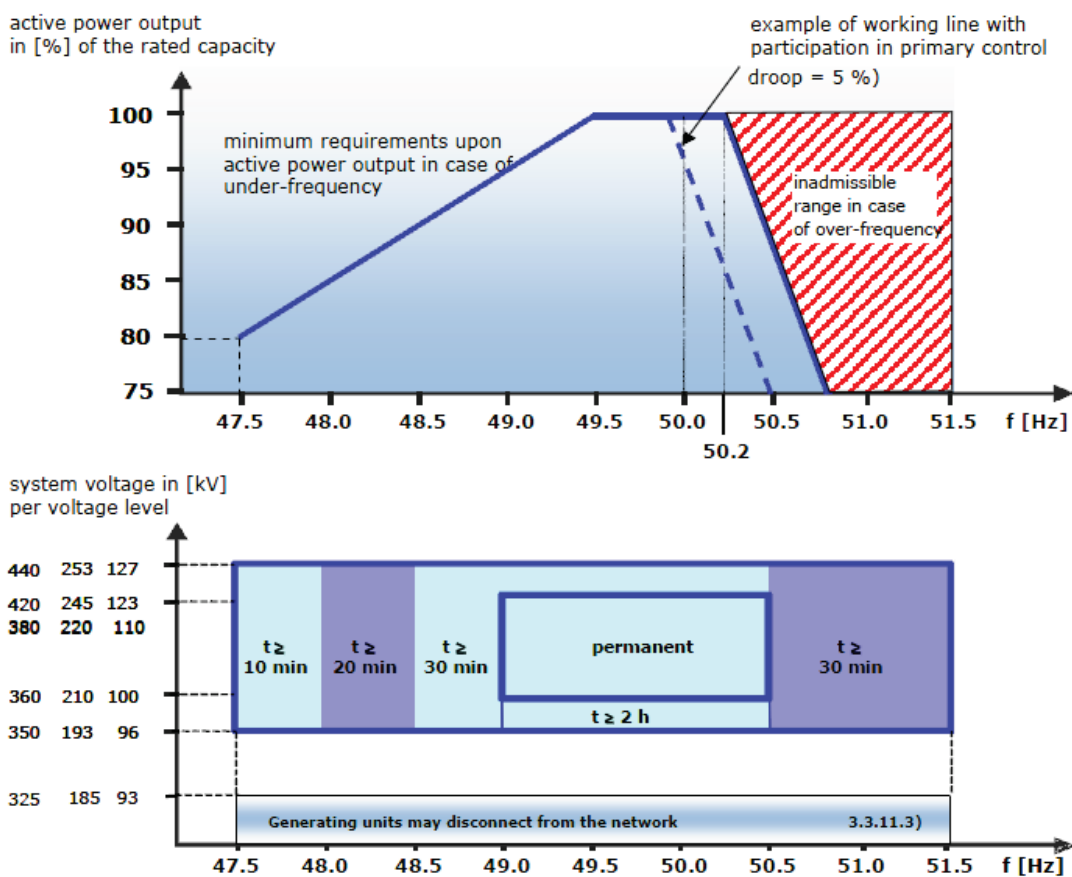


Figure 2.20 Voltage/Frequency operating ranges [36].

Figure 2.21 provides a comparison of the operating frequency limits in countries using 50 Hz.

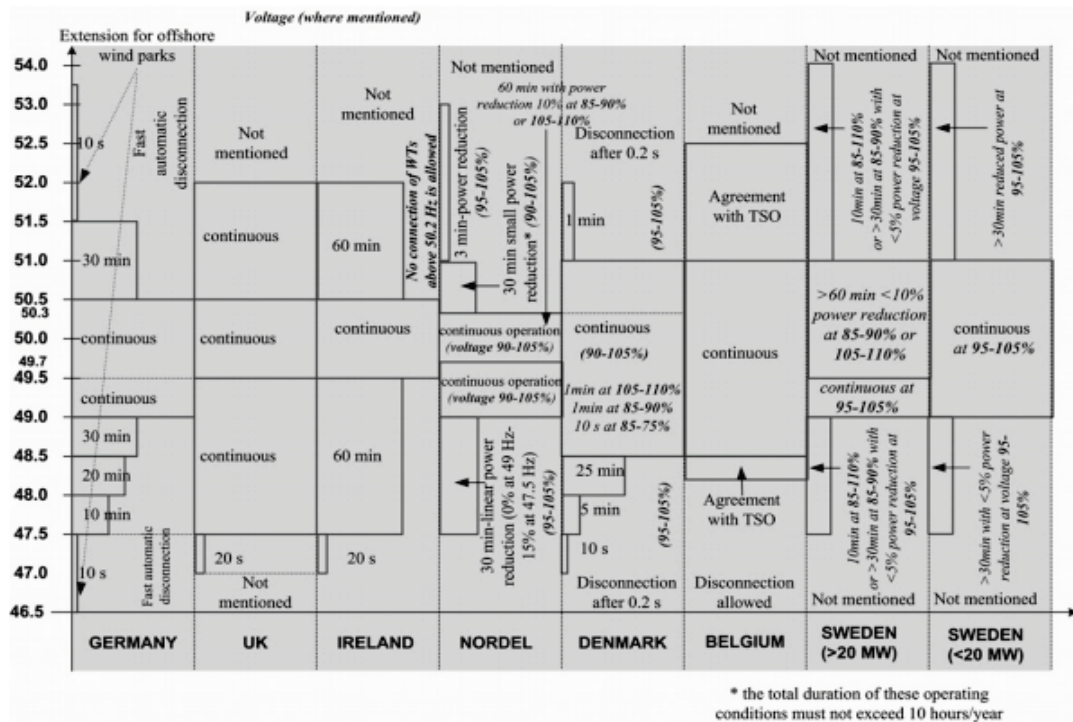


Figure 2.21 Comparison of the operating frequency limits in European countries [33].

2.5.4. Fault Ride Through Capability

Short circuits are the main reasons of voltage faults on wind turbine terminals. They might occur in several different locations of the power system in various ways such as line-to-ground and line-to-line faults. Type of the fault and electrical distance to the location of the fault determine the amplitude of a voltage dip on an individual wind turbine or entire wind power plant. In the past, wind turbines were used to be disconnected from the grid just after abnormal voltage conditions occurred. However, this way of response to voltage faults is not suitable for use in power systems having high wind penetration. Disconnection of great number of wind turbines from the grid responding to voltage faults might result in instability problems for the entire system. Furthermore, the disconnection might even create

system blackouts. For prevention of these problems, wind power plants are required to operate continuously. Even in the situations where voltage dip drops drastically, voltage recovery is supported by injection of reactive current and active power restoration is achieved after clearing the fault with limited ramp values. Therefore, wind turbines employing developed technology stay connected to the grid during voltage faults having certain durations and depths, and continue to operation normally right after the fault clearance. This situation is named as fault ride through (FRT) capability, and holds for both low and high-voltage cases [29].

Wind turbine FRT capability is explained further:

- i. FRT with low and high voltage ride through (VRT) as well as recovery slope for symmetrical and asymmetrical faults which wind power plants have to bare without disconnecting from the grid,
- ii. Limitation of active power and reactive power when faults and recovery occur,
- iii. Injection of reactive current for supporting voltage when fault and recovery occur,
- iv. Active power restoration with limited ramp after clearing the fault.

Generally in grid codes, Figure 2.22 describes the FRT as the limiting voltage curve at the grid connection point. The explanation of the shaded areas is made below:

- i. In zone 1, 3-phase short circuits or symmetrical voltage drops, because the disturbances must not cause instability or disconnection of the wind turbines from the power system.
- ii. In zone 2, there are two possibilities. First one is that wind turbines have to remain connected to the grid during the fault. If wind turbines are not able to meet the requirement, change of the borderline occurs by agreement with the TSO. The second one is a short-time disconnection of the wind turbines from the power system which is permitted by agreement with the TSO. If the wind turbines become instable during the passage through the fault or the generator protection is activated.

- iii. In zone 3, short-time interruption of the wind turbines from the grid is acceptable. Furthermore, the disconnection of the turbines along protection systems is allowable.

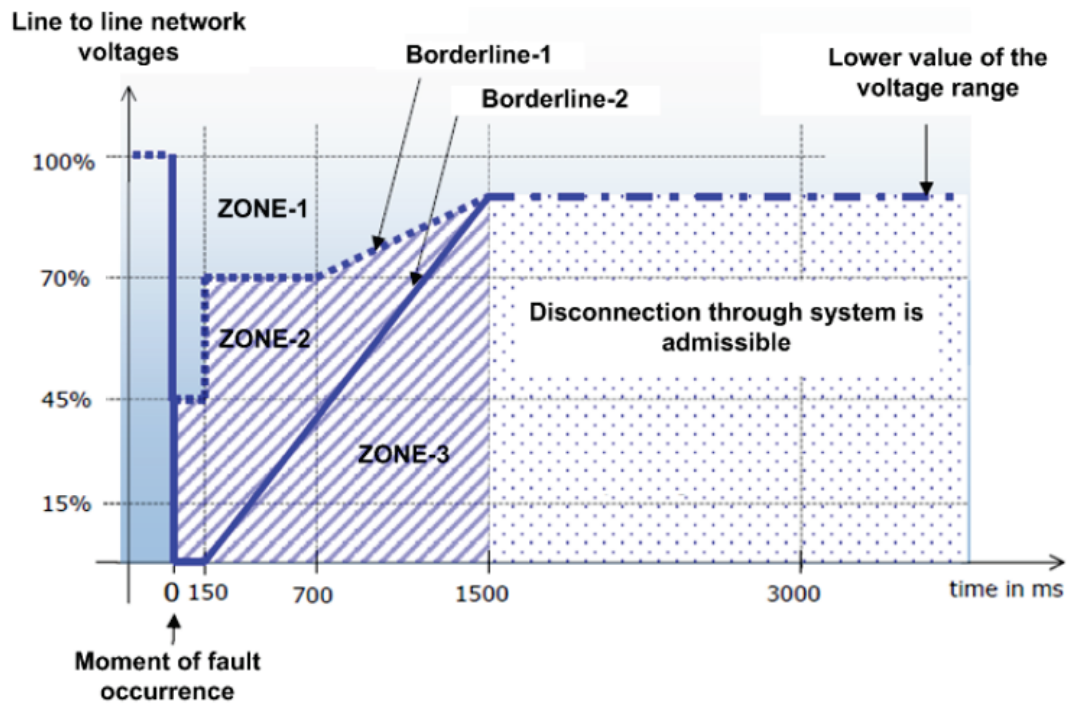


Figure 2.22 Limiting voltage curves at PCC [36].

When a voltage drop occurs, the wind turbines have to be able to support the grid voltage by injection of additional reactive current as described in Figure 2.23. Additionally, reactive current injection dead, rise, and settling time together with the post fault support time are specified regarding the grid codes.

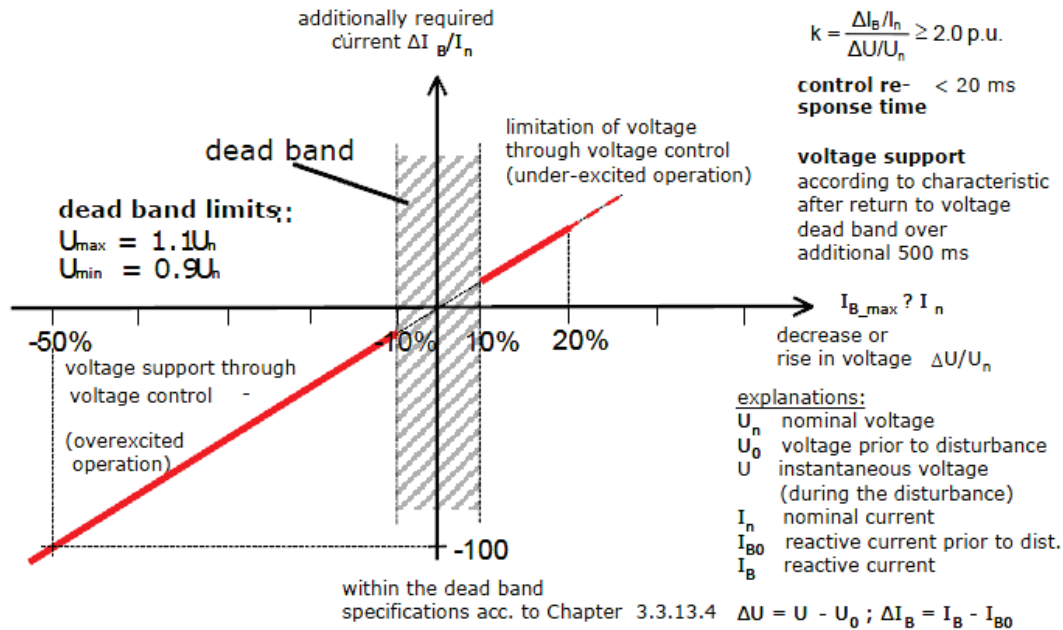


Figure 2.23 Principle of voltage support during a grid fault [36].

2.5.5. Overview of International Standards Concerning Power Quality Inserted by Wind Farms into the Grid

Harmonic current emission of wind turbines is described in standards considering measurement and assessment of power quality. Degree of variation is determined at the point of common connection (PCC) in which consumer and supplier responsibilities match. Limits for harmonic emissions are usually provided for only harmonic currents, not for harmonic voltages. Therefore, harmonic voltages have to be determined from the harmonic current emission of the wind turbine; meantime the frequency dependent short circuit impedance might be varying. Due to the grid impedance varying with frequency, utilities are not always capable of providing the frequency dependency of the grid impedances. This situation causes calculations to be difficult [47]. Harmonic background distortion resulting in great uncertainty is another consideration to be taken into account.

Harmonic emission is regarded as a power quality concern for modern wind turbines which are capable of operating with varying wind speed. Therefore, related standards such as IEC 61400-21 have requirements in terms of the measurement of

harmonics and their inclusion in the power quality certification for wind turbines [48]. Wind turbines having power electronic converters have a potential for causing harmonic distortion, thus knowledge in their harmonic current emissions is required for prediction of wind power plant behavior and design of reliable wind power plants [47]. Harmonic contribution at the point of common coupling of a wind power plant having multiple wind turbine generators arises from the harmonic generation of single wind turbines [47]. Harmonics can be divided into characteristic harmonics and non-characteristic harmonics with a power electronic equipment point of view where the distribution of phase angle is achieved randomly over different wind turbines. If loads, transmission and distribution systems are balanced, there is only characteristic harmonics. Non-characteristic harmonics are not related to the converter topology. However, they are determined by the operating point and control of the individual converter used in the wind turbine [47].

All things considered, harmonic current emission of each wind turbine should be of particular interest. Resulting harmonic voltages can either be calculated by estimating or measuring the frequency dependent grid impedances. As a remark, stiffness of the grid must be put special emphasis since this impedance is a function of short-circuit power and has a great impact on the grid impedance. Details concerning the stiffness of the grid will be provided in the following subsection.

There are a number of grid codes addressing testing and measurement techniques of the harmonic currents injected by each wind turbine to the grid. IEC 61400-21 is the most common and extensive standard that TSOs and WPP developers widely uses. It is devoted to grid-connected wind turbines and presents the procedure of harmonic measurement and analysis for grid connected wind turbines particularly for those equipped with power electronic converters. In this standard, other beneficial and required standards are also addressed in order to provide detailed testing and measuring techniques. For instance, IEC 61000-4-7, IEC 61000-4-30 are suggested standards of measuring methods on harmonic emissions. Also, IEC 61000-3-6 is used to indicate current harmonic distortion limits. Furthermore, IEC 61000-2-2 is the standard defining the current interharmonic distortion limits. As a remark, IEEE-

STD-519 is the general standard addressing recommended practices and requirements for harmonic control in electrical power systems. The last but not the least standard for WPPs suggested by IEC 61400-21 is EN50160 that addresses the international voltage harmonic distortion limits.

2.5.5.1. Current and Voltage Harmonic Standards Considered in the Design Phase

In the light of abovementioned current and voltage harmonic standards, grid connection requirements for wind energy systems in terms of voltage and current harmonics is depicted below in Figure 2.24. As a remark, the boundaries and restrictions addressed by these standards will be directly used as input to the VSC and filter design phases. The designed VSC with *LCL*-filter must yield grid currents compatible to the current harmonic distortion limits; meantime guaranteeing proper converter and filter design suitable to conventional design methodology. It should be noted that harmonic emission of the designed system must be computed by following the instructions in IEC 61400-21 and sub-standards in Figure 2.24.

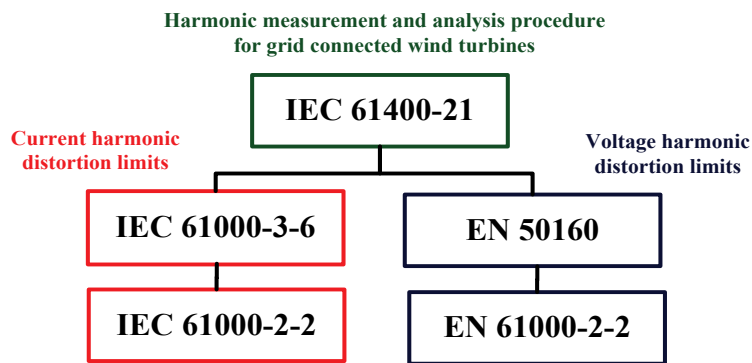


Figure 2.24 Suggested harmonic standards for grid-connected wind turbines.

2.5.5.1.1. Harmonic Voltage Injection Limits Set by EN 50160

This standard addresses the international voltage harmonic limits that can particularly be used for wind farm applications [49]. As shown in Figure 2.24, EN 50160 also mentions EN 61000-2-2 EMC standards particular for low voltage

characteristics. To sum up, the restrictions addressed by EN 50160 can be highlighted as below.

- i. Voltage unbalance for three phase inverters: max. 3%
- ii. Voltage amplitude variations: max +/-10%
- iii. Frequency variations: max +/-1%
- iv. Voltage dips: duration < 1 sec, deep < 60%
- v. Voltage harmonic levels. (5th-6%, 7th-5%, 11th-3.5%, 13th-3%, THD < 8% in LV and THD < 5% in MV and THD < 3% in HV).

where THD stands for total harmonic distortion and it is calculated as:

$$\text{THD (\%)} = \frac{\sqrt{\sum_{i=2}^n (I_{LLi})^2}}{I_{LL1}} \times 100 \quad (2.10)$$

and where i is the harmonic order and I_{LLi} is the amplitude of the i^{th} line-to-line harmonic current and n is the highest harmonic order to be involved.. Note that for voltage THD, I's in (2.10) can simply be replaced with voltage [52]. Besides, the maximum values of individual harmonic voltages up to 25th component are highlighted in Table 2.5

Table 2.5 Values of individual harmonic voltages at the supply terminals for orders up to 25, given in percent of nominal voltage U_n [49].

Odd Harmonics				Even harmonics	
Not multiples of 3		Multiples of 3			
Order h	Relative voltage (%)	Order h	Relative voltage (%)	Order h	Relative voltage (%)
5	6	3	5	2	2
7	5	9	1.5	4	1
11	3.5	15	0.5	6...24	0.5
13	3	21	0.5		
17	2				
19	1.5				
23	1.5				
25	1.5				

Additionally, IEC 61400-21 suggest that the wind turbines connected directly to the medium voltage network through a standard step-up transformer should have a total voltage harmonic distortion, THD_v less than 5% including all harmonics up to order 50 measured as 10 min average data at the HV-side of the wind turbine step-up transformers (MV-level). It is also reported that harmonics below 0.1% of rated voltage should be neglected [48]. In addition, IEEE-STD-519 recommends THD_v should be less than 5% on power lines below 69 kV including that lower harmonic limits are forced on higher supply voltages [52].

2.5.5.1.2. Harmonic Current Injection Limits Set by IEC61000-3-6

IEC 61000-3-6 provides a useful guideline as well as limits for harmonic current. In the IEC 61400-21 guideline, harmonic measurements are not actually necessary for wind turbines operating at fixed speed of which the induction generator connection is directly to the grid. Harmonic measurements are needed only for wind turbines operating at variable wind speed which normally have electronic power converters. Generally, wind turbine power converters are pulse-width modulated inverters which have carrier frequencies ranging from 2 to 3 kHz, and mostly produce inter-harmonic currents [51].

The harmonic contribution of each wind turbine is different since the operating point and system properties are unique for each turbine. Therefore, it is very unlikely that all wind generators in a wind farm inject worst case harmonic currents with the same phase angle at the same time. In Europe, the standard IEC 61400-21 recommends to apply the current harmonic standard IEC 61000-3-6 that involves the superposition of the harmonics by grouping harmonics within certain intervals. IEC 61000-3-6 is valid for pulling loads requiring the current total THD smaller than 6-8% depending on the type of the network. For the individual low current harmonics specifications, Table 2.6 can be applied [51].

Table 2.6 Values of individual harmonic currents at the supply terminals, given in percent of fundamental rated current I_r [51].

Harmonic order	Limit
5th	5-6 %
7th	3-4 %
11th	1.5-3 %
13th	1-2.5 %

IEC 61000-3-6 provide a guide for summing the harmonic current distortion from loads [51]. With the help of this guidance, the harmonic current at the PCC with a given number of wind turbines can be estimated by application of equation (2.11):

$$I_{h\Sigma} = \sqrt{\sum_{i=1}^{N_{WT}} \left(\frac{I_{h,i}}{n_i} \right)^\beta} \quad (2.11)$$

where

N_{WT} is the number of wind turbines connected to the PCC;

$I_{h\Sigma}$ is the h^{th} order harmonic current distortion at the PCC;

n_i is the ratio of the transformer at the i^{th} wind turbine;

$I_{h,i}$ is the h^{th} order harmonic current distortion of the i^{th} wind turbine;

β is an exponent with a numerical value to be selected according to Table 2.7 and the points below.

Table 2.7 Specification of exponents according to IEC 61000-3-6.

Harmonic order	β
$h < 5$	1,0
$5 \leq h \leq 10$	1,4
$h > 10$	2,0

If the wind turbines have the same properties and capacity, and the line of their converters are commutated, the harmonics are tend to be in phase and $\beta = 1$ can be used for all harmonic orders. Equation (2.11) does not take into consideration using transformers having different vector groups which might cancel out some particular harmonics. If this is the case, adequate measures should be included to involve the effect of it. Equation (2.11) can be employed for current interharmonics and higher frequency components as well. Since current interharmonics and higher frequency components are assumed to be uncorrelated, it is recommended to use $\beta = 2$ in (2.11) for summing these.

2.5.5.2. The Impact of Injected Harmonics According to Stiffness of the Grid

The harmonic currents cause harmonic voltage drops along the line impedance, in return distorting the voltage. The extent of this distortion is mainly related to the distorting load power and the short-circuit power of the equivalent network, so even small power distorting loads can affect significantly the bus voltage if the line short-circuit power is low [47]. Thus, the short-circuit power (SCC) is an important indicator shading light on the stiffness of the grid.

Since wind farms are typically located far from major load centers and central generation, most of the time there is no option other than connection to the weak grids [47]. In the literature, stiffness of the grids is generally represented by the term short-circuit ratio (SCR). It is defined with the ratio of SCC to the installed VA capacity of the system S_n . The terms SCC and SCR can be calculated as follows in (2.12) and (2.13), respectively.

$$SCC = \frac{V_{rated}^2}{|Z_{line}|} \quad (2.12)$$

$$SCR = \frac{SCC}{S_n} \quad (2.13)$$

where Z_{line} is the impedance of the line connecting the grid with wind farm and V_{rated} is the rated voltage of the grid.

In the literature, if the SCR is less than 8-10, grid is considered as weak grid; whereas, grids with SCRs higher than 20-25 are regarded as stiff (strong) grid [50].

In case of WT injecting full power to the weak grid at the PCC with a voltage U_{PCC} , changes for different combinations of P and Q can be seen in Figure 2.25 (a). WT provides feed in active power all the time, thus P and $\cos(\varphi)$ always stay positive while reactive power can be inductive or capacitive [50]. Therefore, for weak grids, stable operation cannot be achieved unless there is aid of either additional compensation (FACTS-STATCOM) or oversized grid-side converter [50].

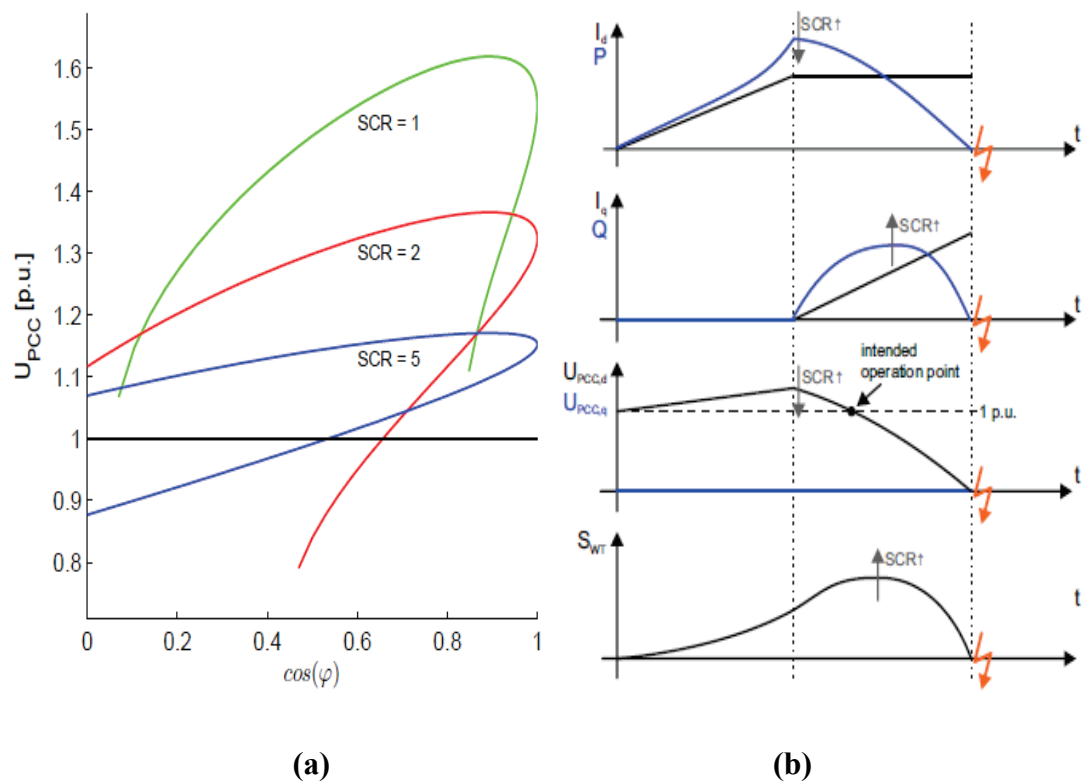


Figure 2.25 (a) U_{PCC} at power injection of $SWT = 1$ p.u. (b) Outline of a process of grid instabilization for a weak grid with a low SCR [50].

Possible grid instabilization process can be seen in Figure 2.25(b). Constant increase in the active current I_d leads to increasing active power P which equals to total power S_{WT} , as a result, to increasing U_{PCC} . By means of injecting a reactive current I_q PCC voltage can be lowered till the intended operation point is achieved. If the injection of I_q is increased more, system operation becomes impossible when U_{PCC} falls down to zero volts. The grey arrows Figure 2.25(b) indicate where the maxima of the single curves would move if SCR was increased [50].

In the light of abovementioned SCR definition and analyses, it can be deduced that SCR reflects the capability of injecting the reactive power required by the transmission line and transformers. Z_{line} is the sum of the impedances of many grid components and typically differs from region to region. If the transmission distances increase, as present in offshore wind applications, or Z_{line} increases due to a certain reason SCC will diminish and hence so will SCR, in return the grid gets weaker.

2.5.5.2.1. The Impact of Grid Stiffness on Harmonic Current Injection Limits Set by VDEW

VDEW is the guideline which provides guidance in connection and parallel operation of generators at the medium voltage grid [53]. The maximum allowed values for harmonic current components ($I_{v,\mu,allowed}$) can be calculated by multiplying the constants shown in Table 2.8 ($i_{v,\mu,allowed}$) by the short-circuit power SCC at the connecting point as shown in (2.14):

$$I_{v,\mu,allowed} = I_{v,\mu,zul} \cdot SCC \quad (2.14)$$

Limits for other voltage levels can be obtained by direct calculation using the given values, considering those are inversely proportional to the voltage value. Triple harmonic components and harmonics up to 25th order have their limits based on the ones of next given order (for example, the 9th harmonic order limit is equal to the 11th one) with the condition that produced zero-sequence currents are not inserted on

the grid. The index ν describes the integer harmonics and the index μ the interharmonics.

Table 2.8 Allowed rated harmonic currents (VDEW [53]).

Harmonics Order ν, μ	Allowed rated harmonic currents $I_{\nu,\mu,allowed}$ in A/MVA	
	10 kV Grid	20 kV Grid
5	0.115	0.058
7	0.082	0.041
11	0.052	0.026
13	0.038	0.019
17	0.022	0.011
19	0.018	0.009
23	0.012	0.006
25	0.010	0.005
>25 or pairs	$0.06/\nu$	$0.03/\nu$
$\mu < 40$	$0.06/\mu$	$0.03/\mu$
$\mu > 40^*$	$0.18/\mu$	$0.09/\mu$

* Integer and not integer within a Bandwidth of 200 Hz

VDEW sets certain limits on individual harmonics regarding the stiffness of the grid, providing the most elaborate current harmonic standards in the literature [53]. Since SCC vary over grid to grid, harmonic standards monitored by VDEW provide fair restrictions on current harmonic emissions.

2.6. Conclusions

In this chapter, a number of statistical data concerning cumulative and annual installed capacity of WTs at the end of 2013 have been provided. A possible forecast in terms of total installed capacity of wind energy throughout the world within the next 4-5 years has been stated. Furthermore, the proportion of WT applications to the total installed capacity both in domestic and worldwide aspects has also been mentioned. Extensive information about the structure of WPPs and voltage connection levels according to the power capacity of WPPs has been demonstrated. Plus, the transformer structures on PCC connection in the light of individual and

farm applications have been mentioned. Then, as being one of the elements of WPPs, the general structure of individual WTs have been taken into consideration by focusing on the special power electronics part namely, grid-side DC/AC converter of the back-to-back PWM-VSC for full-scale wind turbine structure. Additionally, insights on WT applications have been broadened in terms of capacity factor and operational efficiency. A novel operational efficiency definition has been provided as a figure of merit of WTs. Moreover, international grid codes particular for WTs, involving active power, reactive power, voltage and frequency control, fault ride through capability and power quality injected to the grid have been demonstrated in quite detail.

Amongst the numerous grid standards, IEC 61400-21 is the fundamental standard for grid-connected WTs since it provides harmonic measurement and analysis procedure and proposes additional standards to calculate and measure voltage/current harmonics/interharmonics properly. However, IEC 61400-21 and the other standards addressed by it provide general limitations on current/voltage harmonics and do not take the grid stiffness into account. But, it has been shown that grid stiffness is the most important variable determining the individual harmonic limits. For this reason, the German code VDEW has been widely used all over the world by TSOs, WPP developers and WT manufacturers. As VDEW affords the most detailed harmonic current limits and considers the medium voltage level together with the grid stiffness, it will be utilized for the assessment of the designed PWM-VSCs throughout this dissertation.

CHAPTER 3

DETERMINATION OF SWITCHING FREQUENCY CONSTRAINT REGARDING EFFICIENCY TARGET OF THE DESIGN

First two chapters define the borders of this study. Particularly, Chapter 2 provides detailed information about the specifications for the grid interface. To start converter design process, this chapter is dedicated to shed a light on the determination of a suitable switching frequency or a frequency interval for the design of grid-side converter of back-to-back VSC employed in the recent wind turbines. The methodology is simple, first of all efficiency criterion (expected efficiency) must be determined. Efficiency is one of the most important inputs of converter design procedure regardless of the type of system, so every design should aim the highest achievable efficiency. On designation of a suitable efficiency target, power rating of the converter plays the key role. Taking the type of the converter and the power rating into account, equivalent designs in the market can be enquired in order to have the insight of which converter topologies, semiconductor types, switching techniques, efficiency targets and so on are dominating the choices. For instance, for a proper design of back-to-back VSC, modern wind turbine converters having the same power rating should be investigated thoroughly and widely favored means of topology, semiconductor, switching strategy together with the possible output efficiency value should be obtained. As a matter of fact, each type of system has a distinct maximum achievable efficiency target since it is primarily limited by the recent technological developments on that area. For instance, the output efficiency expectations of wind turbine converters and PV converters are quite different nowadays due to different input penetration capability. Next section provides rewarding information about the grid-connected converters of recent wind turbines

according to power rating and voltage level (low-voltage/medium voltage) of diverse products of distinct manufacturers.

3.1. A Brief Survey on Recent Converter Properties

Electric power obtained from wind generators is not constant due to wind speed variations. The generated electric power and the loss in WTG systems change corresponding to the wind speed variations, and consequently the efficiency and the capacity factor of the system also change [104]. In this chapter, the losses and prospective efficiencies of wind generator systems having back to back VSCs are explained. The wind characteristic of each area is different and thus the optimal WTG system for each area is different. In the determination of optimal WTG system, annual energy production and capacity factor are very important factors. In order to capture more energy from wind, it is essential to analyze the loss characteristics of converters within WTG systems. For this purpose, wind turbine converters of well-known WT manufacturers such as ABB, Siemens, Vacon and so on will be examined regarding the proposed switching frequency intervals and energy efficiency at the converter's rated point. Widespread generator configurations preferred in the products and favored topologies and voltage-levels in the back-to-back VSCs are investigated regarding the power rating of the products.

3.1.1. Features of Low-Voltage and Medium Voltage Wind Turbine Converters

As mentioned in Chapter 1-2, partial-scale and full-scale converters are the most favored structures in today's WT systems. For instance, ABB low voltage wind turbine converters, ACS800 series offers 0.6-6 MW converters in these two configurations [105]. It is better to tabulate the features of this series in Table 3.1.

As evident in Table 3.1, low-voltage converters operate around 96.5%-98% efficiency at the rated load. Although higher power levels can be reached by full-scale topology, semiconductor losses escalates in return slightly lower efficiency is obtained. Besides, full-scale converters utilize paralleled two-level and/or three-level

VSC topologies consisting of IGBTs [105]. Also, full power converter over 2 MW offers a redundancy design option for parallel connected sub-converters. Very low total harmonic distortion is also attained for both configurations.

Table 3.1 ACS800 low-voltage wind turbine converters [105].

Converter model	ACS800-67	ACS800-67LC	ACS800-77LC	ACS800-87LC
Converter type	Partial-scale (DFIG)		Full-scale (Permanent magnet / Asynchronous generator.)	
Power range	0.9-2.2 MW	1-3.8 MW	0.6-3.3 MW	1.5-6 MW
Optional sub-converter configuration	-	-	Available from 1.9 MW	Available from 3.6 MW
Electrical data				
Rated grid voltage	525 to 690 V AC, 3 ph, $\pm 10\%$			
Nominal frequency	50 \pm 3 Hz / 60 \pm 3 Hz			
Efficiency at converter's rated point	$\geq 98\%$	$\geq 97\%$	$\geq 96.5\%$	
Grid harmonics Total harmonic current distortion (n = 2 to 40)	Max 3% with DFIG generator current		Max 4%	

On the other hand, PCS 6000 for large wind turbines medium voltage, full power converters up to 9 MVA is another series of ABB [106]. In medium voltage designs, full-scale converter structure is preferred. Particularly, 3L-NPC topology using IGCTs is preferred for this series. Three distinct power levels of 4 MVA, 4.5 MVA and 9 MVA are offered with 98% efficiency. Also, grid voltage level is 3.3 kV [106].

To sum up, multi-megawatt converter series of ABB for wind power applications are classified as below:

PCS 500 – low voltage: 0.5 – 2 / 4 MVA

PCS1000 – medium voltage: 2 – 5 MVA.

PCS6000 – medium voltage: 5 – 9 MVA.

Last, VACON 8000 wind turbines offer two power levels 1.5 MW and 2 MW connected to 690 V_{AC} grid voltage. DFIG configuration is favored and switching frequency is confined to 1.5-3.6 kHz interval [107].

According to above industrial designs, low-voltage converters are confined to 2-4 MVA while two-level and three-level converter topologies are employed in the full-scale converters. Beyond this range, converters are designed according to medium-voltage network. As the demanded power rating increase, partial-scale converters are replaced by full-scale converters.

3.1.2. Types of Power Semiconductors According to Power Rating

After discussing available converter topologies, it is time to focus on preferred semiconductor types (according to power levels) in commercial products. The available power semiconductors are mainly turn-off devices up to high power ratings. The ultra-high power area is still covered by the thyristors, which can only turn-on and need commutation by the power circuit (Figure 3.1) [108].

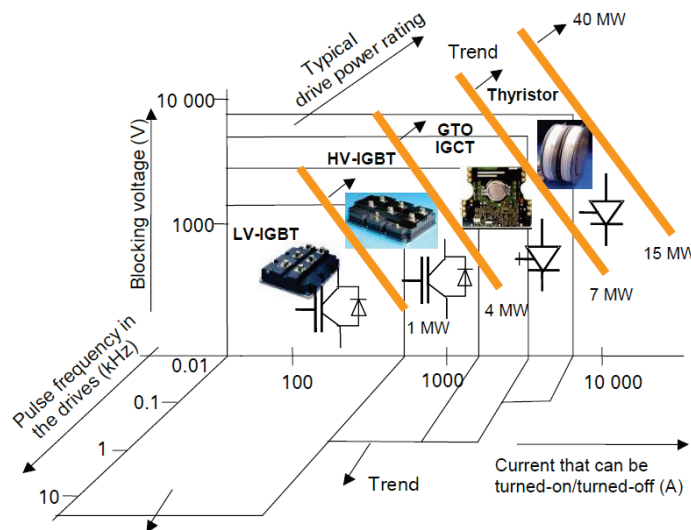


Figure 3.1 Power semiconductors [108].

Further properties of the revealed semiconductor types according to power level are summarized in Table 3.2.

Table 3.2 Transistors overview [108].

Base Technology			Special Features	Short Cct. Lim.	Switching Losses	Conduction Losses
Transistor	Voltage driven turn on/off technology, low control energy, high switching frequency	Low Voltage Insulated Gate Bipolar Transistor (LV-IGBT)	Cost effective, module size	Yes	Low	High
		High Voltage Insulated Gate Bipolar Transistor (LV-IGBT)	Module size, mainstream	Yes	Low	High
		Press Pack IGBT (PPI)	Press packed (single source)	Yes	Low	High
		Injection Enhanced IGBT (IEGT)	High ratings (single source)	No	Medium	Medium
Thyristor	Current driven turn-on/-off technology, high ratings, low conducting losses	Gate turn off thyristor (GTO)	Need of large snubber	No	High	Low
		Integrated gate commutated thyristor (IGCT)	High ratings, mainstream	No	Medium	Low
		Symmetrical gate commutated thyristor (SGCT)	Reverse blocking for CSI	No	Medium	Low
	Only turn on, very high ratings	Silicon controlled rectifier (SCR=thyristor)	Need of commutation	No	Low	Low

Consequently, the low-voltage and medium voltage VSCs suitable to wind turbine applications mostly involve HV-IGBTs, IGCTs and GTOs due to their highlighted properties in Table 3.2. Apart from their features shown in the table, blocking voltage vs. current vs. switching frequency attributes according to power level are depicted in Figure 3.1.

3.1.3. Modulation Strategies of Wind Turbine Converters

In recent years, several space vector algorithms extended to voltage-source converters have been found in the research. Most of them are particularly designed for a specific number of levels of the converter and the computational cost and the

algorithm complexity are increased with the number of levels. Recent space vector modulation (SVM) strategies have drastically reduced the computational effort and the complexity of the algorithms compared with other conventional SVM and sinusoidal PWM modulation techniques [109]. These techniques provide the nearest state vectors to the reference vector forming the switching sequence and calculating the corresponding duty cycles using extremely simple calculations without involving trigonometric functions, look-up tables, or coordinate system transformations. Therefore, these methods drastically reduce the computational load maintained, permitting the online computation of the switching sequence and the on-state durations of the respective switching state vectors. In addition, the low computational cost of the proposed methods is always the same and it is independent of the number of levels of the converter [109]. Specific types of space vector modulation techniques, namely space vector pulse width modulation (SVPWM) and discontinuous PWM1 (DPWM1) methods are two of the most widely used techniques in industry. Hence, these two methods will be discussed in the next section. Further details of SVPWM and DPWM1 can be found in [112].

3.2. Determination of Switching Frequency Constraint Regarding Efficiency Target of the Design

As evident from the survey, power rating and efficiency values are shared in the manufacturer catalogs and datasheets. Using these two information, converter topology must be determined as the first step of the design. As a remark, power rating and efficiency are given for a specified converter topology in the datasheets, so selection of the topology based on these values is already confined to few choices. 2L-VSC and 3L-VSC topologies are the most preferred topologies based on the findings in the survey. If higher efficiency is required, selection of 3L over 2L is always favored. However, 2L-VSC is still widely used due to its simplicity and mass production. As a remark, voltage-level is also important on topology selection. If the converter is connected directly to the medium voltage-level, peak output current gets quite lower compared to low-voltage connected converter. This enables the designer to keep the efficiency at quite high values. On the contrary, high power low-voltage

applications limit the design options due to the limited semiconductor technology. This situation is overcome by paralleling the modules or converters which in return increases the initial costs. After determining the topology, the performance of the converter under different switching frequencies must be investigated. In order to assess the converter performance in terms of efficiency, a set of switching frequencies is used and efficiency (η) vs. switching frequency (f_{sw}) characteristics of the design is obtained. The frequency spectrum that f_{sw} set should span depends on power rating of VSC. For instance, for tens of kilowatt VSC design, f_{sw} can be ranged up to 20-30 kHz; however, for multi-megawatt VSC designs, 4-5 kHz can be achieved at most. Finally, evaluation on efficiency vs. f_{sw} characteristics determines the achievable switching frequency interval since the switching frequency primarily affects the semiconductor loss, the filter loss, and the other losses having various attributes against varying switching frequency. Thus, output efficiency of entire system (converter + grid interface) is dependent on the switching frequency. It should also be noted that to attain such a performance analysis, PWM method should also be determined in advance since each part of the system must be definite to run simulation/calculation analysis. For this reason, this analysis can be conducted under distinct PWM patterns and the one offering better efficiency characteristics is opted.

Combining all of the steps, Figure 3.2 summarizes the procedure to obtain switching frequency constraint for the wind turbine converter design.

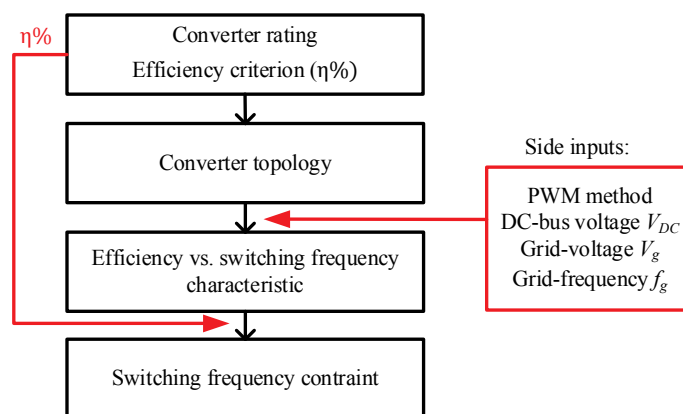


Figure 3.2 Determination of f_{sw} constraint regarding efficiency target of the design.

Frankly, this flow diagram is also suitable for any kind of power electronics converter design taking the maximum achievable efficiency of particular concern.

3.3. Illustration through a Numerical Design

In this section, an exemplary switching frequency constraint designation case is provided. The procedure described in the diagram is followed. It should be noted that the red box on the right hand-side of the flow diagram (Figure 3.2) reveals the necessary inputs to be able to run a simulation or calculation to evaluate the efficiency of the system. These are in short, PWM method, the grid frequency (f_g), the grid voltage (v_g), the DC-link voltage (V_{DC}) as depicted in Figure 3.2.

First of all, converter rating is selected as 1 MVA. According to catalog information, 1 MVA converters yield efficiency at the converter terminals around 98.5-99%. Secondly, instead of selecting a certain type of topology, illustration case is broadened by evaluating the three most favored VSC topologies, namely two-level (2L), three-level neutral point clamped (3L-NPC) and three-level T-type (3L-T). Before the analysis to obtain efficiency (η) vs. switching frequency (f_{sw}) characteristics for each topology, PWM pattern is selected. For the illustrative case, SVPWM and DPWM1 methods are used. Figure 3.3 depicts efficiency vs. f_{sw} characteristics for each topology under SVPWM. For the efficiency target of 98.5-99%, achievable f_{sw} interval has been unveiled as 1-2.5 kHz for 2L-VSC (f_{sw-2L} interval), posing a switching frequency constraint. For the same efficiency target, switching frequency is confined to 2-4.5 kHz interval for both 3L-VSC (f_{sw-3L} interval) topologies as evident in Figure 3.3.

To sum up, upper and lower boundaries of f_{sw} is determined for the targeted efficiency interval. Thus, if f_{sw} is selected within the determined interval, then desired efficiency target is guaranteed. It should be noted that the accuracy of this assumption mainly depends on the accuracy of semiconductor loss, filter loss, damping loss and other losses calculation mechanisms. If some of the losses are neglected in efficiency calculations or loss calculation methods are not so reliable, then it is very likely that assumed and obtained efficiency values do not match

perfectly. Additionally, when determining f_{sw} interval, there should always be a margin to compensate for the unpredictable losses likely to occur during converter operation.

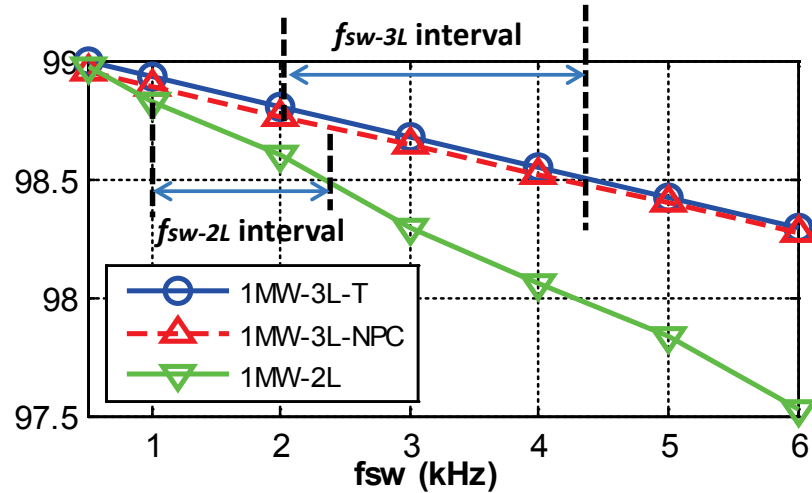


Figure 3.3 η (%) vs. f_{sw} plot of three VSC topologies under SVPWM.

Finally, in addition to SVPWM method, efficiency vs. f_{sw} attributes of 2L-VSC has also been derived under DPWM1 method in Figure 3.4.

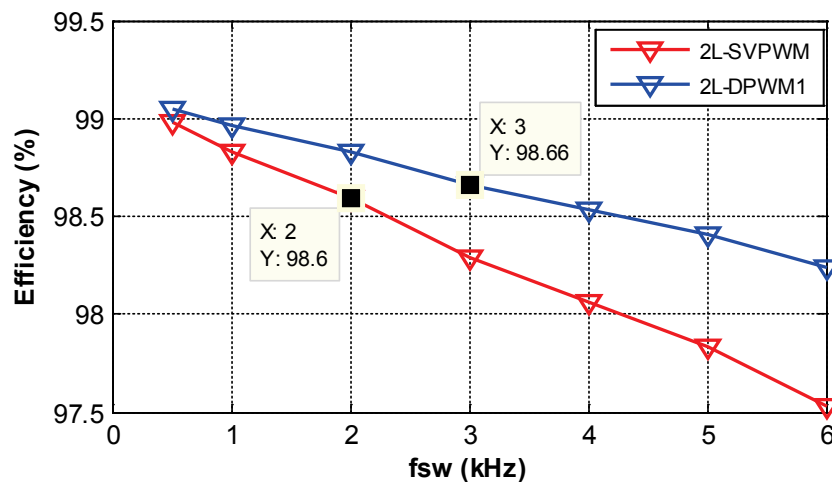


Figure 3.4. η (%) vs. f_{sw} (SVPWM and DPWM1).

As evident in the figure, efficiency value differs considerably at the same f_{sw} . Therefore, the interval of 1-2.5 kHz (2L-SVPWM) should be updated as 1.5-4 kHz

for 2L-VSC under DPWM1. Consequently, for the targeted efficiency, switching frequency constraint is obtained for 1 MVA converter for three distinct VSC topologies under two different PWM methods.

3.4. Summary and Conclusions

This chapter has mentioned mainstream design specifications for recent wind turbine converters. In this aspect, possible inputs, expected outputs, favored converter topologies, modulation techniques, preferred semiconductor types have been investigated through manufacturer catalogs and datasheets for distinct power levels. Thus, all of the aspects of grid-side converter of the back to back VSC converter in WTs have been covered and an expected efficiency interval has been unveiled that the recent converters try to achieve. Then, in order to fulfill this efficiency specification, a switching frequency interval has been determined, leading to switching frequency constraint of the design procedure.

This kind of approach on converter design procedure is the most convenient way since it minimizes the iterations and tries to offer one-path design. Since all of the substantial losses can be modeled as a function of switching frequency, constraining it will guarantee an output efficiency complying with the efficiency target. However, it should be noted that there should always be a margin while determining switching frequency interval to compensate for the unpredictable losses likely to occur during converter operation.

With the proposed method, power rating, topology, PWM method, efficiency characteristics, and switching frequency range are determined in order. After completing the converter design part, the next step is the design of grid interface i.e. *LCL*-filter design. For this purpose, the next two chapters provide a thorough filter design methodology based on a comprehensive theoretical insight.

CHAPTER 4

A COMPREHENSIVE *LCL*-FILTER STUDY REGARDING CONTROL AND STABILITY ANALYSES

Most of the grid-connected wind turbines utilize back-to-back converter topology as presented in the first three chapters and design of the grid-side converter of the back-to-back converter topology is the focus of this dissertation. However, the design procedure also involves the grid interface design. For the grid interface, *LCL*-filters are used. Since the converter design has been presented in the former chapter, *LCL*-filter design and stability analysis are shown in the following two chapters. Particularly, this chapter is devoted to the entire control background and stability analysis of the grid-connected PWM VSCs utilizing *LCL*-type filters. The advantages brought by *LCL*-filters mentioned in Chapter 1 will be extended in this chapter.

Modern grid-connected PWM VSCs in wind energy systems widely use voltage-oriented current control strategy owing to its superiority in both steady-state and transient-state performance [54]-[61]. Voltage-oriented current control method can be deemed as nested two control blocks: outer block is in charge with dc-link voltage control whereas the inner loop regulates the output current [55]-[59][65]. Thorough information regarding voltage oriented current control will be provided in this chapter. As a remark, inner current control loop requires special emphasis. As stated widely in the literature, current control is very complex for the systems employing *LCL*-filters due to the presence of resonance [54]-[68]. The merit of this chapter becomes evident at this point. It refines the extensive but disoriented information about current control techniques in the literature, modifies the

approaches regarding the objectives of wind power applications and provides novel arguments that literature lacks.

4.1. Improvements Provided by *LCL*-Filters

As mentioned previously, the connection to the electric utility is provided through *LCL*-line filters rather than single *L*-filters in modern PWM-VSCs. *LCL* line filters have been found to be superior to the usual *L* filters in size and weight aspects. Especially in high power applications, where the switching frequency is limited to a few kHz, single *L*-filters become bulky and costly. Additionally, the dynamic response of the converter is improved owing to the third order characteristics of the *LCL*-network. Besides, *LCL*-filters ensure a more compact system (smaller passive elements) and better ripple and PWM switching harmonic attenuation (60 dB/dec) due to its third order characteristics compared to the conventional *L*-filters (20dB/dec). Particularly, reduction in size makes *LCL*-line filters more favorable in high power VSCs. As a result, they have been widely used in renewable energy systems of over hundreds of kilowatts [54]-[58]. In spite of these prevailing advantages over simple *L*-filters, the utilization of *LCL*-filters as the grid interface for VSCs, makes the control design very complex. Since, the presence of *LC* part brings about resonant pole pair at the resonant frequency (f_{res}) and this pole pair leads to the amplification of undesired harmonic components around the closed-loop stability boundary [54]-[56]. This amplification through the filter is emerged due to the fact that the *LCL*-filter has zero or very low impedance around the resonant frequency. The harmonics created by the VSC at this frequency are amplified through the filter and injected to the grid and hence closed-loop instability is inevitable. In the literature, this phenomenon is dealt with the employment of various resonance damping methods such as passive damping (PD) provided with resistors connected in several ways to the *LCL*-filter [54][56]; active damping (AD) supplied with the modification of the current control structure using filter capacitor current [55]-[58], or capacitor voltage [55]; inherent damping (ID) achieved by only using converter-side current feedback [57]; and sensorless AD based on estimation of the state variables by using complex state observers.

PD techniques provide a rugged and simple solution. In PD techniques, resistors are added to the filter capacitor (C_f) branch in several different ways to suppress the resonance [66]. The variation of the *LCL*-filter parameters over time or the existence of stray inductance and capacitance in the system alter the initially appointed resonant frequency; however, the change in the resonant frequency does not affect the stability of the system since there is always nonzero impedance at the filter capacitor branch blunting the resonance [60]. Hence, PD guarantees the stable and long-lasting operation of the system. Besides, unlike AD techniques, there is no need to use additional voltage and/or current sensors in PD methods. Although, the elimination of extra sensor requirements is attractive; yet, the dynamic response of the system deteriorates considerably and high frequency oscillations arise at the edge of load changing instants. Since at higher frequencies, damping resistors may reduce the order of the *LCL*-filter to a second order system and hence nullify the enhancements brought by the third-order attenuation capability [57]. Moreover, the extra losses due to PD not only lead to undesirable temperature rise and decrease in the life time of filter elements but also degrade the efficiency of the system considerably.

AD methods; on the other hand, alter the reference voltage information to create a fictitious damping term with no additional power losses [60]. So, harmonics at resonant frequency are not excited and closed-loop stability is maintained. The verification of the AD methods is stated explicitly in the literature; however, the complexity in the controllers and adjustment of *LCL*-filter parameters to achieve a suitably damped system requires more effort. Besides, AD methods usually involve additional sensors, which bring an extra cost [54]-[58]. Thus, the increase in the overall system cost and implementation complexity is unavoidable, orienting designers to reduce the number of the sensors or to develop sensorless AD methods, where the necessary state variables are estimated by means of complex state observers. Nonetheless, complex state observer based solutions are not reliable since they are highly dependent on the system parameters that may change over a period of time or under distinct operation conditions [54].

To summarize, each damping method has its own characteristic features which may be appealing in terms of design simplicity or cost. The cost minimization for the operation of the converter should be considered by the designer and then optimum damping method should be opted. The power rating is also an important constraint since high power applications are generally not suitable for AD due to very limited switching frequencies around a few kHz [63].

4.2. System Description and Modeling

Figure 4.1 demonstrates a three-phase VSC connected to the grid via an *LCL*-filter. In order to model the behavior of the grid at the point of common coupling (PCC) accurately, the grid resistance (R_{grid}) and the grid inductance (L_{grid}) are taken into account. Any load connections to the grid are achieved through PCC. Hence, it is better to say that *LCL*-filter is settled between the VSC and PCC.

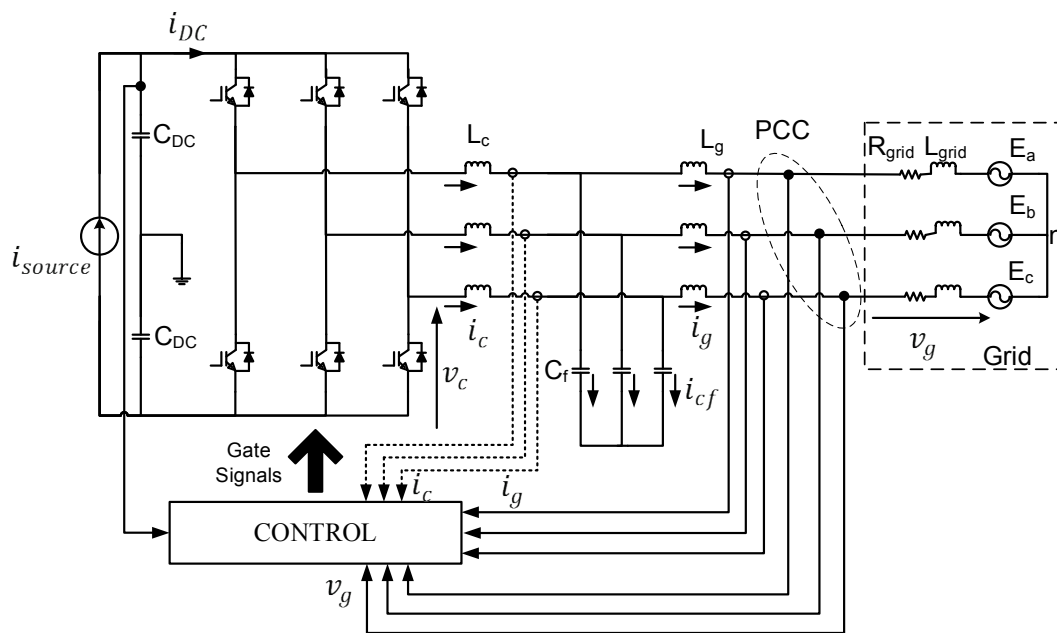


Figure 4.1 Grid connected three-phase VSC with control block.

PWM in conjunction with cascaded closed-loop control structure with outer dc-link voltage control and inner current control loop is utilized very frequently in grid-connected VSC applications. Unlike simple L -filters, LCL -filters have two available current feedback state variables providing flexibility in the measurements regarding the trade-off between resonance damping and dynamic performance [70]. Inner current loop utilizes either the converter-side current (i_c) or the grid (line) side current (i_g) as the feedback variable as shown in Figure 4.1. However, deciding on the type of the current feedback is not an easy task. On the one hand, if the industrial unit contains current sensors embedded in the converter (i.e. for protection purposes), feeding back the converter-side current is rational. Yet, power factor (PF) compensation becomes mandatory due to the presence of the filter phase shift in this method. On the other hand, if the primary objective is to control PF at the PCC, the employment of grid-side current feedback is reasonable. Then, the line current phase angle can be directly controlled. However, the requirement of the line current measurement brings additional cost of current sensors and decreases reliability [54]-[61]. Overall, the priority of the objectives of the design generally determines the current feedback variable.

Dannehl *et al.* [61] have come up with the fact that grid current feedback is slightly more stable than the converter current feedback for the designed set of LCL -parameters. However, it should be born in mind that the position of the resonant frequency in the frequency domain completely affects the stability performance of the each feedback type. Thus, Holmes *et al.* [58] identify two distinct regions (separated by critical resonance frequency) regarding the location of resonant frequency when grid current feedback is employed and comments on the possible outcomes when the converter current feedback is utilized. In the light of those developments in the literature, this dissertation tries to cease the ambiguity of which type of current control provides better dynamic performance while not compromising resonance damping will be clarified fully under distinct resonant frequencies in the following sections.

4.3. Control Overview and Controller Design

In this work, stabilization is not regarded as the only aim of the controller design procedure, damping extent of the resonance poles are also investigated and correlated with high frequency oscillations occurring at the transient periods. Apart from resonance poles, low frequency system poles (dominant poles) of the system are also considered to comment on overshoot percentages of the dynamic responses presented by means of MATLAB[®] and SIMPLORER[®] outputs.

The ideal *LCL*-filter consumes only reactive power; nevertheless, the components in real life have resistive parts. However, the core and copper loss of grid-side filter inductors (L_g) and converter-side filter inductors (L_c) and the equivalent series resistances (ESRs) of filter capacitors (C_f) are neglected in controller design phase to model a worst case undamped scenario.

4.3.1. Control Overview

Figure 4.2 shows the cascaded control structure of a three-phase VSC. The outer control loop regulates the dc link voltage V_{DC} to the constant reference value V_{DC}^* by producing the reference value for the current controllers. The inner control loop regulates the active and reactive components of the current feedback variable in the light of the reference value generated by the outer loop. Hence, this nested control loop structure can be named as “voltage-oriented current control technique”. Both of the outer and the inner loop achieve regulation in synchronous reference frame which are locked directly to the grid voltage vector as depicted in Figure 4.2. The phase angle of line voltages are determined using phase-locked loop (PLL) algorithm stated in [63]. Either grid current feedback or converter current feedback can be set as the current feedback variable as shown in Figure 4.2 noting that the *LCL*-filter transfer function differs in each case.

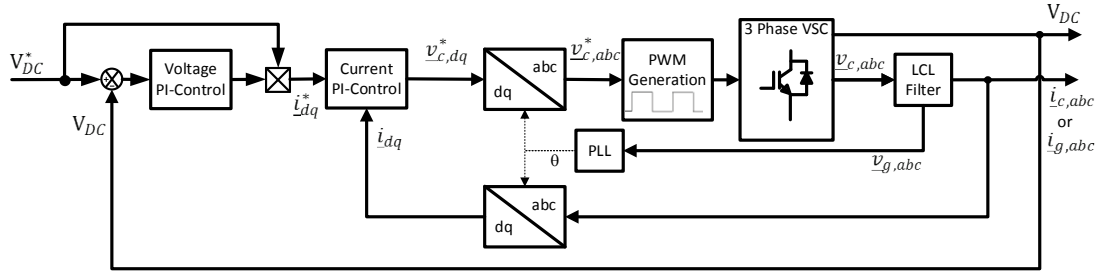


Figure 4.2 Current control structure.

In order to acquire current control with rapid dynamic response, a rotating frame is frequently preferred in the current controller designs. Nevertheless, there are also other current controllers such as resonant controllers employing stationary frame. In this work, the control loop is designed as a two-phase dq -reference frame rotating at the grid frequency ω_g as shown in Figure 4.4. Thus, the control of three-phase ac signals is evolved to the control of two-phase rotating dq -reference frame dc signals. It is more advantageous to control dc values because as a well-known linear control technique, namely PI controller performs reference tracking with zero error in steady-state employing dc values. Thus, reliability (zero error in the steady-state) and simplicity (two PI current controllers rather than three) is ensured by implementing the current control design in dq -frame.

In Figure 4.2, the outer dc-link voltage control loop produces the dq current reference vector (\underline{i}_{dq}^*) for the inner current control loop. Then, \underline{i}_{dq}^* is compared with the actual value of the current feedback variable \underline{i}_{dq} transformed into the dq -frame and the output of the inner current control loop then determines the reference value for the dq -frame VSC output voltage vector $\underline{v}_{c,dq}^*$. Subsequently, this reference voltage value is back-transformed into the stationary abc -reference frame and then this three-phase voltage vector is employed to generate PWM signals for the switching of the VSC.

Before descending the particulars of the control design stated in Figure 4.2, the transformation of balanced three-phase signals with respect to the rotating dq -frame will be elaborated in the following subsection.

4.3.1.1. Three Phase abc -frame to Two Phase dq -frame Conversion

Let i_a , i_b , and i_c be a set of balanced three-phase current waveforms travelling in space in abc sequence (clockwise direction, CW) with grid frequency in the stationary abc -reference frame as shown below in (4.1).

$$\begin{bmatrix} i_a \\ i_b \\ i_c \end{bmatrix} = \begin{bmatrix} \hat{I} \cos(\omega t) \\ \hat{I} \cos(\omega t - 2\pi/3) \\ \hat{I} \cos(\omega t + 2\pi/3) \end{bmatrix} \quad (4.1)$$

Firstly, these vectors are transformed into two-phase stationary $\alpha\beta$ -reference frame as shown in Figure 4.3. The transformed current waveforms in $\alpha\beta$ -reference frame are represented with i_α and i_β and they also travel in CW direction in space.

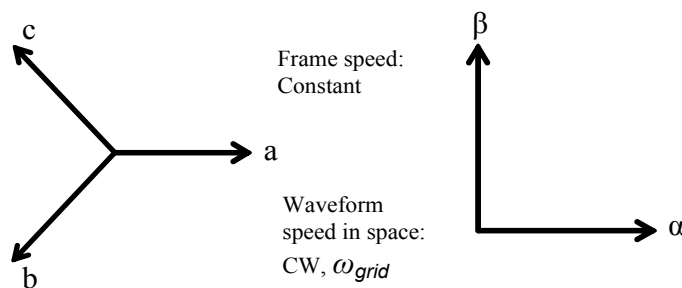


Figure 4.3 Stationary abc -frame and stationary $\alpha\beta$ - frame.

Resolving abc phase vectors along α and β axes yields three equations with three unknowns as shown in (4.2). The magnitude of each component in $\alpha\beta$ -frame is represented with N_2 ; whereas, N_3 is used for the components in abc -frame.

$$\begin{aligned}
N_2 i_\alpha &= N_3 i_a + N_3 i_b \cos\left(\frac{4\pi}{3}\right) + N_3 i_c \cos\left(\frac{2\pi}{3}\right) \\
N_2 i_\beta &= 0 + N_3 i_b \sin\left(\frac{4\pi}{3}\right) + N_3 i_c \sin\left(\frac{2\pi}{3}\right) \\
N_2 i_0 &= k N_3 i_a + k N_3 i_b + k N_3 i_c
\end{aligned} \tag{4.2}$$

Then, these three equations in (4.2) are organized in matrix notation in (4.3).

$$\begin{bmatrix} i_0 \\ i_\alpha \\ i_\beta \end{bmatrix} = \frac{N_3}{N_2} \underbrace{\begin{bmatrix} k & k & k \\ 1 & -1/2 & -1/2 \\ 0 & -\sqrt{3}/2 & -\sqrt{3}/2 \end{bmatrix}}_{\mathbf{A}} \begin{bmatrix} i_a \\ i_b \\ i_c \end{bmatrix} \tag{4.3}$$

By using the orthogonality condition of the matrices $A_t^* A = I_{3 \times 3}$ [71], A and N_3/N_2 turn out to be as following in (4.4) where A_t^* is conjugate transpose of A , $I_{3 \times 3}$ is 3x3 identity matrix.

$$\begin{bmatrix} i_0 \\ i_\alpha \\ i_\beta \end{bmatrix} = \sqrt{\frac{2}{3}} \begin{bmatrix} 1/\sqrt{2} & 1/\sqrt{2} & 1/\sqrt{2} \\ 1 & -1/2 & -1/2 \\ 0 & -\sqrt{3}/2 & -\sqrt{3}/2 \end{bmatrix} \begin{bmatrix} i_a \\ i_b \\ i_c \end{bmatrix} \tag{4.4}$$

Zero component will not be benefitted for the further transformation analysis. Thus, for simplicity, it is omitted and the reduced matrix is shown in (4.5).

$$\begin{bmatrix} i_\alpha \\ i_\beta \end{bmatrix} = \sqrt{\frac{2}{3}} \begin{bmatrix} 1 & -1/2 & -1/2 \\ 0 & -\sqrt{3}/2 & -\sqrt{3}/2 \end{bmatrix} \begin{bmatrix} i_a \\ i_b \\ i_c \end{bmatrix} \tag{4.5}$$

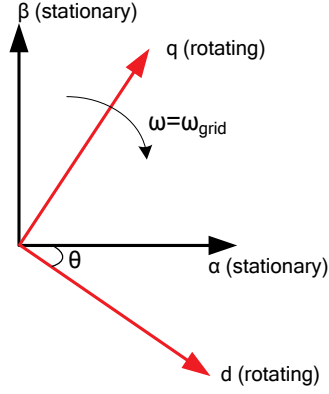


Figure 4.4 Vector diagram of PWM-VSC control structure.

Next, the transformed vectors into the stationary $\alpha\beta$ -reference frame are referred to the rotating dq -reference frame depicted in Figure 4.4. The transformed current waveforms in dq -reference frame are represented with i_d and i_q . The frequency of rotation of the dq -reference frame is the grid frequency, $\omega = \omega_g$. In the light of Figure 4.4, stationary $\alpha\beta$ -reference frame variables can be represented using (4.6). The stationary reference frame variables in (4.5) can be transformed into synchronous dq -reference frame using (4.7) where the displacement angle θ varies between $0-2\pi$ radians in clockwise direction.

$$\underline{i}_{\alpha\beta} = i_{\alpha} + j i_{\beta} \quad (4.6)$$

$$\underline{i}_{dq} = \underline{i}_{\alpha\beta} e^{j\theta} \quad \theta = \int \omega dt \quad (4.7)$$

Transforming $\alpha\beta$ vectors using (4.5), (4.6) and (4.7) along d and q axes yields two equations with two unknowns as shown in (4.8) (in matrix form in (4.9)).

$$\begin{aligned} N_2 i_d &= N_2 i_{\alpha} \cos\theta + N_2 i_{\beta} \sin\theta \\ N_2 i_q &= -N_2 i_{\alpha} \sin\theta + N_2 i_{\beta} \cos\theta \end{aligned} \quad (4.8)$$

$$\begin{bmatrix} i_d \\ i_q \end{bmatrix} = \underbrace{\begin{bmatrix} \cos \theta & -\sin \theta \\ \sin \theta & \cos \theta \end{bmatrix}}_{\mathbf{B}} \begin{bmatrix} i_\alpha \\ i_\beta \end{bmatrix} \quad (4.9)$$

B satisfies the orthogonality condition i.e. $B_t^* B = I_{2 \times 2}$; where B_t^* is conjugate transpose of B and $I_{2 \times 2}$ is 2x2 identity matrix.

Successively, substituting the phase components of (4.1) into (4.5) yields $\alpha\beta$ waveforms as in (4.10).

$$\begin{aligned} i_\alpha &= \sqrt{\frac{2}{3}} \left(i_a - \frac{1}{2} i_b - \frac{1}{2} i_c \right) = \sqrt{\frac{3}{2}} \hat{I} \cos(\omega t) \\ i_\beta &= \sqrt{\frac{2}{3}} \left(\frac{\sqrt{3}}{2} i_b - \frac{\sqrt{3}}{2} i_c \right) = \sqrt{\frac{3}{2}} \hat{I} \cos(\omega t - \pi/2) = \sqrt{\frac{3}{2}} \hat{I} \sin(\omega t) \end{aligned} \quad (4.10)$$

where $\omega = \omega_g = 100\pi$ rad/sec. Abovementioned integration in (4.7) with respect to time variable t yields $\theta = \omega t + \delta$. Thus, physical structure between $\alpha\beta$ and dq frames is correlated with respect to time where the displacement angle θ is defined as the distance between α and d axes as demonstrated in Figure 4.4. The constant term δ can be regarded as the initial angle between α and d axes demonstrated in Figure 4.4. Then, substituting (4.10) in (4.9) by assuming $\theta = 100\pi t + \delta$ delivers dq vectors as depicted in (4.11).

$$\begin{aligned} i_d &= \sqrt{\frac{3}{2}} \hat{I} \cos(\delta) \\ i_q &= \sqrt{\frac{3}{2}} \hat{I} \sin(\delta) \end{aligned} \quad (4.11)$$

It is obvious in (4.11) that dq components are reduced to dc values since δ stands for a scalar angle making cosine and sine terms constants. For small values of δ ,

$$\cos(\delta) \cong 1 \quad \sin(\delta) \cong \delta \quad (4.12)$$

and (4.11) can be linearized as depicted in (4.13) by using the approximation in (4.12).

$$\begin{bmatrix} i_d \\ i_q \end{bmatrix} \cong \sqrt{\frac{3}{2}} \hat{I} \begin{bmatrix} 1 \\ \delta \end{bmatrix} \quad (4.13)$$

Consequently, the transformation of three-phase values to the two-phase dq -reference frame that rotates synchronously with the grid voltage vector is completed.

4.3.1.2. Mathematical Model of the LCL -Filter for Controller Design

In order to model LCL -line filter in the synchronous rotating dq -reference frame, transformation equations stated in Section 4.3.1.1 are utilized. The LCL -filter model is provided in dq -frame since the current control is done in the same reference frame with the d-axis aligned to the grid voltage space vector [65]. Based on these transformations, LCL -filter equations can be derived as depicted in (4.14).

$$\begin{aligned} L_g \frac{d\underline{i}_{g,dq}}{dt} &= \underline{v}_{cf,dq} - \underline{v}_{g,dq} - (R_g + j\omega L_g) \underline{i}_{g,dq} \\ C_f \frac{d\underline{v}_{cf,dq}}{dt} &= \underline{i}_{c,dq} - \underline{i}_{g,dq} - j\omega C_f \underline{v}_{cf,dq} \\ L_c \frac{d\underline{i}_{c,dq}}{dt} &= \underline{v}_{c,dq} - \underline{v}_{cf,dq} - (R_c + j\omega L_c) \underline{i}_{c,dq} \end{aligned} \quad (4.14)$$

where $\underline{v}_{g,dq}$, $\underline{v}_{c,dq}$, and $\underline{v}_{cf,dq}$ are space vectors of the grid, converter and filter capacitor voltages in dq -frame; $\underline{i}_{g,dq}$, $\underline{i}_{c,dq}$ are space vectors of the grid and converter currents, R_g and R_c are modeled copper losses of the grid and converter-side inductances, respectively.

Based on LCL -filter equations in (4.14), per phase equivalent circuit of LCL -filter in rotating dq -reference frame can be modeled as in Figure 4.5. The model of LCL -

filter for control design based on space vector notation in Figure 4.5 neglects the core loss of the grid-side filter inductors (L_g) and the converter-side filter inductors (L_c) and ESRs of filter capacitors (C_f) to model a worst case undamped scenario. Only the copper loss (winding resistance) of the converter-side inductor (R_c) and the grid-side inductors (R_g) are taken into account and modeled as series resistances.

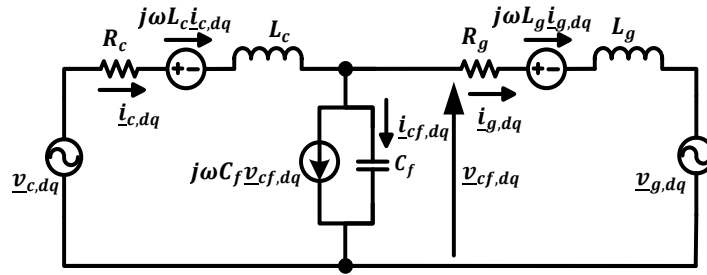


Figure 4.5 Equivalent circuit of LCL network under dq -synchronous frame [65].

4.3.1.3. Frequency Characteristic of the LCL -Filter for Controller Design

LCL -filters converge to simple L -filter (of value L_c+L_g) at low frequencies. This approximation holds true due to the fact that the impedance of the capacitor branch is negligibly small at grid frequency (f_g). However, at higher frequencies, the merit of the LCL -filter becomes evident since the impedance of the capacitor branch decreases considerably and high frequency ripple attenuation extent rises from 20dB/dec to 60dB/dec as can be realized in Figure 4.6. Thus, LC part of the LCL filter is in charge with attenuation of the high-frequency current ripple and current controllers do not have to dealt with the high-frequency ripple reduction. Besides, PI-based current controllers have limited control bandwidth that primarily depends upon the sampling frequency of the system and this limited control bandwidth does not enable the controllers to regulate the high frequency oscillations. Particularly, switching frequency and hence the sampling frequency must be kept sufficiently low at high power applications due to efficiency constraints. In the light of these two facts, PI-based current control design should be done in accordance with the L -filter

approximation by neglecting the influence of capacitor branch. Thus, the upgrade into *LCL*-filter does not bring an extra complexity in the PI-controller design.

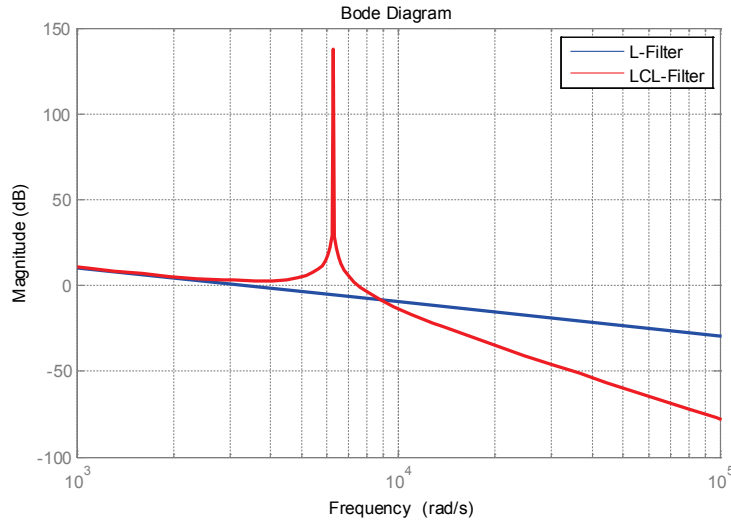


Figure 4.6 The magnitude responses of *L*-filter and *LCL*-filter.

When the filter capacitor C_f is neglected for the control design, converter-side current and grid-side current can be deemed as identical, thus $i_{c,d}$ and $i_{c,q}$ will be preferred in the notations. Then the general system equations in (4.14) reduce to (4.15).

$$\underline{v}_{c,dq} = (R_c + R_g)\underline{i}_{c,dq} + (L_c + L_g)\frac{d\underline{i}_{c,dq}}{dt} + \underline{v}_{g,dq} \quad (4.15)$$

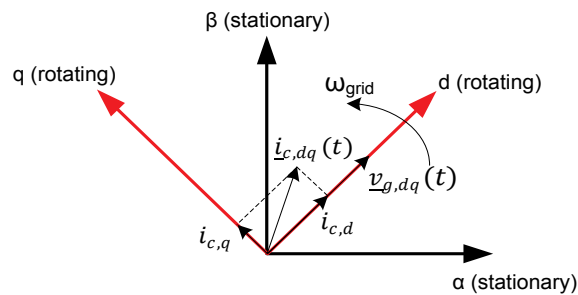


Figure 4.7 Decomposition of vectors in *dq*-frame.

The resolution of the grid voltage vector in rotating dq -reference frame by means of the vector diagram in Figure 4.7 is depicted in (4.16).

$$\begin{aligned}
 v_{c,d} &= (R_c + R_g)i_{c,d} + (L_c + L_g)\frac{di_{c,d}}{dt} + v_{g,d} - \omega(L_c + L_g)i_{c,q} \\
 v_{c,q} &= (R_c + R_g)i_{c,q} + (L_c + L_g)\frac{di_{c,q}}{dt} + v_{g,q} + \omega(L_c + L_g)i_{c,d}
 \end{aligned}
 \tag{4.16}$$

4.3.1.4. Controller Design Regarding the Rotating dq -Frame

The complete control structure in Figure 4.2 is elaborated in Figure 4.8. In Figure 4.8, the inner current control loops employ the dq -frame current components that are to be controlled by the proper selection of the dq -frame VSC output voltage equations derived in (4.16). It should be noted that the current control structure in Figure 4.8 exemplifies the converter current feedback method. The grid-side current feedback could also be embodied. However, determination of the current feedback method will not be made in this section and in order to provide a general control approach, the reference dq -frame current feedback components are represented by dropping c and g subscripts in the control blocks in Figure 4.2 and Figure 4.8.

d -axis is oriented on the grid voltage space vector, $\underline{v}_{g,dq}$ as depicted in Figure 4.7. The reference value of the active current component i_d^* is generated by the dc-link voltage controller such that it regulates the dc voltage of the VSC depending on the power demand of the load. On the other hand, the reference value of the reactive current component i_q^* is set depending on the anticipated reactive power. Thereby, i_d^* is in charge with the dc voltage control whereas i_q^* ensures the correct alignment of the dq -frame. If the grid-side current feedback is employed, i_q^* should be set to zero to guarantee the zero displacement between the grid current and the grid voltage (i.e. unity power factor). On the other hand, if the converter-side current feedback is used, the influence of the filter capacitor should be considered since the grid current

is not directly controlled and hence a nonzero reference value for the q component (i.e. $i_q^* \neq 0$) is required. For instance, the vector diagram in Figure 4.7 also represents the converter current feedback technique and $\underline{i}_{c,dq}$ has a nonzero q component as its reference value commands to do so. Regardless of the current feedback technique, $\underline{i}_{g,dq}$ is always aligned to $\underline{v}_{g,dq}$ only if the unity power factor is warranted.

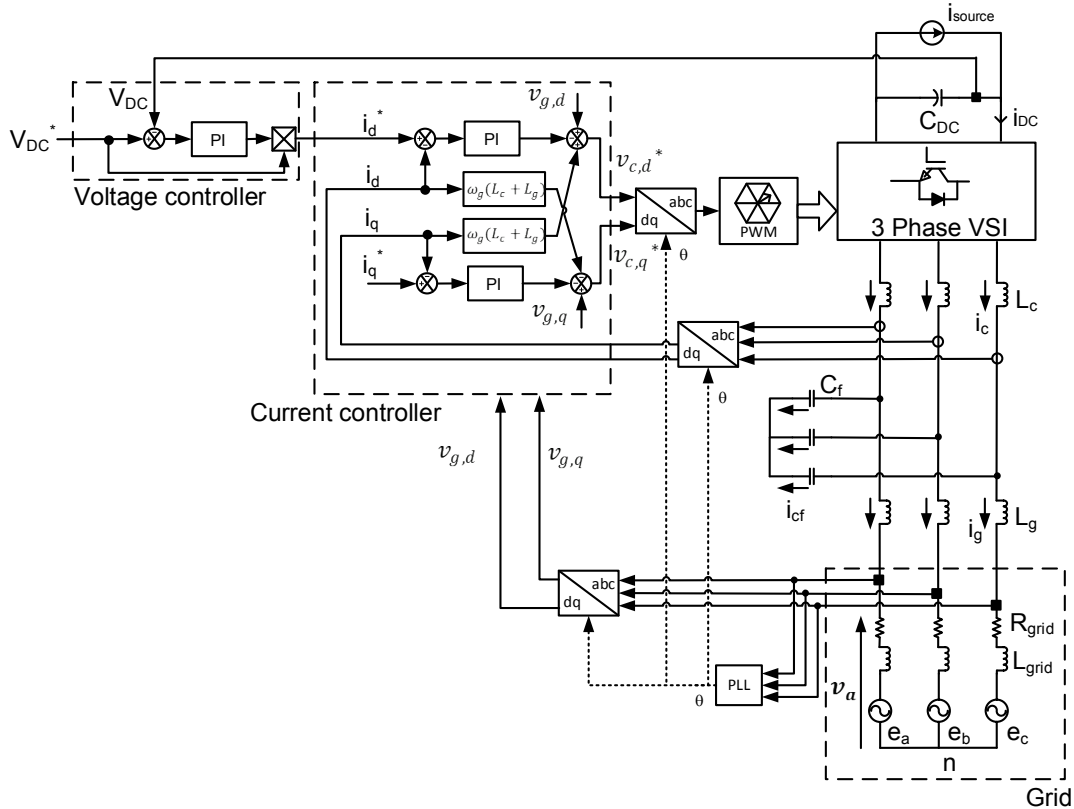


Figure 4.8 Block diagram of voltage oriented current control loop.

For both dc-link voltage control and the current control, the PI controllers are utilized owing to their superiority in reference tracking with zero steady-state error. The design of the PI controller defined in (4.17) relies on the pole-zero placement methodology and the proportional gain constant K_p and the integral time constant T_i are tuned according to symmetrical optimum [61].

$$G_{PI}(s) = K_p \frac{sT_i + 1}{sT_i} \quad (4.17)$$

4.3.2. Current Control Loop Design (Inner Loop Design)

The current controller part highlighted in Figure 4.8 will be elaborated in this section by considering both of the converter current feedback and grid current feedback. For this purpose, Figure 4.9 illustrates these two methods by putting emphasis with c and g subscripts onto the current feedback variables. As mentioned in the preceding section, converter current feedback takes the filter capacitor into account and the q -axis current reference should be set to $\omega_g \cdot C_f \cdot v_{g,d}$ rather than zero [57]. Conversely, grid current feedback requires zero q -axis current reference since grid-current is directly controlled.

Additionally, once the d and q current dynamics are decoupled and compensations of the grid voltage $v_{g,d}$ and $v_{g,q}$ are done, both d and q current loops become identical and they can be tuned using the same controller parameters [54][57][61][62][65]. In order to decouple d and q current dynamics, decoupling term $\omega_g(L_c+L_g)$ is added to the PI controller output as shown in Figure 4.9. However, the sign convention of these decoupling terms is different for d and q -axis variables. d -axis component of the simplified system equation in (4.16) contains $-\omega_g(L_c+L_g)i_{c,q}$ term; whereas, q -axis component contains $+\omega_g(L_c+L_g)i_{c,d}$ term. Thus, in order to eliminate the dependency of the d -axis current dynamics on the q -axis current dynamics, and vice-versa, $+\omega_g(L_c+L_g)i_{c,q}$ term is added to the output of d -axis PI controller; whereas, $-\omega_g(L_c+L_g)i_{c,d}$ is added to the output of q -axis PI controller as depicted in Figure 4.8 and Figure 4.9. Measured dq -grid voltages $v_{g,d}$ and $v_{g,q}$ are also added to compensate grid voltage as evident in these figures [74].

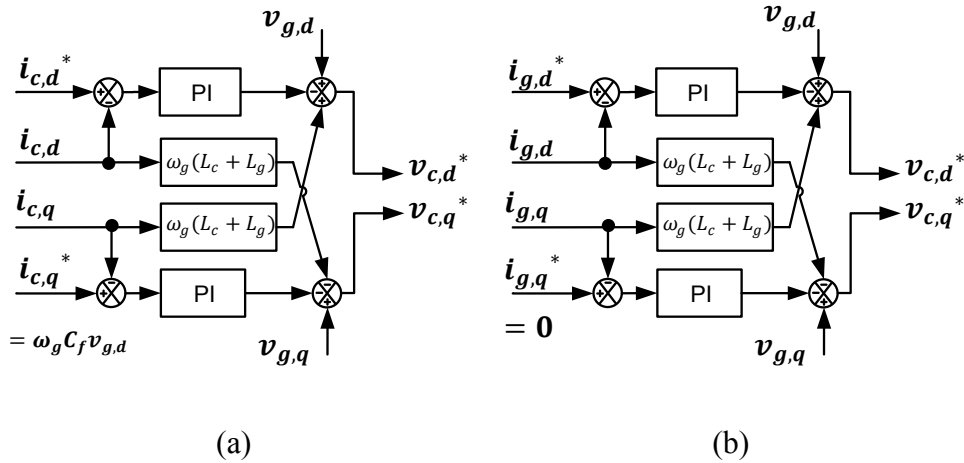


Figure 4.9 Current controller block diagram (a) Converter-side current feedback
(b) Grid-side current feedback.

As a result, identical parameters can be used for the d and q current controllers and the resultant outputs of the dq -frame PI controllers yield the dq -frame reference of the converter voltages $v_{c,d}^*$ and $v_{c,q}^*$. Then, these signals ($v_{c,d}^*$, $v_{c,q}^*$) are back transformed to the two-phase stationary $\alpha\beta$ -frame and subsequently to the three-phase stationary abc -frame. The back-transformed three-phase signals are employed as commands based on the preferred PWM technique for the modulation of the IGBT switching signals as can be seen in Figure 4.8.

There are a number of significant delays in the control loop such as digital processing delay and the PWM transport delay which have to be reflected in the control scheme modeling [54][58][61][62][65][70]. Processing delay is regarded in terms of one-sample delay whereas the PWM transport is taken into account in terms of one half-sample delay [54]. Besides, decoupling the d and q axes reduces the LCL -filter behavior to a first order delay element and hence tracking capability of the PI controllers is improved [62]. Thereby, the resulting block diagram of the current control loop is obtained as shown in Figure 4.10 where T_{smp} is sampling time, u_{dis} is disturbance voltage modeling the impact of variations in the utility voltage, K_i is proportional gain constant of the current PI controller, T_i is integral time constant of the current PI controller, K_{PWM} is proportional gain constant of the

PWM block, K_{LCL} is proportional gain constant of the LCL -filter plant, and T_{LCL} is time constant of the LCL -filter plant [62].

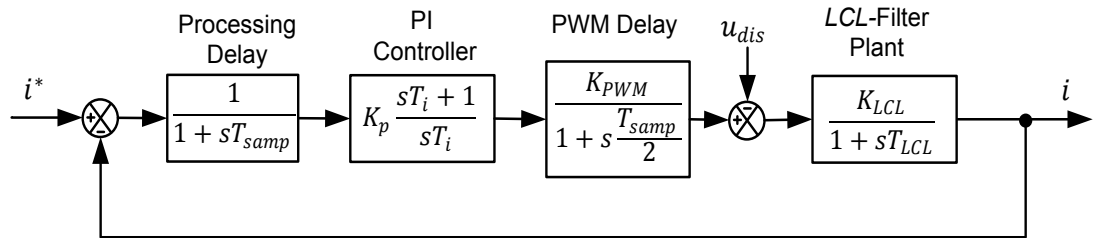


Figure 4.10 Block diagram of current control loop.

In general, all delays are grouped together to simplify the control design procedure. For this purpose, the processing delay time constant and the PWM delay time constant can be merged and regarded as the equivalent delay time constant of the system (T_{eq}). Thus, T_{eq} corresponds to $T_{eq}=1.5T_{samp}$ and the block diagram of the simplified current control loop is depicted in Figure 4.11. Since the dc-link voltage is kept constant owing to the voltage-oriented current control structure, any swing in the grid voltage can be deemed as the disturbance signal, u_{dis} [62].

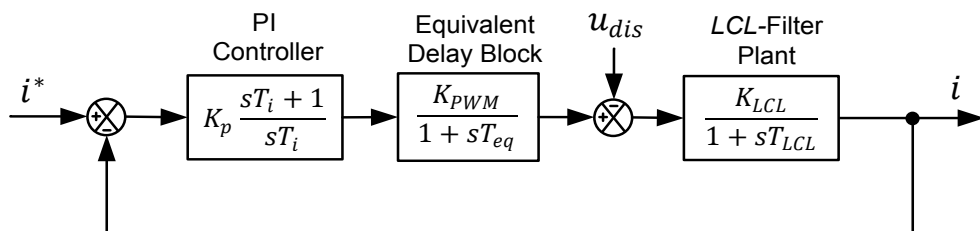


Figure 4.11 Block diagram of simplified current control loop.

As mentioned previously, PI controller parameters are tuned according to symmetrical optimum technique [59] and the influence of the filter capacitor is neglected in the current control design. Thus, PI current controller parameters (K_p , T_i) can be represented as shown in (4.18).

$$K_p = \frac{L_c + L_g}{\alpha_i T_{s\text{amp}}} \quad (4.18)$$

$$T_i = \alpha_i^2 T_{s\text{amp}}$$

where, α_i is the proportion of T_i to T_{eq} [62]. The relationship between α_i and phase margin ψ can be represented with (4.19) below [62].

$$\alpha_i = \frac{1 + \cos \psi}{\sin \psi} \quad (4.19)$$

In order to have a satisfactory disturbance rejection in conjunction with an acceptable overshoot to the step change of the reference, phase margin should be maximized (i.e. $\psi \geq 45^\circ$). Once $\psi \geq 45^\circ$ substituted in (4.19), it yields α_i such that $\alpha_i \geq 2.4$ [62]. Dannehl *et al.* [55] state that $\alpha_i=3$ yields an overshoot of approximately 4% and the settling time of 3-4 sampling (control) periods.

4.3.2.1. Impacts of Sampling Mode in Current Control Loop

The sampling and PWM updating strategy is a vital element of current control loop. There are three main methods having the same PWM switching periods throughout one PWM cycle (switching period) but differing in measurement sampling and PWM updating points [64], namely single-update PWM-method with sampling at the start of the switching period, single-update PWM-method with sampling in the middle of the switching period, and double-update PWM-method with sampling twice in each PWM period. In single-update PWM-methods, control duty cycle is

updated once in each switching period; whereas, it is updated twice in each PWM switching period [64].

Figure 4.12(a) reveals single-update PWM method with the sampling at the beginning of each switching period. Since the sampling is started and the modulation index (m_i) is updated at the beginning of the switching period, system is not able to record the recent state until the next update. This phenomenon is called sampling delay (PWM transport delay) in the literature [58][64]. In this case, the delay time introduced by updating and sampling method leads to one-sample delay in the control loops, equal to the switching period [64].

In the other case of single-update PWM method, sampling is done in the middle of the switching period as depicted in Figure 4.12(b). The modulation index is updated in the beginning of the next carrier wave leading to an update half of a carrier (control) period later. So, the modulation index set in the former control cycle together with the actual modulation index rule the control loop during one carrier cycle. Hence, the delay time yielded by the sampling updating procedure is the mean value of the former and actual converter voltage reference values [64].

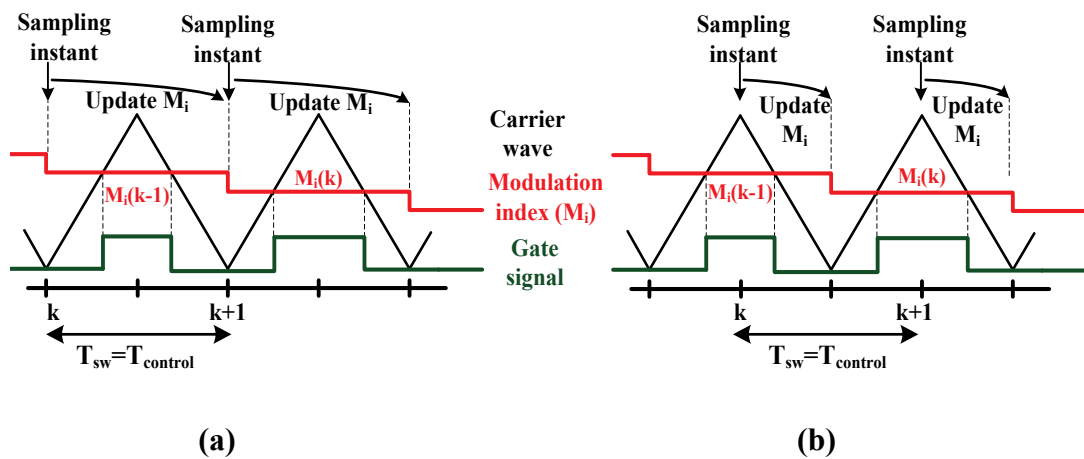


Figure 4.12 (a) Single-update PWM method (sampling at start) (b) Single-update PWM method (sampling at middle).

In the double-update PWM case depicted in Figure 4.13, the sampling and updating is done twice each switching period at the both triangle peaks within a control cycle. In each control cycle the actual modulation index is updated regarding the previous reference values [64]. Therefore, delay-time introduced in the current loop is in one control cycle period length in this case, which is half of the switching cycle as evident in Figure 4.13.

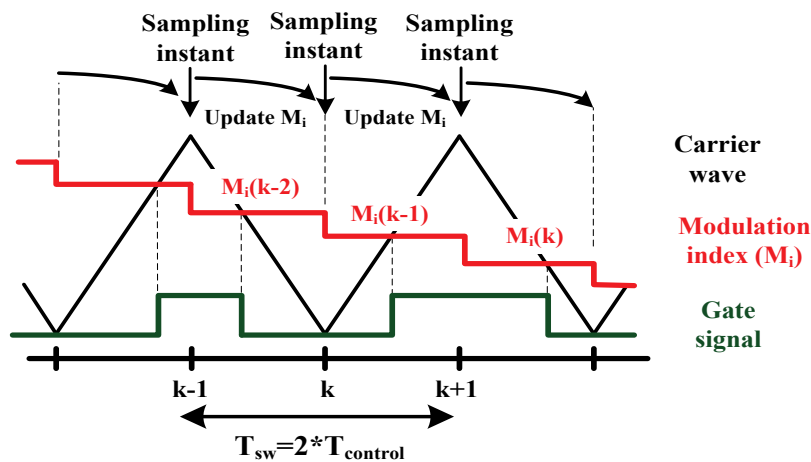


Figure 4.13 Double-update PWM method.

In the light of abovementioned PWM sampling methods, double-update technique is favorable over the other PWM sampling since the bandwidth of the current controller is doubled. However, elevated bandwidth of the current controllers generally leads to decrease in phase margin and hence larger overshoots are expected. It should be noted that impact of the sampling method leads to different responses under grid-side feedback (GCF) and converter-side feedback (CCF). The impact of sampling method is less critical under GCF method since the large portion of current ripple is absorbed by filter capacitor and almost a pure cosine wave is controlled which does not degrade bandwidth considerably. On the other hand, CCF method utilizes unfiltered cosine wave containing large ripple magnitudes, increasing the dependency on controller bandwidth. Consequently, doubling the

controller bandwidth using double-update PWM method is more critical for CCF method compared to GCF method.

To conclude, double-update PWM sampling is preferred in the systems utilizing low switching frequencies in the order of a few kilohertz to compensate the very low control bandwidth. Since the focus of this thesis work involves high power applications requiring low switching frequencies, the controlling action is executed at a sampling frequency (f_{samp}) which is twice of the switching frequency f_{sw} . Therefore, the preferred sampling mode is double update sampling mode as in [55] and $f_{samp} = 2 \cdot f_{sw}$ throughout this study.

4.3.3. DC Link Voltage Control Loop Design (Outer Loop Design)

The dc-link voltage control relies on the power exchange between the source and the load. The reference value for the current controllers (\underline{i}_{dq}^*) is altered depending on the power extent to be injected to the grid (i.e. power demand of the loads connected to the PCC). It should be noted that inner current loops aim to achieve short settling times and unity gain whereas outer voltage loop targets the optimum regulation and stability. Hence, these two nested loops can be considered decoupled and voltage control loop could be designed 5-20 times slower [63]. To obtain a suitable decoupling between the voltage control loop and the current control loops, the bandwidth of the dc-link voltage controller should be considerably smaller than the bandwidth of the current controllers.

In order to design the dc-link voltage PI controller parameters (K_{DC} , T_{DC}), the dc-link voltage dynamics should be derived beforehand as stated in (4.20) [61][65][73].

$$C_{DC} \frac{dv_{DC}}{dt} = i_{source} - i_{DC} = i_{source} - \frac{3}{2} \frac{i_{g,d} v_{g,d}}{v_{DC}} \quad (4.20)$$

where C_{DC} is the dc-link capacitor, i_{DC} is the source current, i_{inv} is the injected current to the VSC, $i_{g,d}$ and $v_{g,d}$ are the d -axis grid-side current and the grid voltage, respectively.

The design of K_{DC} , T_{DC} includes the influence of the inner current loop by considering one period of the inner loop (T_{inner}) as a four-sample delay element ($T_{inner} = 4T_{samp}$, where T_{samp} is sampling time) [54][61][65]. Considering dc-link voltage dynamics in (4.20) in conjunction with the inner current loop influence, the simplified dc-link voltage control loop shown in Figure 4.14 is obtained. Since the dc-link voltage, V_{DC} is controlled to its constant reference value V_{DC}^* , the PI controller parameters are also tuned according to the symmetrical optimum described in [59]. Therefore, resulting K_{DC} and T_{DC} variables can be calculated by employing (4.21).

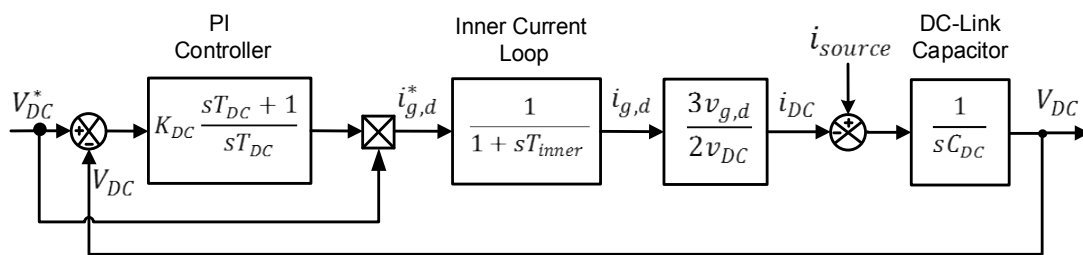


Figure 4.14 Block diagram of outer voltage control loop.

$$K_{DC} = \frac{2}{3} \frac{V_{DC}^* C_{DC}}{\alpha_{DC} T_{inner} v_{g,d}}$$

$$T_{DC} = \alpha_{DC}^2 T_{inner} \tag{4.21}$$

$$T_{inner} = 4T_{samp}$$

where K_{DC} is proportional gain constant and T_{DC} is integral time constant of the dc-link voltage PI-controller, α_{DC} is the proportion of T_{DC} to T_{eq} [62].

Outer loop is designed α_{DC}^2 times slower than the inner loop as can be seen in (4.21). In order not to shrink the bandwidth of the dc-link voltage controller considerably, Dannehl *et al.* [59] suggest $\alpha_{DC}=3$ for proper decoupling of the outer loop and the inner loop.

4.4. Stability Analysis

The stability of the cascaded control loop system relies primarily on the stability of the inner current loop and hence most papers concentrate on the inner current loop regulation in the first place. Therefore, it is very common to discard dc-link voltage control loop and model it as a simple DC voltage supply in the literature [54]-[59][66]. In this dissertation, dc-link stabilization is also within the scope and detailed outcomes concerning both of the loops will be provided.

As the second common approach in the literature, discrete z-domain analysis in conjunction with root locus method is generally utilized in stability analysis due to the discrete nature of the control algorithm implementation [55][58][61][64]. For this purpose, z-domain transfer functions are derived and extensive analyses are conducted. Nevertheless, in this study continuous-time s-domain (Laplace domain) systems are of the primary concern since the designed systems are simulated by means of SIMPLORER[®] one of the power electronics simulation software in the market. SIMPLORER[®] uses continuous-time algorithms in convergence calculations. Thereby, there is no processing delay and PWM transport delay encountered throughout the simulations. As a remark, continuous time system set up in the simulation environment is discretized by means of zero-order hold blocks [55]; thus the simulation system can be deemed as digitalized system (z-domain) without any delays.

PWM transport delay [58] in discrete control systems can be emulated in the continuous-time domain (s-domain) by inserting a delay element equal to one-sample delay time. After normal analysis regarding delay, the case involving one-sample delay will also be highlighted and a brief comparison will be made.

Apart from simulation studies, stability analysis of the designed system are also conducted via MATLAB[®] by means of bode diagrams, root loci, step-responses and so on. Likewise, the continuous-time transfer function of the open loop/closed-loop *LCL*-filter model is discretized into z-domain by zero-order hold method [55][61][64] with the sampling frequency of the system as done in simulation case.

To reflect the PWM transport delay [58] on the stability performance conducted in MATLAB[®] as done in simulation studies, the plant dead-time dynamics in the z-domain are modeled using the back-shift operator z^{-1} [55][58][64].

All things considered, a thorough study involving both simulation outputs and MATLAB[®] outputs will be provided in order to conduct stability analysis of the designed parameters/systems.

4.4.1. Filter Modeling for Stability Analysis

The stability and dynamic response of the overall system is examined by employing the poles of the closed-loop current controller. Closed-loop poles of the *LCL*-network can be founded by deriving the admittance transfer function, which is the fraction of grid-side current to the converter-side voltage in s-domain. However, the transfer function of the closed-loop system depends upon the utilized resonance damping technique and it differs for grid current feedback (GCF) and converter current feedback (CCF). Transfer functions for each method will be derived explicitly in the next section. For the moment, a brief comparison between undamped and damped *LCL*-filter plant is provided, damping method is not mentioned explicitly yet.

Figure 4.15(a) and (b) depicts the undamped per phase equivalent circuit and equivalent block diagram of *LCL*-network, respectively. In Figure 4.15(a), the grid is deemed to be containing only positive-sequence fundamental component hence it can be treated as a short circuit with zero impedance when performing system stability analysis. The ideal *LCL*-filter consumes only reactive power; nevertheless, the components in real life have resistive parts. Although the copper loss is taken into account in the equivalent circuit of *LCL*-filter in Figure 4.5, the core and copper loss of grid-side filter inductors (L_g) and converter-side filter inductors (L_c) and ESRs of filter capacitors (C_f) are neglected in stability analysis to nullify all internal damping terms. Hence, the idealized system is made more unstable that models the worst case scenario for the stability analysis.

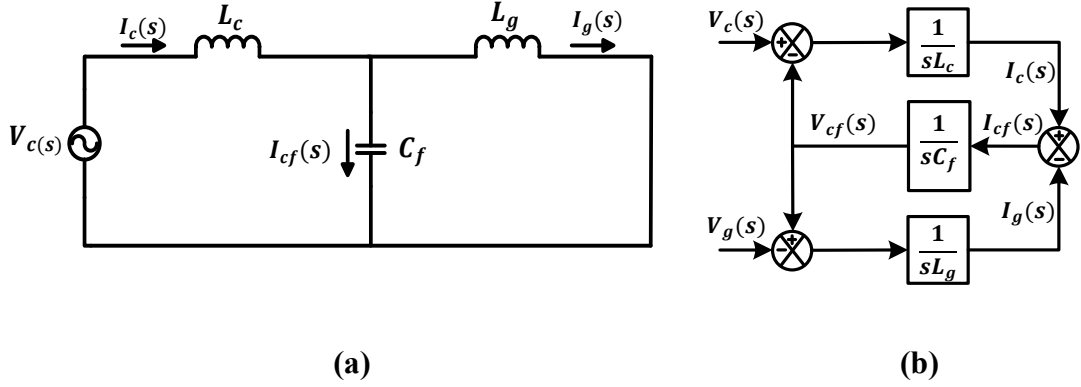


Figure 4.15 Undamped per phase (a) equivalent circuit (b) equivalent block diagram of *LCL*-network for stability analysis.

The admittance *LCL*-filter transfer function in s-domain, $Y_{LCL}(s)$ between the grid-side current (I_g) and the converter output voltage (V_c) is derived in (4.22). The relation between I_g and the filter capacitor current (I_{cf}) is defined in (4.23) by using the equivalent block diagram shown in Figure 4.15(b). As a remark, v_g , i_g , and i_c represent the variables in the time domain while their capitalized notations V_g , I_g , and I_c represent the variables in the Laplace domain (*s*-domain).

$$Y_{LCL}(s) = G_p(s) = \frac{I_g(s)}{V_c(s)} = \frac{1}{s^3 C_f L_c L_g + s(L_c + L_g)} \quad (4.22)$$

$$\frac{I_{cf}(s)}{I_g(s)} = s^2 C_f L_g \quad (4.23)$$

By using the undamped transfer function shown in (4.22), magnitude and phase response of the undamped *LCL*-filter is plotted in Figure 4.16. Figure 4.16 reveals obviously the resonance phenomenon of the designed *LCL*-filter with the ‘undamped’ label. Resonance shall be avoided with the employment of inherent or

active or passive damping methods [54]-[58] since the rapid phase transition occurring at the resonant frequency (f_{res}) may cause instability of current controllers. With the utilization of damping methods [54]-[61], the resonance can be suppressed as seen in Figure 4.16 at the magnitude response labeled with ‘damped’ waveform and the rapid phase transition at the resonant frequency is softened. Overview of damping methods, namely inherent, active and passive damping methods is covered in detail in following section.

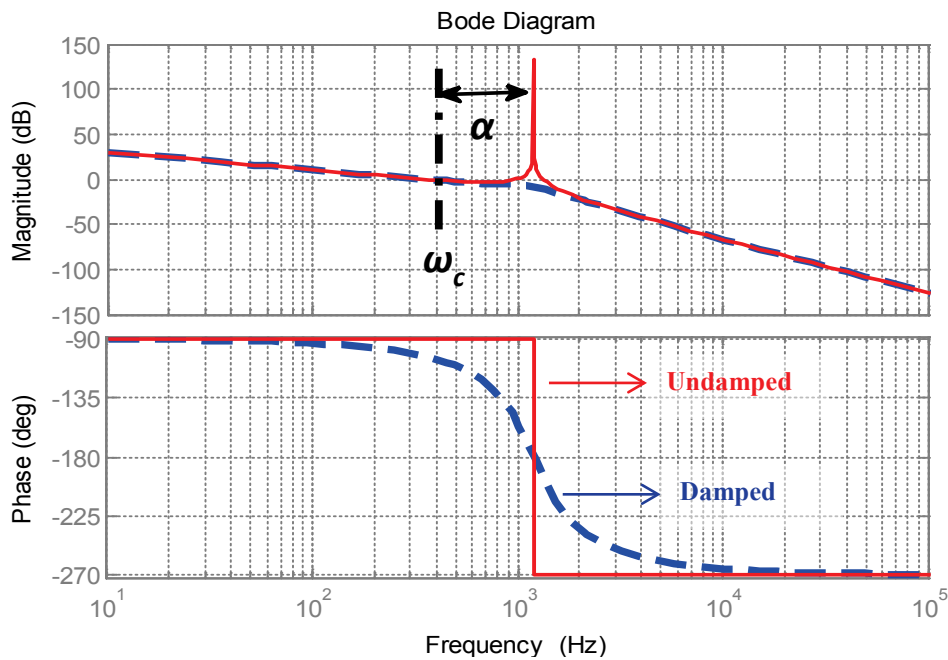


Figure 4.16 Bode plot of the open-loop VSC system with *LCL*-filter.

Figure 4.17 reveals the effectiveness of damping clearly. Undamped resonance peak shown in the magnitude response amplifies the harmonic components around the resonant frequency and the resulting waveform contains enormous ripple components oscillating at the resonant frequency. Once the damping is enabled, the resonance peak in the magnitude response is blunted and the harmonic components (if any) present around resonant frequency will not be amplified, indeed they will be attenuated owing to the gains below zero dB.

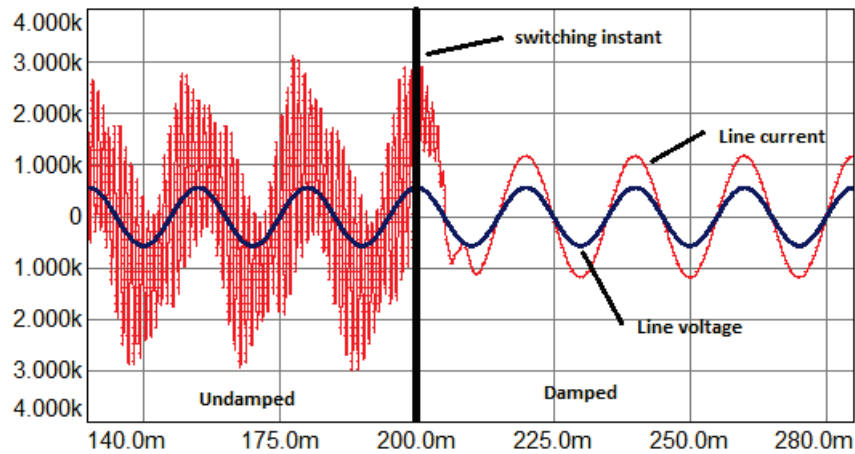


Figure 4.17 Line voltage/current of undamped vs. damped system.

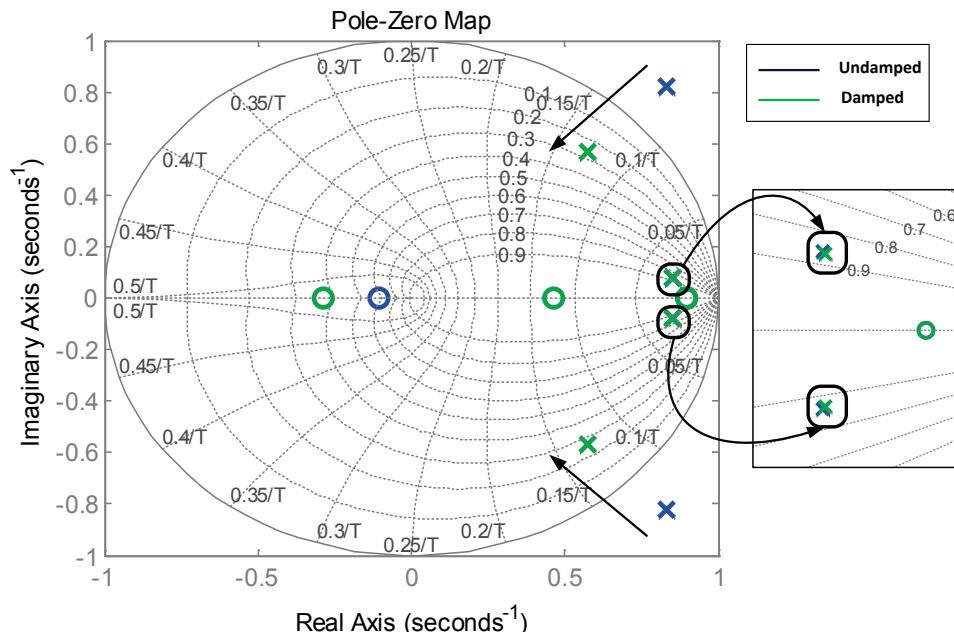


Figure 4.18 Position of poles in undamped to damped cases.

The resonant poles of the undamped system reside outside of the unit circle as shown in Figure 4.18. These undamped poles cause very high harmonic components in magnitude as evident in Figure 4.17. With the activation of the damping, resonant poles are pushed inside the unit circle and the system becomes more stable. From the

analysis concerning the low-frequency poles of the system in Figure 4.18, it is obvious that the dynamic response does not change at all with the introduction of damping, since these two complex poles move only slightly. The proof of this situation is apparent due to the overlapping attenuation characteristics of L -filter and LCL -filter in the low frequency range.

4.4.2. Overview of Resonance Damping Techniques

In order to deal with the resonance problem, active or passive damping methods are developed and widely used in the literature [54]-[61]. In recent studies, active damping (AD) seems favorable over conventional passive damping (PD) solution since AD method modifies the reference voltage information as if a virtual damping term is inserted in the system with no additional power losses (Figure 4.19). Thus, harmonics around the resonant frequency are not excited and closed-loop stability is maintained. The verification of the AD methods is stated explicitly in the literature; however, the complexity in the controllers and adjustment of LCL -filter parameters to achieve a suitably damped system requires more effort. Besides, AD methods usually involve additional sensors, which bring an extra cost.

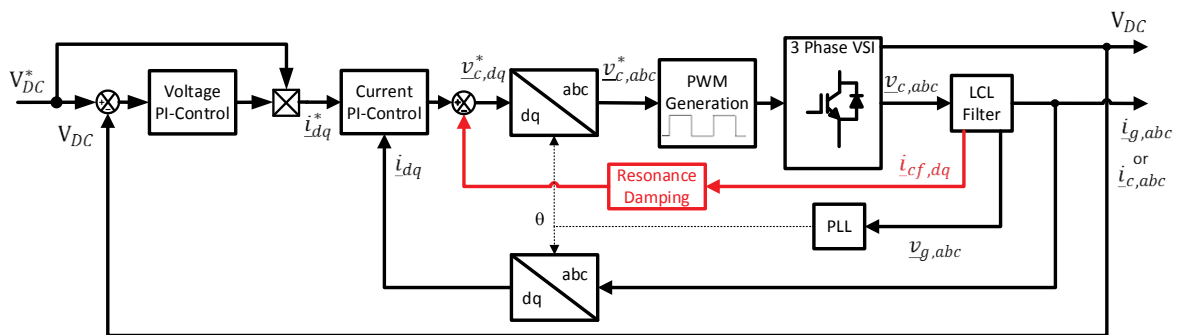


Figure 4.19 Modified current control loop with the addition of resonance damping.

In the literature, there is a number of active damping techniques utilizing the current/voltage information obtained through the sensors attached to the filter

capacitor, converter-side inductor or grid-side inductor as well as sensorless estimation of the state variables based on complex state observers. In this dissertation, filter capacitor current information will be processed so as to achieve AD in the current control loop.

On the other hand, PD techniques provide a simple solution to the resonance phenomena. In PD techniques, resistors are added to the filter capacitor (C_f) branch in several different ways to suppress the resonance [66][67]. As an advantage of PD technique, any change in the resonant frequency owing to the aging, stray inductance/capacitance in the system, or large tolerance in the components and so on does not affect the stability of the system since there is always nonzero impedance at the filter capacitor branch blunting the resonance [60]. Hence, PD guarantees the stable and long-lasting operation of the system. Besides, unlike AD techniques, there is no need to use additional voltage and/or current sensors in PD methods.

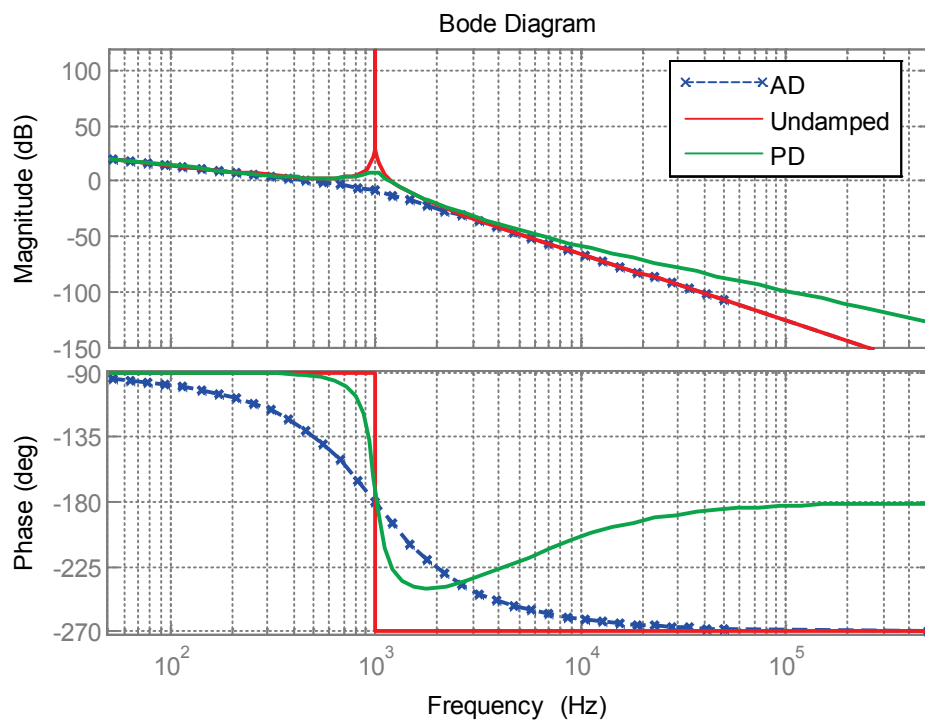


Figure 4.20 Attenuation capability of *LCL*-filter under distinct damping methods.

Although the elimination of extra sensor requirements is attractive in PD; yet, the dynamic response of the system deteriorates considerably and high frequency oscillations may arise at the edge of load changing instants [55][59][60].

Besides, towards higher frequencies in the frequency band, damping resistors start to reduce the order of the *LCL*-filter and hence nullify the enhancements brought by the third-order attenuation capability as can also be agreed in Figure 4.20. According to the selected damping resistor, attenuation capability may further be degraded. Further details concerning determination and tuning of damping resistors will be provided in Chapter 5. Additionally, the phase response in PD method shows that rapid phase transition occurs at the resonant frequency as opposed to the softened transition provided by AD methods (Figure 4.20). Moreover, the extra losses due to PD not only lead to undesirable temperature rise and decrease in the life time of filter elements but also degrade the efficiency of the system considerably.

Before proceeding to the next section, it would be better to mention inherent damping (ID) with a few words. First of all, inherent damping is not a damping method as AD and PD. It is more like the realization of the inherent resonance damping feature of the current loop only if converter-side current feedback is utilized in the control loop. In other words, grid-side current feedback does not have an inherent damping trait [57]. Further details concerning inherent damping will be provided under the section about converter-side feedback technique.

4.4.3. Passive Damping Technique

Passive damping (PD) is the most preferred method in conventional design since it ensures the stability of the *LCL*-filter based grid connected converters under all circumstances while compromising the filter effectiveness and place a burden to the system in terms of damping losses [54]-[60][66].

In a lossless *LCL*-filter, any weakly blunted resonance peak is very likely to excite resonance if any small amount of harmonics exists around the resonant frequency [60]. There are two types of harmonics that can exist around the resonant frequency.

The first one is resonant harmonics caused by insufficient damping of resonant poles of the system. The second one is the switching harmonics caused by the PWM switching. In the cases that switching frequency has to be kept very low such as high power low-voltage applications, resonant harmonics cannot be isolated from switching harmonics unless gigantic filter inductors are employed [69]. Thereby, switching harmonics would excite the resonance as long as the weakly blunted resonance peak is present. In terms of blunting the resonance under any circumstances, PD methods are more reliable than AD methods since it does not depend on the change in parameter values over temperature, aging, parasitic elements, and so on, warranting a stable and long-lasting operation [60]. For the implementation of PD, simple resistors are added in the filter in a number of ways as present in [60][66]-[67]. Minimization of the damping losses is the vital point deciding on the most suitable PD configuration [60]. Nevertheless, in the light of comprehensive analyses regarding distinct resistor configurations, simple damping resistor delivers the least passive damping losses [60] while causing the highest degradation in attenuation capability of *LCL*-filter [66]. In this dissertation, PD configuration with simple resistors inserted to the filter capacitor branch is investigated since distinct PD configuration examination is beyond the scope.

Three-phase *LCL*-filter based VSC utilizing PD method with simple series resistors is represented in Figure 4.21 with a per phase equivalent circuit. The admittance transfer function in s-domain, $Y_{LCL}(s)$ between the grid-side current (I_g) and the converter output voltage (V_c) is derived in (4.24) by means of the equivalent block diagram in Figure 4.21. For low frequency range, the impact of damping resistor is not considerable since the impedance of the damping resistor is much smaller than that of filter capacitor. In higher frequency range, the impedance of the capacitor becomes much smaller than the impedance of damping resistors and a path is opened for high frequency current components flowing through damping resistors. This behavior is proven in Figure 4.20.

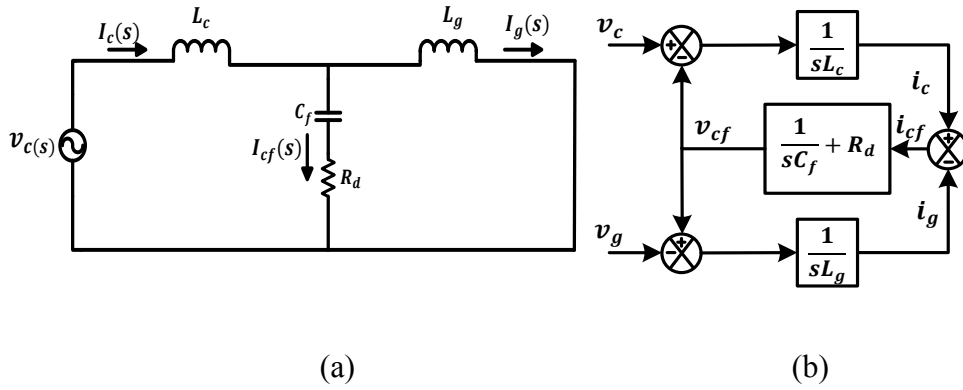


Figure 4.21 *LCL*-filter with PD per phase circuit (a) Equivalent circuit
(b) Equivalent block diagram of *LCL*-network.

$$Y_{LCL}(s) = \frac{I_g(s)}{v_c(s)} = \frac{sC_f R_d + 1}{s^3 C_f L_c L_g + s^2 C_f R_d (L_c + L_g) + s(L_c + L_g)} \quad (4.24)$$

As a remark, as the damping resistor increases attenuation capability of *LCL*-filter begins to diminish considerably and passive damping losses are escalated in great extent [67]. If only a lossless filter were possible and no damping resistors were used, the switching ripple injected into the grid would almost be zero since the capacitor branch would create a short-circuit path for the switching frequency harmonics. Yet, once a damping resistor is placed in series with the filter capacitor, the switching harmonics injected into the grid starts to decline in proportion to the ratio of the passive damping resistor over the grid reactance [67]. Therefore, the tradeoff between stability and low switching ripple injected into the grid is delicately balanced and optimal damping resistor value (R_d) requires particular interest not to cause much degradation in the filter effectiveness and excessive damping losses. This subtle balance is examined thoroughly by means of bode diagrams, root-loci, etc., on MATLAB[®] and findings are further validated by simulation studies on SIMPLORER[®] under both CCF and GCF techniques in Chapter 5 within the *LCL*-filter parameter designation phase. So, critical value of a damping resistor to achieve stability as well as the optimal value proving sufficient damping and attenuation through formulas and algorithms will be well examined in the next chapter.

4.4.4. Active Damping Technique using Filter Capacitor Current Feedback

In order to achieve active damping, it is reasonable to process the current/voltage information of the filter capacitor since the resonance is caused by these filter capacitors [55]. As mentioned formerly, filter capacitor current will be utilized for this purpose. Thus, AD using capacitor voltage technique [55] is beyond the scope of this dissertation.

With the introduction of AD block $K(s)$ using filter capacitor current, cascaded structure of the LCL -filter along with the damping block can be depicted as in Figure 4.22. In the literature, $K(s)$ using filter capacitor current can be modeled as a simple P-controller with a proportional gain constant K_d [55][57][58]. As can be seen in the block diagram, the reference voltage value of the converter current v_c^* is modified by this P-controller with the gain constant K_d and the resulting closed-loop transfer function $G_{lcl,ad}(s)$ can be defined as (4.25).

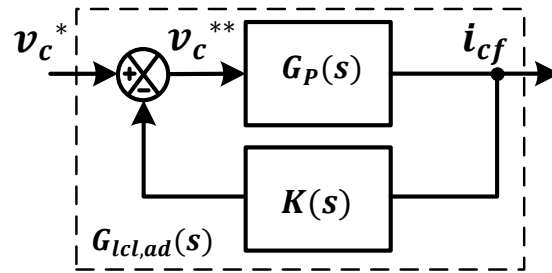


Figure 4.22 Block diagram of inner control loop with AD.

$$G_{lcl,ad}(s) = \frac{G_P(s)}{K(s) + G_P(s)} \quad (4.25)$$

$$G_{AD}(s) = \frac{v_c^{**}}{v_c^*} = \frac{s^3 C_f L_c L_g + s(L_c + L_g)}{s^3 C_f L_c L_g + s^2 K_d C_f L_g + s(L_c + L_g)} \quad (4.26)$$

where $G_P(s)$ stands for the undamped LCL -plant transfer function in (4.22).

The closed-loop transfer function in (4.25) damps the resonance out since an s^2 – term appears in the denominator which is missing in the undamped transfer function $G_P(s)$ shown in (4.22). The parameters that s^2 –term involves depends on the preferred damping technique, so explicit notation of it will be delivered in the corresponding subsections regarding CCF and GCF methods. Although the closed-loop transfer function in (4.25) behaves as if a fictitious damping resistor is inserted, the actual filter is not modified at all. Hence, it can be seen equivalent as adding an active damping block subsequent to the unmodified voltage reference $v_{c,dq}^*$ as depicted in Figure 4.23.

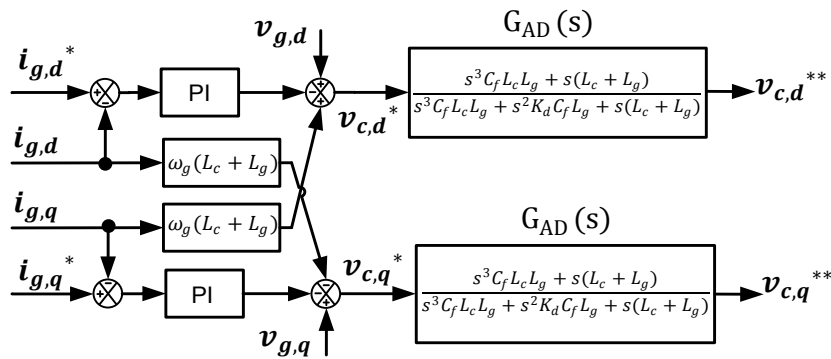


Figure 4.23 Current controller block diagram with AD.

The transfer function of the AD block is derived in (4.26) and it can be deduced from the bode plots of Figure 4.24 that it functions as a notch filter [60] providing a negative peak response as opposed to undamped LCL -filter resonance. Provided that an optimal K_d value is selected, these two peaks at the resonant frequency cancel each other out and a properly damped system is obtained as highlighted in Figure 4.24.

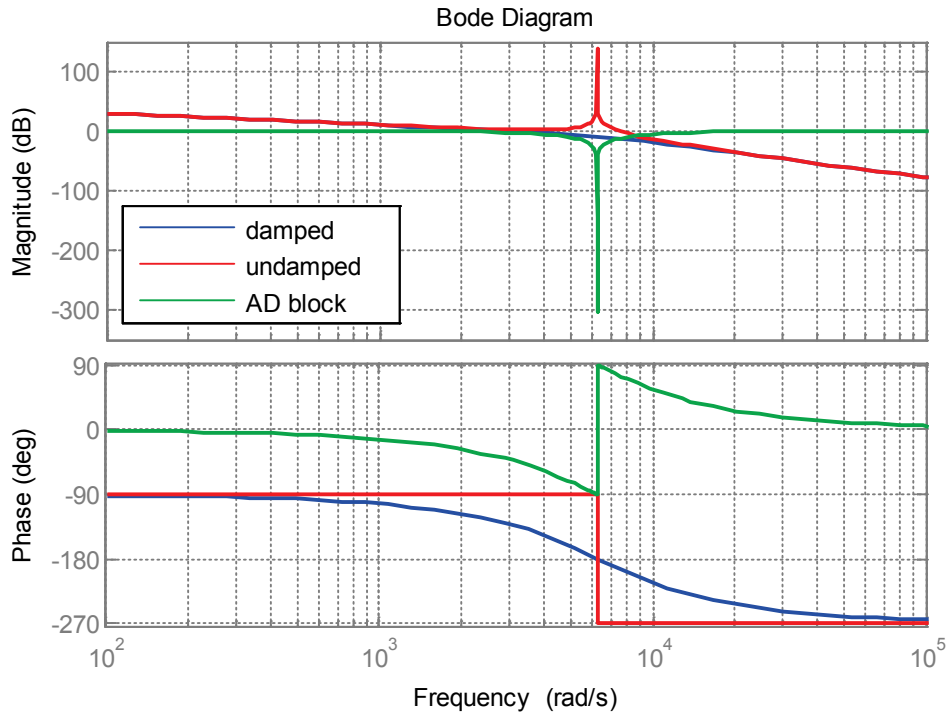


Figure 4.24 Impact of AD block on resonance damping.

4.4.4.1. Active Damping under Grid-Current Feedback

In Figure 4.25, the open-loop system consisting of LCL -filter plant $G_p(s)$ and PI-current controller $G_c(s)$ is fed back with the grid-side current (i_g). The open-loop transfer function of the LCL -plant is derived in (4.22), previously. The open-loop system will be unstable if the loop is closed due to the missing s^2 damping term in the denominator of LCL -plant.

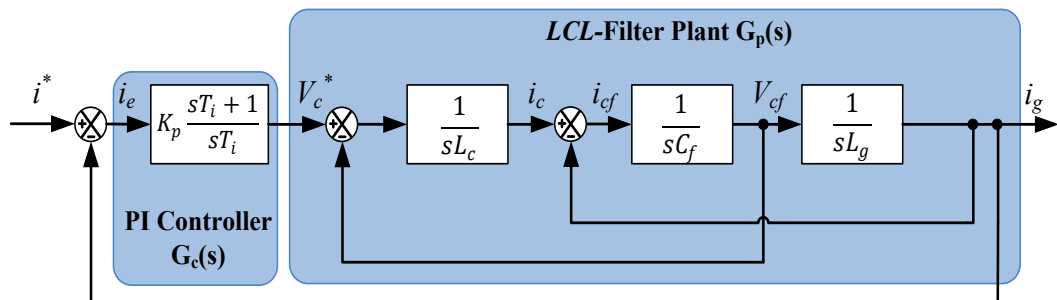


Figure 4.25 Block diagram of GCF control.

$$\frac{I_g(s)}{I_e(s)} = G_c(s)G_p(s) = \frac{K_p(s + 1/T_i)}{s^4 C_f L_c L_g + s^2(L_c + L_g)} \quad (4.27)$$

Likewise, the forward open-loop transfer function $G_c(s) \cdot G_p(s)$ is derived as in (4.27) and the constant of the third order term in the denominator is zero. Thus, the overall system cannot reach stability when the loop is closed. To deduce, introduction of the current controller does not have a resonance damping impact under grid-side current feedback (GCF) method. Internal losses such as ESRs of passive elements cannot be relied on; they generally deliver inadequate damping [57]. Plus, underdamped systems have poor dynamic performance with very low control bandwidth. Consequently, PD or AD must be added to blunt the resonant peak and to improve the dynamic behavior of the current loop.

Figure 4.26 shows the case when AD using filter capacitor current (i_{cf}) is utilized under GCF method. (4.28) reveals the case when $G_{lcl,ad}(s)$ is derived. As evident from the denominator, s^2 term is unveiled by means of AD gain block. Similarly, damping term s^3 appears in the denominator of the forward open-loop transfer function in (4.29). Note that there is no damping term introduced by the current controller in the resulting s^3 term, revealing once again that $G_c(s)$ has no impact on resonance damping under GCF. With the finite s^3 term introduced to the denominator, closed-loop stability of (4.29) can easily be tuned by varying the feedback gain K_d properly. Design tips about finding the optimum value of K_d will be shown in detail in Section 4.4.5.

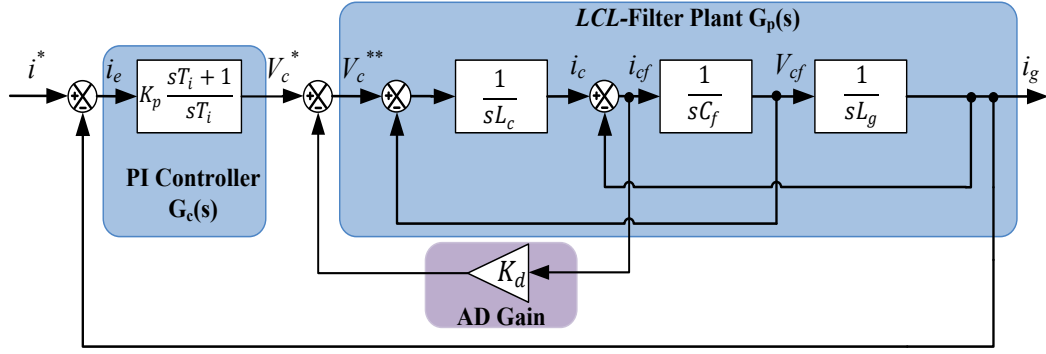


Figure 4.26 Block diagram of GCF with AD control.

$$\frac{I_g(s)}{V_c^*(s)} = \frac{1}{s^3 C_f L_c L_g + s^2 K_d C_f L_g + s(L_c + L_g)} \quad (4.28)$$

$$\frac{I_g(s)}{I_e(s)} = \frac{K_p (s + 1/T_i)}{s^4 C_f L_c L_g + s^3 K_d C_f L_g + s^2 (L_c + L_g)} \quad (4.29)$$

The degree of the damping introduced in the current loop depends on the AD controller gain and size of the filter components as can be seen in the denominator of (4.29). For example, to achieve the optimum damping factor $\zeta=0.707$ recommended in the literature [57]-[59], tuning of the variables can be done by proportioning the constant terms of the second highest variable (s^3 in this case) to the constant terms of the highest variable (s^4 in this case) as shown in (4.30).

$$\frac{K_d C_f L_g}{L_c C_f L_g} = 2\zeta \omega_{res} = 2\zeta \sqrt{\frac{L_c + L_g}{L_c L_g C_f}} \quad (4.30)$$

where ω_{res} is the resonant frequency of the *LCL*-filter determined solely by the passive component values and shown explicitly in (4.30).

4.4.4.2. Active Damping under Converter-Current Feedback

The converter current can alternatively be utilized for the current feedback control as depicted in Figure 4.27. As mentioned previously, q -axis current reference is set to $\omega_g \cdot C_f v_{g,q}$ rather than zero to ensure unit power factor since the grid current is not directly controlled. Nevertheless, it is evident in Figure 4.27 that obtaining the open-loop transfer function within this configuration is not convenient since the loop is closed in the middle of the open-loop path. Therefore, this structure should be modified by using the relation between converter current and grid current. Fortunately, converter current is the summation of grid current and filter capacitor current.

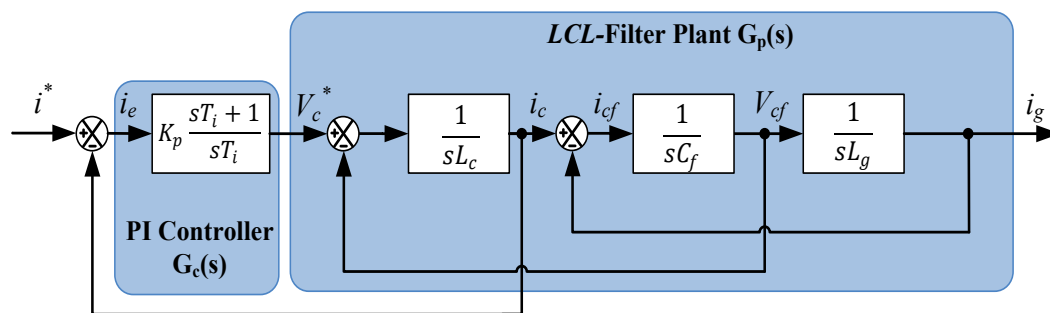


Figure 4.27 Block diagram of CCF control.

CCF is equivalent to GCF except for the additional i_{cf} -term. Thus, CCF method can be modeled by moving the feedback node to the end of the diagram and additionally subtracting i_{cf} term from the forward path as demonstrated in Figure 4.28. All in all, this modified block diagram is exactly the same as the one in Figure 4.27 since the system cannot sense any difference except for the simplicity to calculate its open-loop transfer function [57].

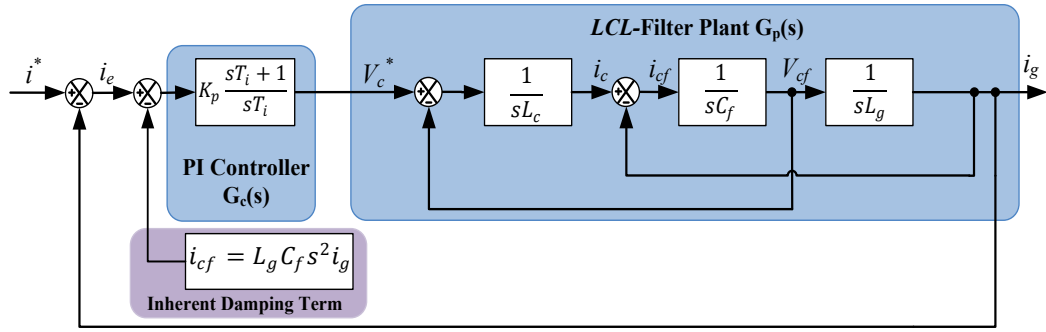


Figure 4.28 Block diagram of equivalent CCF control.

Using the modified block diagram, open-loop transfer function can be found as shown in (4.31). Then, substituting (4.23) into (4.31) yields the ultimate open-loop transfer function derived in (4.32).

$$\frac{I_g(s)}{I_e(s) - I_{cf}(s)} = \frac{K_p(s + 1/T_i)}{s^4 C_f L_c L_g + s^2 (L_c + L_g)} \quad (4.31)$$

$$\frac{I_g(s)}{I_e(s)} = \frac{K_p(s + 1/T_i)}{s^4 C_f L_c L_g + s^3 K_p C_f L_g + s^2 (K_p C_f L_g / T_i + L_c + L_g)} \quad (4.32)$$

As evident in the denominator of (4.32), there is an additional s^3 -term unlike (4.27) providing damping by pushing the resonant poles further into the unit circle without using AD (Figure 4.29). The degree of the damping introduced in the current loop depends on the controller gain and size of the filter components as can be seen in the denominator of (4.32). For instance, to achieve the optimum damping factor $\zeta=0.707$ recommended for critical damping case in the literature [57]-[59], tuning of the variables can be done by proportioning the constant terms of the second highest variable (s^3 in this case) to the constant terms of the highest variable (s^4 in this case) as shown below in (4.33).

$$\frac{K_p G_J L_g}{L_c G_f L_g} = 2\zeta\omega_{res} \quad (4.33)$$

where ω_{res} is the resonant frequency of the *LCL*-filter.

According to (4.33), either K_p or L_c can be adjusted in order to further push the resonant poles inside the unit circle in Figure 4.29 and vice-versa. The impact and corresponding boundaries of these adjustments are well studied in Section 4.4.5.

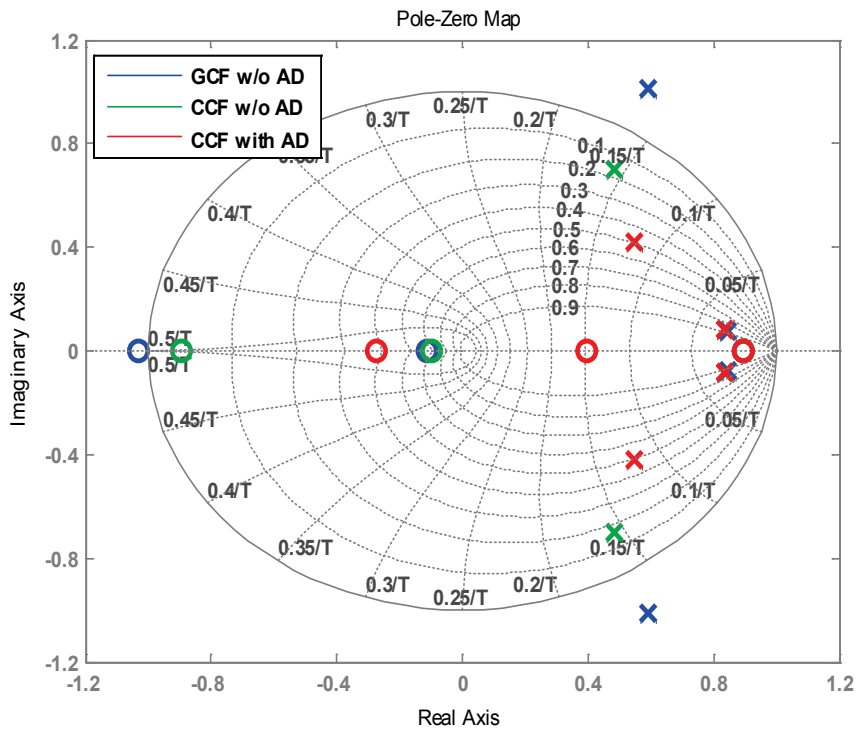


Figure 4.29 Pole locations under GCF and CCF without AD.

If the optimum damping cannot be provided by adjusting K_p and L_c , then additional damping terms must be introduced by utilizing AD. For this purpose, previously constructed AD configuration in Figure 4.26 can be adopted for CCF method as well. The modified structure is shown in Figure 4.30.

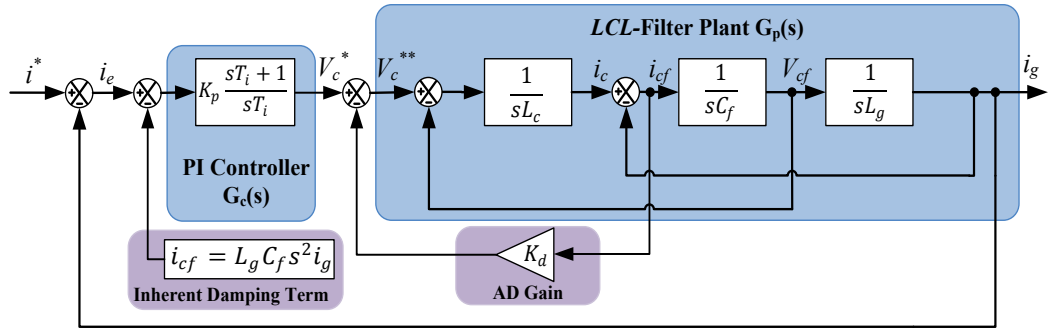


Figure 4.30 Block diagram of equivalent CCF control with AD.

Likewise, the open-loop transfer function with AD is derived as displayed in (4.34). Again, substituting (4.23) into (4.34) yields the final open-loop transfer function in (4.35) involving the damping contributed by both the current controller gain and AD gain.

$$\frac{I_g(s)}{I_e(s) - I_{cf}(s)} = \frac{K_p(s + 1/T_i)}{s^4 C_f L_c L_g + s^3 K_d C_f L_g + s^2 (L_c + L_g)} \quad (4.34)$$

$$\frac{I_g(s)}{I_e(s)} = \frac{K_p(s + 1/T_i)}{s^4 C_f L_c L_g + s^3 (K_p + K_d) C_f L_g + s^2 (K_p C_f L_g / T_i + L_c + L_g)} \quad (4.35)$$

According to denominator of (4.35), the extent of damping introduced can be tuned by adjusting the gains K_p and K_d and they should fulfill the following condition for optimum damping case.

$$\frac{(K_p + K_d) C_f L_g}{L_c C_f L_g} = 2\zeta\omega_{res} \quad (4.36)$$

Use of AD under CCF further pushes the resonant poles inside the unit circle and augments the closed-loop damping factor as evident in Figure 4.29. As a final remark, in practical applications calculated K_d value for the optimum damping

becomes higher than the required value owing to the internal resistances of the system that provides a definite extent of resonance damping [57]. Note that for all three distinct cases in Figure 4.29, low frequency poles moves only slightly, keeping the dynamics identical while resonance damping differs.

Consequently, the realization of the inherent resonance damping (ID) feature of the current loop under CCF technique is enlightened via extended block diagrams and pole-zero maps. The optimum values of the gain constants on achieving desired damping factors will be elaborated in Section 4.4.5.

4.4.5. Controller and Active Damping Gain Determination

Irrespective of the favored damping method (AD, PD, ID), fine-tuning of the controller parameters, active damping gains, and damping resistor values is essential on reaching the stability. For this reason, this section is devoted to provide a comprehensive background and methodology concerning the optimum damping issues for the systems damped by AD, PD, ID without AD and ID with AD.

In this section, most of the illustrations are made by means of a grid-connected *LCL*-filter based VSC utilizing GCF method in the control loop. For this reason, transfer function derived in (4.28) will be of primary concern. Besides, several illustrations regarding the CCF method will also be involved in the analyses. Before descending into particulars, the transfer function in (4.28) is rearranged with the aid of resonance frequency definition stated in (4.30) and the following simplified actively damped system model in (4.37) is obtained. Closed-loop stability of (4.37) can easily be tuned by varying the feedback gain K_d appropriately with regard to the desired damping factor ζ , representing the extent of resonance damping [68].

$$G_p(s) = \frac{1}{sL_cL_gC_f} \cdot \frac{\omega_{res}^2}{s^2 + 2\zeta\omega_{res}s + \omega_{res}^2} \quad (4.37)$$

As previously mentioned, PI current controller design is simplified by regarding the LCL system as a single inductor of the value $L_T = L_c + L_g$ in the low frequency range towards to the left of the resonant frequency. Bode diagrams of (4.37) under various damping factors can now be plotted as in Figure 4.31, using parameters listed in Table 4.1. Plus, first-order curve related to a simple L -filter, whose inductance is set to $L_T = L_c + L_g$ is also plotted for comparison.

Table 4.1 System parameters used for simulation.

Elements	Parameters	Values
Converter	S_n	1 MVA
	$^*f_{sw}$	2 kHz
	f_{samp}	4 kHz
	V_{DC}	1070 V
Grid	V_g	400 V _{rms-line}
	f_g	50 Hz
	PF	0.95-1
** LCL -filter	L_c	173 μ H (11.2%)
	L_g	173 μ H (11.2%)
	C_f	332 μ F (5%)

*Switching frequency is calculated using the methodology given in Chapter 3.

**Filter parameters are computed by the algorithm to be provided in Chapter 5.

Although the magnitude response of the L -filter and the LCL -filter matches perfectly in low frequency range regardless of the preferred damping factor, their phase responses deviate considerably as depicted in the bode plot of the open-loop system under various damping factors in Figure 4.31. The maximum phase lag of simple L -filter is $\varphi_L = \pi/2$ while that of an LCL -filter always exceeds this value. As the damping factor extent increases, deviation becomes even larger as can be realized in Figure 4.31.

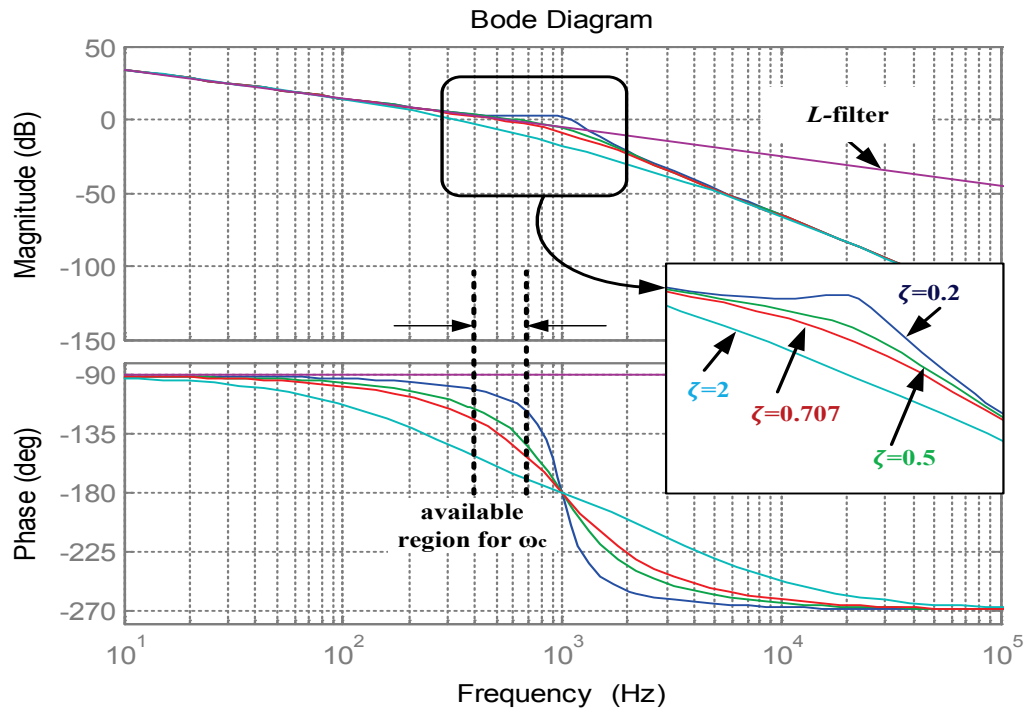


Figure 4.31 Magnitude and phase response of *LCL*-filters under distinct damping factors.

Due to large phase lag of the *LCL*-filter, damping factor ζ of the *LCL* resonance must be tuned optimally. Optimum damping control is essential since there will be serious transient oscillations in the dynamic response to the step change if the resonance is underdamped. On the other hand, overdamped systems will rigorously decrease the system phase margin and decelerate the dynamic response. As reference to Figure 4.31, the resonance peak is not blunted sufficiently for the case $\zeta=0.2$ and the system is underdamped. Nonetheless, the system is overdamped for the case $\zeta=2$ and a very large phase lag is apparent.

Furthermore, the maximum value of zero dB gain crossover frequency ω_c cannot exceed or even be close to the resonance frequency, since there is a 180° phase lag at the resonant frequency resulting influence of which is an insufficient phase margin for closed-loop control. Plus, inevitable delays caused by sampling and modulation constrains the system crossover frequency, forcing ω_c to be fixed sufficiently below ω_{res} regardless of utilized damping technique, based on the suggested ω_c tuning

region highlighted with two vertical dotted lines in Figure 4.31. To deduce, ω_c is primarily limited by the phase lag of the LCL -filter and ω_c should be selected as a fraction of the undamped resonant frequency to achieve an adequate phase margin. This fraction can be represented as $\omega_c = \alpha \omega_{res}$ provided that $\alpha < 1$ (Figure 4.33).

The explicit notation of phase lag φ_{LCL} is provided in (4.38). Phase lag φ_{LCL} can be represented as a function of its damping factor ζ and the ratio of gain crossover frequency to resonant frequency, α as below. 3D-plot shown in Figure 4.32 visualizes the phase lag characteristics under various ζ and α [57].

$$\varphi_{LCL} \approx \frac{\pi}{2} + \arctan\left(\frac{2\zeta\alpha}{1-\alpha^2}\right) \quad (4.38)$$

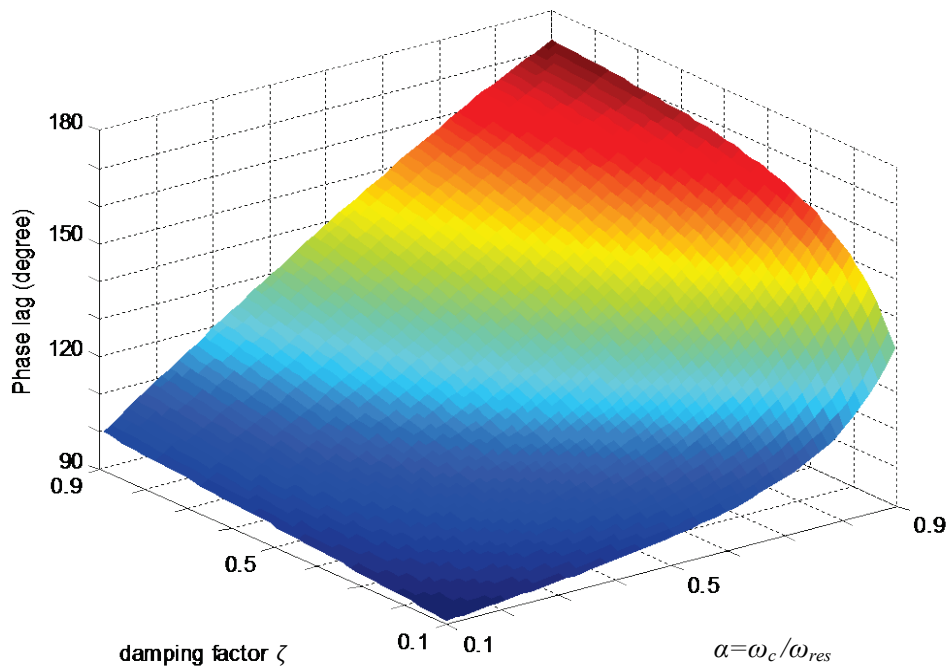


Figure 4.32 Phase lag of LCL -filter as a function of damping factor and the ratio of crossover frequency to resonant frequency.

The available tuning zone for gain crossover frequency ω_c is highlighted in Figure 4.31. In order to clarify the importance of this region, Figure 4.33 is referred. Figure 4.33 reveals the bode plot of damped and undamped transfer function of *LCL*-plant $G_p(s)$ and the cascaded open-loop forward transfer function $G_p(s) \cdot G_c(s)$ provided in (4.28) (equivalent to (4.37)) and (4.29), respectively. With the introduction of PI current controller plant $G_c(s)$, the location of the gain crossover frequency is altered within the frequency axis owing to the nonzero gain of the controllers as revealed in Figure 4.33 (i.e. from 504 Hz to 222 Hz). Thus, there should be boundaries limiting the excursion of ω_c caused by the introduction of K_p . Maximum and minimum values of this boundary can be determined as follows.

The optimum damping condition of *LCL* resonance is deemed as $\zeta=0.707$ in the literature [55]-[59]. Therefore, by referring the bode plot for the case $\zeta=0.707$ in Figure 4.31, the rightmost boundary of ω_c is determined such that closed-loop control can have sufficient phase margin higher than 45° . Similarly, the leftmost boundary of ω_c is determined when the phase response of the case $\zeta=0.707$ begins to deviate from -90° . In addition, the distance between the modified crossover frequency and the undamped resonant frequency (actually the frequency that the phase margin starts to descend below -180°) defined by α (Figure 4.33) has crucial impact on the achieved phase margin and dynamics of system.

In order to achieve the proper choice of the proportional gain constant K_p of the PI controllers to place ω_c in the desired location within suggested tuning region, further tuning may be needed. For the fine-tuning of ω_c in the highlighted zone, calculated K_p value by means of (4.18) (which is found according to symmetrical optimum criterion delivering $\zeta=0.707$) can be slightly modified by using the relationship between K_p and ω_c depicted in (4.39) [57][58].

$$K_p \approx \omega_c (L_c + L_g) \quad (4.39)$$

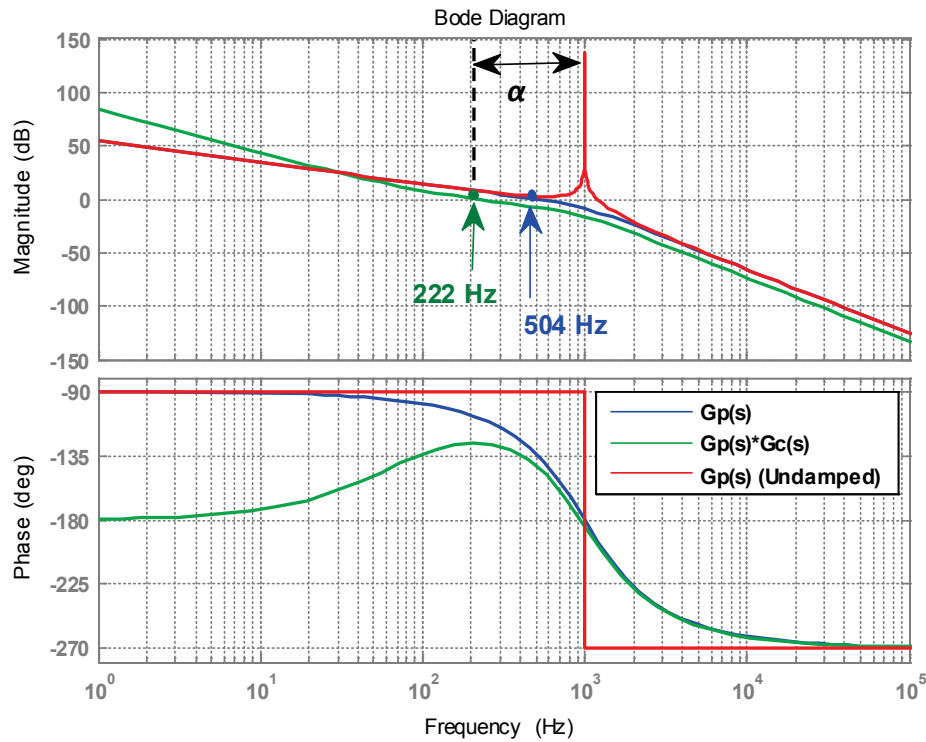


Figure 4.33 Impact of PI-controller on magnitude and phase response.

For the optimum damping of *LCL* resonance ($\zeta = 0.707$), setting $\alpha \approx 0.3$ (i.e. $\omega_c \approx 0.3\omega_{res}$) is recommended in the literature as well, since it not only succeeds an adequate phase margin but also avoids the rapid phase transition securely as can be seen in Figure 4.33 [57][58]. The combination of $\zeta = 0.707$ and $\alpha \approx 0.3$ yields a phase lag of the *LCL*-filter about 115° , which is not a severe degradation compared to *L*-filter (90°). So, *L*-filter approximation for the PI current controller design holds true for the suggested combination of ζ and α .

In the most applications, the transient response of the system is of particular concern. In order to enhance the transient response, control bandwidth should be increased (to increase the control bandwidth, ω_c must be increased). For this purpose, the damping factor may be decreased to 0.5 so that higher ω_c can be acquired (Figure 4.31 and Figure 4.32) [57]. The relationship between the crossover frequency and the control system bandwidth can be detailed as follows. As it is obvious in Figure 4.31 that lower damping factor provides a better match between *L*

and *LCL* filter in terms of low frequency magnitude and phase characteristics. The system bandwidth is limited by the rightmost boundary of the ω_c tuning zone in Figure 4.31. Beyond the rightmost borderline, the deviation between *LCL* and *L*-filter characteristics becomes considerable (intolerable). The rightmost borderline of the ω_c tuning region is mainly determined by the phase lag and the phase lag is determined by the preferred damping factor (damping factor \rightarrow phase lag \rightarrow boundary of ω_c). If a higher damping factor is desired, phase lag gets larger and hence the rightmost borderline of the ω_c tuning zone has to shift to left in the frequency band (i.e. the system control bandwidth is decreased since ω_c is forced to be selected lower) to limit the discrepancy between *L* and *LCL* filter responses. On the other hand, if a lower damping factor is desired, phase lag gets lower and hence the rightmost borderline of the ω_c tuning zone can be shifted to right in the frequency band (i.e. the system control bandwidth is increased since ω_c can be selected higher). All in all, high damping factors constraint the system bandwidth and severely degrades the phase margin.

As yet, the necessity of PI-current controller design in the low frequency region in *LCL*-filter stabilization, the requirement of a crossover frequency tuning region to guarantee a sufficient phase margin, the correspondence of the crossover frequency with the control system bandwidth, and the explicit impact of the damping factor on the phase lag and its implicit impact on the system control bandwidth are studied in detail. Hereafter, apart from the impact of the resonance poles, the impact of the real pole on the system response and the trade-off between transient performance (rise time, settling time, etc.) and resonance damping will be illustrated.

Decrease in the desired open-loop damping factor of the resonant poles from 0.707 to 0.5 is illustrated in Figure 4.34 in terms of pole-zero movements for the set of *LCL*-filter parameters shown in Table 4.1. As can be realized in Figure 4.34, smaller damping factor would force the real closed-loop pole to move towards the imaginary axis, hence increasing its impact, and attenuating the domination of the two conjugate poles.

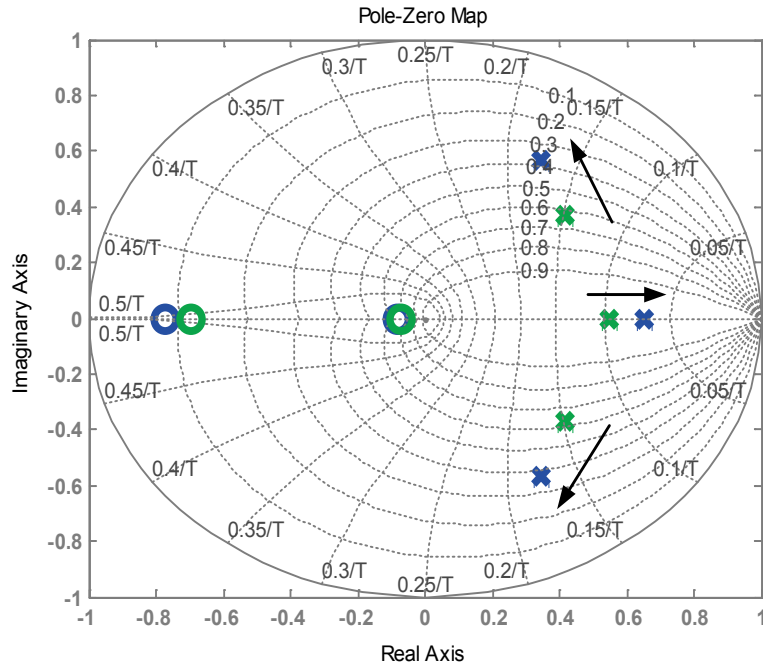


Figure 4.34 Impact of decreasing damping factor shown by pole-zero map.

As a remark, PI-controller transfer function $G_c(s)$ can be reduced to K_p for the pole-zero and root-loci analyses since the resonance gain has negligible impact above ω_g [58]. Thus with this simplification, low-frequency conjugate poles reduces to one real low-frequency pole as in Figure 4.34. The impact of the real pole cannot be neglected, but should be clarified by comparing the step response of the closed-loop system with the following second order system $G_s(s)$ in (4.40) under different damping factors:

$$G_s(s) = \frac{\omega_{res}^2}{s^2 + 2\zeta\omega_{res}s + \omega_{res}^2} \quad (4.40)$$

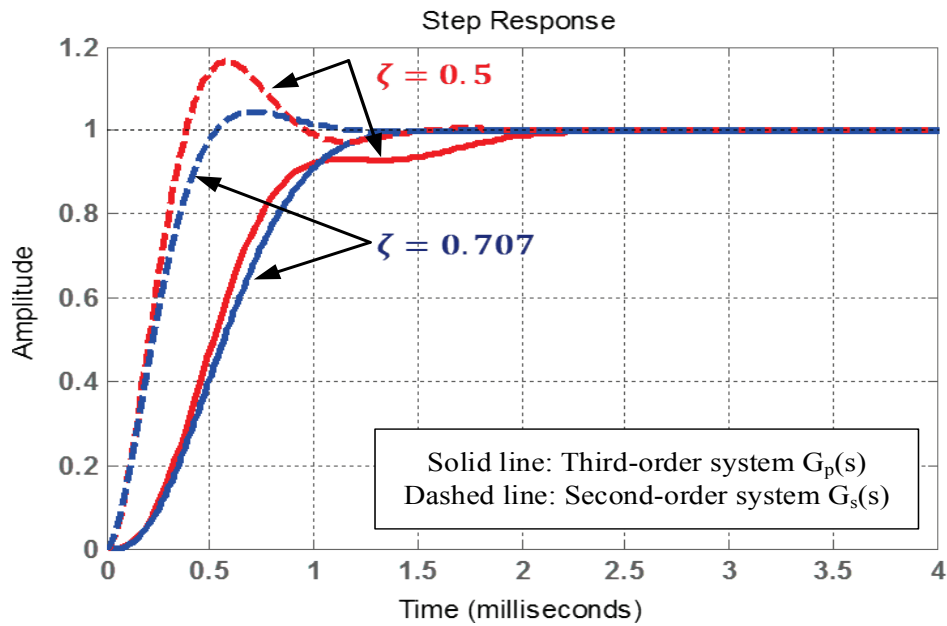


Figure 4.35 Step responses of $G_p(s)$ and $G_s(s)$.

In the light of the results plotted in Figure 4.35, it can be inferred that the real pole is slowing down the overall step response, hence bringing about a longer settling time. However, it damps transient oscillations more powerfully, leading to smaller overshoots at all damping factors.

In order to state the trade-off between transient performance (rise time, settling time, etc.) and resonance damping, open-loop phase margin provided by each damping factor is examined. Phase margins for the case $\zeta=0.5$ ($\omega_c \approx 2\pi 289$ rad/sec, $\alpha = 0.2891$) and $\zeta=0.707$ ($\omega_c \approx 2\pi 278$ rad/sec, $\alpha = 0.2779$) are found to be 55.5° and 49.3° respectively as shown in Figure 4.36. Hence, increased phase margin delivers higher ω_c and therefore higher bandwidth leading to a faster current loop.

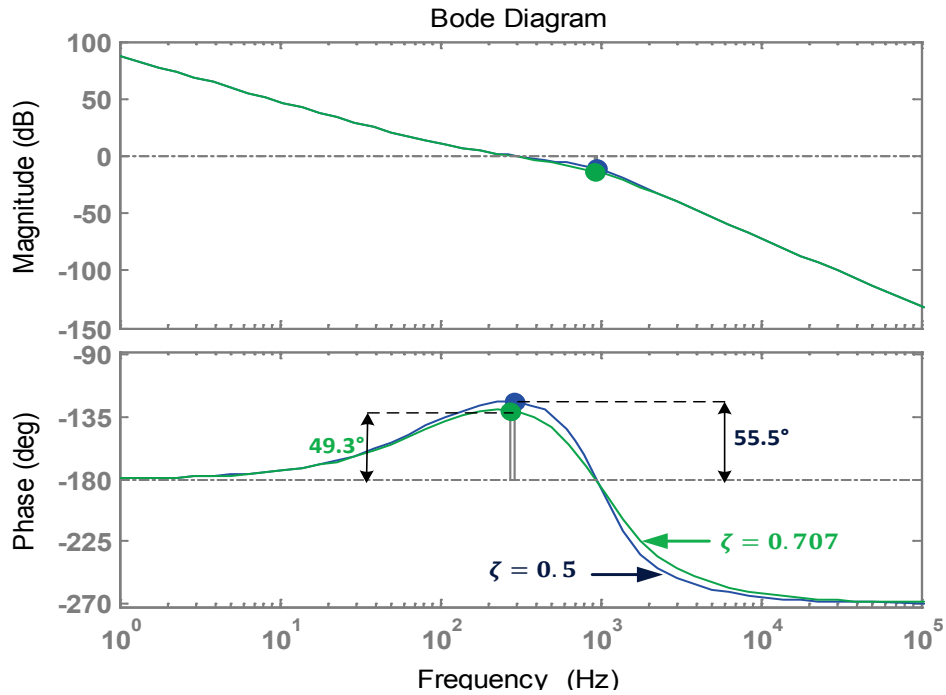


Figure 4.36 Impact of damping factor on phase margin (CCF).

Hereafter, the general representation of the damping factor ζ will be explicitly shown according to the favored method of current feedback technique. For instance, Figure 4.37 depicts the bode plot of open-loop transfer function $G_p(s) \cdot G_c(s)$. Open loop transfer function $G_p(s)$ is derived regarding converter-side current feedback and hence the system is inherently damped as expected and it is further proven in Figure 4.37. Therefore, K_p provides gain adjustment for the current control loop as well as adjusts the damping factor of the resonant poles. There is not any other additional damping. In order to ensure a stable closed-loop control system, K_p value should not be so high. Excessive K_p shifts up the magnitude response of the *LCL* system too much, then ω_c gets higher as depicted in Figure 4.37. This tendency is also verified by the formula defined in (4.39). However, the control system bandwidth would not increase forever with the increase of ω_c . Since, the *L*-filter approximation starts to deviate considerably prior to resonant frequency under excessive gain constants as can be agreed in Figure 4.37.

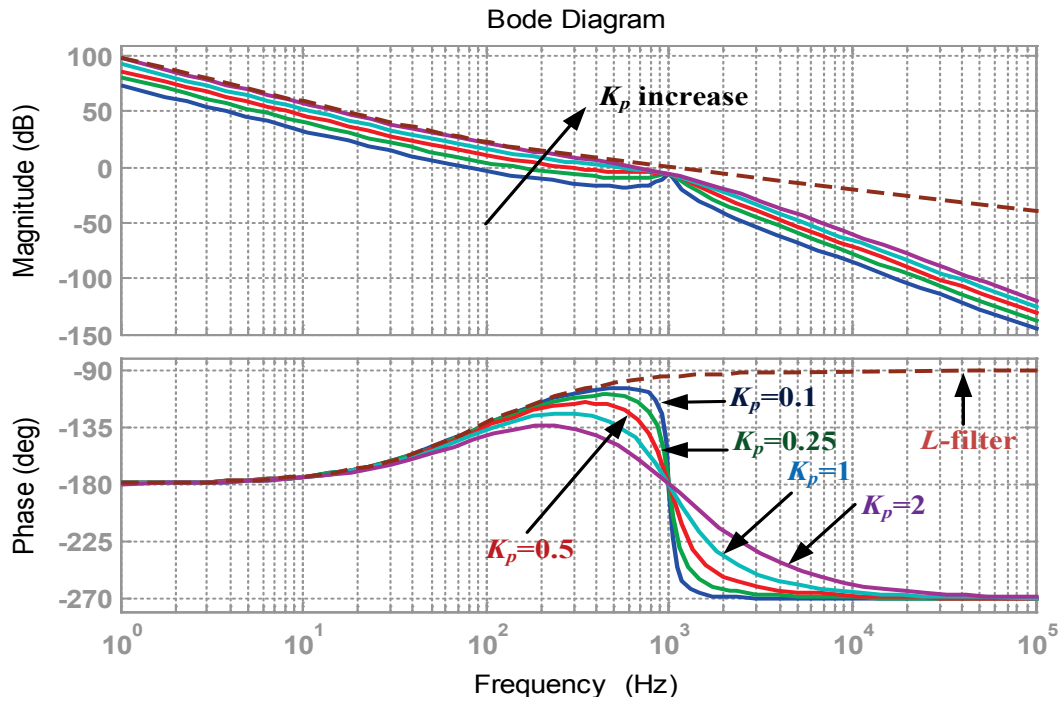


Figure 4.37 Impact of K_p change on open-loop bode plot (CCF).

In addition, Figure 4.38 presents root locus analysis to visualize the closed-loop pole movements of the system using converter-side feedback under various K_p values. In Figure 4.38, the resonant poles initially track well inside the unit circle and hence the system is kept stable until K_p is increased too much. Thereby, tuned ω_c should reside within the boundary that is set to reserve sufficient phase margin for the closed-loop control. Beyond the maximum borderline of the ω_c tuning region, the system phase margin is severely reduced, degrading transient response rigorously. Consequently, the reason why the ω_c tuning zone is confined to the low frequency range in Figure 4.31 becomes more evident.

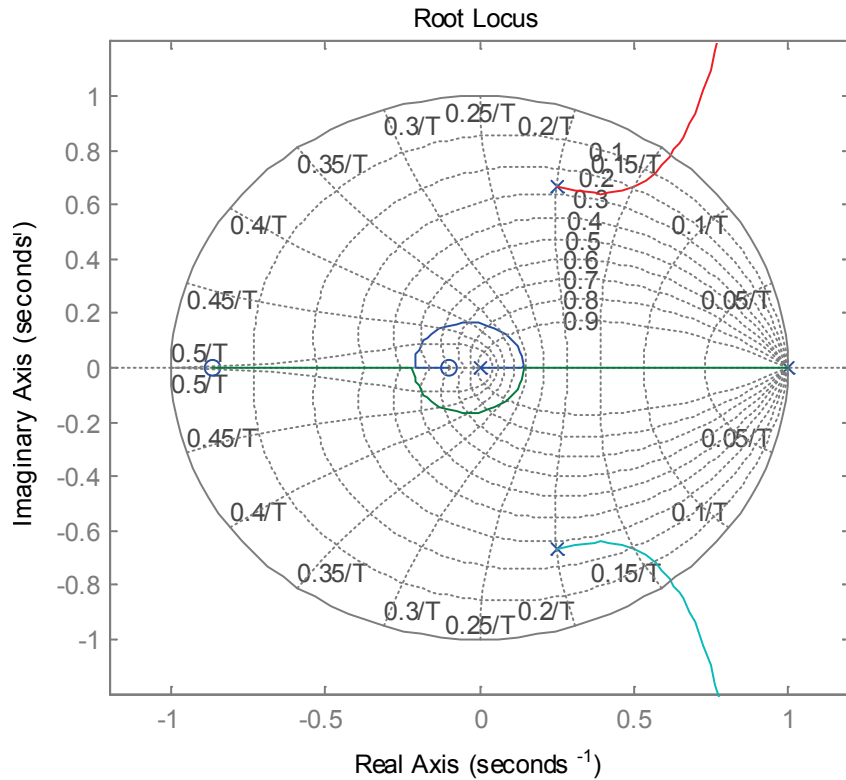


Figure 4.38 Root locus under K_p change (CCF).

Note that the symmetrical optimum approach in K_p designation targets the maximum ω_c boundary to maximize the bandwidth of the system while guaranteeing a sufficient phase margin [57][58]. As a consequence, (4.18) deliver K_p concerning the optimum damping factor $\zeta=0.707$ together with the optimum distance of $\alpha \approx 0.3$. Hence any K_p opted higher than the calculated K_p value would start to degrade phase margin and transient response.

Figure 4.39 depicts the bode plot of open loop transfer function consisting of PI current controller and LCL plant. Open loop transfer function is derived regarding grid-side current feedback and the system is damped using active damping method. Therefore, K_p only provides gain adjustment for the current control loop. The K_p values and the color codes are identical with the ones in Figure 4.37. The same restrictions concerning K_p increase apply for the grid-side current feedback method

definitely. Increase in K_p shifts up the magnitude response of the LCL system, then ω_c shifts to higher frequencies as depicted in Figure 4.39. However, in this case the phase response remains the same while K_p changes. Since, the damping factor supplied by the active damping gain constant K_d is adjusted to yield $\zeta=0.707$ and does not change at all. Excessive K_p puts ω_c out of the borderline of the ω_c tuning region. As a consequence, the system phase margin is diminished severely, and transient response is worsened.

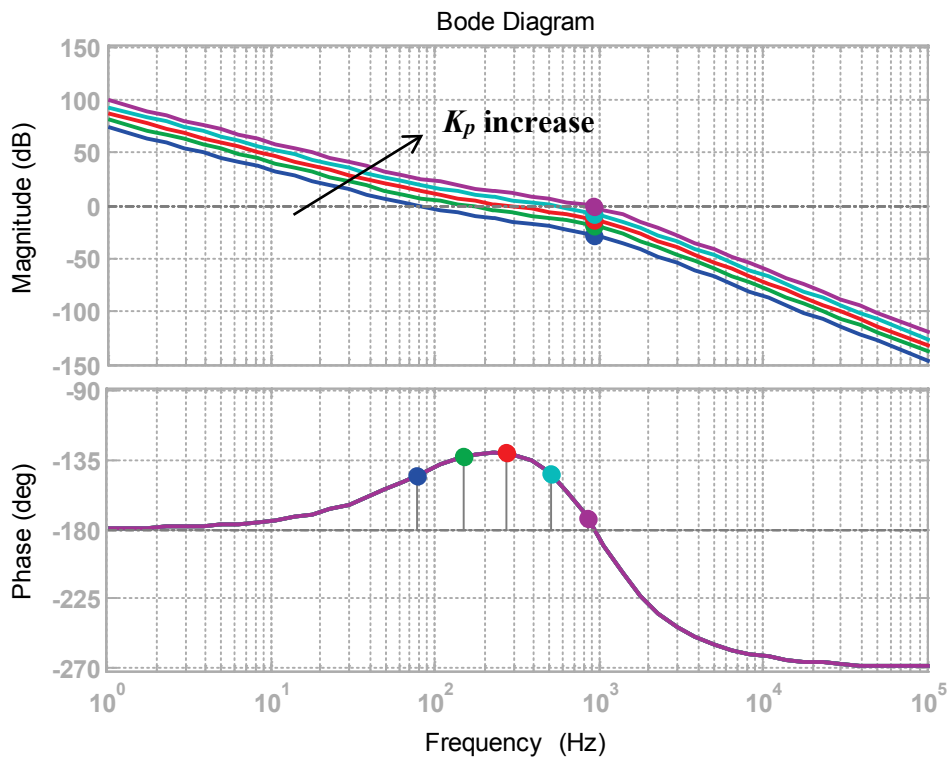


Figure 4.39 Impact of K_p change on open-loop bode plot (GCF).

Similarly, Figure 4.40 presents root locus plot for the closed-loop pole movements of the system using grid-side feedback under various K_p values. In Figure 4.40, the resonant poles are damped sufficiently owing to the employed active damping loop. However, low-frequency system poles are shifted towards outside of the unit circle for the large K_p gains.

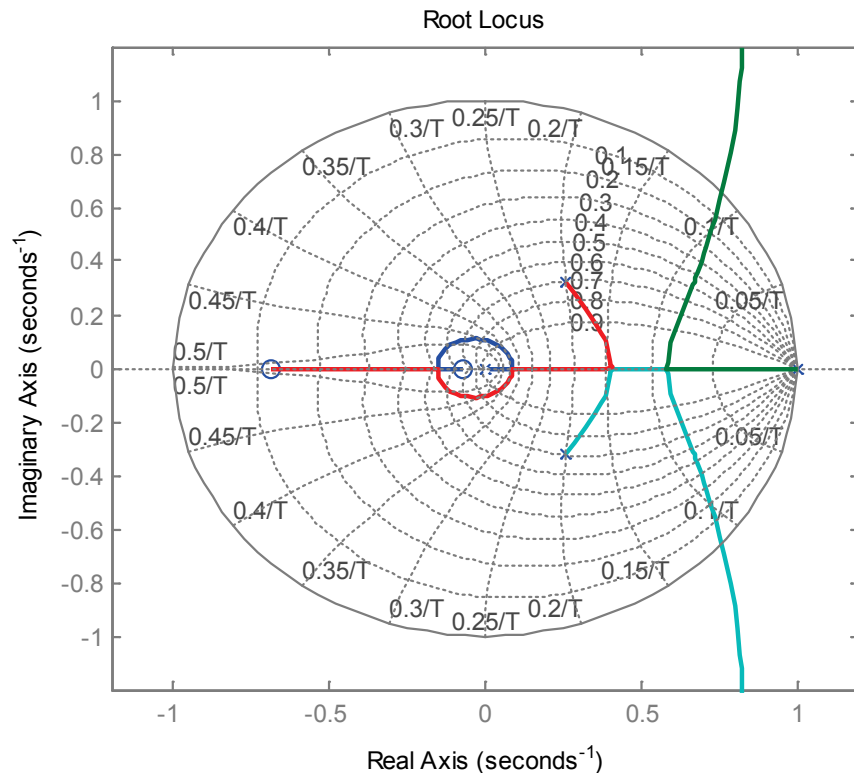


Figure 4.40 Root locus under K_p change (GCF).

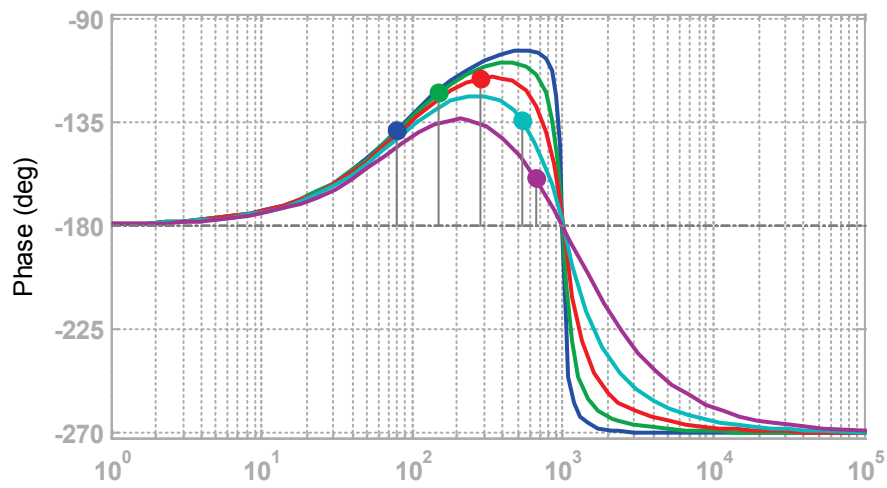


Figure 4.41 Impact of K_p change on phase response (CCF) – detailed.

Figure 4.39 and Figure 4.41 visualizes the change in the corresponding phase margins against various K_p under GCF and CCF, respectively. Note that Figure 4.41 is the detailed portion of the phase response in Figure 4.37. It can be inferred that the increase in K_p from 0.1 to 0.5 improves the phase margin considerably in both methods. Nevertheless, further increase in K_p tends to diminish the phase margin and degrade the transient response in both methods. Thus, the optimum K_p can be regarded as 0.5 which is the same value as the one calculated by means of (4.18). Note also that the formula provided in (4.39) yields values very close to the ones delivered by (4.18). As a remark, $K_p=0.5$ value provides the maximum achievable phase margin and yields $\alpha \approx 0.29$ proving that the suggested condition of $\alpha \approx 0.3$ is determined such that it warrants the optimum phase margin anyhow.

4.4.6. Identification of Active Damping Regions for *LCL*-Filters

The relationship between the resonant frequency and PI-current controller stability is well-elaborated in Section 4.4.5 via magnitude and frequency responses of the forward path transfer functions ($G_p(s) \cdot G_c(s)$) along with individual *LCL*-plant $G_p(s)$, pole-zero maps, root loci and simulation studies by means of MATLAB[®] and SIMPLORER[®]. Not only stability of the *LCL*-plant current controller design is regarded but also the sufficiency of the damping extent is examined through comprehensive analyses and simulation.

As yet, the internal structure of the current feedback mechanisms and their damping methods are considered. Nevertheless, the feasibility of these damping methods under distinct parameters has not been investigated yet. This section is dedicated to enlighten that there are three distinct regions of significance for the *LCL*-filter resonance – high resonant frequency region, critical resonant frequency region and low frequency resonant region [58]. The low resonant frequency region and high resonant frequency region is separated by the critical resonant frequency region where it is not possible to design a proper PI-controller with effective damping [57]. Therefore, it can be inferred that the resonant frequency of the *LCL*-filter is not an arbitrary number. Its value can completely change the effective stability extent and

the method to achieve stability. All in all, how and when active damping is needed in *LCL*-filter control as the resonant frequency varies is embodied in this dissertation under this section.

Through extended literature review [54]-[58][60][61][64]-[68] and comprehensive self-study on this issue [56][59][63][69], the regions that the active damping can be applied effectively or active damping is useless is well-clarified under GCF and CCF current feedback methods and they are tabulated in Table 4.2.

Table 4.2 Regions of effective AD control under CCF and GCF.

	Low-resonant frequency	High-resonant frequency
CCF	<ul style="list-style-type: none"> • System is stable without AD. • AD does not contribute to stability and it has nearly no impact on resonant damping extent. 	<ul style="list-style-type: none"> • System is stable without AD. • AD does not contribute to stability however it has beneficial impacts on increasing resonant damping extent.
GCF	<ul style="list-style-type: none"> • System is not stable without AD. • AD is mandatory for stability and damping extent depends primarily on K_d. 	<ul style="list-style-type: none"> • System is stable without AD. • AD does not contribute to stability but it has beneficial impacts on increasing resonant damping extent.

Note that the refined information provided in Table 4.2 is obtained by assuming a lossless *LCL*-filter network in order to simulate the worst-case scenario on achieving stability. The deductions made in Table 4.2 should be interpreted – for instance, below critical resonant frequency i.e. in low resonant frequency region, AD become necessary to achieve stability nevertheless, above critical resonant frequency i.e. in high resonant frequency region, there is no need to use AD methods since current regulators are sufficient to ensure stability when GCF is employed.

Figure 4.42 shows the closed-loop pole movements under CCF and GCF methods without AD in the low and high resonant frequency regions. In Figure 4.42(a) and (c), poles are initially pushed well inside the unit circle under both GCF and CCF methods. Thus, stability is maintained by only current feedback loop i.e. without AD until excessive gain constant K_p is applied in high resonant frequency region. On the other hand, in the low resonant frequency region, the resonant pole pair always follows a trajectory away outside the unit circle as agreed in Figure 4.42(b) under GCF method without AD. Thus, system cannot be stabilized without using AD, proving the statement in Table 4.2 However, in low resonant frequency region under CCF method (Figure 4.42(d)) system is stable for small controller gains without AD and resonant pole pair initially tracks inside the unit circle until excessive K_p values are applied. Consequently, these four root-loci outputs further validate the findings in Table 4.2.

The abovementioned critical resonant frequency region is determined by a so-called critical *LCL*-filter resonance frequency (ω_{crit}) and it can be calculated by means of (4.41) [58].

$$\omega_{crit} = \frac{\pi}{3T_{samp}} \quad (4.41)$$

where T_{samp} is the system sampling frequency. In the light of Table 4.2, controller design and gain determinations in low and high resonant frequency regions are addressed briefly.

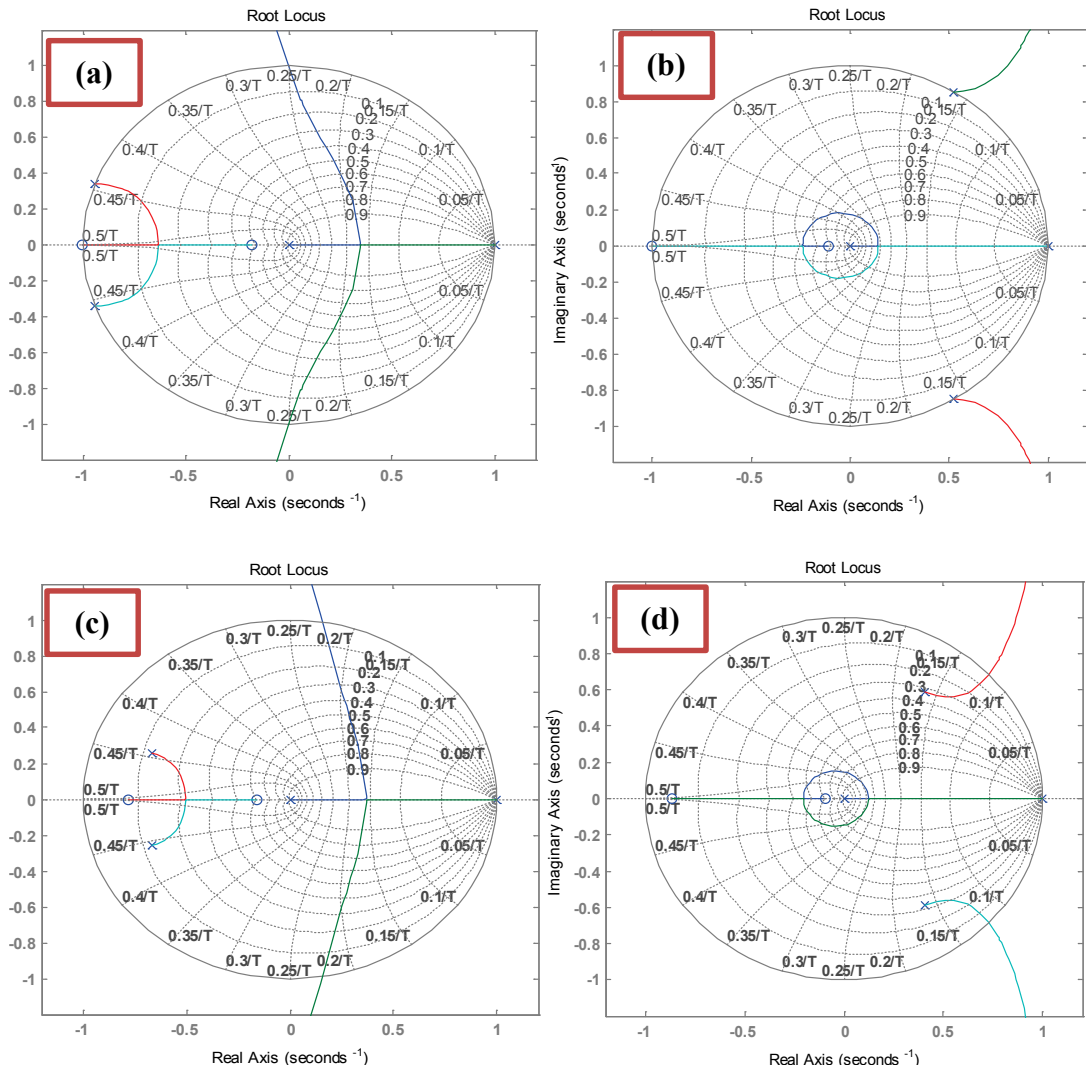


Figure 4.42 Root loci under (a) GCF in high f_{res} (b) GCF in low f_{res} (c) CCF in high f_{res} (d) CCF in low f_{res} .

4.4.6.1. *LCL* Resonance Frequency above Critical Resonance Frequency

Once the *LCL*-filter resonant frequency, ω_{res} is higher than ω_{crit} , employment of AD using capacitor current feedback does not promote stability and simply GCF is sufficient to ensure stability with the usage of conventional PI-current regulators [59]. CCF method can also be adopted as the main feedback variable and a stable system can be obtained without use of AD methods. However, the utilization of AD using capacitor current feedback may flourish the damping capability of the system

and improve the harmonic and ripple performances for both CCF and GCF at high resonant frequency region [59].

It is evident from Figure 4.42(a) and(c) that the main constraint limiting the controller gain is the position of the low frequency poles within the unit circle rather than the resonant poles of the *LCL*-filter. Thus, when $\omega_{res} > \omega_{crit}$, maximum controller gains can be computed using the *L*-filter approach as mentioned previously.

4.4.6.2. *LCL* Resonance Frequency below Critical Resonance Frequency

Once the *LCL*-filter resonant frequency, ω_{res} is lower than ω_{crit} , only CCF is sufficient for stable control and utilization of AD provides neither stability performance improvement nor damping extent escalation. However, if GCF is employed, then AD is essential to attain stability [59]. Utilization of AD using filter capacitor current and optimization of damping gain constant K_d under CCF and GCF are well studied in Section 4.4.4 and 4.4.5, respectively.

Regardless of the damping method, the low frequency current controller is still ruled by the total inductance of the *LCL*-filter neglecting the capacitor branch [58] Thus, *L*-filter approximation holds true in this region as well and controller parameters can be calculated as done before as long as the crossover frequency is set sufficiently below the resonant frequency. Section 4.4.5 should be referred for more details.

As of this point, the provided theoretical background up until will be verified in simulation environment (SIMPLORER[®]). Also, further tips regarding stability and dynamic response will be provided via root-loci and step responses with the aid of MATLAB[®].

Fixing the problems caused by inadequate damping is as crucial as the stabilization of an *LCL*-filter current regulator. Therefore, stabilization is not the only aim of the controller design procedure; sufficient damping must be provided to damp high frequency oscillations caused by resonant poles. As a remark, *LCL*-filter parameters should not be designed such that the resonant frequency becomes so close to critical

resonant frequency. Since, there is an uncertain and probably unstable region of operation around ω_{crit} [58].

4.5. Case Studies

In this section, steady-state and transient-state performances of the outputs of a proposed *LCL*-filter will be assessed regarding the regions of resonant frequency. The system parameters studied in the case studies are given in Table 4.3.

Table 4.3. System parameters used in case-studies.

Elements	Parameters	Values
Converter	S_n	250 kVA
	f_{sw}^*	4 kHz
	f_{samp}	8 kHz
	V_{DC}	750 V
Grid	V_g	230 V _{rms-line}
	f_g	50 Hz
	PF	0.95-1
** <i>LCL</i> -filter	L_c	200 μ H (9.8%)
	L_g	200 μ H (9.8%)
	C_f	150 μ F (3%)

*Switching frequency is calculated using the methodology given in Chapter 3.

**Filter parameters are computed by the algorithm to be provided in Chapter 5.

4.5.1. Simulation Results via SIMPLORER® for GCF Control

Although 1 MVA PWM-VSC is simulated in Section 4.4.5, in this section a 250 kVA PWM-VSC will be simulated for two reasons. First reason is to augment the power scale diversity assessed within the thesis and secondly to process the theoretical data under a decent switching frequency higher than 2-3 kHz in order to highlight the dissimilarities between control methods more evidently.

Simulation studies require different sets of *LCL*-parameters: below ω_{crit} , and above ω_{crit} as listed in Table 4.4. The inductors are kept constant while C_f is changed to

shift ω_{res} between low and high ω_{res} regions. Control (sampling) frequency is also kept constant throughout the analysis, yielding different ratios of resonant frequency to sampling frequency. Since this ratio is vital on commenting on the performance of the *LCL*-filter in control and resonance damping aspects [55]. As a remark, the ratio of resonant frequency to sampling frequency will be represented by λ correspondingly in the following parts.

Table 4.4 Selection of C_f below and above critical region.

Reactive power absorption ratio	C_f	f_{res}	$\lambda = f_{res}/f_{smp}$
3%	150 μ F	1.19 kHz (low)	0.15
2.8%	142 μ F	1.33 kHz (critical)	0.17
0.6%	30 μ F	2.91 kHz (high)	0.36
0.4%	20 μ F	3.56 kHz (high)	0.44

Sections 4.5.1.1, 4.5.1.2 and 4.5.1.3 illustrates Case I-GCF with AD in low resonant frequency region, Case II - GCF without AD in high resonant frequency region for $C_f = 20 \mu$ F and Case III- GCF without AD in high resonant frequency region for $C_f = 30 \mu$ F, respectively. First of all, all of the related waveforms are provided in Figure 4.43, Figure 4.44, and Figure 4.45, then three cases are evaluated comparing these waveforms.

4.5.1.1. Case I– GCF with AD in Low-Resonant Frequency Region

Figure 4.43 reveals dynamic-state and steady-state grid current, converter current and grid current in dq -frame under specified combination.

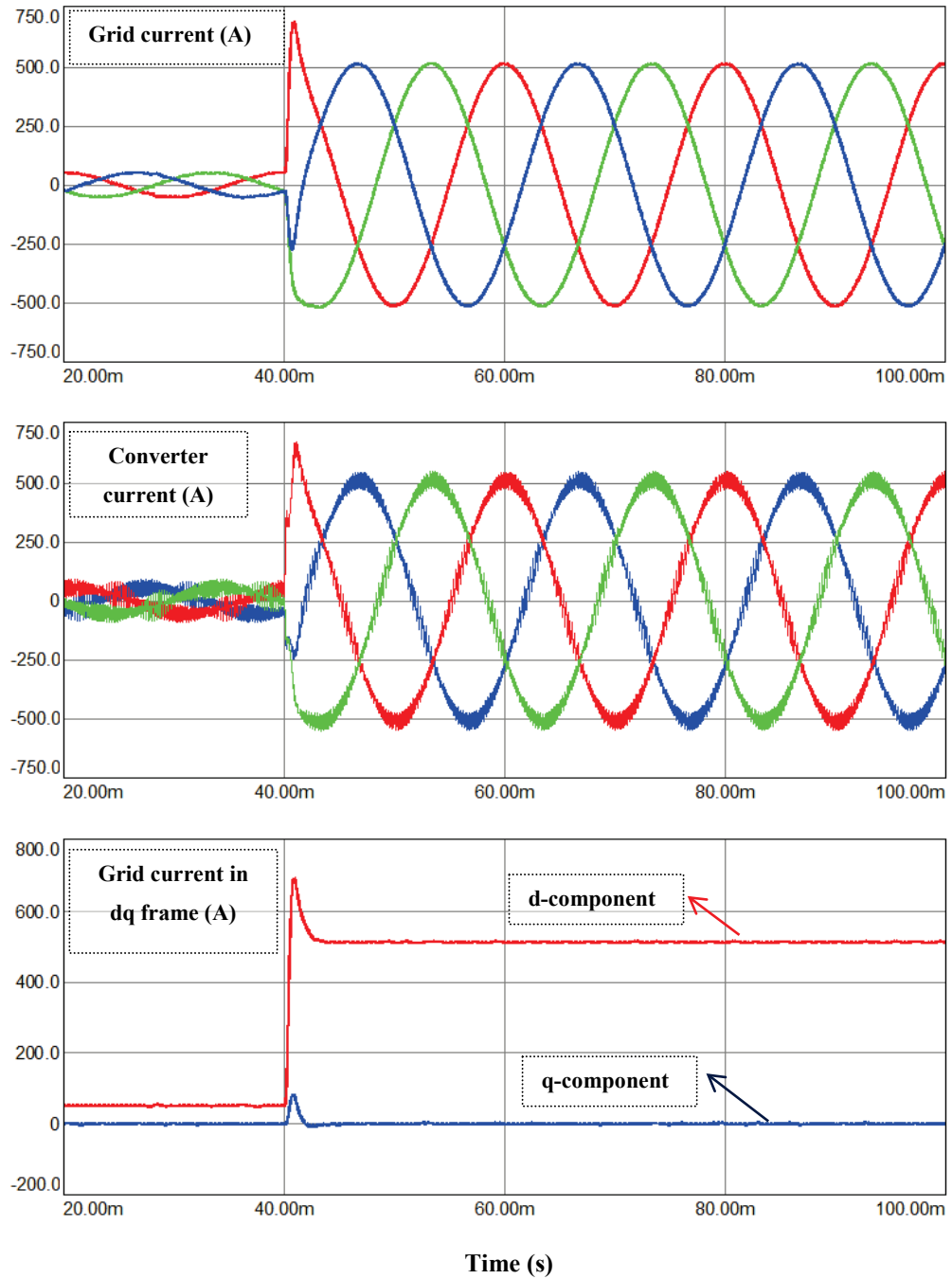


Figure 4.43 Simulation outputs GCF with AD (low f_{res}).

4.5.1.2. Case II– GCF without AD in High-Resonant Frequency Region ($C_f=20\ \mu\text{F}$)

Figure 4.44 depicts dynamic-state and steady-state grid current, converter current and grid current in dq -frame under specified combination.

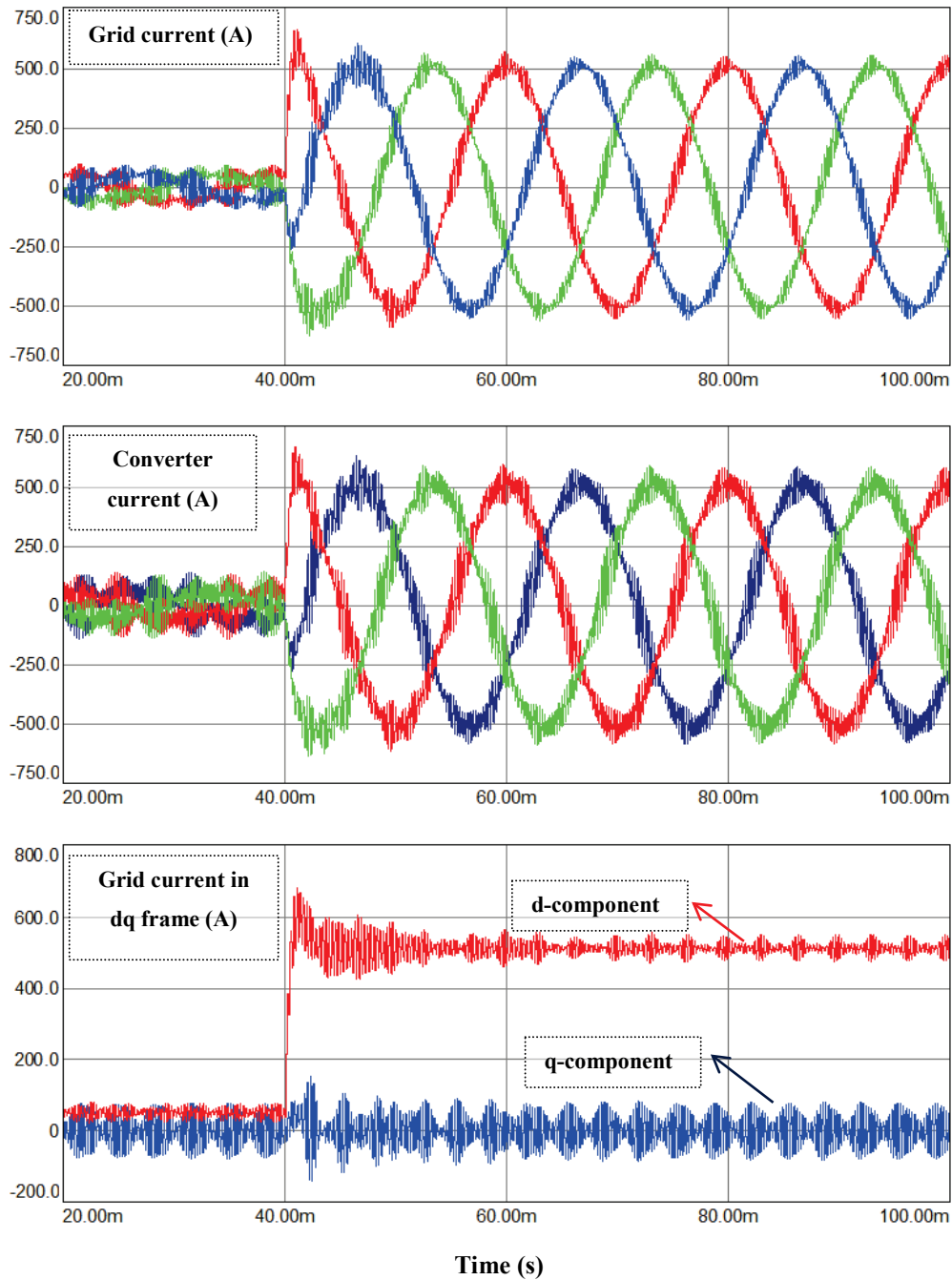


Figure 4.44 Simulation outputs under GCF without AD (high f_{res} , $C_f=20\mu\text{F}$).

4.5.1.3. Case III– GCF without AD in High-Resonant Frequency Region ($C_f=30\ \mu\text{F}$)

Figure 4.45 reveals dynamic-state and steady-state grid current, converter current and grid current in dq -frame under specified combination.

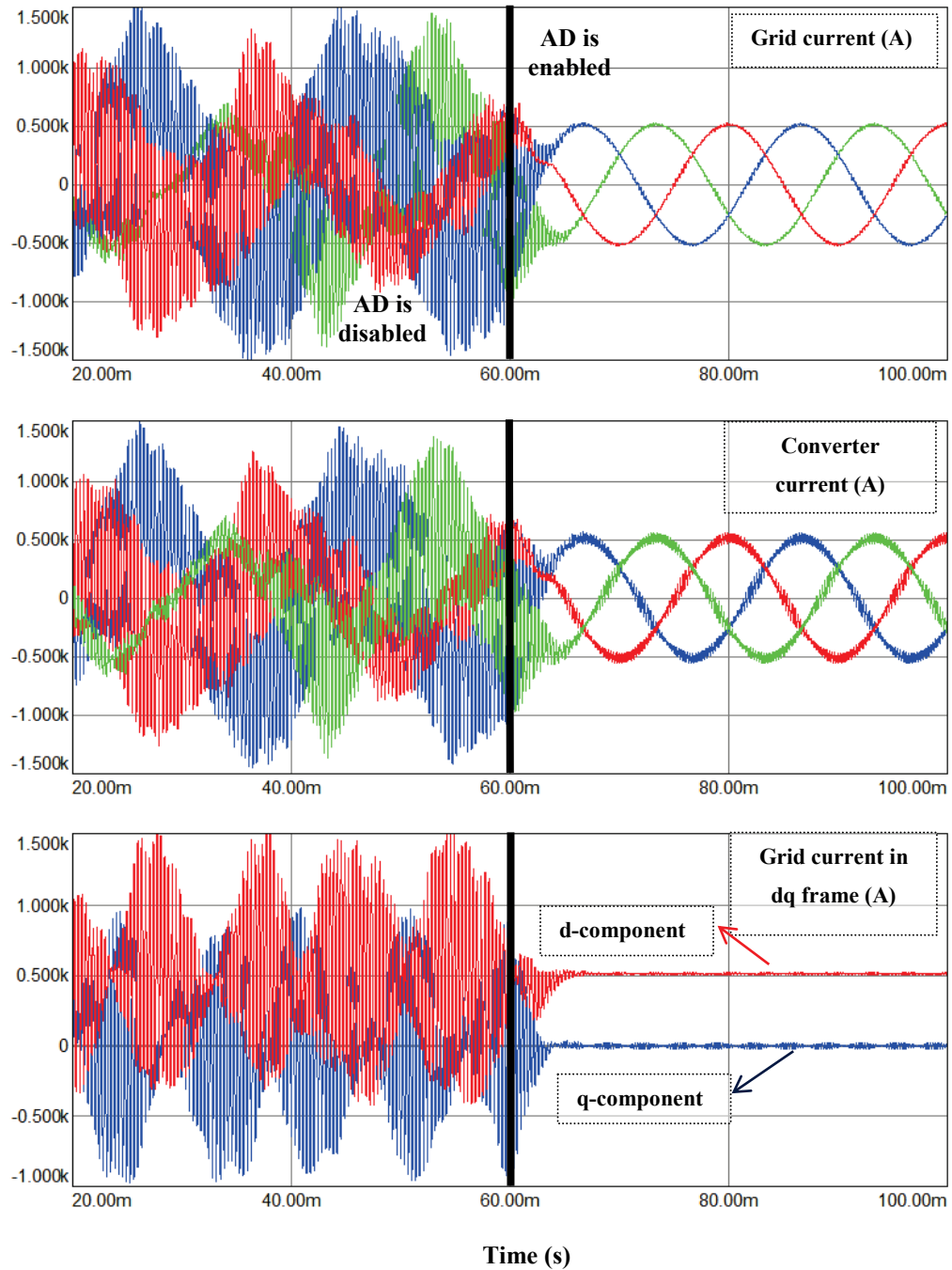


Figure 4.45 Outputs under GCF and enabled/disabled AD (high f_{res} , $C_f=30\mu\text{F}$).

Simulation was conducted in SIMPLORER[®] environment to confirm the effectiveness of the theoretical background. Simulation outputs were obtained in three different cases consisting of three distinct filter capacitor values to range the filter for GCF method. For each case a step change in commanded output current from 10% to 100% is used to display dynamic performance and to excite underdamped resonance if any present. The parameters in Table 4.3 were used throughout the simulations while corresponding filter capacitor values in Table 4.4 were selected to embody the distinct resonant frequency regions.

In Case-I, the effectiveness of GCF method with AD (using filter capacitor current feedback) is examined. For this purpose, three-phase grid-side current, three-phase converter-side current and grid-side current in dq -frame are revealed in Figure 4.43. According to Figure 4.43, it is evident that the system can be kept stable and performs well under both steady-state and transient-state.

In Case-II, same variable outputs are used to reveal the effectiveness of GCF method in high resonant frequency region when AD is deactivated. In this case filter capacitor value is decreased to 20 μF so that the resonant frequency can be shifted to higher values, i.e. 3.56 kHz ($\lambda=0.44$). Figure 4.44 displays that filtering performance of the LCL -filter is degraded for the high resonant frequency case and the benefits provided by LCL -filter have been limited severely.

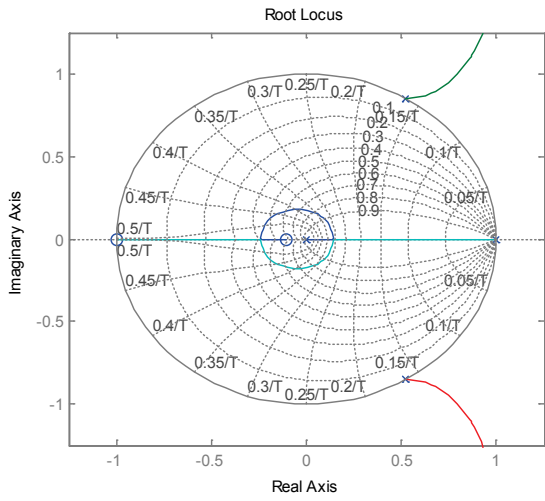
As a remark, for the low resonant frequency case, the overshoot at the transition from light load to full load is slightly higher than the high resonant frequency case.

In Case-III, resonant to sampling frequency ratio is decreased in order to display the sensitivity of the design against the resonant frequency variation in high resonant frequency range. For this purpose, C_f is adjusted to 30 μF yielding $f_{res}=2.91$ kHz and $\lambda=0.36$. As can be seen in Figure 4.45 until AD is enabled, GCF method without AD cannot provide a stable system with a damped resonant pole pair. Thus, it can be deduced that apart from the critical resonant frequency region addressed in [58], there is also a critical ratio λ (resonant frequency to sampling frequency ratio) in high resonant frequency region determining the effectiveness of AD for the systems

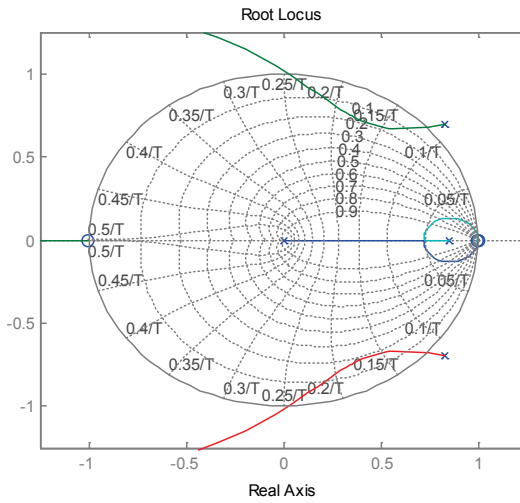
using GCF method. This critical ratio identification is inherent to this thesis work, so it can be deemed as a novel approach on commenting on the effectiveness of the AD methods in high resonant frequency regions. As evident in Figure 4.45, use of AD is essential for such λ ratios which are not high enough to succeed stable operation without AD. Since ratio $\lambda=0.44$ (Case-II) has achieved stable operation without AD whereas the ratio $\lambda=0.36$ (Case-III) has required AD to provide stable operation of the controllers. Overall, the analysis of the GCF in high resonant frequency region showed that as long as the maximum achievable control bandwidth is lower than the resonance frequency, the PWM converter with *LCL*-filters can be controlled with the voltage oriented PI-control with GCF in high resonant frequency region [61].

4.5.1.4. Stability Analysis of the Simulated System via MATLAB®

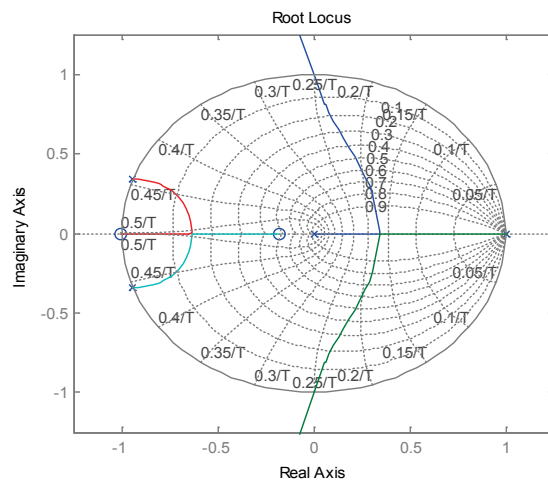
Figure 4.46 shows the movements of low-frequency poles as well as resonant pole pair under the studied cases. In Figure 4.46(a), displays the Case I when AD is disabled. As agreed in the root locus, resonant poles always track outside for any gain constant K_p . Nevertheless, by enabling AD in Case I, resonant poles track inside for proper K_d values and stability can be achieved as evident in Figure 4.46(b). However, too much K_d will make the poles track back outside the unit circle and stability will be lost. In Figure 4.46(c), system is stable despite the absence of AD since resonant poles are damped internally as agreed in Case II. However, the limiting point in this case is the gain constant K_p (PI-controller) and too much K_p would cause loss of stability as agreed in Figure 4.46(c). In Figure 4.46(d), resonant poles initially track away from the unit circle and stability cannot be achieved for any K_p value for Case III once AD is deactivated. The large magnitudes of resonant harmonics visible in Figure 4.45 validate the root locus output. Fortunately, with the introduction of AD, resonant poles are pushed inside the unit circle for proper choices of K_d as evident in Figure 4.46(e) and stability can be achieved, as also observed in Figure 4.45.



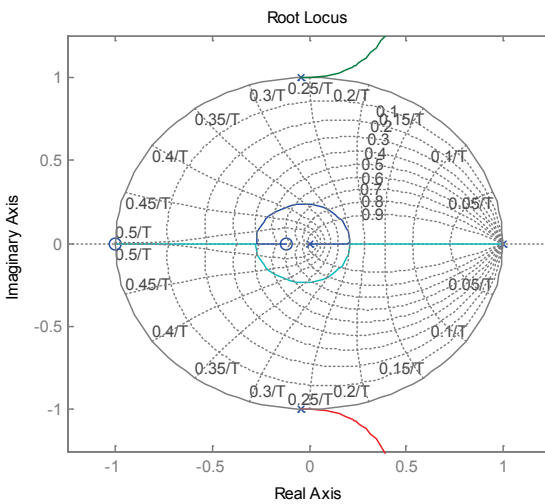
(a) Case I – AD disabled (variable: K_p).



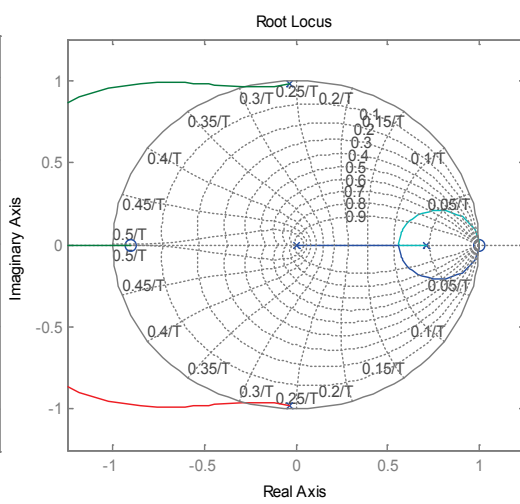
(b) Case I– AD enabled (variable: K_d).



(c) Case II– AD disabled (variable: K_p).



(d) Case III – AD disabled (variable: K_p).



(e) Case III– AD enabled (variable: K_d).

Figure 4.46 Various root-loci for Case I-II-III under GCF.

4.5.1.5. FFT Analysis of the Simulated System

In this subsection, the impact of AD on frequency spectrum will be examined regarding Case II and Case III by activating and deactivating AD, respectively.

Figure 4.47 depicts the FFT of grid-side current and converter-side current (Case II) as fraction of the fundamental component for each variable. Since the resonant pole pair is damped sufficiently (Figure 4.46(c)), employment of AD gives no positive contribution to suppress resonant harmonics any more as shown in Figure 4.47(a) and (b).

On the contrary, resonant poles are undamped in Case III when AD is disabled (Figure 4.46(d)). Thus, very large magnitudes of harmonics around resonant frequency are visible in the FFT of grid and converter currents in Figure 4.48(a). The distorted waveforms having undamped large magnitude resonant harmonics are also evident in Figure 4.45. With the introduction of AD, resonance poles are pushed inside (Figure 4.46(e)) and the large magnitude resonant harmonics are mitigated to very low percentages as depicted in Figure 4.48(b).

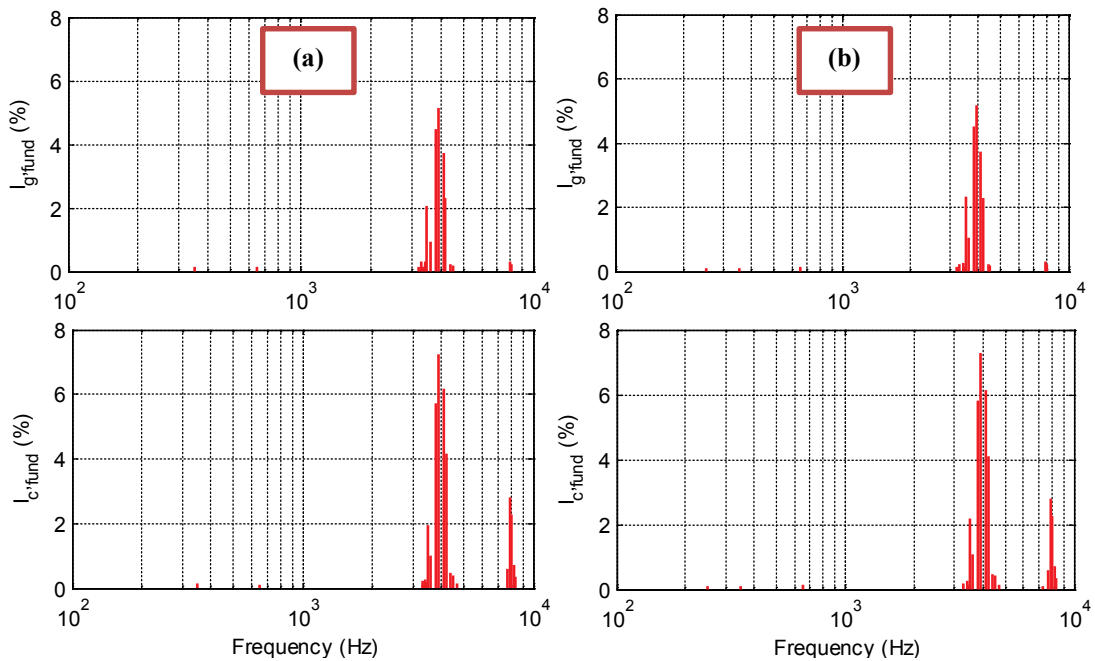


Figure 4.47 FFT of I_g and I_c ($C_f=20\mu\text{F}$) under GCF (a) w/o AD (b) with AD.

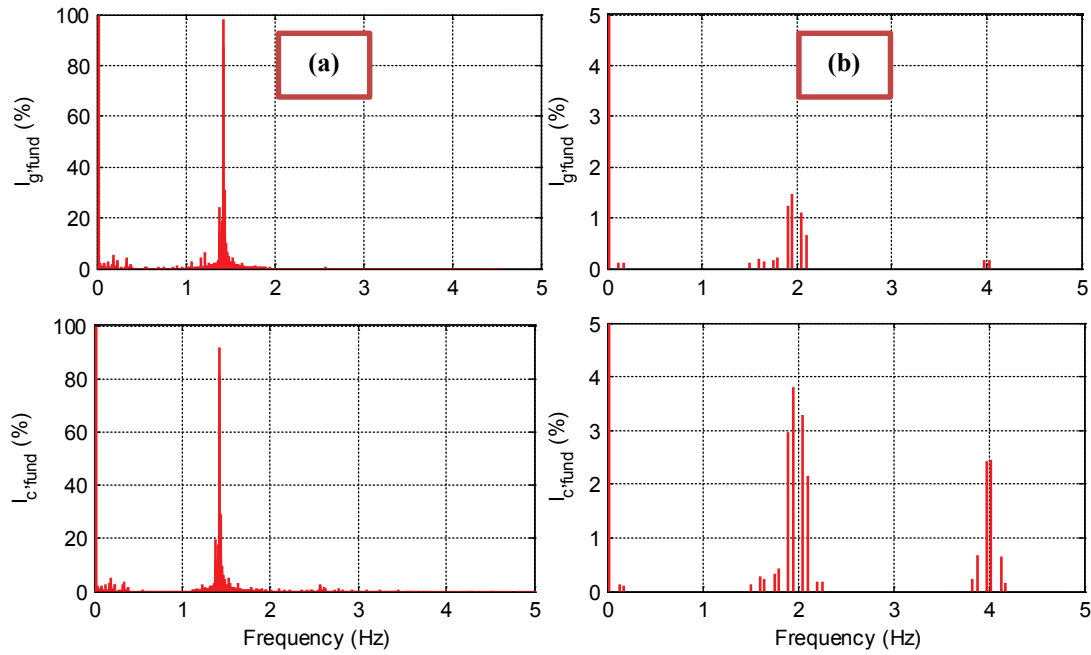


Figure 4.48 FFT of I_g and I_c ($C_f=30\mu\text{F}$) under GCF (a) w/o AD (b) with AD.

4.5.2. Simulation Results via SIMPLORER[®] for CCF Control

Sections 4.5.2.1, 4.5.2.2 and 4.5.2.3 illustrates Case I-CCF without AD in low resonant frequency region, Case II - CCF without AD in high resonant frequency region for $C_f=20\ \mu\text{F}$ and Case III- CCF with AD in high resonant frequency region for $C_f=20\ \mu\text{F}$, respectively. First of all, all of the related waveforms are provided in Figure 4.49, Figure 4.50 and Figure 4.51, then three cases are evaluated comparing these waveforms.

4.5.2.1. Case I-CCF without AD in Low-Resonant Frequency Region

Figure 4.49 depicts dynamic-state and steady-state grid current, converter current and grid current in dq -frame under specified combination.

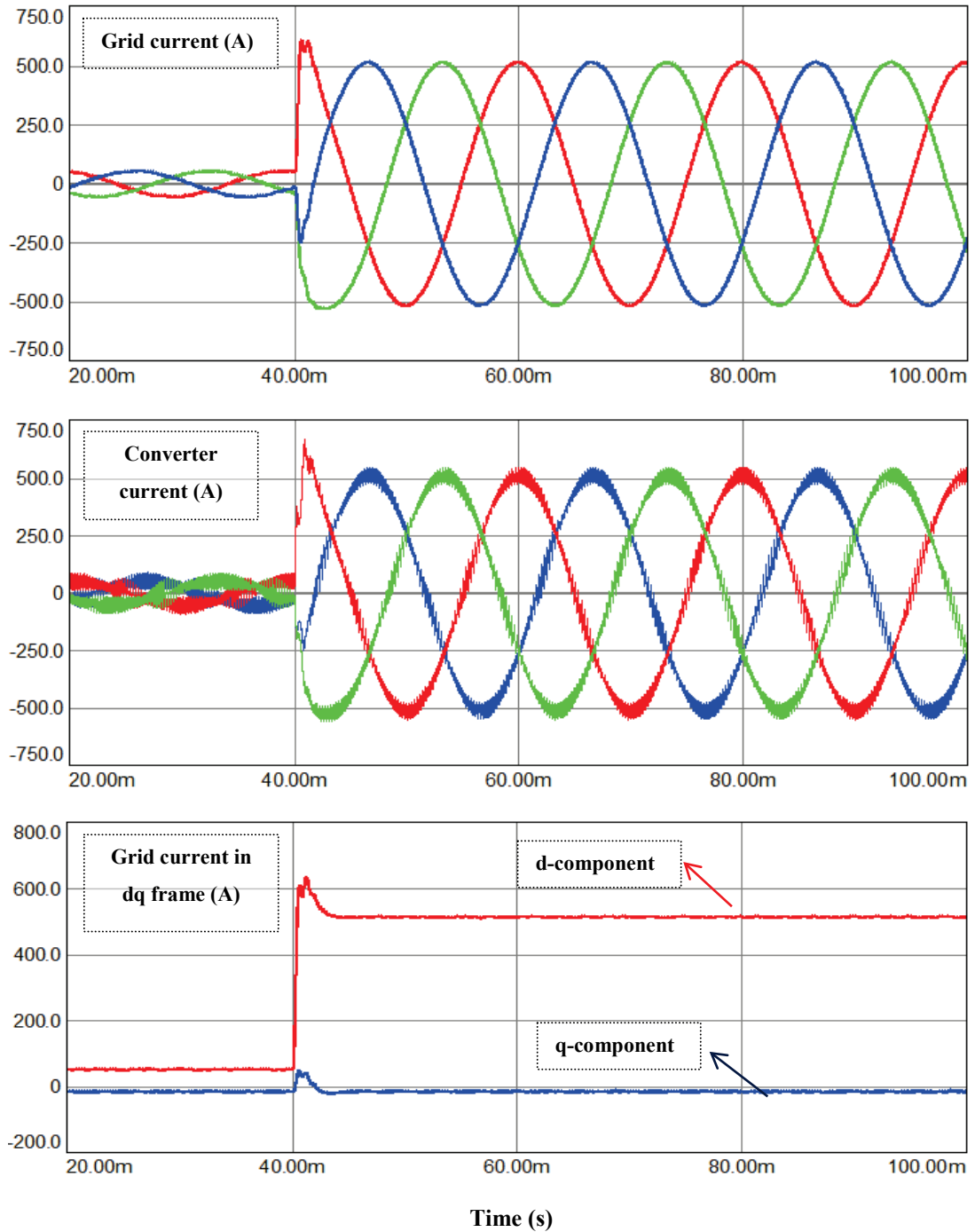


Figure 4.49 Simulation outputs under CCF without AD ($low f_{res}$).

4.5.2.2. Case II– CCF without AD in High-Resonant Frequency Region

Figure 4.50 shows dynamic-state and steady-state grid current, converter current and grid current in dq -frame under specified combination.

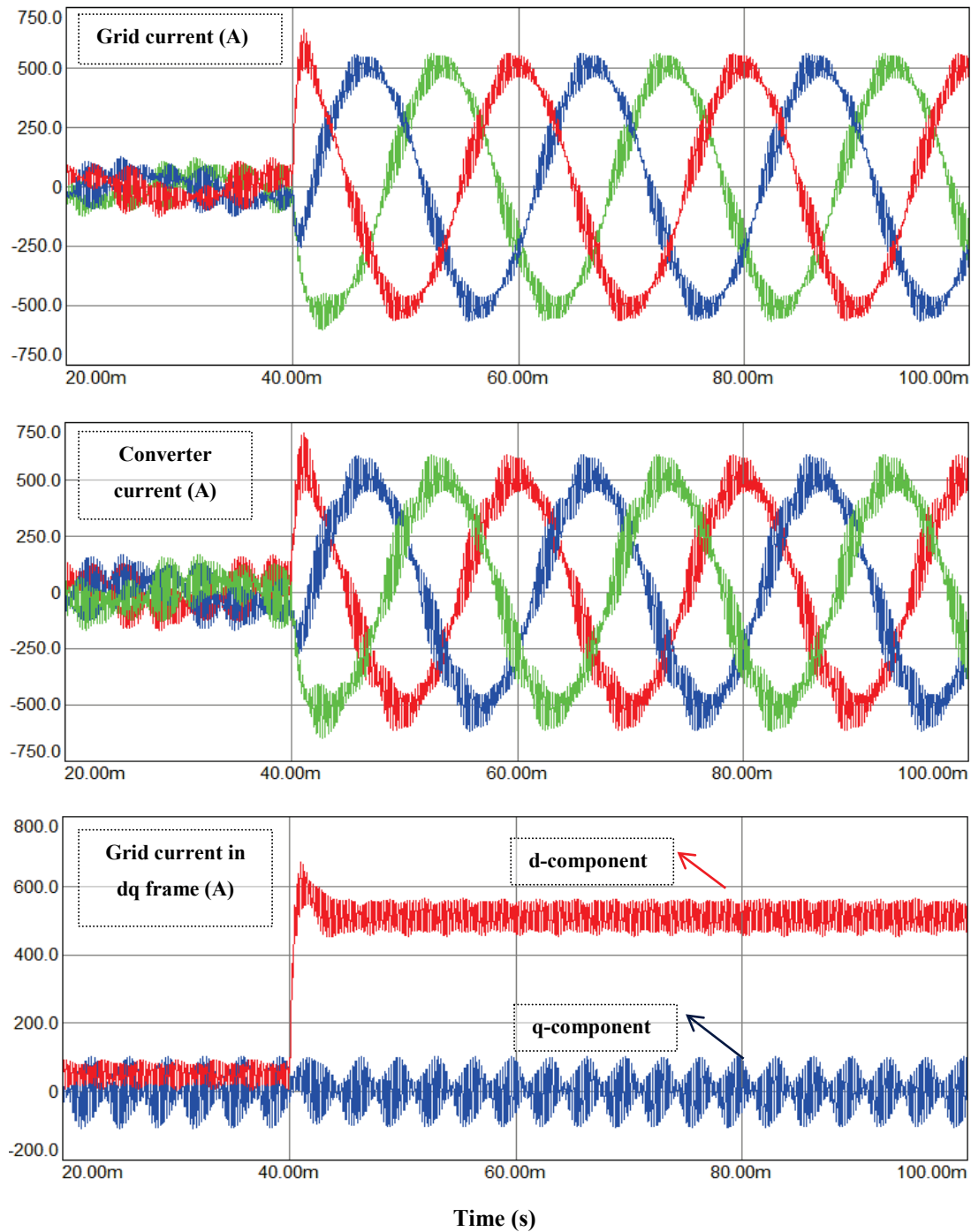


Figure 4.50 Simulation outputs under CCF without AD (high f_{res} , $C_f=20 \mu\text{F}$).

4.5.2.3. Case III– CCF with AD in High-Resonant Frequency Region

Figure 4.51 depicts steady-state grid current, converter current and grid current in dq -frame under specified combinations involving enabling and disabling AD.

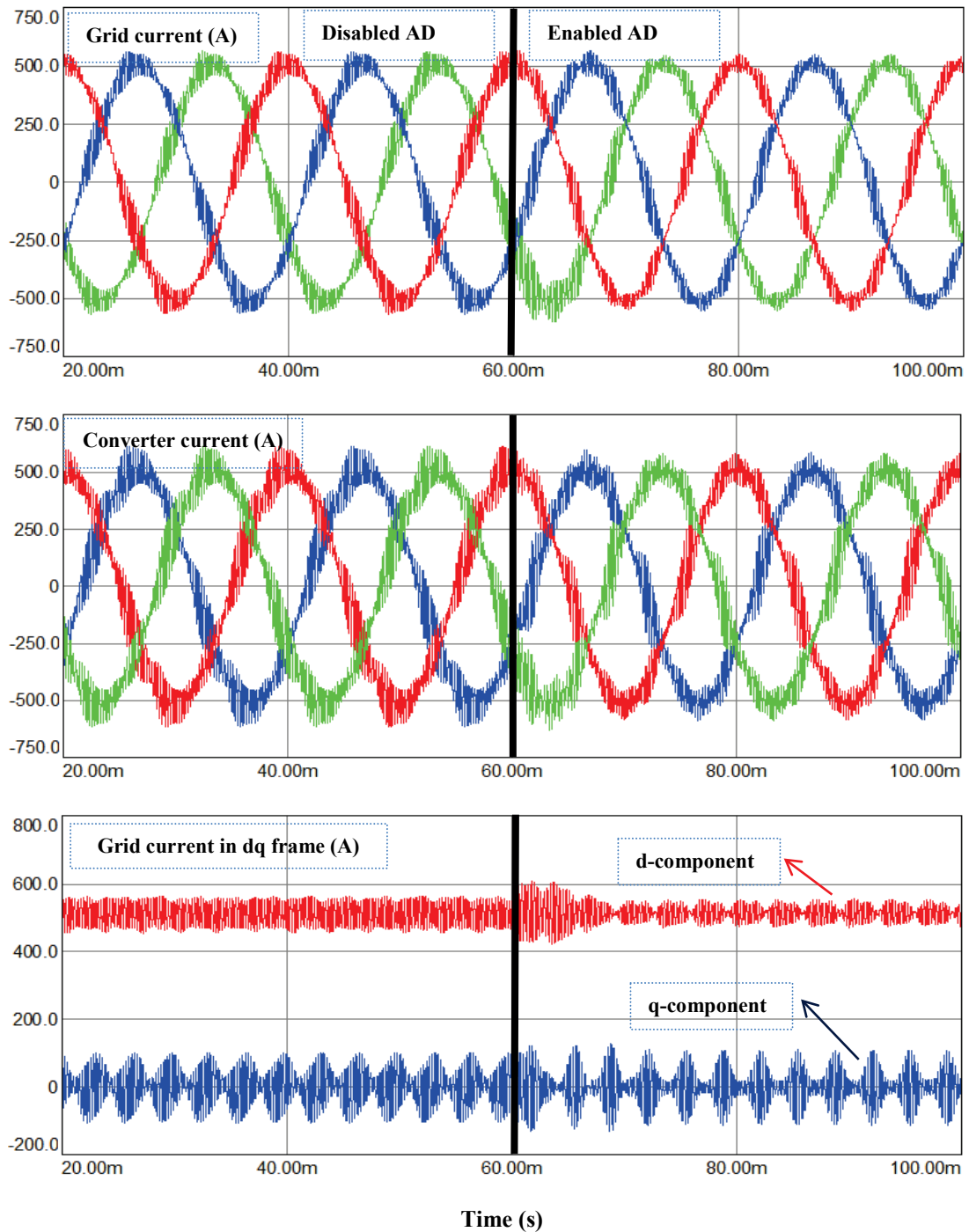


Figure 4.51 Simulation outputs under CCF with AD (high f_{res} , $C_f=20 \mu\text{F}$).

In Case-I, the effectiveness of CCF method with AD (using filter capacitor current feedback) is examined. For this purpose, three-phase grid-side current, three-phase converter-side current and grid-side current in dq -frame are revealed in Figure 4.49. It is evident in Figure 4.49 that the system is stable and performs well under both steady-state and transient-state. However, there exist resonant harmonics causing high frequency oscillations during the transition from light load to full load due to the underdamped closed-loop gain. Underdamped resonant pole pair is also evident in Figure 4.53(a). If AD is implemented in Case I, the high frequency oscillations would be blunted as demonstrated in Figure 4.52. The critically damped poles with the introduction of AD are obvious in Figure 4.53(b).

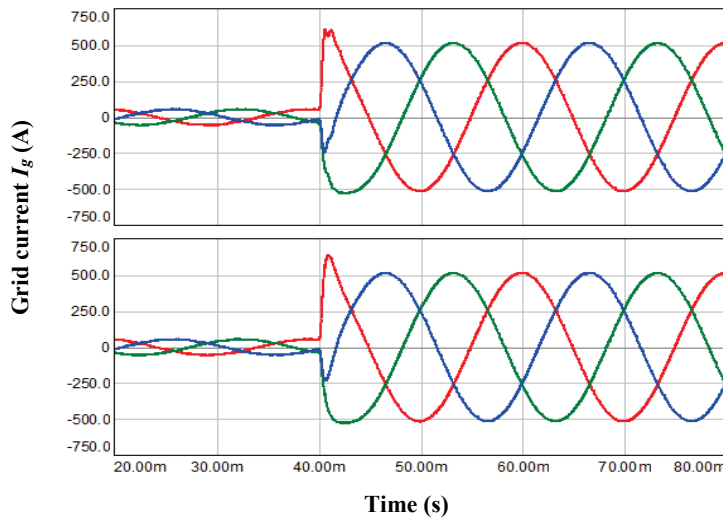


Figure 4.52 Dampening the resonance effect in CCF by AD (low f_{res}).

In Case-II, same variable outputs are used to disclose the effectiveness of CCF method in high resonant frequency region when AD is deactivated. Figure 4.50 displays that filtering performance of the LCL -filter is degraded for the high resonant frequency region similar to GCF case. In fact, the LCL -filter behaves like a simple L -filter as the limiting factor is the movement of the low frequency poles in the unit circle (Figure 4.53(c)). Thus, very little benefit is acquired by LCL -filter in this high resonant frequency region.

In Case-III, impact of AD implementation to Case II is examined. As evident in Figure 4.51, use of AD is beneficial on mitigation of resonant harmonic magnitudes. The mitigation and elimination of individual harmonics are also depicted in FFT analysis of grid-side and converter-side current in Figure 4.54.

Overall, the related statements in Table 4.2 are further proven with the simulation outputs shown in Case I, II and III. In the forthcoming sections, internal causes of these phenomena are shown explicitly in terms of root loci and FFT analysis of the currents.

4.5.2.4. Stability Analysis of the Simulated System via MATLAB®

Figure 4.53 displays the movements of low-frequency poles and resonant pole pair under the studied cases in CCF case just as done in GCF case. In Figure 4.53(a), it is clear that resonant poles are initially damped without any additional damping. In this case, gain constant K_p is varied and it has been found that rise in K_p makes the poles initially track inside the unit circle until too much K_p is applied, then stability is lost for excessive gains. Figure 4.53(b) shows the effect of AD for fixed values of K_p , yielding a better damping of resonant poles with the increase of damping gain K_d . However, excessive K_d values will make the poles track back outside the unit circle and stability will be lost.

In Figure 4.53(c), system is stable despite the absence of AD since resonant poles are damped internally as agreed in the figure. Yet, the limiting point in this case is the gain constant of PI-controllers and too much K_p would cause loss of stability as depicted in Figure 4.53(c). In Case III with the activation of AD, damping of resonant poles is even increased for proper choice of K_d as evident both in Figure 4.51 and Figure 4.53(d). Again, too much K_d pushes the poles outside the unit circle and stability will be lost.

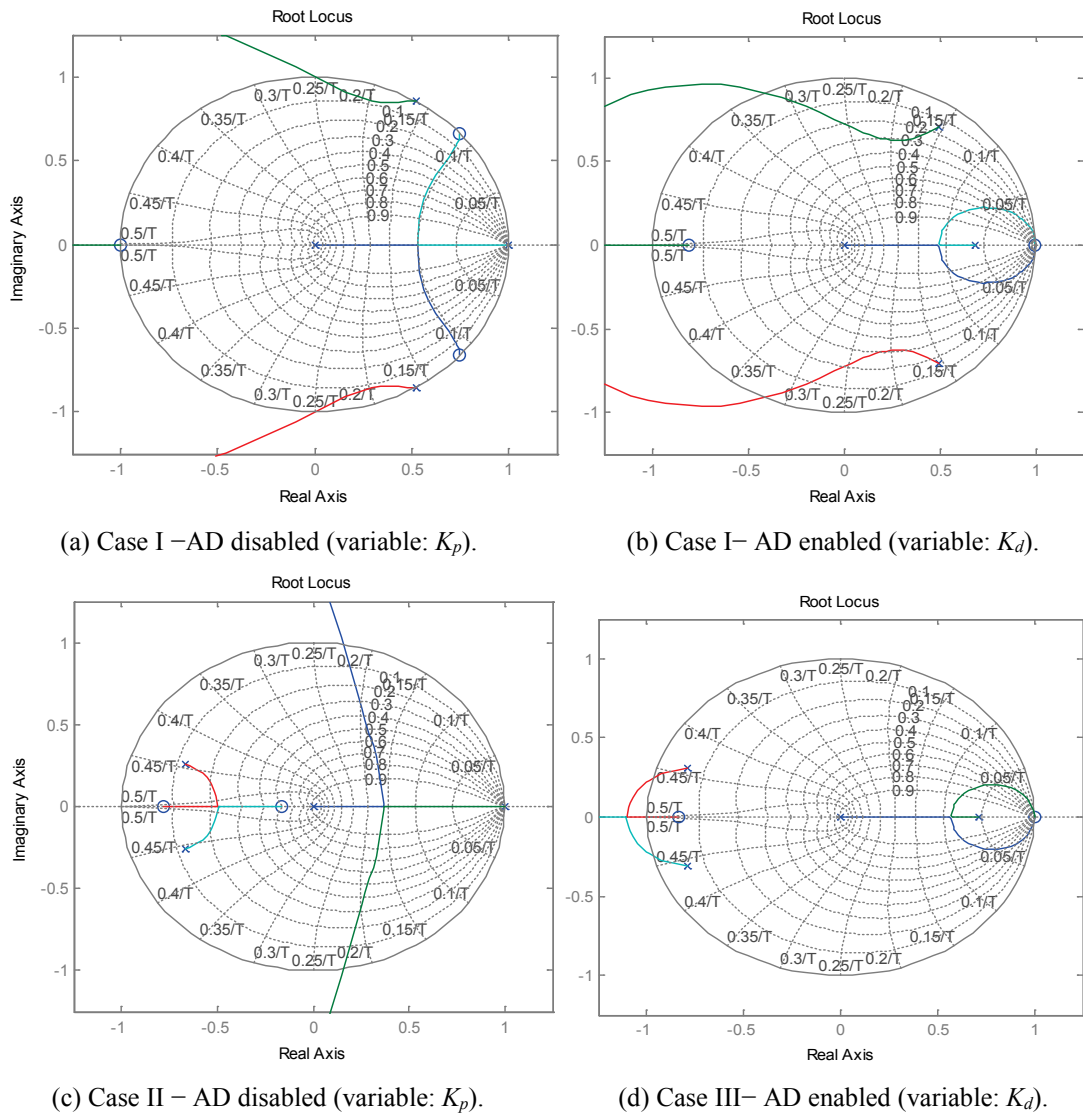


Figure 4.53 Various root-loci for Case I-II-III under CCF.

4.5.2.5. FFT Analysis of the Simulated System

In this subsection, the impact of AD on frequency spectrum will be examined regarding Case III by enabling and disabling AD in the high resonant frequency region with respect to the revealed current waveforms in Figure 4.51. Figure 4.54 depicts FFT of these grid-side current and converter-side current as fraction of the fundamental component for each variable. Since the resonant pole pair is damped insufficiently in the case without AD in Figure 4.51, employment of AD provides a

significant contribution to further suppress resonant harmonics as can be compared in Figure 4.54 (a) and (b). The mitigation of the harmonics is also evident in Figure 4.51.

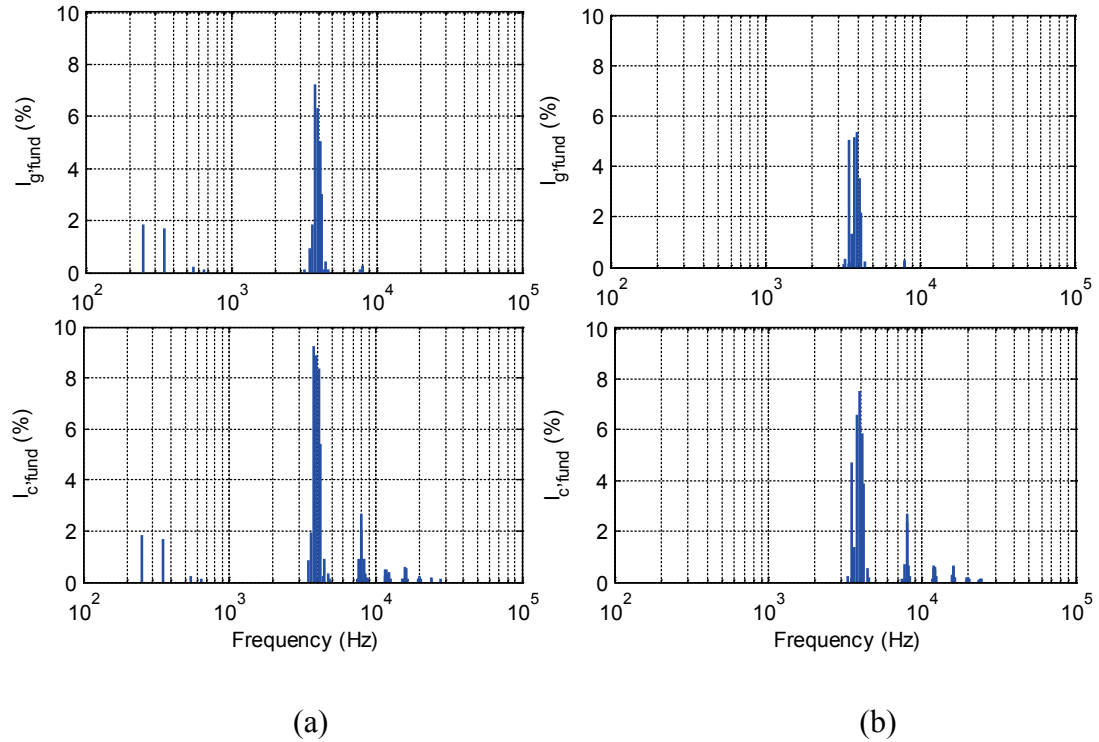


Figure 4.54 I_g harmonics (%) with CCF method for $C_f=20\mu\text{F}$ (a) I_g and I_c (b) I_g and I_c (AD).

4.5.3. Dynamic and Resonance Damping Performance Comparison between GCF and CCF

As evident in (4.30) and (4.33) that optimum damping factor is adjusted by means of K_d in GCF method whereas it is adjusted by K_p in CCF method provided that the filter elements are kept constant. Therefore, K_p has an extra duty in CCF method except for regulation of dynamic performance. The optimum values of PI parameters are calculated using (4.18), providing maximum phase margin around the critical damping factor $\zeta=0.707$. Nevertheless, Figure 4.55 reveals that calculated K_p value provides insufficient closed-loop damping factor leading to underdamped resonant

pole pair. On the contrary, calculated K_p has no impact on resonance damping in GCF method and necessary K_d value is calculated by means of (4.30) to provide sufficient closed-loop damping factor. Thus, the resonant pole pair in Figure 4.55 seems perfectly damped under GCF method.

In the light of abovementioned facts, GCF and CCF cannot be compared directly. There are two possible ways providing a fair comparison between these two techniques [58][70]. The first one is keeping the same K_p value found by (4.18) to provide the same controller bandwidth in return the same dynamic response (same dynamics, poorer resonance damping in CCF). The second approach is equating the resonance damping in both methods by adjusting the same damping factor. For this purpose, K_p value is increased in CCF method in order to yield the same damping factor achieved in GCF method. Fine-tuning of this value can be managed by means of iterative analysis in pole-zero maps as in Figure 4.55. Thus, second approach guarantees the same resonance damping for both methods, whereas, the bandwidth is reduced in CCF case owing to the increase in K_p value beyond its optimal value.

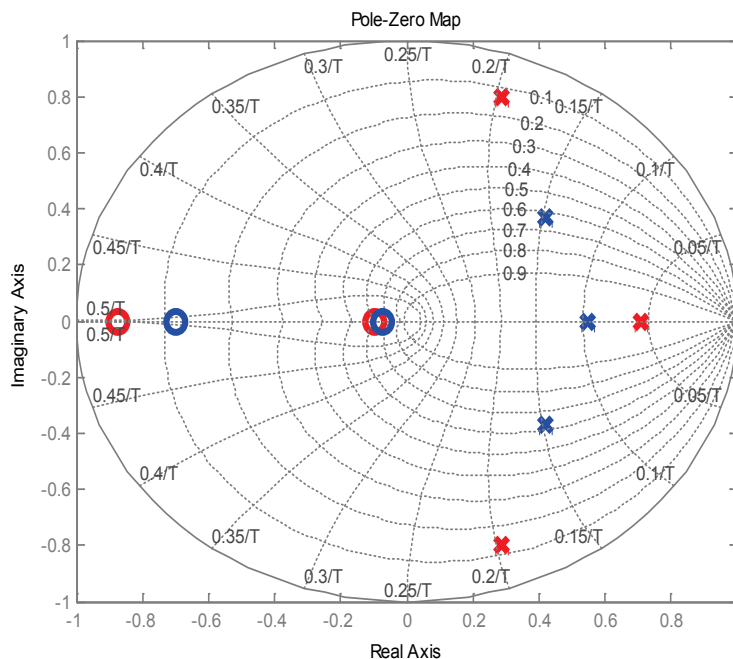


Figure 4.55 Pole locations (Red CCF, blue GCF).

The proposed comparison approaches are also implemented in simulation environment. For this purpose, the system parameters provided in Table 4.3 are used. Figure 4.56 and Figure 4.57 reveals the fact that for insufficient damping factors determined by K_d values (GCF case), dynamic response contains high frequency oscillations due to the excited resonance by underdamped resonant peak in the magnitude response.

As of this point abovementioned two fair comparison cases will be provided as follows:

Gain Option 1 – Same System Bandwidth

The same bandwidth is obtained with the proportional gain and resonance time constant from (4.18):

$$K_{p,CCF} = K_{p,GCF} = 1.07 \qquad T_{i,CCF} = T_{i,GCF} = 1.125\text{ms}$$

The reduced resonance damping of this system can be seen in Figure 4.55, where the closed-loop poles are closer to the unit circle stability boundary. The transient results show some amount of resonance in Figure 4.58 compared to case in Figure 4.57.

Gain Option 2 – Same Resonance Damping

The same resonant pole damping can be obtained by using a root locus to place the resonant poles. This gives a gain of:

$$K_{p,CCF} = 1.51$$

The extra gain constant required to superpose the pole damping characteristics leads to a larger current overshoot as can be seen in the transient results of Figure 4.59.

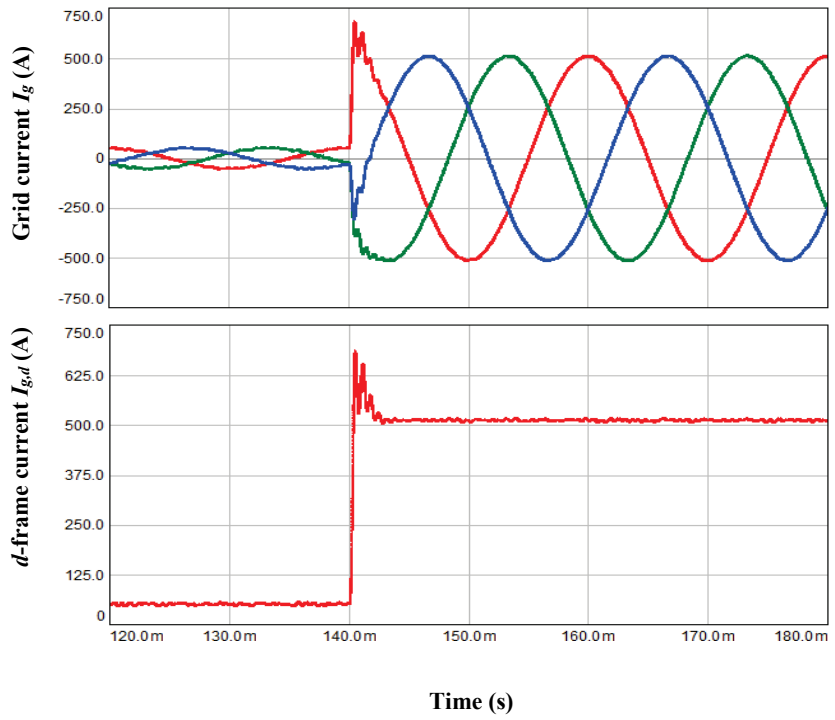


Figure 4.56 Step response of I_g under GCF: $K_p=1.07$ ($\zeta=0.3$).

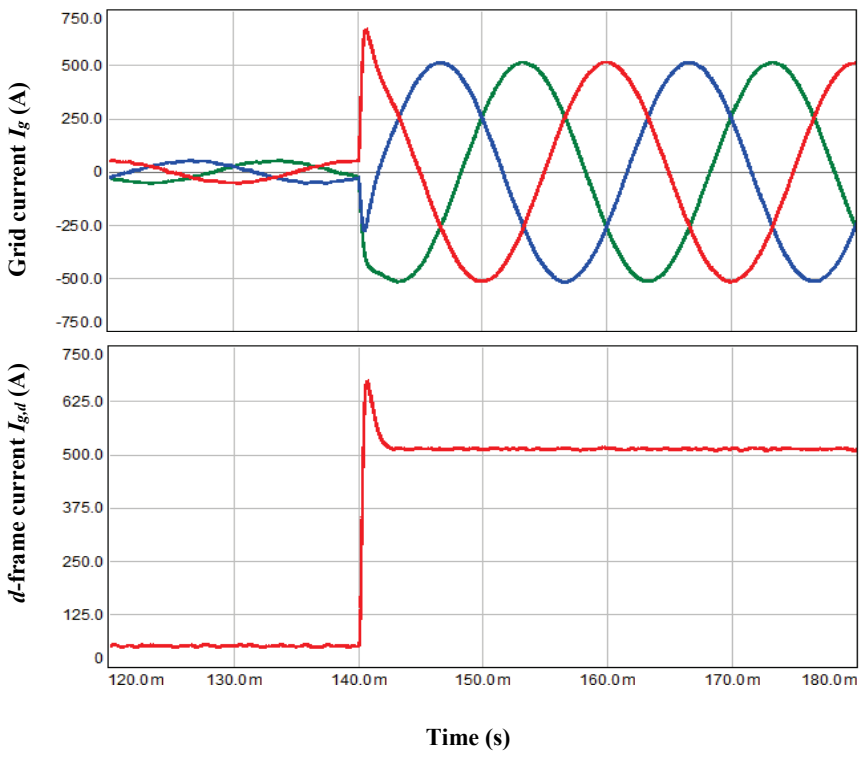


Figure 4.57 Step response of I_g under GCF: $K_p=1.07$ ($\zeta=0.707$).

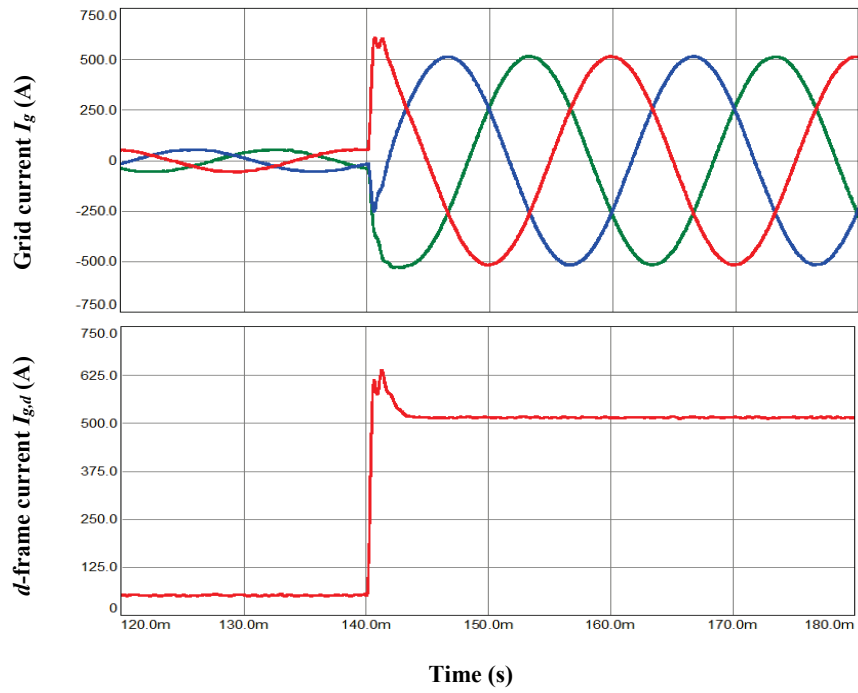


Figure 4.58 Step response of I_g under CCF: $K_p=1.07$ (Matched bandwidth with GCF).

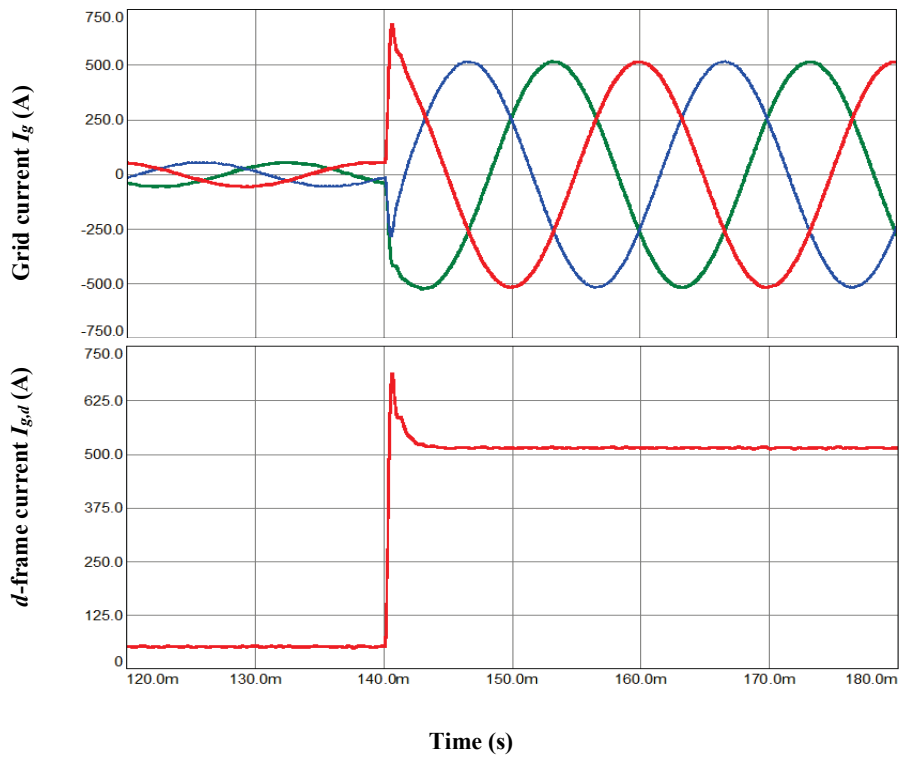


Figure 4.59 Step resp. of I_g under CCF: $K_p=1.51$ (Matched res. damp. with GCF).

As evident from the transient results, there is a tradeoff between transient performance (overshoot, rise time, settling time) and resonance damping. Further advantages and disadvantages of CCF and GCF methods can be summarized as follows:

Firstly, CCF does not directly regulate the grid current. In order to control real and reactive power flow (and power factor) the current flowing into the grid must be controlled. Thus, CCF will require current reference compensation, introducing more complexity.

Secondly, GCF provides the fastest transient performance, best resonance damping and directly regulates the grid current without steady state error. However the best placement of current measurement transducers is in both inductor current paths, to provide overcurrent protection.

Thirdly, if the system design is limited to a single current transducer then CCF will provide a degree of active damping, with a tradeoff of transient performance. Further damping can be obtained by using AD with the capacitor current. However, this will further reduce dynamic performance [70]. The summary of this comparative study is provided in Table 4.5.

Table 4.5. Differences between GCF and CCF control.

Type	Stable	I_g traction	Damping	Transient	Sensors
GCF	No	N/A	N/A	N/A	1
GCF with AD	Yes	Yes	Good	Good	2
CCF	Yes	No	Poor	Good	1
CCF with AD	Yes	No	Good	Poor	2

4.6. Summary and Conclusions

With the recent developments in wind energy area, *LCL*-filters have gained much importance due their superiority in size, cost and attenuation capability, leading to a substantial increase in publications in this area. This chapter can be deemed as a novel theoretical study of *LCL*-filters compiling the extended but disoriented information in the literature; meanwhile proposing novel findings on *LCL*-filter control and stability issues and providing comparative studies between widely used techniques. First of all, the improvements brought by *LCL*-filters in place of conventional *L*-filters have been discussed in quite detail and the reasons why *LCL*-filters are more suited for high-power conversion systems widely employed in wind farms of over hundreds of kilowatts have been clarified. Secondly, control overview of *LCL*-filters has been mentioned thoroughly. With the use of control overview, stability of *LCL*-filters has been discussed by merging the methodology in the literature with the novel findings within the scope of this dissertation. Third, the impact of AD (both inherent and AD using capacitor current) has been well elaborated by means of thorough case studies conducted on SIMPLORER[®] and MATLAB[®]. Thus, a unique, extensive, well-detailed and top to bottom study has been unveiled enabling one to be able to comment on the steady-state and transient-state behavior of the *LCL*-filters according to the location of the resonant frequency in the frequency spectrum. Assessment of the steady-state and transient performance of the *LCL*-filter with respect to the location of the resonant frequency is one of the merits of this dissertation. Important deductions made concerning *LCL*-filter control and stability can be summarized as below:

- i. The grid and converter-side inductances should be equal so as to maximize the filtering capability of inductors. In other words, it may inevitably increase the cost and volume of passive filtering elements. On the other hand, small converter-side inductance directly translates into significant current ripples on the output of the inverter. This may result in considerable losses in the inductor and cause serious overheating.

- ii. For dampening the resonance, employing PD provides a simple and effective solution while introducing damping losses that may inevitably lead to higher losses exceeding acceptable thresholds (i.e. 1% of the rated power). Also it compromises the attenuation of high frequency harmonics. On the other hand employing AD techniques provides stability with no additional losses; whereas realization of these schemes requires more sensors, complex state observes and so on. Plus, the effectiveness of these techniques mostly depends upon the accuracy of filter parameters. Consequently, existing current control schemes with either PD or AD included for *LCL*-filtered three-phase VSCs are found to be incapable of achieving high efficiency and simplicity simultaneously, despite an improvement in stability.
- iii. This study has comprehensively explored the inherent damping (ID) characteristic of an *LCL*-filter, which so far has not yet been discussed much in the literature. It specifically shows that the current control loop has an inherent damping term embedded when the converter current is employed for current feedback (CCF). This inherent damping term can be used for optimal damping of the *LCL* resonance without demanding additional PD or AD, only if the filter components are designed suitably. Such inherent damping unfortunately does not exist when the grid current is measured for feedback control (GCF); hence leading to the general conclusion that CCF is more stable than GCF as long as additional damping is not used under each method.
- iv. The immediate influence brought by deviation of passive filter element values caused by aging, temperature variation, and system uncertainty is an elevated difficulty in achieving optimum damping, especially if only the inherent damping characteristic of CCF is relied on. To compensate for this, detailed examination for tuning the damping factor is proposed, which would preserve the advantage of using only CCF (without damping), but at the expense of a more compromised transient response compared to GCF case.

Simulation and experimental results for validating those findings have been provided at the end of the chapter.

- v. CCF does not directly regulate the grid current. In order to control real and reactive power flow (and power factor) the current flowing into the grid must be controlled. Thus, CCF will require current reference compensation, introducing more complexity. If GCF technique is utilized, the output current of the converter cannot be controlled directly, meaning that it is impossible to provide instantaneous over current protection to the PWM converter, while this feature is quite essential in practical implementation. Nevertheless, in practical applications sensors are placed on both sides irrespective of current feedback variable since power factor control and over current protection are equally important aspects of the system.
- vi. In the light of extensive analysis in case studies, GCF with AD has provided faster transient performance compared to CCF without damping case without compromising resonance damping. On the other hand, CCF without AD case has provided a degree of resonance damping, with a tradeoff of transient performance. Further damping has been obtained by using AD with the capacitor current. However, this has further reduced dynamic performance of CCF. It should be noted that the plant response is dynamically slow under GCF without AD case owing to very small control bandwidth caused by the sharp resonance peak, indicating that the overall system is nearly impossible to be closed-loop stable (internal losses are generally insufficient to blunt the resonance peak). Improvement to it can only be introduced by additional damping to dampen the infinite gain at the resonant frequency. Table 4.5 summarizes above conclusions.
- vii. It has been found that additional filtering improvement of *LCL*-filter is compromised as the resonant frequency moves to high resonant frequency region. This is due to the fact that *LCL*-filter behaves very similar to a single *L*-filter as demonstrated by the simulation outputs and root loci. Thus, the

benefits introduced by *LCL*-filter are almost nullified if the resonant frequency passes beyond critical resonant frequency.

- viii. Apart from the critical resonant frequency region, there is also a critical ratio λ (resonant frequency to sampling frequency ratio) in high resonant frequency region determining the effectiveness of AD for the systems using GCF method. This critical ratio identification is inherent to this thesis work, so it can be deemed as a novel approach on commenting on the effectiveness of the AD methods in high resonant frequency regions. As long as the maximum achievable control bandwidth is lower than the resonance frequency, the PWM converter with *LCL*-filters can be controlled with the voltage oriented PI-control using GCF (without AD) in high resonant frequency region.

In the light of above deductions, GCF with AD method seems superior over all cases as depicted in Table 4.5. Although CCF case is stable without additional damping, it cannot be relied on practical applications such as high power grid-side VSC of WTs. Thus, CCF provides a simpler solution only in theory. Using same number of sensors but providing better transient response as well as grid current traction, GCF with AD will be the preferred method for the converter design within the scope of this dissertation. However, this chapter does not involve the comparison of CCF and GCF methods under PD technique. Since PD technique turns *LCL*-filter into a second-order filter which does not suffer from resonance, stability and control analyses covered in this chapter to eliminate the impact of resonance peak do not apply for PD case. Nonetheless, the impact of CCF and GCF methods under PD will be mentioned in the next chapter.

To conclude, control and stability analysis of *LCL*-filter have been provided in quite detail in this chapter. In the next chapter, the comprehensive studies conducted in this chapter are directly used to propose a novel *LCL*-filter design procedure and a detailed study considering the fine tuning of the controllers are provided.

CHAPTER 5

***LCL*-FILTER DESIGN METHODOLOGY FOR GRID CONNECTED VOLTAGE SOURCE CONVERTERS**

Each chapter of this dissertation presents important topics within the scope of the main focus. The output of a chapter is the input for the latter, like individual links of a chain. Thus, each chapter represents an individual topic while each of them is combined to each other. In this manner, provided information in one chapter is used in the next one, and every deduction is an input for the following step. In this way, they form a chain that is firmly combined and yielding the desired product via step by step approach. In this regard, Chapter 1 and 2 has described the entire system and pointed out the focus of this study. Chapter 3 has provided a market survey and yielded valuable information about determination of the switching frequency constraint together with the favored PWM method for the design of favored converter types. In short, it has presented the converter design procedure step by step. After that the design of grid interface had to be provided. As mentioned several times, *LCL*-type filter is used for the grid interface. For this purpose, Chapter 4 has analyzed the advantages and disadvantages of this type of filters. Besides, it has discussed the control methods to stabilize the system (utilizing *LCL*-filter) and pointed out the favored method supported with profound analysis. As of this point, Chapter 5 will use the findings in the former chapters to provide a proper *LCL*-filter design methodology.

As presented in the conclusion part of the previous chapter, GCF control with AD has found to be the best technique in terms of steady-state and transient-state outcomes. Consequently, having determined the topology, PWM technique, switching frequency constraint and the favored current control technique, *LCL*-filter

is set to be designed. However, the approach in this chapter does not only rely on revealing the favored methods. On the contrary, all possible methods (control, damping, etc.) are considered throughout the analysis. Since, for other types of applications, the preferred methods may differ and this situation constrains the feasibility of this work. For this reason, one of the main targets of this study is to yield all possible methods with their advantages and disadvantages and to select the best combination conforming to requirements of the specified application for this work. Before proceeding to filter design methodology, some of the important conclusions made in the former chapters are summarized in the next section.

5.1. Overview of Control Methods and Damping Techniques

Controlling the resonance phenomenon is the most difficult part of the *LCL*-filter design procedure. Therefore, *LCL*-filter design is an iterative process and minimizing the iterations should be the primary objective. The complexity of the *LCL*-filter design procedure relies on the preferred resonance damping technique. For instance, the location of the resonant frequency is very crucial on achieving active damping (AD) and for certain regions in the frequency band, AD become useless to damp resonance. Therefore, any change in the initially determined resonant frequency due to variation of the *LCL*-filter parameters over time and the existence of stray inductance and capacitance in the system are very likely to cause the loss of stability in AD methods. Apart from the location of the resonant frequency, preferred current feedback variable amends the effectiveness of the AD method. The performance examination of the AD methods under converter-current feedback (CCF) and for grid-current feedback (GCF) regarding each of low and high resonant frequency regions is well-explained in the previous chapter.

On the other hand, in passive damping method (PD), the stability of the system is not affected from the variation of resonant frequency since there is always nonzero impedance at the filter capacitor branch blunting the resonance. In the literature, the proposed *LCL*-filter design methods employing PD provide a simple solution to the resonance damping problem. Liserre *et al.* [54] state that the only constraint for the

resonant frequency is to reside in the range between ten times the grid frequency and one-half of the switching frequency to avoid resonance problems in the lower and upper parts of the harmonic spectrum. Additionally, Sul *et al.* clarify the situation in [60] such that if the resonant peak in the magnitude response is underdamped, resonance is very likely to be excited by the PWM switching in a lossless *LCL*-filter if any small extent of harmonics exists around the resonant frequency even if all the resonant harmonics are eliminated. Thus, either setting the resonant frequency below half of the switching frequency to isolate the resonant harmonics from the PWM switching harmonics or blunting the response peak with damping resistors is proposed to avoid the resonance excitation in [60]. However, PD technique turns *LCL*-filter into a second-order filter which does not suffer from resonance. Thus, stability and control analyses covered in Chapter 4 to eliminate the impact of resonance peak do not apply for PD case.

In contrast, if the damping is achieved in the control loop by changing the voltage reference vector (AD and inherent damping), the design algorithm becomes more complex. Because, designed filter parameters must guarantee the controllability of the system due to the presence of the undamped resonant frequency.

Inherent damping feature of the converter-side feedback can be regarded as the equivalent of grid-side feedback employing AD with filter capacitor current with proportional damping constant (K_d) as unity. Thus, either method requires special emphasis on damping the oscillations caused by the large magnitude excursion above unity gain at the resonant frequency and on reserving sufficient phase margin (PM) for the closed-loop control.

Consequently, control technique (CCF or GCF) and the damping technique (AD, ID, PD) should be determined beforehand and regarded as input to the *LCL*-filter design procedure. Since different *LCL* parameters are yielded depending on the opted current feedback variable and the damping technique.

This chapter consists of two main parts. In the first part, conventional *LCL*-filter design methodology widely used in the literature is provided. In the second part, a

novel *LCL*-filter design algorithm inherent to this study is addressed. Conventional design case involves the comparison between CCF and GCF control under PD (as assured in the end of 4th chapter). Additionally, controller gain/AD gain adjustment hints (Section 4.4.5) are used for the fine tuning of the filter parameters that the novel *LCL*-filter design algorithm has yielded.

5.2. Conventional *LCL*-Filter Design Algorithm

The conventional *LCL*-filter design procedure provided in the literature is straightforward. Controllability and stability concerns are not included in the design procedure. Instead, the designated filter components checked in the last step whether they are confined to the interval between ten times of the grid frequency and half of the switching frequency. The underlying reason of confining the resonant frequency in that interval is as follows. The closed-loop system has to have adequate phase margin so that PI current controllers function properly and the resonant should be far away from the switching frequency in order to maximize high order harmonic attenuation. Additionally, the achieved closed-loop damping factor is tested at the very end in order not to excite resonance during the step changes [57].

The conventional *LCL*-filter design is presented with a step-by-step procedure in Figure 5.1. The input variables of the algorithm are the rated power of the grid connected VSC (S_n or P_n), frequency of the grid network (f_g), grid-voltage (v_g – the low-side voltage of the grid interface transformer), DC-link voltage of the modeled energy source (V_{DC}), and power factor requirement on PCC (PF –determines the boundary of filter capacitance). It should be noted that f_{sw} input is provided through the analysis done in Chapter 3.

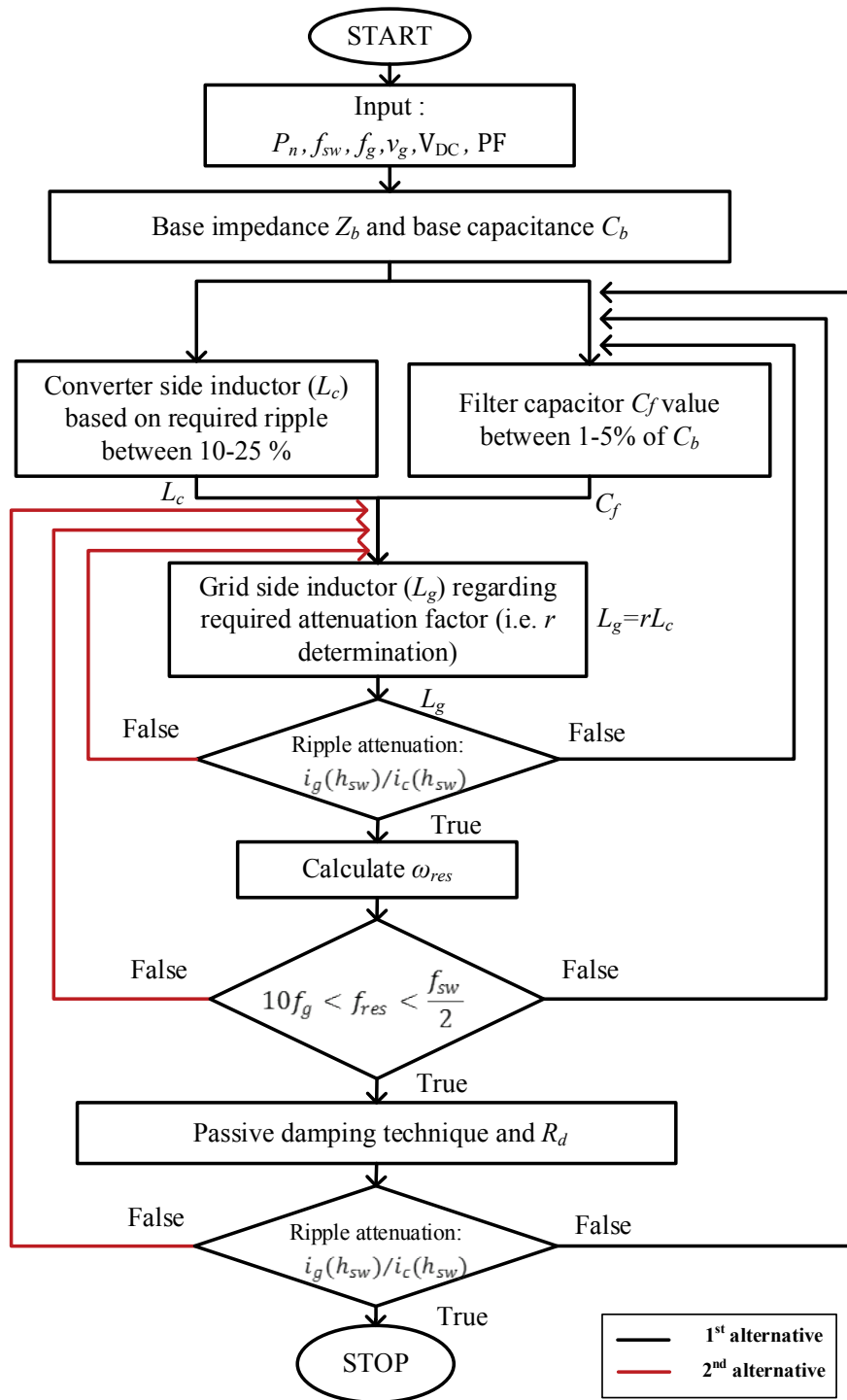


Figure 5.1 LCL-filter design algorithm for passively damped resonance.

Step-1: Base impedance Z_b and the base capacitance C_b are defined by (5.1) and (5.2) in order to represent the filter components as percentages of the base values (i.e. per unit (p.u.) approach).

$$Z_b = \frac{v_g^2}{P_n} \quad (5.1)$$

$$C_b = \frac{1}{Z_b \omega_g} \quad (5.2)$$

where $\omega_g = 2\pi f_g$.

Step-2a: The reactive power absorption (x) by the filter capacitance C_f is determined regarding the power level and the power factor target of the design. C_f is generally confined into 1-5% of C_b to deliver a PF within 0.95-1 [54]:

$$\begin{aligned} C_f &= x C_b \\ 0.01 &\leq x \leq 0.05 \end{aligned} \quad (5.3)$$

Apart from PF deviation, $x > 5\%$ leads to more reactive power flow on the filter capacitor and causes higher current demands from the DC-link. In exchange, higher filter and semiconductor losses will be yielded.

Step-2b: Design rules to limit the stress on semiconductors compel the worst case peak to peak converter side current ripple (Δi_{max}) to reside generally in 10-25% of peak rated load current (\hat{I}_r). So, the required current ripple on the converter side can be determined by using (5.4) [69].

$$L_c = \frac{V_{dc}}{12 f_{sw} \hat{I}_r \Delta i_{max}} \quad (5.4)$$

where $\Delta i_{max} = 0.1-0.25$.

Step-3: Grid-side inductance is defined proportional to the designated converter-side inductance (L_c) as depicted in (5.5). r is usually selected as $r=1$ to maximize the filter attenuation extent and minimize the filter size [57].

$$L_g = r L_c \quad (5.5)$$

Step-4: The current ripple injection from converter-side to grid-side is calculated by neglecting losses and damping of the filter by means of (5.6). According the restrictions ruled by the corresponding grid codes, minimum 80% of the converter-side current ripple attenuation (maximum 20% ripple injection) is generally aimed.

$$\frac{i_g(h_{sw})}{i_c(h_{sw})} = \frac{1}{|1 + r(1 - L_c C_b \omega_{sw}^2 x)|} \quad (5.6)$$

where ω_{sw} is the switching frequency in rad/sec. If designated r cannot fulfill the desired ripple attenuation, either r value should be updated or another value for the absorbed reactive power should be selected as depicted in Figure 5.1. In general, instead of substituting r value on (5.6), current ripple reduction is plotted against varying r and the corresponding r value is determined regarding the desired ripple attenuation amount. This approach eliminates iterations to obtain the final value of r and saves time.

Step-5: The resonant frequency is calculated by using (5.7).

$$\omega_{res} = \sqrt{\frac{L_c + L_g}{L_c L_g C_f}} \quad (5.7)$$

The resonant frequency should reside between ten times the grid frequency and one-half of the switching frequency to eliminate the interface between harmonic compensation and resonance damping as Liserre *et al.* [54] suggested. If the condition is not met, algorithm either steps backwards to step-2 to update the

absorbed reactive power extent (change x) or r value yielded in step-3 should be changed. Note that r is generally selected as unity particularly for the applications requiring minimum filter size. For this reason, updating r value should not be applied as the first remedy to fulfill the requirements; instead reactive power absorption amount should be updated in the first place. This priority option is highlighted by the red arrows in Figure 5.1.

Step-6: Sufficient damping should be achieved with either AD (virtual resistor) or PD (real resistor) to provide non-zero impedance in the filter capacitor branch to limit the resonance peak. Conventional algorithms favor the PD method and tune its value in order to minimize the undesirable losses while achieving sufficient damping of the resonance poles. Besides, several damping resistor connection methods are also discussed in [60][66] and the simple series connection to the filter capacitors usually yields the least damping loss while compromising the filter attenuation. As mentioned in Chapter 4, this simple resistor configuration will be used throughout this work.

Blaabjerg *et al.* in [66] state that the value of the critical damping resistors is generally set to one third of the impedance of filter capacitor branch at the resonant frequency. Thus, the formula shown in (5.8) determines the minimum value of the damping resistor R_d that brings the unstable system on the brink of the stability. Although the optimum value of the damping factor ζ is 0.707 for proper damping, it is recommended to limit ζ around 0.5 to minimize damping losses [57]. For a desired damping factor ζ , (5.9) can be used to determine the required damping resistor value R_d .

$$R_d \geq \frac{1}{3\omega_{res}C_f} \quad (5.8)$$

$$\zeta = \frac{C_f\omega_{res}R_d}{2} \quad (5.9)$$

As a remark, tuning of R_d can also be done by proportioning the constant terms of the second highest variable (s^2 in this case) to the constant terms of the highest variable (s^3 in this case) of the transfer function in (4.24), as adopted in AD methods in Chapter 4.

$$\frac{\epsilon_f R_d (L_c + L_g)}{\epsilon_f L_c L_g} = 2\zeta \omega_{res} \quad (5.10)$$

If ω_{res} definition in (5.7) is substituted into (5.10), resulting definition will be the same formula given in (5.9). Thus, the validity of these definitions is proven.

After achieving damping, filter attenuation is checked again. If the attenuation is not sufficient, algorithm may be returned to step-3 to update r value. However, increasing r beyond unity does not enhance the attenuation performance significantly but increases the filter size considerably [54]. Therefore, the algorithm should go back to step-2 and a higher value of reactive power absorption should be selected.

Step-7: Verify the filter performance under varying load conditions and switching frequencies.

5.2.1. LCL-Filter Design Case-Study

In this section, the conventional LCL-filter design methodology will be followed step-by-step and detailed analyses by means of the mathematical tools of MATLAB[®] will be provided. In the end, conducted analyses will further be proven by means of simulation outputs.

Table 5.1 lists the required input parameters for the filter design. In this case study, space vector PWM (SVPWM) is the favored PWM pattern. Besides, PWM sampling and updating method is double update PWM, leading to a sampling frequency (control frequency) twice of the switching frequency.

Table 5.1 *LCL*-filter design specifications.

Elements	Parameters	Values
Converter	S_n	250 kVA
	f_{sw}^*	4 kHz
	f_{samp}	8 kHz
	V_{DC}	750 V
Grid	V_g	400 V _{rms}
	f_g	50 Hz
	PF	0.95-1

*Switching frequency is calculated using the methodology given in Chapter 3.

Step-1: Base impedance and capacitance of the system:

$$Z_b=0.64 \Omega, C_b=4.97 \text{ mF.}$$

Step-2a: The reactive power absorption extent and selected filter capacitance:

$$\text{Let } x=0.03 \rightarrow C_f=0.03*4.97 \text{ mF} \approx 150\mu\text{F (3\%)}$$

Step-2b:

$$\hat{I}_r = (250*10^3 / \sqrt{3}*400)* \sqrt{2} \approx 513\text{A}$$

$$L_c = 750 / (12*4000*513*0.15) \approx 200\mu\text{H (9.8\%)}$$

Step-3: For the filter inductors: $r=1$ and $L_g=L_c$.

$$L_c = \left(1 + \frac{1}{r}\right) \frac{1}{C_f \omega_{res}^2} = \frac{2}{C_f \omega_{res}^2}$$

Step-4: As proposed, instead of substituting r value on (5.6), current ripple reduction is plotted against varying r and corresponding r value is determined regarding the desired ripple attenuation amount.

In Figure 5.2, for various r values, ripple attenuation amounts are calculated and plotted. For $r=1$, corresponding attenuation in Figure 5.2 becomes approximately 0.08 (8%), injecting 8% of the 15% converter-side ripple to the grid. Thus, total ripple injection extent to the grid becomes 1.20% of \hat{I}_r .

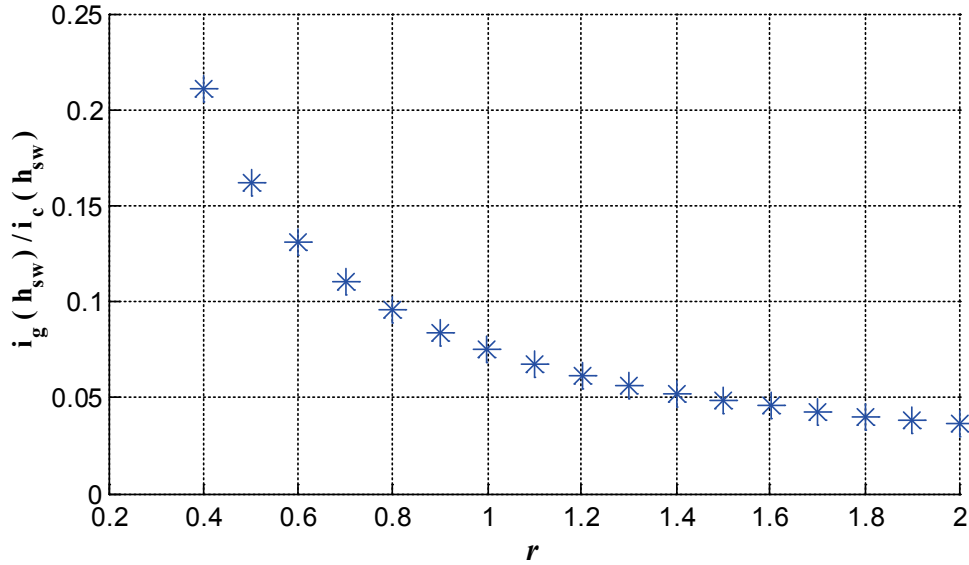


Figure 5.2 Harmonic attenuation against r .

Step-5:

$$\omega_{res} = \sqrt{\frac{2}{L_c C_f}} = 8165 \text{ rad/sec} \equiv 1300 \text{ Hz}$$

$$500 < f_{res} < 2000 \quad \checkmark$$

Step-6: Critical value of the damping resistor R_d computed by means of (5.8) is 0.27Ω . Desired open-loop damping factor is set initially to $\zeta=0.5$ to minimize the damping losses and it leads to a damping resistor $R_d = 0.82 \Omega$. However, closed-loop damping factor should also be verified by means of mathematical tools and fine-tuning of damping resistors ought to be made to further diminish the damping losses. For this reason, the magnitude and frequency response of the *LCL*-filter under critical, optimum and excessive R_d values are embodied in Figure 5.3. As can be seen in this figure, critical resistance value holds the system on the verge of stability; hence the underdamped resonance peak is quite visible. On the other hand, the optimum R_d value calculated to deliver an open-loop damping factor of 0.5 ($R_d = 0.82 \Omega$) is found to be sufficient to bring down the resonance peak. Nevertheless,

damping resistors higher than 1.15Ω (for $\zeta=0.707$) would cause overdamping of the resonance and degrade the attenuation capability of the *LCL*-filter substantially. As R_d increases, reduction in the third-order characteristics of the *LCL*-filter is evident from the decreasing slope of the magnitude response in Figure 5.3.

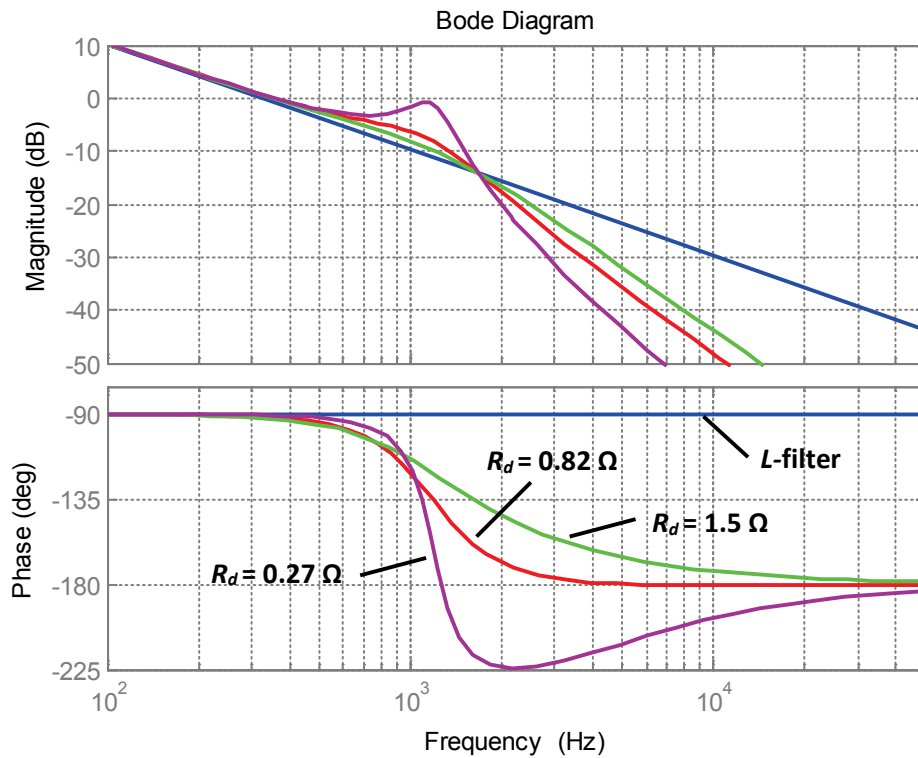


Figure 5.3 Magnitude and phase response of *LCL*-filter under various R_d .

Figure 5.4 depicts contribution of $R_d = 0.27 \Omega$ and $R_d = 0.82 \Omega$ to the open-loop damping of the resonant pole pair. As calculated with (5.8), 0.82Ω delivers an open-loop damping factor of 0.5. On the other hand, 0.27Ω provides an open-loop damping factor close to 0.2. Frankly, these open-loop damping factors only give side information about the stability, they do not ensure closed-loop stability. For this reason, the impact of the current controllers to the closed loop response should also be regarded and closed-loop damping ratio must be assessed.

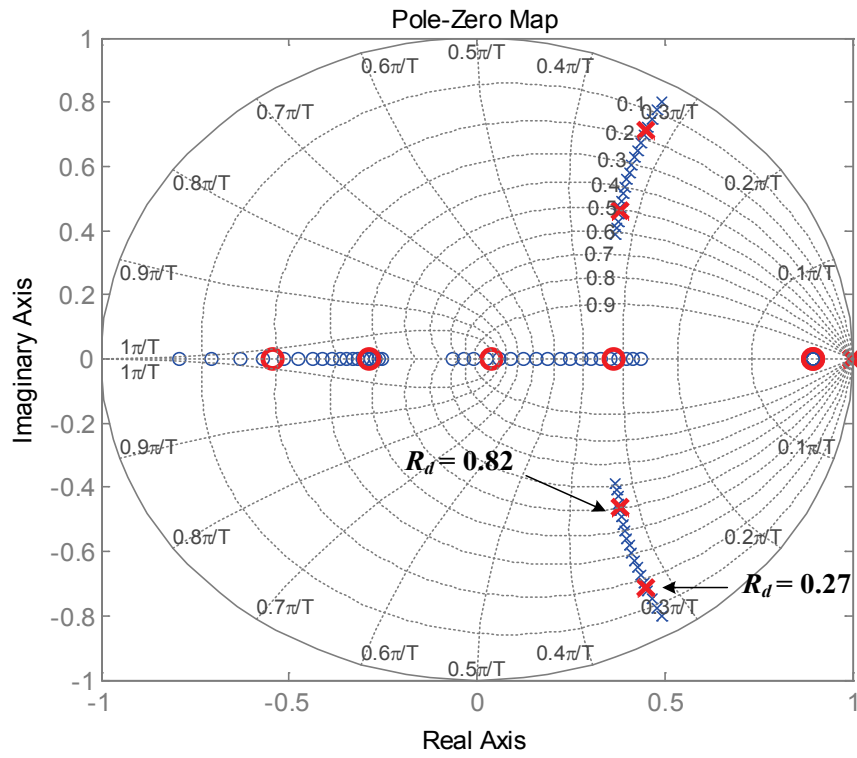


Figure 5.4 Open-loop pole-zero map under GCF ($\zeta_{ol} = 0.5$).

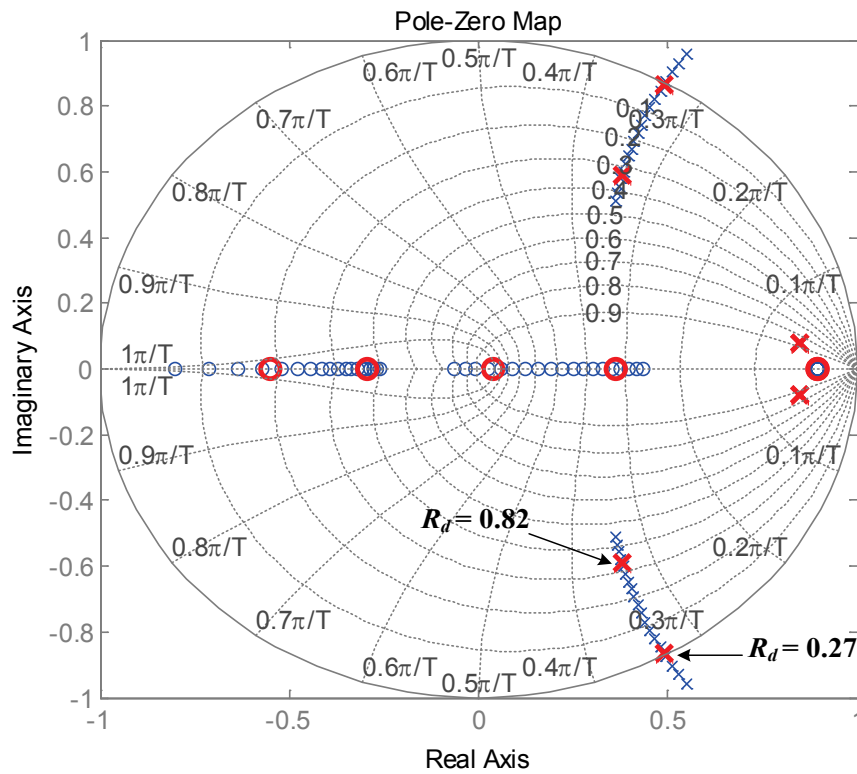


Figure 5.5 Closed-loop pole-zero map under GCF ($\zeta_{cl} = 0.332$).

As can be agreed in Figure 5.5, stability is attained for $R_d = 0.27$ that moves the undamped resonant poles to the boundaries of unit circle. To further push the poles inside the unit circle R_d should be elevated. For $R_d = 0.82$, proper damping is provided through a closed-loop damping ratio of $\zeta_{cl} = 0.332$.

As a remark, the final value of R_d depends on the preferred current feedback variable. Since CCF provides an inherent damping feature, the necessary R_d value to achieve the desired damping ratio under CCF method is always smaller than the necessary R_d value under GCF method. Since the formula given in (5.9) provides the optimum R_d value for the systems using GCF method (since (4.24) is derived under GCF case), required R_d value delivering open-loop damping factor $\zeta = 0.5$ under CCF method should be computed. For this purpose, root locus of the system employing CCF should be obtained as depicted in Figure 5.6 and the R_d value delivering an open-loop damping factor $\zeta_{ol} = 0.5$ ought to be designated. Note that similar procedure would also be adopted for CCF case such that the transfer function under CCF case could be derived and optimum damping resistor value could be found by the same approach in (5.10).

For $R_d = 0.4$, $\zeta_{ol} = 0.5$ is achieved under CCF method as depicted in the open-loop pole-zero characteristics in Figure 5.6. Once the loop is closed, system reaches stability and resonant pole pair is damped with a closed-loop damping ratio of $\zeta_{cl} = 0.329$. It is evident that reduced R_d value in CCF case provides both the same open-loop and closed-loop performance as R_d value in GCF method (Figure 5.7). Thereby, passive damping losses are almost halved owing to the inherent damping nature of the current loop in CCF.

5.2.2. Assessment of the Designed LCL-Filter through Simulations

In this section, the assessment of the design procedure is conducted via simulation software SIMPLORER[®] by using the system specifications and designed filter parameters listed in Table 5.2.

Table 5.2 Designed filter and controller parameters.

Elements	Parameters	Values
LCL-filter	L_g	200 μ H (9.8%)
	L_c	200 μ H (9.8%)
	C_f	145 μ F (3%)
Damping Resistor	$GCF-R_d$	0.82 Ω
	$CCF-R_d$	0.40 Ω
Controller	K_p	1.07
	T_i	0.001125

First of all, the performance of designed filter will be tested using GCF method. For GCF case, the damping resistor value shown in Table 5.2 is used. Before showing the outputs of critically damped case, impact of underdamping will be realized by using $R_d=0.27\Omega$. For $R_d=0.27\Omega$, simulated waveforms are shown in Figure 5.8, where serious transient oscillations occur at the step transition from light load (10%) to full load (100%). It is evident that system is not damped sufficiently and these oscillations are very likely to originate instability of the controllers. Apart from the transient oscillations, it takes more than half period for the grid-side current reaching the steady-state after the step-up change. Therefore, R_d should be increased in order to damp the oscillations properly and diminish the settling time of the controllers. Once the critical damping resistor value is picked, $R_d=0.82\Omega$ case, simulated waveforms in Figure 5.9 seem to be damped sufficiently and they are well-regulated both in the steady-state and transient-state. When the loading is forced to jump from 10% to 100%, the designed converter has responded quite fast and there is no

oscillation or current overshoot verifying the critically damped design. Thus, the designed system faces neither resonance oscillations nor excessive damping losses during operation.

Secondly, the performance of designed filter under CCF method will be evaluated. For CCF case, the damping resistor value shown in Table 5.2 is used. As proven to be providing the same damping with GCF case, the designed filter has also responded quite fast to the loading jump from 10% to 100% and there is no oscillation and current overshoot visible in transient-state (Figure 5.10).

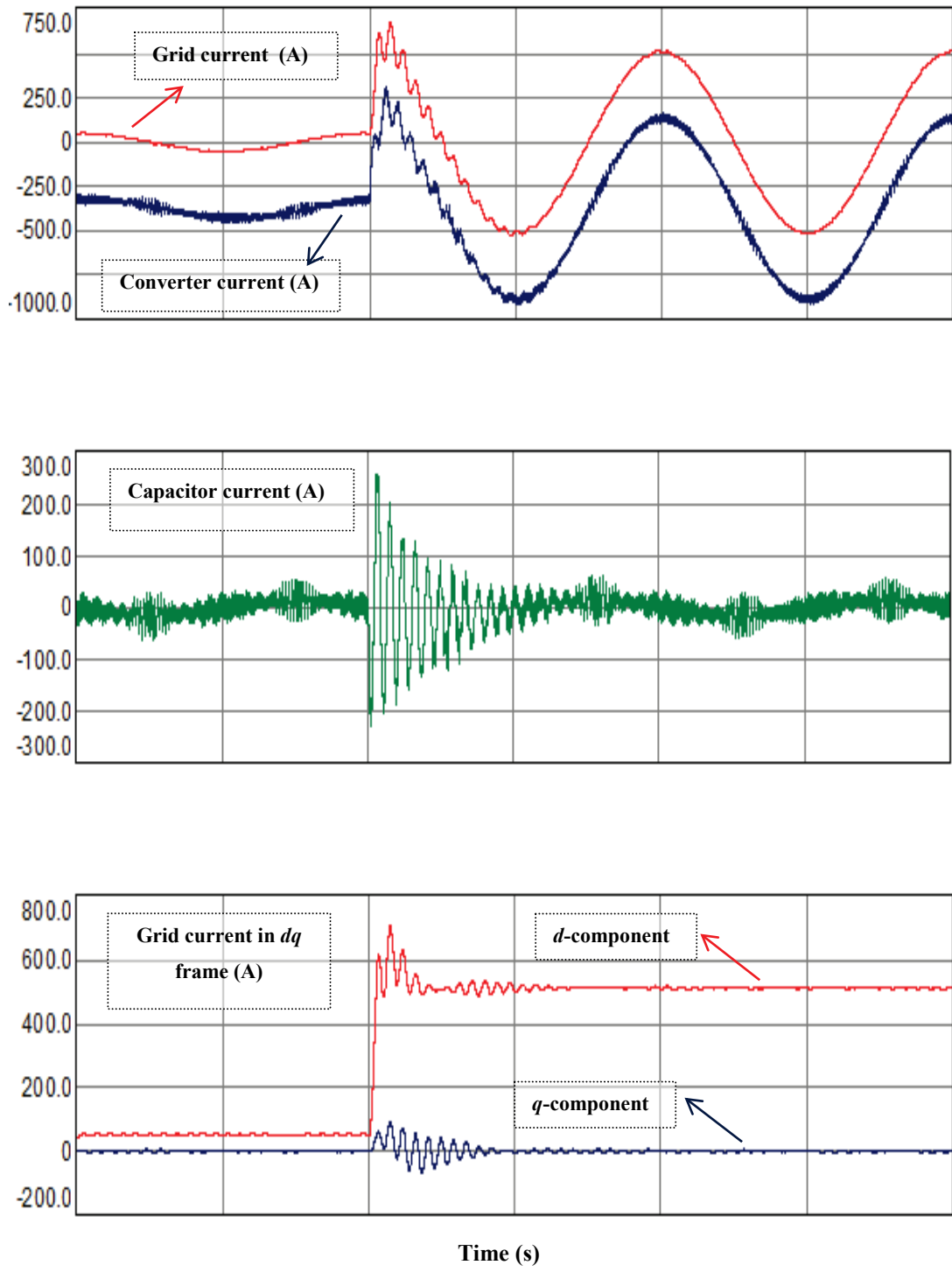


Figure 5.8 Simulation results of LCL -filter based VSC using $R_d=0.27 \Omega$ under GCF.

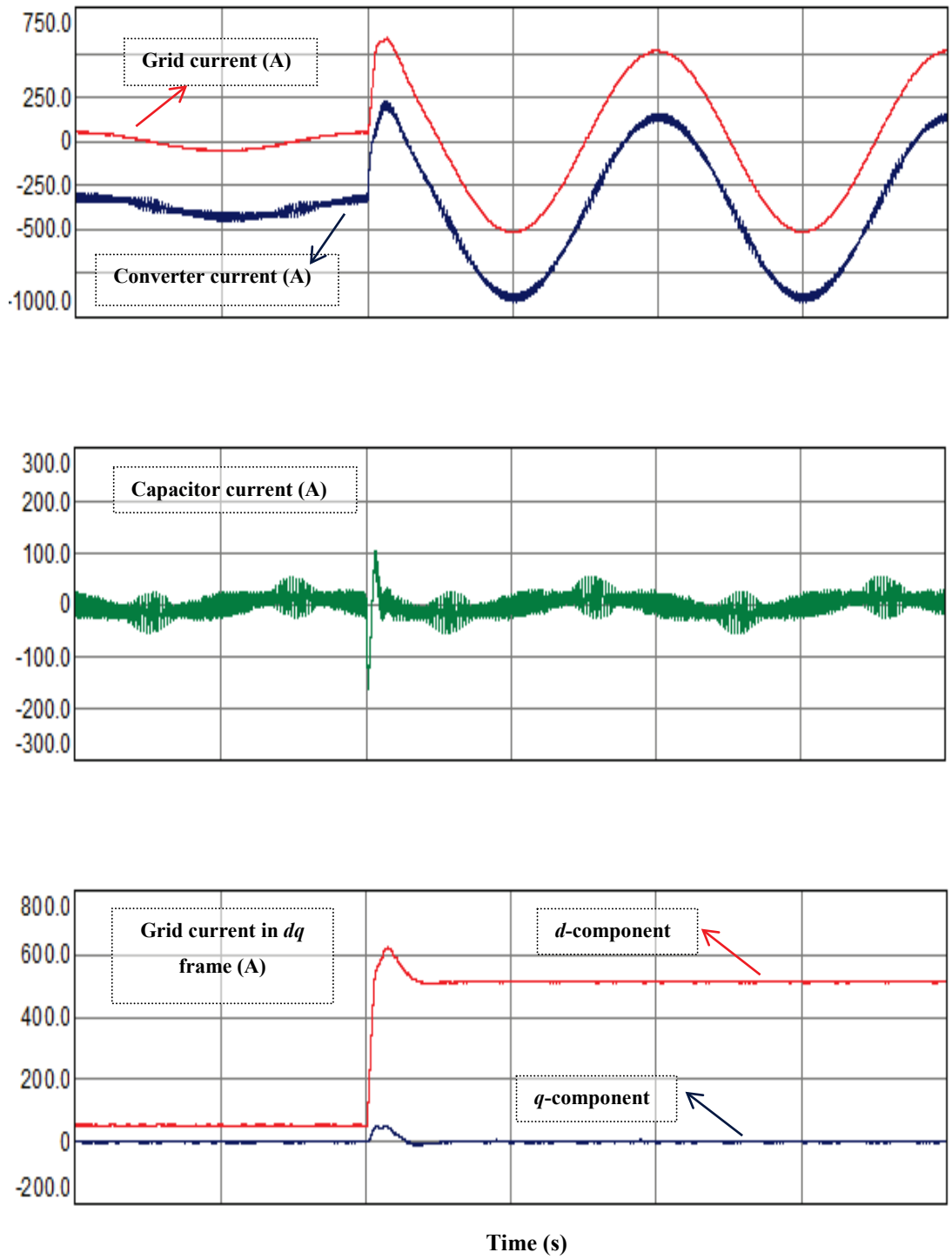


Figure 5.9 Simulation results of LCL -filter based VSC using $R_d=0.82 \Omega$ under GCF.

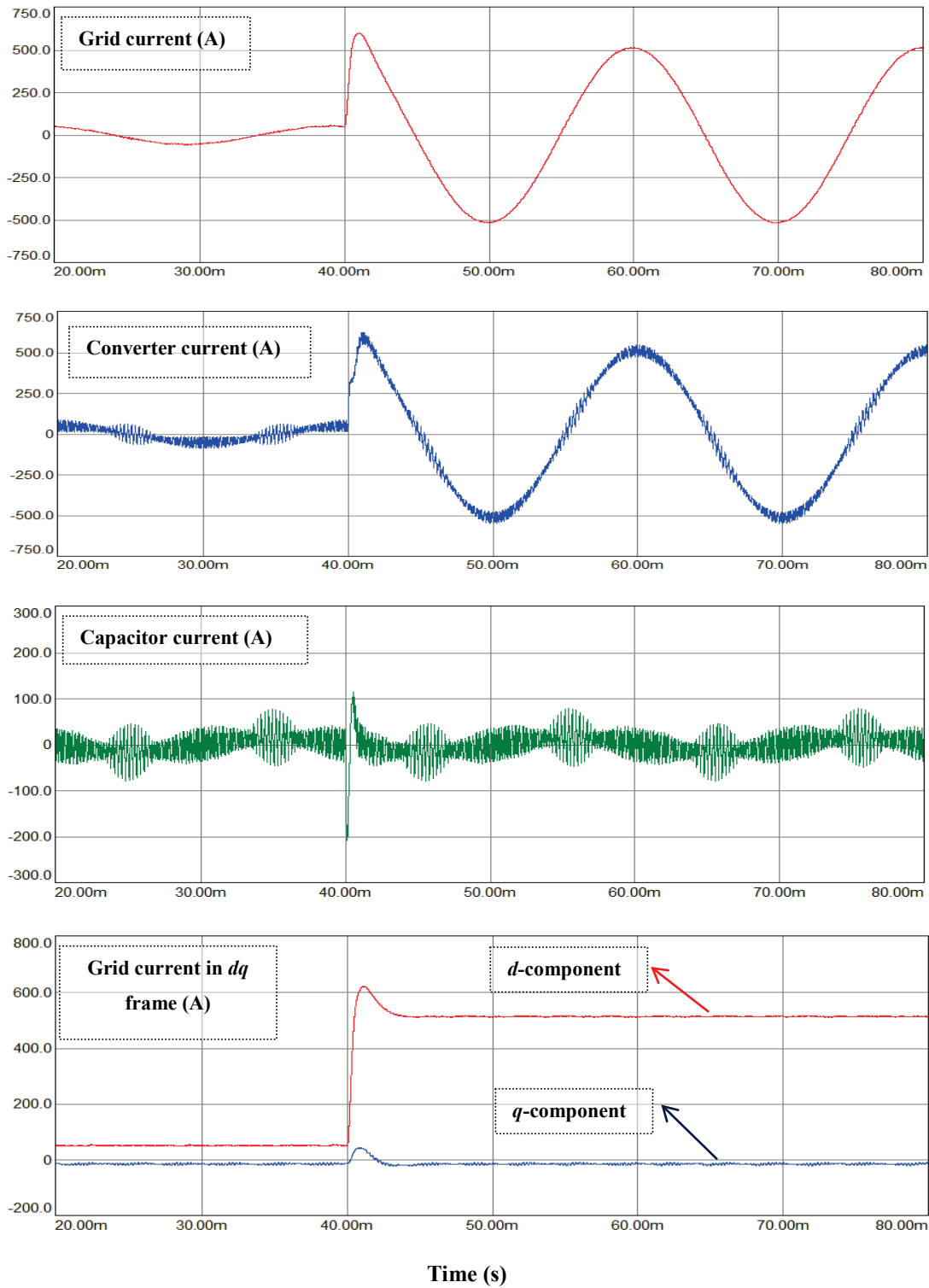


Figure 5.10 Simulation results of *LCL*-filter based VSC using $R_d=0.4 \Omega$ under CCF.

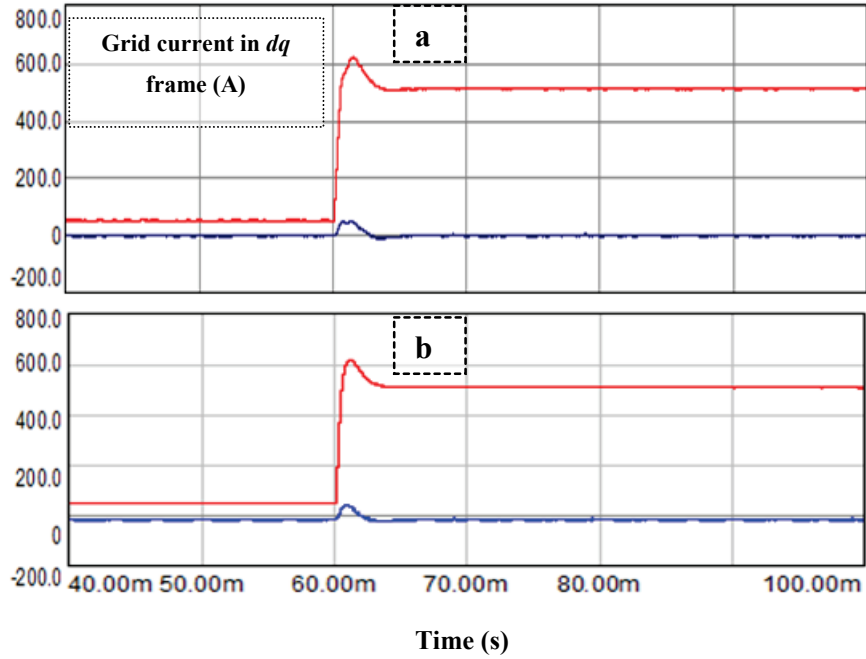


Figure 5.11 Dynamic response of grid-current in dq -frame (a) GCF and (b) CCF.

Figure 5.11 compares transient performance of the designed filter under GCF and CCF methods and reveals that the rise time and settling time under CCF is slightly better compared to those of GCF method. The maximum overshoot percentages are nearly alike owing to the matched damping resistor values. Further performance comparison is made by grading with number of pluses in Table 5.3. Consequently, with lowered damping loss and slightly better transient performance, CCF provides better solution while PD is utilized to flatten the resonant peak.

Table 5.3 Comparison between GCF and CCF

Type	Stable	Damping	Transient performance	Lowered damping loss
GCF	Yes	++	+	+
CCF	Yes	++	++	++

5.2.2.1. Grid Code Compatibility

The designed grid-connected VSC with *LCL*-filter should comply with the stringent grid codes generally specified by IEEE 519-1992. However, stiffness (SCR), voltage level (LV, MV, HV, and extra HV), and location (onshore, offshore, geological causes, etc.) of the grid, and type of the application (PV, wind, etc.) primarily determines the stringency of the requirements. Besides, the compromise between the producer and the consumer at PCC has also large impact on the severity of these codes. Apart from IEEE-519-1992; VDEW, IEC 61400-21, and EN50160 are the most outstanding codes applied in industry. Additionally, voltage harmonic distortion extent of the grid depends upon the loads connected at PCC. Hence, the individual voltage distortion contributed by the inverter on PCC can be roughly calculated with the estimation of the impedance at PCC and by monitoring the current harmonic content injected through PCC (Chapter 2).

Accordingly, harmonic analysis of the grid-side current I_g should be monitored carefully and the maximum limit both for individual harmonics and total harmonic current distortion THD_i should be set in the design phase according to one of the abovementioned grid codes. Since the same resonance damping is guaranteed by each of GCF and CCF techniques, the inspection of the grid-side current under either GCF or CCF will be sufficient.

As reference to IEEE-519-1992 regulations for the grids having SCR lower than 20, the magnitudes of the harmonic components starting from 35th and above should be lower than 0.3% of rated grid-current I_g . Therefore, the switching harmonics and the resonant harmonics (if any) in the harmonic spectrum should be monitored carefully. For the switching harmonics, the sidebands of f_{sw} and its multiples should be put special prominence. In Figure 5.12, side-band harmonics around 4 kHz (at f_{sw}) reach at most 0.19% of I_g which complies with the grid codes. At the multiples of f_{sw} , the harmonic magnitudes diminish considerably. Plus, the maximum magnitude of I_c harmonics reach 1.5% of fundamental component of I_c at f_{sw} , thus there would not be any significant power loss and overheating of converter-side inductor. Resulting

THD_i is I_c and I_g are also figured as THD_i (I_c) =5.41% and THD_i (I_g) =0.78%, respectively.

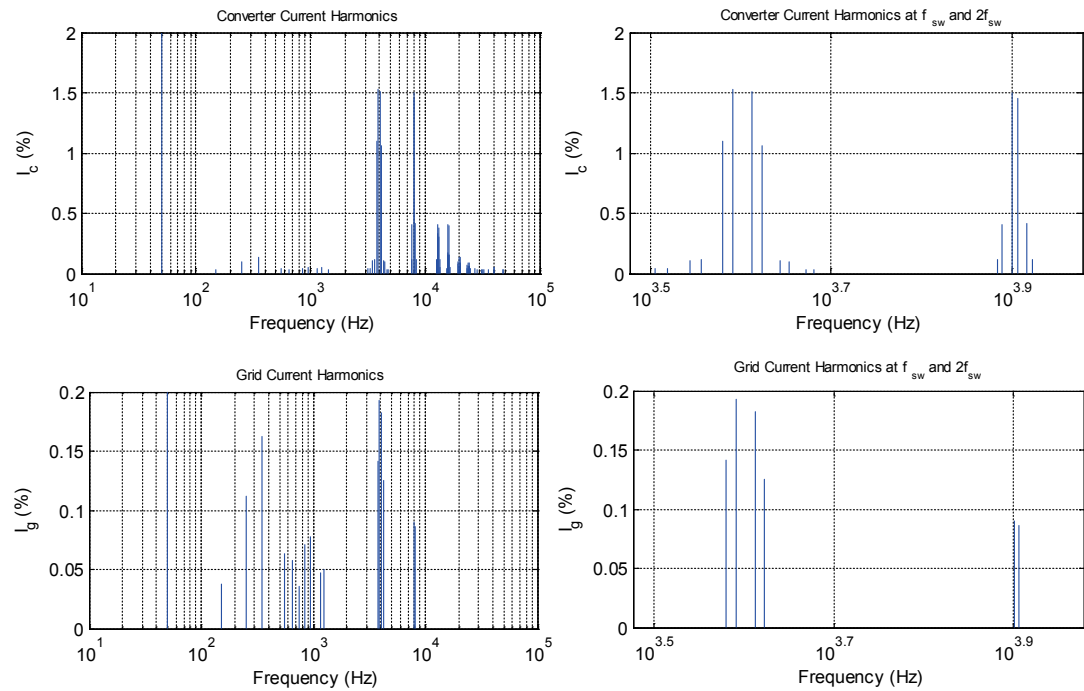


Figure 5.12 THD_i (%) vs. frequency (Hz)

- (a) Converter-side current, I_c (b) Grid-side current I_g (c) I_c zoomed in f_{sw} and $2f_{sw}$
 (d) I_g zoomed in f_{sw} and $2f_{sw}$ (THD_i of I_c =5.41% and I_g =0.78%).

5.2.2.2. The Assessment of Efficiency vs. PWM Method

The success of the two-level VSC design is mostly assessed with its efficiency performance. Filter losses, damping losses together with the switching and conduction losses of semiconductor modules (IGBT) constitutes the main loss mechanisms in the system. But, employed PWM modulation methods have considerable influence not only on THD_i and ripple performance of the designed filter but also on total semiconductor loss extent. Thus, the impact of the preferred PWM pattern is assessed in Figure 5.13. In this section, two of the most popular PWM methods containing zero sequence signal injection, namely space-vector

pulse-width-modulation (SVPWM) and discontinuous pulse-width-modulation (DPWM1) are examined under “*equal switching loss*” principle. For this purpose, f_{sw} is increased by 50% in DPWM1 method so that the switching count and therefore the switching losses could remain the same while ripple of DPWM1 becomes less compared to SVPWM. SVPWM at low m_i and DPWM1 at high m_i have been widely used in industry [69].

As evident in Figure 5.13, DPWM1 method provides better efficiency characteristics than that of SVPWM at $f_{sw}=4$ kHz for loads higher than 50%.

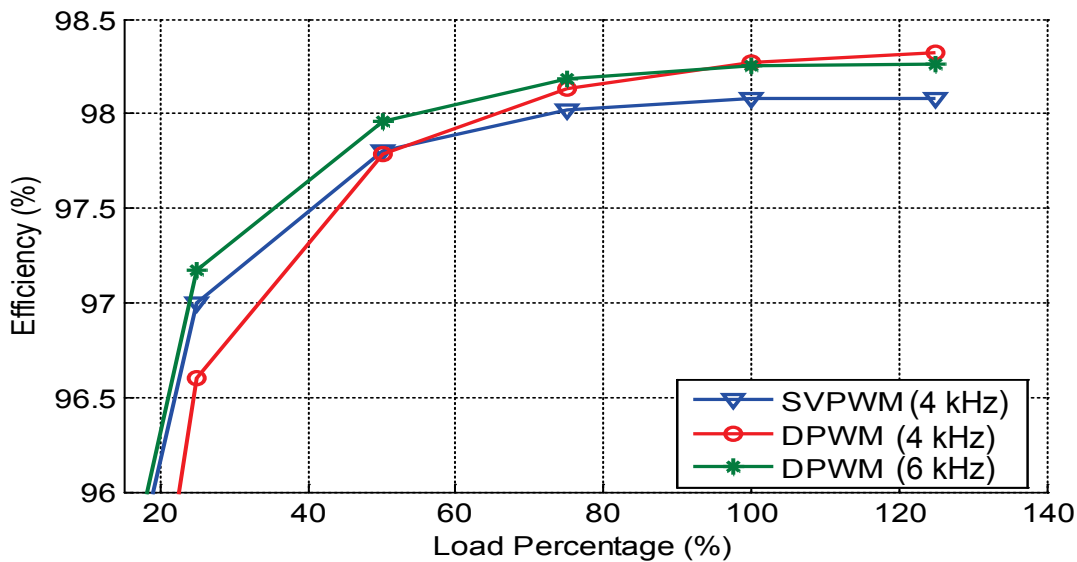


Figure 5.13 Efficiency change vs. load percentage under GCF.

5.2.2.3. Damping Loss Comparison against PWM Method

Passive damping losses can either be calculated with a running average tool in simulation software or by the formula provided in (5.11).

$$P_d = 3 \cdot R_d \cdot \sum_h [i_c(h) - i_g(h)]^2 = \sum_h [i_{cf}(h)]^2 \quad (5.11)$$

where P_d represents damping loss and h indicate the h^{th} harmonic of the current. The main terms of (5.11) are for the index h around h_{sw} (order of switching frequency) and its multiples.

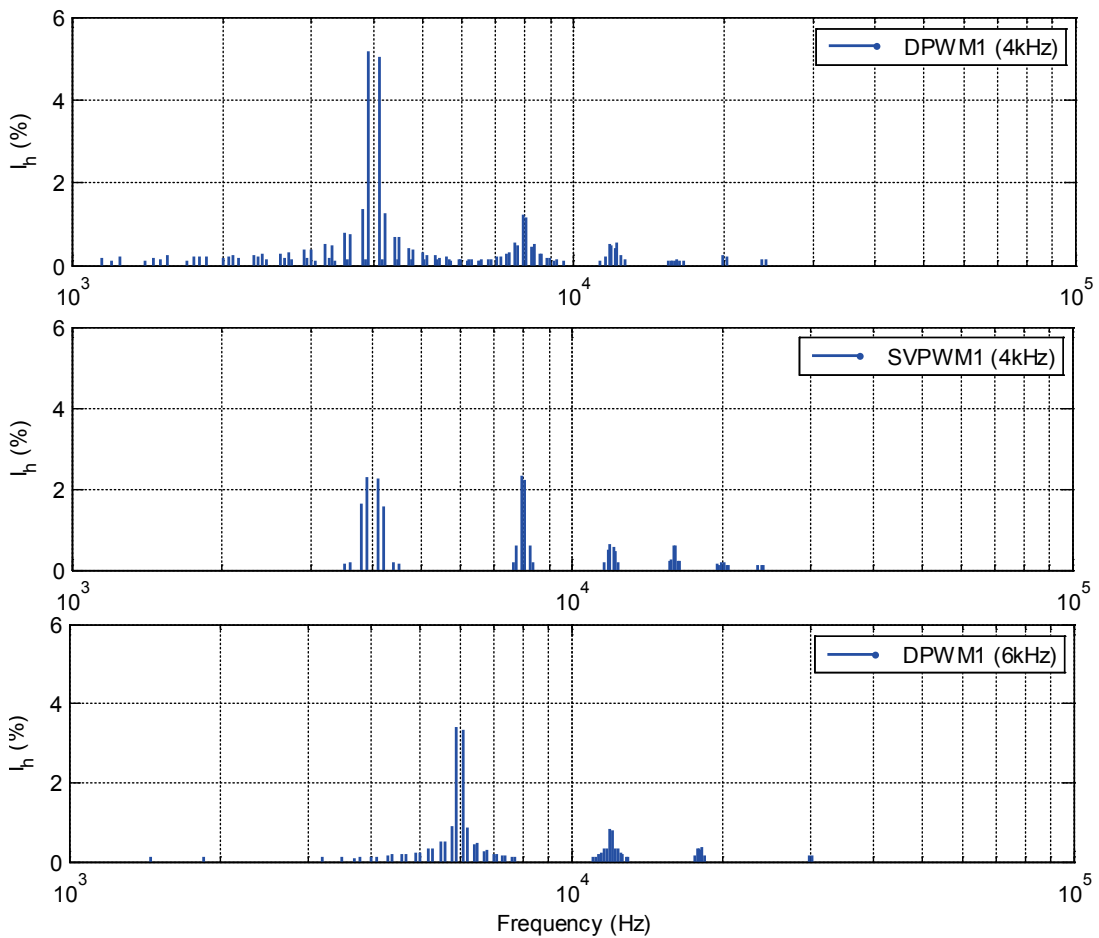


Figure 5.14 Harmonic content of I_{cf} against PWM methods under GCF.

Employing (5.11) under GCF method ($R_d=0.82\Omega$) yields damping losses P_d of 5237W, 2571W, 2541W respectively for the sequence of analysis shown in Figure

5.14. Although employment of DPWM1 reduces the conduction losses significantly, damping losses are doubled compared to SVPWM at $f_{sw}=4$ kHz. FFT analysis in Figure 5.14 reveals that magnitudes of the harmonic components at the side-bands of f_{sw} and its multiples in DPWM1 case are much higher than that of in SVPWM causing almost twice higher damping losses at $f_{sw}=4$ kHz. Consequently, damping losses constitute a higher portion in the total losses at light loads and SVPWM is favorable over DPWM1 in efficiency aspect at $f_{sw}=4$ kHz. Nevertheless, as the load increases conduction losses escalate and prevail over damping losses. Thus, DPWM1 shows better performance compared to SVPWM for the loads higher than 50%.

Nevertheless, the comparison between DPWM1 at $f_{sw}=6$ kHz and SVPWM at $f_{sw}=4$ kHz is the fair assessment since the switching losses are equalized in that case. Note that damping loss for DPWM1 at 6 kHz (2541W) case has diminished substantially compared to the cases of DPWM1 at 4 kHz (5237W) and SVPWM at 4 kHz (2571W) as can be realized from the reduction in harmonic magnitudes of I_c in Figure 5.14. Hence, efficiency has been increased in DPWM1 at 6 kHz case despite the switching frequency rise. In conclusion, utilization of DPWM1 method at 6 kHz has provided the best efficiency performance.

On the other hand, employing (5.11) under CCF method ($R_d=0.4\Omega$) yields damping losses P_d of 1324W, 2753W, 1270W, respectively for the sequence of analysis shown in Figure 5.15. Figure 5.14 and Figure 5.15 can be compared to reveal that the magnitudes of the harmonic content under CCF method are very close to those under GCF method. Therefore, the superiority of DPWM1 method over SVPWM method is evident under CCF method as well. However, owing to the reduced damping resistor value ($R_d=0.4\Omega$), damping losses are almost halved. Consequently, CCF method is favorable over GCF since it provides the same damping by halving the damping losses. If efficiency vs. load curves were derived for CCF case, those in Figure 5.13 for GCF case would be shifted up in proportion to the reduced losses under CCF method.

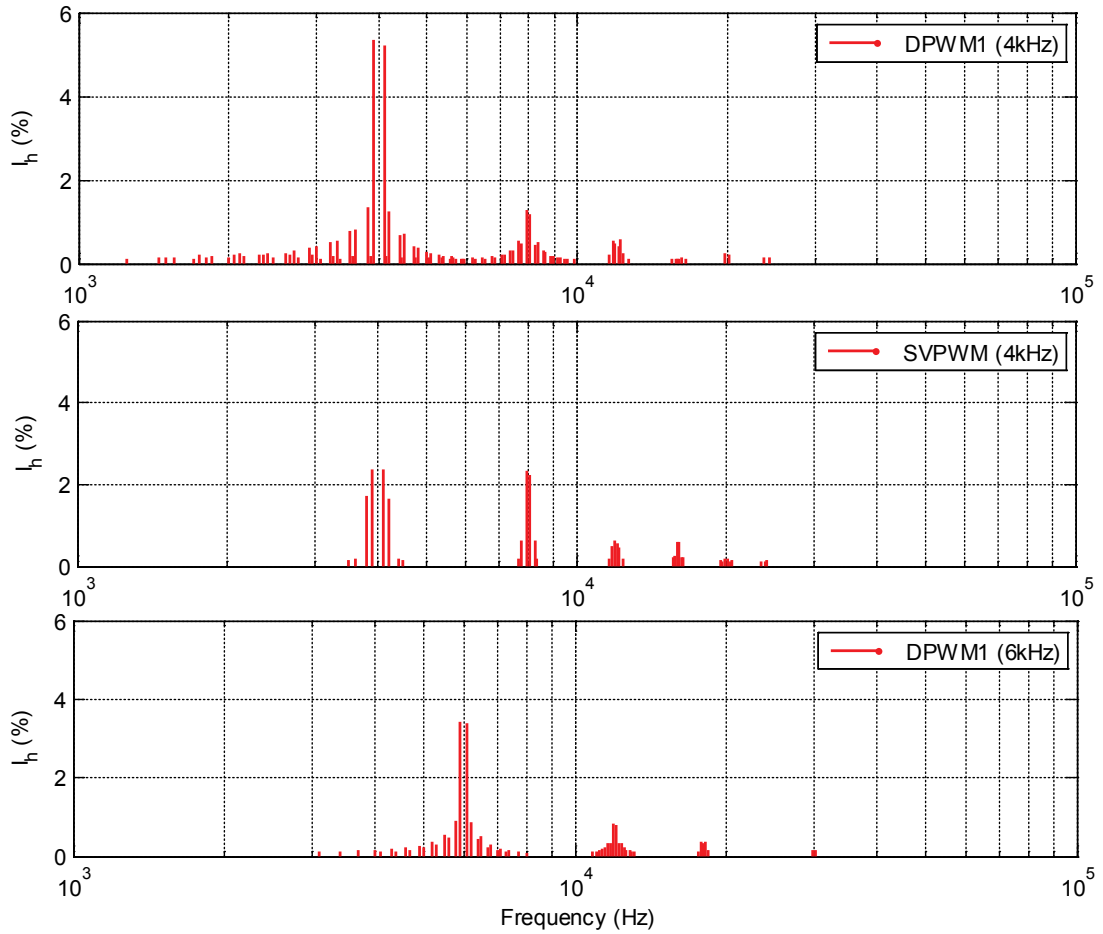


Figure 5.15 Harmonic content of I_{cf} against PWM methods under CCF.

To sum up, in Section 5.2 the conventional LCL -filter design methodology of a grid-connected VSC with LCL -filter is provided. A complete design procedure for LCL -filter is demonstrated with a step-by-step approach through a flow diagram. The verification of the design method has been completed via simulations. The stability and the dynamic response of the designed system are examined considering the sufficiency of resonance damping. Design procedure is followed by inspecting the impact of DPWM1 and SVPWM methods on efficiency under different loadings and switching frequencies. For this purpose, elaborated harmonic examination involving FFT analysis of filter capacitor current is provided to reveal the relationship between the damping loss and harmonic magnitudes. In the end, CCF is found to be superior to GCF when PD is utilized. This outcome is opposite of the findings when AD is

used. However, the difference can be summarized as follows. Inherent damping trait of CCF control is useful on diminishing the damping resistor value and hence damping losses while the dynamics of the system remains unchanged regardless of the control technique. In contrast, relying only on ID feature of CCF is not feasible in practice and AD or PD must be used in addition to CCF control. At this point, since AD or PD is already applied, GCF method prevails over CCF control due to its superior dynamic performance.

In the next section, proposed *LCL*-filter method is presented. Before proceeding to that section, know-how *LCL*-filter design rules used in practice should be mentioned briefly. A senior designer always takes the resonant frequency into the account. Besides, the control method and the switching frequency are always determined in advance. Then, iterations are started with a reasonable initial selection of filter components similar to the presented methodology in this section. During the iterations, resonant frequency is changed rather than switching frequency. To adjust resonant frequency, filter parameters are varied. This procedure lasts until a stable system is reached. For the systems having very low switching frequency, AD cannot be managed most of the time; thus aid of PD is applied and system is stabilized using the lowest possible damping resistor. In case of no solution, changing switching frequency may be useful, however; it is not desired most of the time. To sum up, proposed filter design method in the next section adopts this insight and involves advanced theoretical knowledge to realize a top to bottom filter design algorithm.

5.3. Proposed *LCL*-Filter Design Algorithm Including Controllability Issues

The proposed *LCL*-filter design procedure is not as straight-forward as the conventional design algorithm. Controllability and stability concerns are also included in the design procedure.

Conventional design procedure focuses on utilization of converter-side inductance calculation formulas by assuming reasonable ripple attenuation as the design criterion. Besides, after determining the filter components corresponding resonant

frequency is confined in the interval of $10f_g < f_{res} < 0.5f_{sw}$, achieving the elimination of interface between the switching harmonics and the resonance harmonics [54][60]. Although this approach is valuable for the systems with high switching frequency, it becomes impractical for high power applications utilizing low switching frequency. For instance, systems higher than 300-500 kW scale employ switching frequencies in the range of a few kHz. In this case, confining the resonant frequency in the interval of $10f_g < f_{res} < 0.5f_{sw}$ requires a very low resonant frequency, making the filter components especially the filter inductors bulky. Therefore, this kind of approach makes the design superficial and does not embrace all the power levels. For this reason, the literature needs a top to bottom *LCL*-filter design algorithm that can span a wide power scale of grid connected PWM converters. For this purpose, the perspective on the resonant frequency must be broadened.

First of all, resonant frequency must be set by the designer. As explained in detail in the previous chapter, the location of the resonant frequency has great impact on stability issues as well as the attenuation capability of the filter. The most optimum damping technique that optimizes the filter size and attenuation performance for the defined resonant frequency region (i.e. low/high resonant region) relies primarily on the preferred current feedback variable. For this reason, GCF and CCF even yields distinct *LCL*-filter parameters depending on the location where the resonance frequency settles. The optimum solution always relies on the compromise between cost (and/or size) and performance. The location where the resonance frequency should reside is determined by priority of the design in terms of cost or performance under the preferred current feedback variable. Holmes *et al.* [58] and Dannehl *et al.* [55] clarify the regions of resonant frequency and the optimum damping methods for each of corresponding regions. Preceding chapter presents a comprehensive study concerning effectiveness of the current feedback methods and damping methods regarding the resonant frequency regions (Table 4.2). Therefore, the favored current feedback variable is also an input to the *LCL*-design procedure.

Once the resonant frequency is certain, controllability of the system is no longer an issue. The behavior of the designed system becomes foreseeable and stabilization

turns into an easy task. To elaborate, the distance between the resonant frequency ω_{res} and zero dB gain crossover frequency ω_c plays the key role on ensuring *LCL*-filter stabilization by achieving an adequate phase margin [56][59][69]. To provide sufficient phase margin, ω_c must be fixed sufficiently below ω_{res} regardless of the damping method. The relationship between the current regulator stability and the *LCL*-filter resonant frequency is evaluated through frequency responses of the forward path transfer functions (open-loop transfer functions) containing *LCL*-plant $G_p(s)$ cascaded with PI-controller block $G_c(s)$. Corresponding transfer functions regarding each current feedback methods are derived by means of detailed control block diagrams in Section 4.4.4. By using these transfer functions with a proper selection of K_p (symmetrical optimum), ω_c is designated. Then, the correlation between ω_c and ω_{res} is represented with $\omega_c = \alpha \omega_{res}$ where $\alpha < 1$. The main reason why ω_c is fixed sufficiently below ω_{res} and why ω_c is tuned with K_p is simply to reserve sufficient phase margins higher than 45° for the closed-loop control. Numerous combinations of ω_{res} and ω_c will be examined by the proposed design algorithm in this section regarding the resultant phase margins. In order to guarantee phase margins higher than 45° for the closed-loop control, a ω_c tuning zone should be defined as described in Section 4.4.5 in Figure 4.31.

To illustrate, for the *LCL*-filter parameters provided in Table 4.1, bode plot of the open-loop transfer function (4.28) and (4.29) are plotted in Figure 5.16. K_p is derived regarding the symmetrical optimum approach. $\omega_{c,max}$ is placed at 516 Hz where minimum achievable phase margin is 45° . Likewise, $\omega_{c,min}$ is placed at 100 Hz where the frequency attributes of the two filters start to deviate. Consequently, defined ω_c zone is depicted in Figure 5.16 and it can be inferred that α values should be confined into 0.1-0.516 interval (α tuning zone) where the resonant frequency is fixed at 1000Hz.

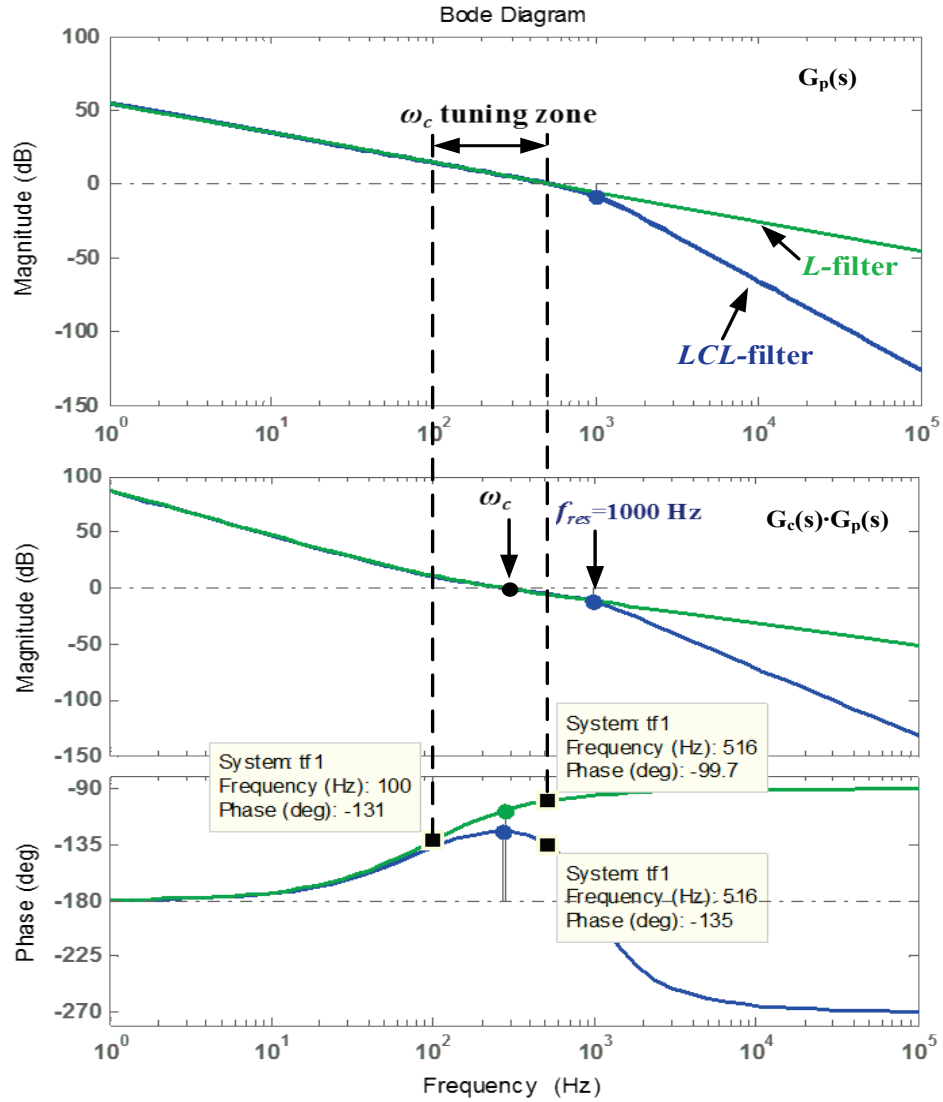


Figure 5.16 Determination of ω_c tuning zone.

Further details of inclusion of stability concerns into the design phase will be stated in each corresponding step. The proposed *LCL*-filter design in Figure 5.17 is presented with a step-by-step procedure below. The input variables of the algorithm are the rated power of the grid connected VSC (S_n), the switching frequency (f_{sw}), frequency of the grid network (f_g), the low-side line-to-line voltage of the grid interface transformer (v_g), DC-link voltage of the modeled energy source (V_{DC}), power factor (PF), and the preferred current feedback variable.

Step-1: Base impedance Z_b and the base capacitance C_b are calculated by means of (5.1) and (5.2) as presented in the conventional design section.

Step-2: The reactive power absorption (x) by the filter capacitance C_f is determined regarding the power level and the power factor target of the design. C_f is generally confined into 1-5% of C_b to deliver a PF within 0.95-1 as depicted in (5.3).

Step-3: In the design algorithm, the resonant frequency ω_{res} is chosen as a fraction of ω_{samp} i.e. $\omega_{res} = \lambda \omega_{samp}$. λ is generally set within 0.1-0.4 as suggested in [56][58]. However, designation of λ primarily depends on the maximum switching frequency (i.e. sampling frequency) and the preferred LCL resonance damping technique.

For instance, at medium power designs (100-500kW) the switching frequency can be set above 2-3 kHz. Thus, active damping is generally feasible for such switching frequencies and $\lambda=0.1$ can be selected as the starting value in the algorithm [69]. On the other hand, for the high power applications (>500 kW) the switching frequency must be kept lower than 2-3 kHz [69]. Owing to this low switching frequency range, low resonant frequency selections result in bulky and costly filter components. To avoid gigantic filter components, the attenuation of the filter must be compromised and the resonant frequency is selected rather high. Thus, 0.18-0.20 should be the onset value of λ . As mentioned in the former chapter, at high resonant frequencies ($\omega_{res} > \omega_{crit}$) active damping does not have any contribution to the stability due to very limited phase margins of the current controllers. Further details will be provided in the case-study illustrations of the LCL -design algorithm.

Lastly, the appointed resonant frequency must be checked whether it satisfies the stability condition stated in (5.12). This stability condition states that stability problems emerge as the control frequency is increased to achieve a higher control bandwidth (BW). Likewise, keeping the control frequency constant and decreasing the resonant frequency to achieve better damping of the switching harmonics also causes stability issues [61].

$$10\omega_g < \omega_{res} < \frac{\omega_{smp}}{2} \quad (5.12)$$

If the stability condition does not hold, resonant frequency must be tuned by updating λ as depicted in Figure 5.17.

Step-4: Grid-side inductance is designated proportional to the converter-side inductance (L_c) as shown in (5.5).

For minimum filter size, total energy stored in the filter must be the smallest [56][57][60][63][68]. Hence, to maximize the filter attenuation around switching harmonics and minimize the filter size, L_c and L_g must be selected as $r=1$.

(5.7) is reorganized as in (5.13) by reflecting r .

$$\omega_{res} = \sqrt{\frac{L_c + rL_c}{rL_c^2 C_f}} = \sqrt{\frac{r+1}{rL_c C_f}} \quad (5.13)$$

Additionally, the analysis of the current ripple attenuation (from converter side to grid side) of the LCL -filter is beneficial before adopting r value. The relationship between the harmonics generated by the converter and injected into the grid can be found by using (5.7).

The primary objective of the LCL -filter is to confine the current ripple on L_c within 10-25%. Then, with the addition of $L_g C_f$ branch, minimum 80% additional current ripple attenuation with respect to the ripple on the converter side (10-25%) is aimed. To deduce, the final target of the LCL -filter is to reduce the current ripple on the grid-side to 2-5% of I_r in total. Thereby, maximum 0.2 (20%) harmonic injection to the grid is allowed.

Step-5: The conservative α tuning region should provide phase margins higher than 45° to ensure closed-loop stability. α is basically computed by proportioning ω_c to ω_{res} as mentioned in the beginning whereas ω_c is arranged using K_p (Figure 5.16). It should be noted that K_p is calculated using symmetrical optimum approach, so (4.18)

is used to calculate K_p in the forward open-loop transfer function. Thus, the design algorithm does not contain K_p tuning phase, it simply calculates the optimal value for each set. But, K_p tuning will be provided as a separate detailed algorithm in the next section. Consequently, $\alpha = \omega_c / \omega_{res}$ where ω_c is found using $G_c(s) \cdot G_p(s)$ and $G_c(s)$ is dependent on K_p , so α calculation is dependent on K_p and it is computed in the algorithm for K_p found by symmetrical optimum.

The possible α tuning zone can be adopted as 0.1-0.5 based on the suggested ω_c tuning zones in [57][58][59]. Plus, the illustration in Figure 5.16 also verifies that interval of 0.1-0.5 is a suitable region for α adjustment. As evident, α tuning region spans a large frequency spectrum and the optimum solution in the control point of view always settles around 0.3 [56][57][59][69]. Nevertheless, setting α to 0.3 does not always provide the optimum solution for the specified type of the application. This approach may lead to overdesign of the filter components by providing phase margins much higher than needed and likewise weak design situations may also occur for the applications requiring higher phase margins. Therefore, desired α can be varied as long as the resulting phase margin satisfies the dynamic requirements of the design. For this reason, α is not constrained strictly in the *LCL*-filter design, only condition for α is to reside in the wide α tuning region of 0.1-0.5. For a more specific α target, detailed control analyses presented in Section 5.3.2 must be done in conjunction with the *LCL*-filter design phase. For a possible solution set inputted to the control algorithm, the conservative α tuning region can be determined and updated α zone can be inputted to the *LCL*-filter design algorithm as demonstrated in Figure 5.17. By doing so, the iterations are relocated around the optimum design point and overdesign or weak design situations are prevented while time consumed during *LCL*-design phase is minimized. Further details will be embodied in the following sections.

Step-6: Resulting filter components are simulated in this step and steady-state analyses are carried out. Then, the quality of grid current is assessed in the light of widely used grid code requirements. According to type of the application, the grid code requirements change significantly. Voltage level and short circuit current ratio

(SCR) of the PCC are two of the most important features of the grid that define the individual harmonic limits and the total harmonic distortion limit for the specified application [75]. If the designed *LCL*-filter delivers an overdesign solution, the resonant frequency should be shifted to higher values so that the attenuation capability of the filter is diminished in this way, so is the filter size. Similarly, in case of a weak design solution, the resonant frequency should be shifted to lower values to increase its attenuation capability. However, the size of the filter would also increase. Since the filter capacitor value is fixed in the beginning of the design algorithm, modified resonant frequency would force change in filter inductance values.

If the filter parameters fulfill all of the requirements, they are qualified for the system. If the desired steady-state performance cannot be obtained for all of the possible combinations, changing the filter capacitance and starting over the design algorithm is needed. Besides, it is beneficial to assess distinct design outputs under a number of different values of the filter capacitances. Distinct combinations may provide satisfactory performances in terms of steady-state and dynamic performances. In that way, the most optimum solution according to priority of the design (size, cost, reliability, and etc.) is acquired from the set of a number of optimum solutions. Finally, changing the switching frequency in the walls of efficiency constraint of the design is another recommended option in case of no optimum solutions (Figure 5.17). Apart from switching frequency adjustment, change of the DC link voltage, PWM pattern to a different modulation method or a converter topology with more voltage levels might provide the expansion of the filter parameter range (i.e. λ and α) [76].

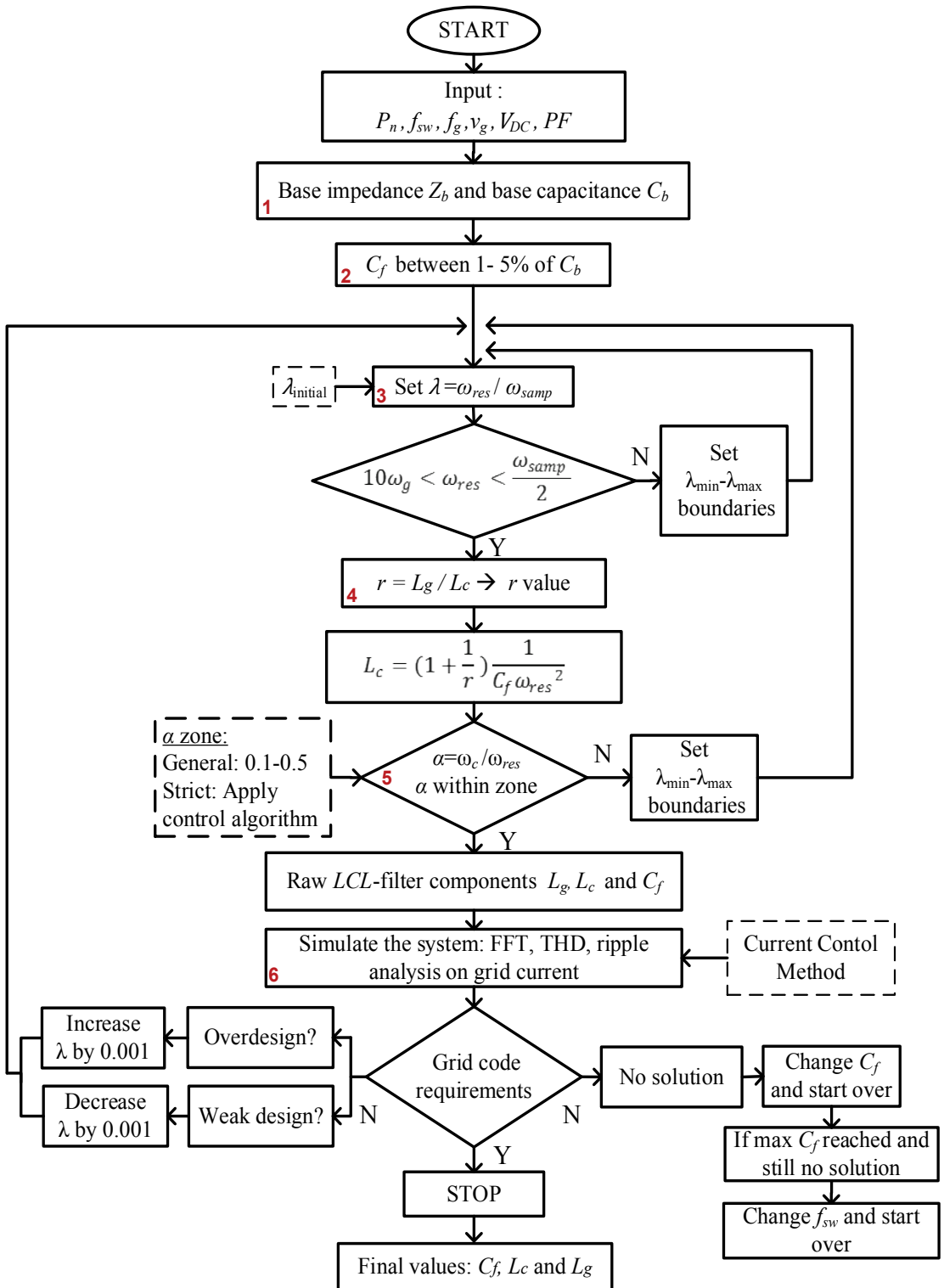


Figure 5.17 Proposed LCL-filter design algorithm.

5.3.1. Case-Studies

In this section, the performance analysis of the three VSC topologies will be conducted through case studies. *LCL*-filter design phase of 0.25 MVA case will be elaborated by following the algorithm in Figure 5.17 in step by step manner. The resultant *LCL*-filter elements of the other two cases will be provided by tabulated results for simplicity. Detailed transient and steady-state performance analyses utilizing the designed filter elements will also be tabulated for each case and 1 MVA case will be used to give further assessment of the dynamic and steady-state performances.

Grid-connected PWM converters employ space-vector PWM (SVPWM). The input data of the design algorithm in Figure 5.17 is provided in Table 5.4.

Table 5.4 Input parameters for case-studies.

Elements	Parameters	Values		
Converter	S_n	250 kVA	1 MVA	3 MVA
	f_{sw}^*	4 kHz	2 kHz	1 kHz
	f_{samp}	8 kHz	4 kHz	2 kHz
	V_{DC}	750 V	1070 V	1070 V
Grid	V_g	400 V _{rms}	690V _{rms}	690 V _{rms}
	f_g	50 Hz	50 Hz	50 Hz
	PF	0.95-1	0.95-1	0.95-1

*Switching frequency is calculated using the methodology given in Chapter 3.

5.3.1.1. Case-Study I: 250 kVA System

Step-1:

$$Z_b=0.64 \Omega, C_b=4.97 \text{ mF}$$

Step-2:

$$\text{Let } x=0.03 \rightarrow C_f=0.03*4.97 \text{ mF}=150\mu\text{F}$$

Step-3: Initial λ value can be started from 0.1 for the opted switching frequency. However, in order to decrease iteration steps and increase the accuracy by narrowing down the λ interval, the approximate rough values of the filter elements could be used as feed-forward terms. For instance, the rough value of the converter-side inductance can be found by using (5.4).

$$\text{Min value: } L_{c,initial} = 750/(12*4000*513*0.25) \approx 121\mu\text{H} (5.94\%)$$

$$\text{Max value: } L_{c,initial} = 750/(12*4000*513*0.10) \approx 304\mu\text{H} (14.92\%)$$

Thereby; for the fixed value of the filter capacitor (150 μ F), minimum and maximum values of the resonant frequency can be set by using (5.7).

$$\text{Min value: } \omega_{res,initial} = 6616 \text{ rad/sec} \equiv 1053 \text{ Hz} \quad (\text{for } L_{c,initial} \text{ max})$$

$$\text{Max value: } \omega_{res,initial} = 10462 \text{ rad/sec} \equiv 1665 \text{ Hz} \quad (\text{for } L_{c,initial} \text{ min})$$

Finally, λ interval to be spanned with an accurate resolution throughout the design procedure can be found as follows:

$$\lambda_{min} = 1053/8000 = 0.1317$$

$$\lambda_{max} = 1665/8000 = 0.2082$$

As proven above, initial value of $\lambda_{initial}=0.1$ contains λ_{min} value for the set of input parameters. Feed-forwarding with rough filter components narrowed down the λ interval, as expected. To further ease the computation of minimum and maximum boundaries of λ , initial L_c values can be set within 0.04-0.15 p.u. [69].

Designated resonant frequency must hold the condition in (5.12). Otherwise, λ_{min} and λ_{max} should be limited to hold (5.12).

Additionally, starting by setting the resonant frequency at the lowest position (λ_{min}) yields the highest possible value of L_c value, i.e. overdesign in general. Therefore, $\lambda_{initial}$ may be set to λ_{max} initially and decreased with an adequate sensitivity in each step. By doing so, design is started with weak-design criterion and optimum filter components are obtained with iterative steps. However, computation of FFT, THD,

and ripple for each combination of the filter components is somewhat laborious. Therefore, the design algorithm presented in Figure 5.17 may be rearranged as follows. Instead of adopting trial-error approach, the set of all possible resonant frequency values and hence corresponding sets of L_c , L_g and α can be constructed easily with the aid of mathematical tools such as MATLAB[®]. Then, by adopting a reasonable α set value from α tuning zone, corresponding L_c and L_g values can be extracted from the solution space where numerous solutions may exist. The resulting updated algorithm is shown in Figure 5.18.

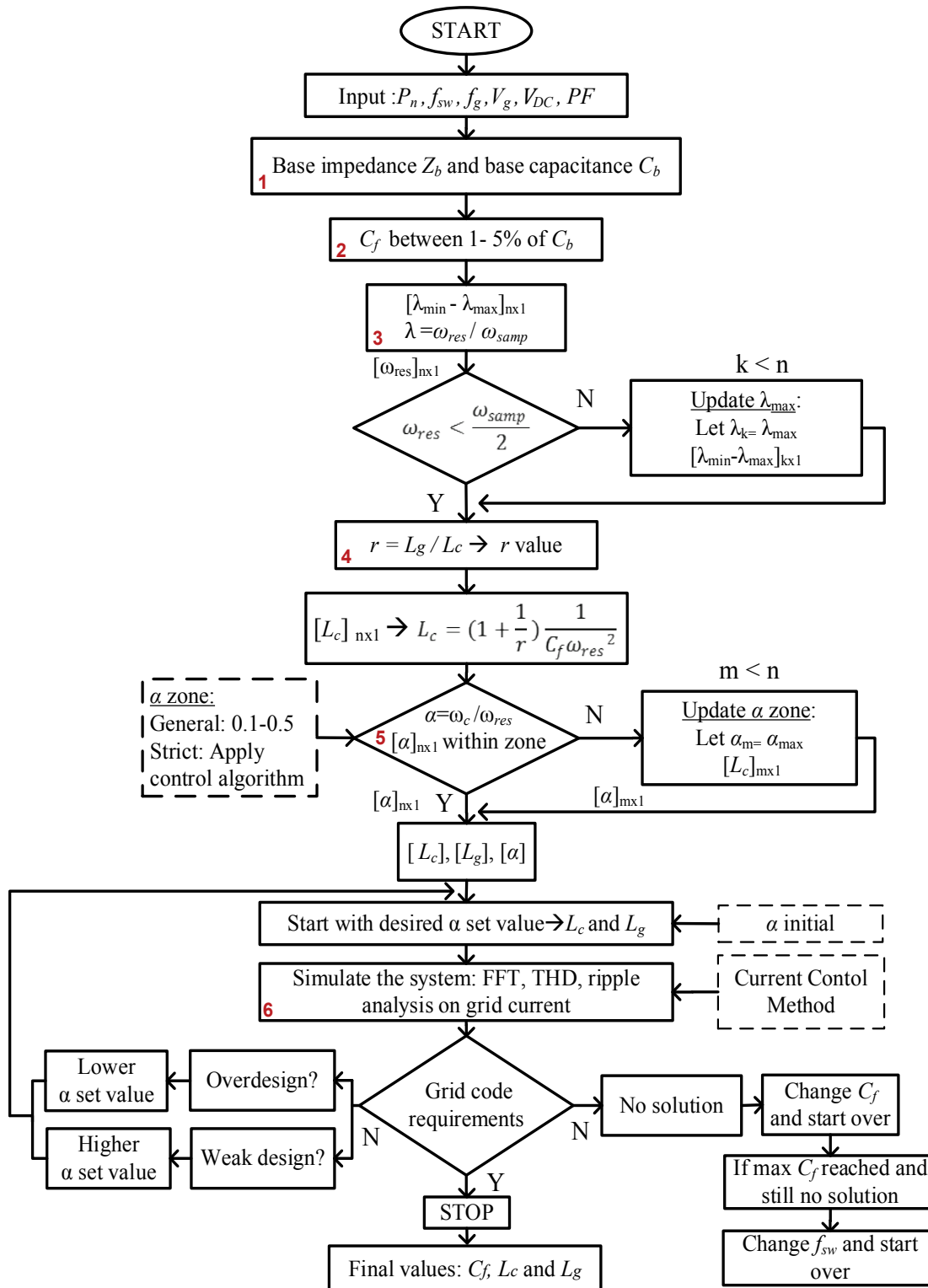


Figure 5.18 Proposed LCL-filter design algorithm (updated).

Step-4 and 5: $r=1$ and $L_g=L_c$

$$L_c = \left(1 + \frac{1}{r}\right) \frac{1}{C_f \omega_{res}^2} = \frac{2}{C_f \omega_{res}^2}$$

λ	: [0.1317 0.1327 0.1337... 0.2072 0.2082]	→ 76x1 matrix
f_{res} (Hz)	: [1665 1657 1650 ... 1065 1057]	→ 76x1 matrix
L_c (μ H)	: [122 123 124 ... 297 302]	→ 76x1 matrix
α	: [0.2727 0.2740 0.2754 ... 0.4234 0.4262]	→ 76x1 matrix

Step-6:

The algorithm aims to deliver optimum filter elements that guarantee sufficient phase margin and control system bandwidth for stability and fast dynamic response. Therefore, special emphasis must be put on the extent of α . Many control books and published papers regarding *LCL*-filter control issues recommend to set α around 0.3 regarding the optimum damping condition $\zeta=0.707$ [57][58]. However, setting α to 0.3 does not always provide the optimum solution for the specified type of the application. This approach may lead to overdesign of the filter components by providing phase margins much higher than needed. Therefore, the distance between the resonant frequency and the crossover frequency may be decreased (i.e. α decreased) if the resulting phase margin satisfies the dynamic requirements of the design. For this reason, yielded α matrix is considered and for several values of α , analyses are conducted as tabulated in Table 5.5.

For the desired reactive power absorption, intervals spanned by λ and α are visualized in Figure 5.19. Overlapping portions state that identical system dynamics can be achieved with distinct filter parameters, priority of the design phase (cost, size, attenuation, etc.) agrees on the optimum parameter set within the solution space.

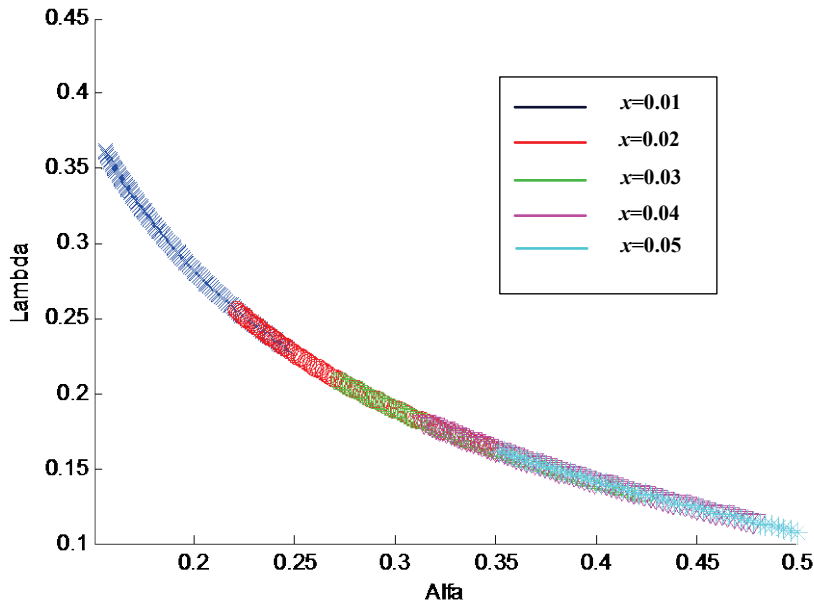


Figure 5.19 Set of λ vs. α .

Apart from the dynamic analyses, the steady-state performance of the designed *LCL*-filter is also examined through simulation in this step. As can be seen in Table 5.5, converging to a distinct α set value alters the filtering performance owing to the distinct filter inductances. Furthermore, GCF and CCF methods also yield different filter inductances as stated in the beginning of section. In the light of steady-state and transient-state performance assessment for three distinct filter designs, the most suitable set of filter components is chosen. Definitely, filter parameters yielded by different α values can also be tested, those three values in Table 5.5 are just selected to highlight the variation of steady-state and transient-state performance. To accelerate the filter design procedure, further tips on designation of α will be provided in Chapter 7.

It should be noted that all of the examinations regarding GCF control employ AD; whereas, analyses under CCF control employ only ID. Because, the main concern of this comparison is to highlight the prominent differences between GCF (with AD) and CCF (only ID) control methods in terms of steady-state and transient-state performance outputs. Hence, this approach is adopted for all three case-studies.

Table 5.5 Performance analysis for $C_f=150\mu\text{F}$ (3%).

	Filter	$\alpha=0.27$	$\alpha=0.30$	$\alpha=0.34$
<i>CCF</i>	<i>L_c Inductance</i>	122 μH	147 μH	189 μH
<i>GCF</i>		112 μH	136 μH	172 μH
	Steady-State Analysis	$\alpha=0.27$	$\alpha=0.30$	$\alpha=0.34$
<i>CCF</i>	<i>Grid Current THD_i</i>	1.22%	0.96%	0.38%
<i>GCF</i>		1.43%	1.12%	0.47%
<i>CCF</i>	<i>Conv. Current THD_i</i>	9.87%	7.97%	5.22%
<i>GCF</i>		11.01%	9.27%	4.97%
<i>CCF</i>	<i>Peak-to-peak conv. current ripple</i>	23.37%	17.51%	12.93%
<i>GCF</i>		25.33%	20.12%	13.79%
	Transient Analysis	$\alpha=0.27$	$\alpha=0.30$	$\alpha=0.34$
<i>CCF</i>	<i>Open-loop</i>	64.5°	62.8°	59.9°
<i>GCF</i>	<i>Phase Margin</i>	51.2°	48.9°	45.9°
<i>CCF</i>	<i>Closed-loop</i>	0.127	0.140	0.158
<i>GCF</i>	<i>damping factor</i>	0.690	0.679	0.651
<i>CCF</i>	<i>Bandwidth(Hz)</i>	404 Hz	421 Hz	457 Hz
<i>GCF</i>		862 Hz	887 Hz	900 Hz

For the selected three different set of filter parameters, it can be inferred that transient performance is compromised as L_c increases. However, resonance is dampened better; concluding the tradeoff between resonance damping and transient-state performance mentioned in the former chapter. In addition, since L_c value is slightly lower for GCF control, steady-state results show slightly worse performance as expected. Besides, undamped resonant peak present in CCF case almost halves the bandwidth of the controllers for all cases, concluding that relying only on ID feature of the current loop limits the bandwidth which in return decelerates the loop response substantially.

5.3.1.2. Case-Study II: 1 MVA System

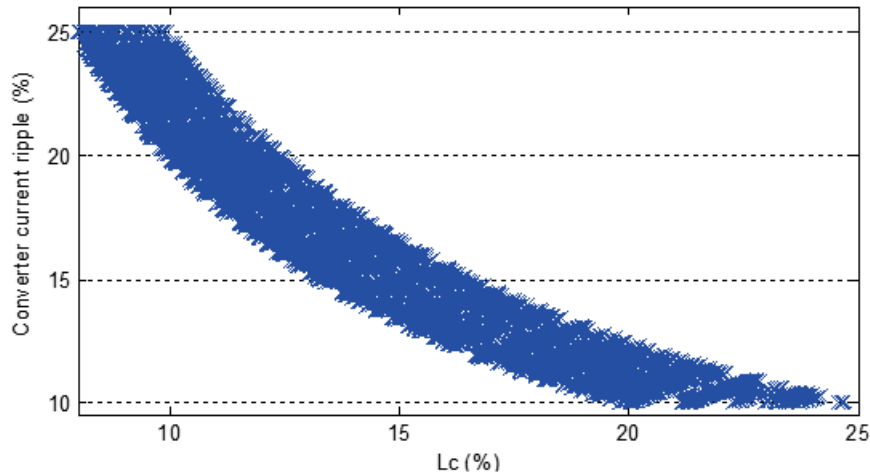


Figure 5.20 Set of solutions for f_{sw} : [2-2.5] kHz, C_f : [0.01-0.05] p.u.

Figure 5.20 reveals the set of solutions generated by the design algorithm (Figure 5.18) in the boundaries of the predetermined λ interval and ω_c tuning zone (i.e. α zone). In order to generate a large solution space, C_f contains the set of values within 0.01-0.05 p.u. whereas f_{sw} is swept within 2-2.5 kHz interval with a proper sensitivity. Each solution is represented with a cross sign 'x' in Figure 5.20. For different combinations of L_c , C_f , and f_{sw} , same filtering performance can be obtained as evident in Figure 5.20. For this reason, when choosing the optimum filter parameters from the set of solutions meeting all requirements, the priority of the design must be well defined. It must be kept in mind that high capacitances require high capacitive reactive power to be supplied by the converter. Moreover, less inductance required for the same filter performance results in a high harmonic content of the converter current. Both aspects cause a high rms value of the converter current, leading as a consequence to a bad utilization of the converter.

On the other hand high inductances work against this effect; but they provoke a large voltage drop at the filter, which must be compensated by the modulation index (m_i)

or an increased DC-link voltage. Thus, a good compromise between the optimal utilization of the converter and low inductance values must be found.

If the main concern of the design is to minimize the filter size, the energy content of the filter inductances as an indicator of volume and weight of the filter can be regarded as an optimization criterion as depicted in (5.14). Due to the quadratic consideration of the converter current, a good utilization of the converter is granted, as well.

$$W_L = \frac{3}{2}(L_c \cdot \hat{I}_c^2 + L_g \cdot \hat{I}_g^2) \quad (5.14)$$

where \hat{I}_c and \hat{I}_g are the peak values of converter-side and grid-side currents, respectively. If the dynamic and steady-state responses are the primary optimization criterion, then the extended analyses involving tuning of control parameters as provided in the following part of this section is required.

The transient analyses together with steady-state analyses for 1 MVA system are tabulated in Table 5.6. For the same α values, GCF and CCF methods yield different resonant frequencies owing to the difference in their transfer functions. The intrinsic characteristics of the current control methods lead to slightly different filter inductances that in return results in distinct steady-state and dynamic responses as depicted in Table 5.6.

For the selected three different set of filter parameters, it can be inferred that transient performance is compromised as L_c increases. However, resonance is dampened better; concluding the tradeoff between resonance damping and transient-state performance. In addition, since L_c value is slightly lower for GCF control, steady-state results show slightly worse performance as expected.

Table 5.6 Performance analysis for $C_f=332\mu\text{F}$ (5%).

	Filter	$\alpha=0.22$	$\alpha=0.25$	$\alpha=0.30$
<i>CCF</i>	L_c inductance	145 μH	186 μH	265 μH
<i>GCF</i>		135 μH	173 μH	244 μH
	Steady-State Analysis	$\alpha=0.22$	$\alpha=0.25$	$\alpha=0.30$
<i>CCF</i>	Grid current THD _i	1.81%	1.04%	0.49%
<i>GCF</i>		2.18%	1.21%	0.59%
<i>CCF</i>	Converter current THD _i	11.87%	8.97%	6.22%
<i>GCF</i>		13.01%	9.77%	6.80%
<i>CCF</i>	Peak-to-peak conv. current ripple	25.37%	18.51%	14.93%
<i>GCF</i>		28.33%	21.12%	15.79%
	Transient Analysis	$\alpha=0.22$	$\alpha=0.25$	$\alpha=0.30$
<i>CCF</i>	Open-loop phase margin	67.3°	65.8°	62.8°
<i>GCF</i>		55.2°	52.8°	49.1°
<i>CCF</i>	Closed-loop damping factor	0.103	0.117	0.140
<i>GCF</i>		0.683	0.667	0.624
<i>CCF</i>	Bandwidth(Hz)	325.20	349.07	389.30
<i>GCF</i>		397.91	418.61	442.91

For instance, $\alpha=0.22$ case is taken into account to further assess the differences between designed *LCL*-filter components under CCF and GCF methods in terms of steady-state and the dynamic performance analyses. CCF method damps the resonance harmonics only by its inherent feature. This inherent feature is sufficient to stabilize the system; however, it provides insufficient resonance damping as can be realized from the weakly blunted resonance peak in Figure 5.21. Open-loop damping factor that the proportional gain constant of PI controller K_p (inherent damping) provides is around $\zeta=0.2$ where it turns out to be 0.103 in the closed-loop system. This weakly blunted resonance peak is very likely to excite resonance in a lossless *LCL*-filter if any small amount of harmonics exists around the resonant frequency. There are two types of harmonics that can exist around the resonant frequency. The first one is the resonant harmonics caused by the insufficient

damping of the resonant poles of the system. The second one is the switching harmonics caused by the PWM switching [60]. In the cases that switching frequency has to be kept very low (as in this case at high power applications), the resonant harmonics cannot be isolated from the switching harmonics i.e. f_{res} cannot be set lower than half of f_{sw} unless gigantic filter inductors are devised. The case $\alpha=0.22$ under CCF sets the resonant frequency at 1025 Hz whereas half of the switching frequency is 1000 Hz. In this situation, the resonant harmonics mixes up with the switching harmonics in the frequency band. Even if the resonant component is eliminated with numerous damping methods, switching harmonics would excite the resonance as long as the weakly blunted resonance peak is present as in Figure 5.21.

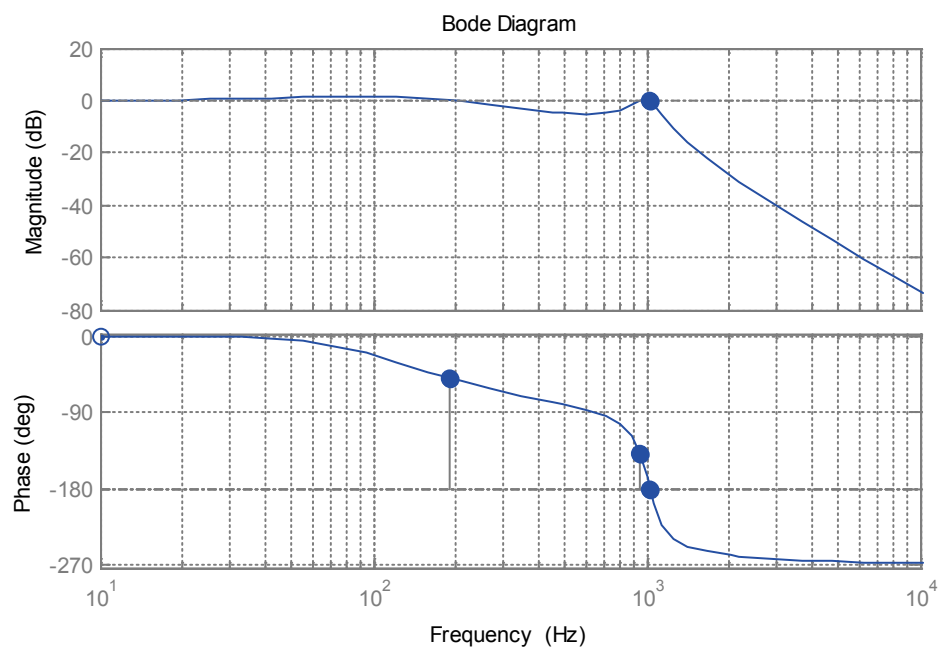


Figure 5.21 Closed-loop bode plot – CCF ($\alpha=0.22$, $L_c=145\mu\text{H}$).

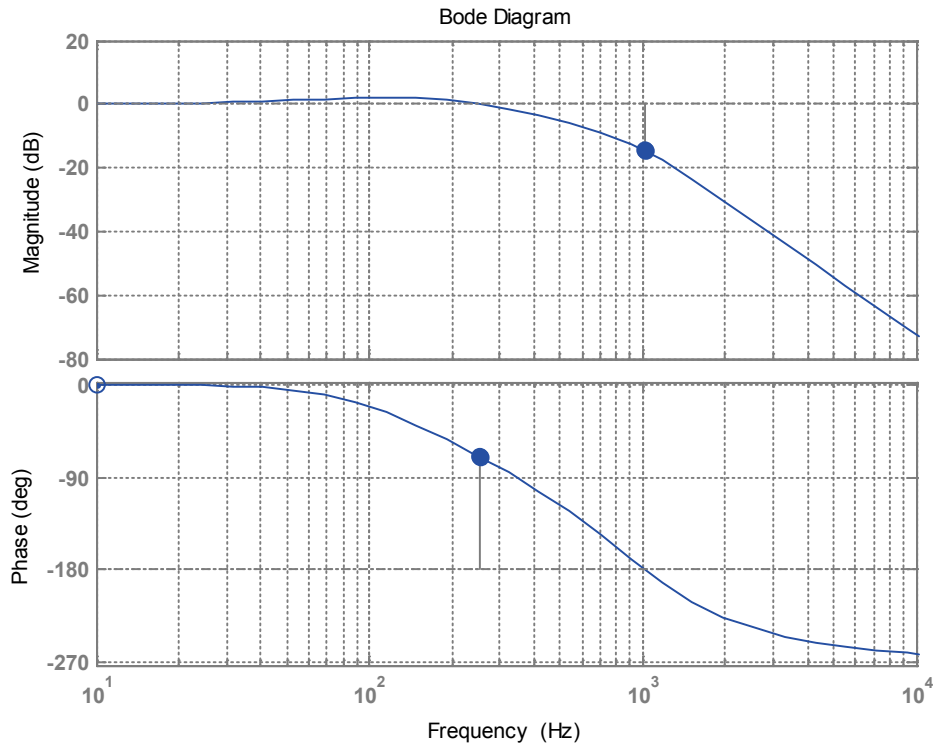


Figure 5.22 Closed-loop bode plot – GCF ($\alpha=0.22$, $L_c=135\mu\text{H}$).

On the other hand, GCF method utilizes active damping feature to damp the resonance oscillations properly. The proportional gain of the active damping controller K_d is adjusted to deliver an open-loop damping factor $\zeta=0.707$ leading to $\zeta=0.683$ in the closed-loop system. Thus, there is not any visible resonance peak in the closed-loop magnitude response as depicted in Figure 5.22.

Moreover, CCF provides much higher phase margins compared to GCF method for all three cases in Table 5.6. This is due to the fact that increasing damping factors degrade phase margins considerably as previously visualized by means of Figure 4.31 and Figure 4.32. Consequently, the trade-off between damping factor and phase margin is verified by the designed *LCL*-filter parameters once again. The dynamic performance of the designed system for $\alpha=0.22$ case is simulated in Figure 5.23.

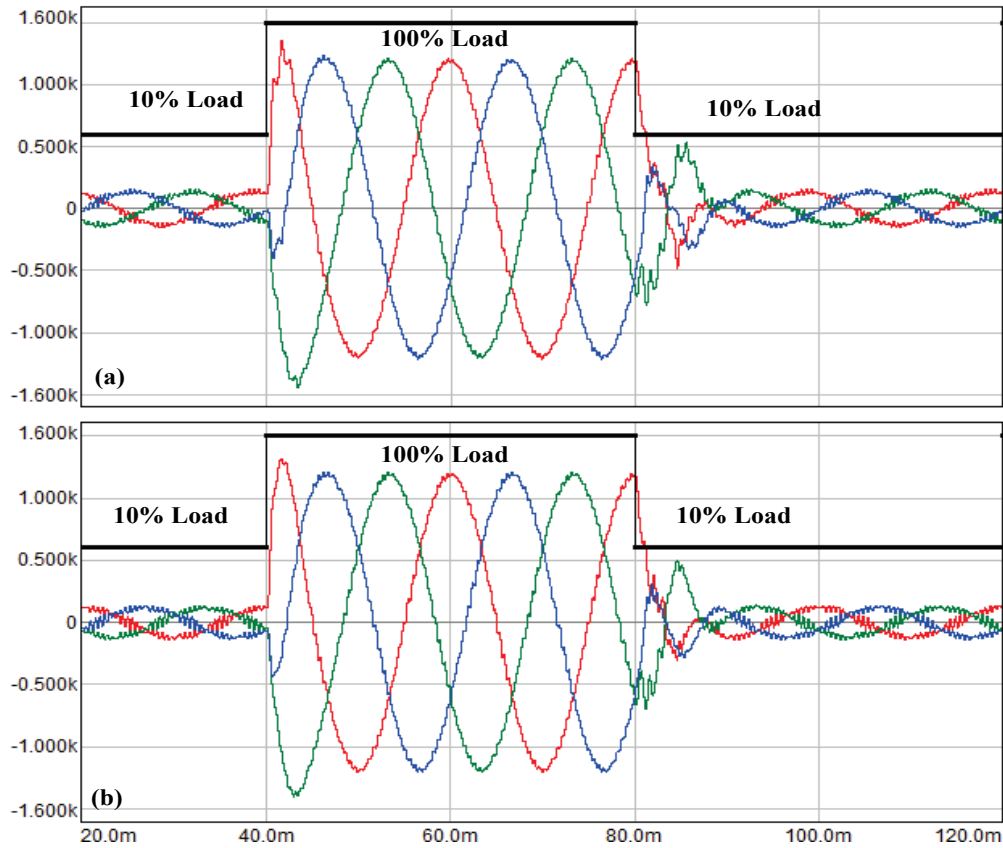


Figure 5.23 Dynamic response for $\alpha=0.22$ (a) CCF, $L_c=145\mu\text{H}$ (b) GCF, $L_c=135\mu\text{H}$.

As expected, serious transient oscillations occur at the transition from light load condition (10%) to full load condition (100%), and vice-versa, in CCF method due to underdamped resonance poles. Therefore, using only CCF method to damp the resonance of the corresponding LCL -filter parameters is not reliable since these oscillations are very likely to unveil instabilities in the controllers. For this reason, using additional damping to further blunt the underdamped resonance peak should be regarded. Additional details will be provided in the following section considering the control algorithm stated in Section 5.3.2. Control algorithm provides fine-tuning of the damping factor ζ in conjunction with proportional gain constant K_p in the light of phase margin and bandwidth targets of the design.

5.3.1.3. Case-Study III: 3 MVA System

The transient analyses together with steady-state analyses for 3 MVA system are tabulated in Table 5.7. For the same α values, GCF and CCF methods yield different resonant frequencies, thus filter inductances differ that in return results in distinct steady-state and dynamic responses as depicted in Table 5.7.

Table 5.7 Performance analysis for $C_f=1000\mu\text{F}$ (5%).

	Filter	$\alpha=0.17$	$\alpha=0.18$	$\alpha=0.19$
<i>CCF</i>	<i>L_c Inductance</i>	116 μH	130 μH	150 μH
<i>GCF</i>		110 μH	123 μH	141 μH
	Steady-State Analysis	$\alpha=0.17$	$\alpha=0.18$	$\alpha=0.19$
<i>CCF</i>	<i>Grid Current THD_i</i>	6.07%	4.77%	4.41%
<i>GCF</i>		6.96%	4.76%	3.24%
<i>CCF</i>	<i>Conv. Current THD_i</i>	14.93%	12.22%	8.17%
<i>GCF</i>		15.94%	12.89%	9.66%
<i>CCF</i>	<i>Peak-to-peak conv. current ripple</i>	23.23%	21.96%	17.60%
<i>GCF</i>		26.16%	23.37%	15.15%
	Transient Analysis	$\alpha=0.17$	$\alpha=0.18$	$\alpha=0.19$
<i>CCF</i>	<i>Open-loop Phase Margin</i>	69.4°	69.0°	68.1°
<i>GCF</i>		59.0°	58.2°	72.6°
<i>CCF</i>	<i>Closed-loop damping factor</i>	0.103	0.117	0.394
<i>GCF</i>		0.704	0.703	0.409
<i>CCF</i>	<i>Bandwidth</i>	151 Hz	153 Hz	157 Hz
<i>GCF</i>		181 Hz	185 Hz	147 Hz

For the selected three different set of filter parameters, it can be inferred that transient performance is compromised as L_c increases. However, resonance is dampened better; concluding the tradeoff between resonance damping and transient-state performance. In addition, since L_c value is slightly lower for GCF control, steady-state results show slightly worse performance as expected. Furthermore, for $\alpha=0.19$, stability could not be achieved by only using CCF method (e.g. ID) and use of additional AD did not help stabilize the system under CCF control. Likewise,

GCF control with AD cannot stabilize the system for $\alpha=0.19$. This was caused by the decreased phase margins of closed-loop controllers due to excessive increase of inductance values. For this reason, PD technique with proper damping resistors was utilized to obtain the steady-state and transient-state outputs for $\alpha=0.19$ case in Table 5.7. Consequently, near $\alpha=0.19$ and above i.e. if the distance between ω_c and ω_{res} further diminishes, phase margin is severely degraded and active damping and inherent damping solutions do not hold any longer. Since, low switching frequency constraints bandwidth of the controllers for such a filter designed for high power VSC. Then, utilization of PD becomes inevitable. It should also be noted that converging around $\alpha=0.30$ would not give the optimal filter elements for 3 MVA system design, which would otherwise lead to overdesign.

5.3.2. Tuning of Control Parameters

Up until, *LCL*-filter design and corresponding steady-state and transient-state analysis have been conducted for three distinct power levels. Even if designed filter parameters satisfy steady-state specifications of the system, in general transient-state specifications require further tuning of the controllers.

For this reason, this section gives a detailed controller tuning methodology with a flow diagram depicted in Figure 5.24. This diagram merges the know-how controller tuning methods into a concrete methodology involving controller tuning for AD and PD methods. With the resulting *LCL*-filter design algorithm outputs; rise time (t_r), fall time (t_f), settling time (t_s), maximum percent overshoot (OS (%)), and the oscillatory behavior on the transient response should be examined in detail. To properly tune controller parameters, desired phase margin and system bandwidth should be updated by adjusting the set values of the damping factor and the proportional gain constant K_p .

The flow of the algorithm will be elaborated by means of case studies demonstrated in the next section. Note that the diagram in Figure 5.24 is more suitable for controllers using GCF. In Section 5.3.2.2, it will be modified for the controllers utilizing CCF via a case-study.

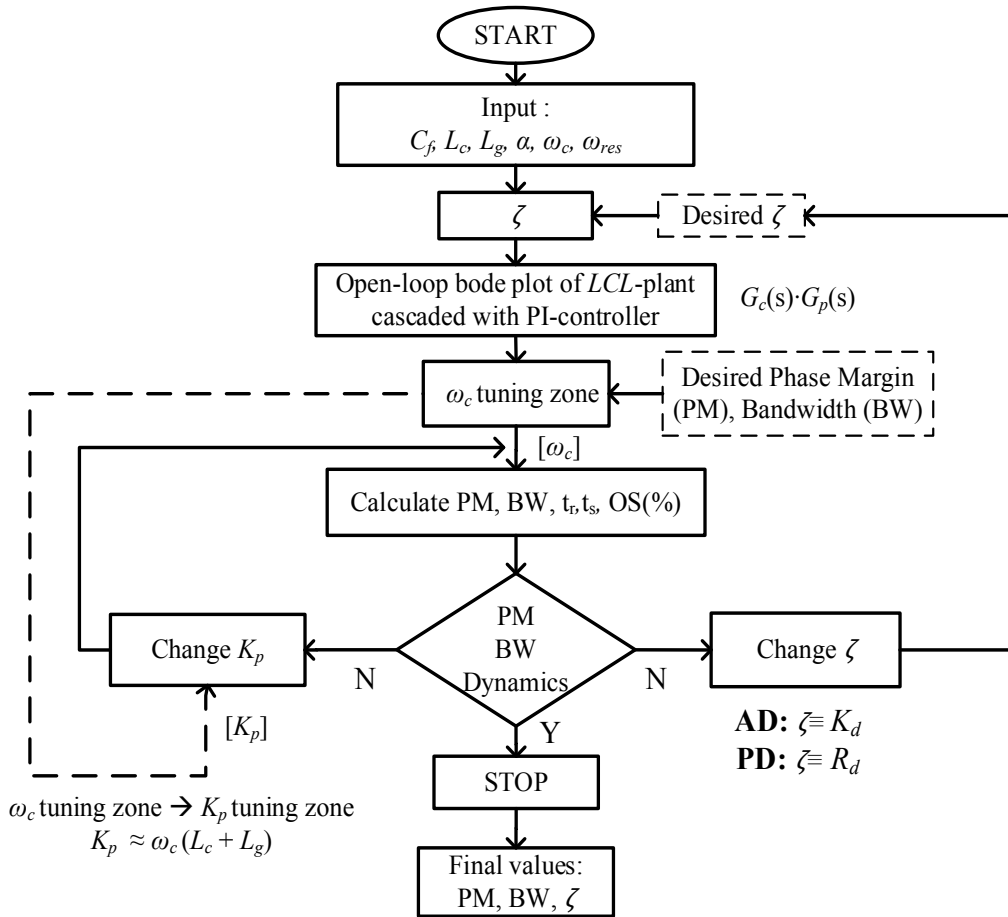


Figure 5.24 Proposed controller tuning methodology for GCF technique.

The parameters provided in Table 5.8 will be employed in the case studies.

Table 5.8 Parameters to be used in case-studies.

Filter	$\alpha=0.22$	
	GCF	CCF
$L_c (=L_g)$ Inductance	135 μ H	145 μ H
C_f Capacitance	332 μ F	
Initial K_p	0.36	0.39
Integral Time Constant T_i	0.00225	

5.3.2.1. Detailed Analysis for 1 MVA Case under GCF Method

In this subsection tuning of control parameters is achieved by following the procedure presented in Figure 5.24. Since this algorithm is suitable for GCF control employing additional damping (AD or PD) to damp the resonance, there should be slight modifications (as to be presented in the next section) in the algorithm for the systems benefitting only ID characteristics of the control loop i.e. not using any additional damping (only possible for CCF method). If additional damping is required for a system utilizing ID method, then the algorithm in Figure 5.24 should be applied to determine required damping factor to damp the resonance appropriately. As a remark, GCF method does not provide any inherent damping in the control loop unlike CCF case. For this reason, in GCF method damping is supplied only by damping factor adjusted with K_d (AD) and R_d (PD) by means of the formulas provided in Chapter 4 as highlighted below.

$$\text{AD: } 2\zeta\omega_{res} = \frac{K_d}{L_c}$$

$$\text{PD: } 2\zeta\omega_{res} = \frac{R_d(L_c + L_g)}{L_c L_g}$$

To start with, desired ζ is set to the optimum value 0.707 initially. Then, magnitude and phase response of the forward transfer function ($G_p(s)$ and $G_c(s)$) is shown in Figure 5.25. The boundaries of ω_c tuning zone are highlighted with dots in Figure 5.25. Note that presence of the PI-controller in the forward path transfer function has shifted phase reversal to 1.01 kHz where the resonant frequency is 1.06 kHz. As a remark, phase reversal occurs at the resonant frequency when only open loop *LCL*-plant is considered as demonstrated in Figure 4.31. As calculated in Table 5.6, open-loop phase margin delivered in GCF method is 55.2° where ω_c zone guarantees phase margins within the interval of 45° - 55° . It is obvious that initial K_p value calculated by (4.18) always provides maximum achievable phase margin regardless of the ζ set value. Next, the K_p tuning zone can be determined by the proposed K_p

calculation formula in (4.39) with regard to ω_c tuning zone depicted with block dots in Figure 5.25. The resulting K_p tuning range yields the interval of 0.17-0.76.

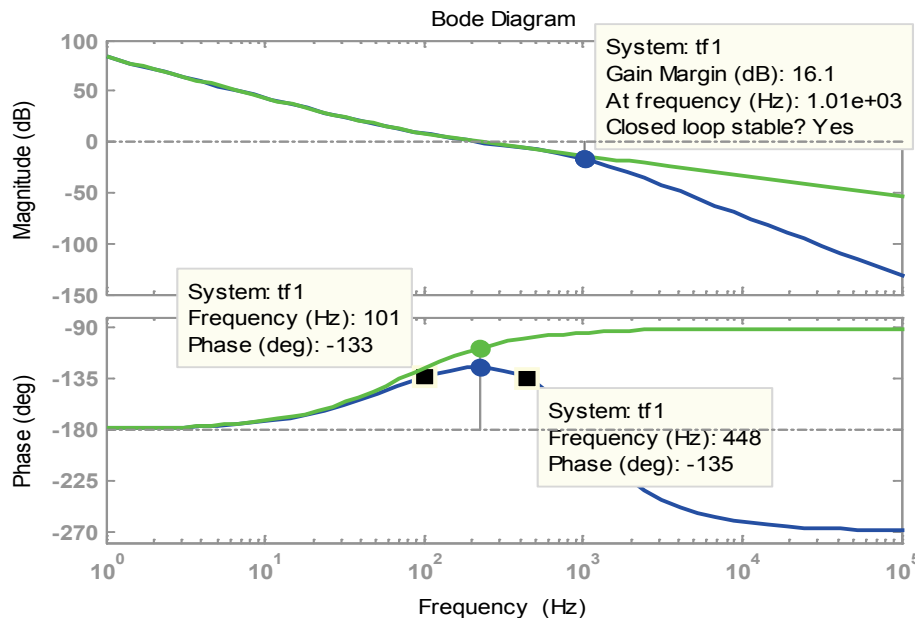


Figure 5.25 Designating ω_c zone for controller tuning.

After determining the tuning zones, the parameters regarding the dynamic performance are computed with the aid of mathematical tools. For instance, the bandwidth of the design turns out to be 397 Hz as stated in Table 5.6. If the design specifications require a faster current loop i.e. higher bandwidth, there are two possible ways to increase the bandwidth. The first one is to increase K_p value so that the crossover frequency ω_c could get higher and hence higher bandwidth is obtained. The other alternative approach is to change the initially determined damping factor ζ . If the damping factor is decreased, the crossover frequency tends to shift to higher frequencies that increase the control system bandwidth in return. However, further reduction of ζ below 0.5 is not recommended, since it will not improve the phase response too much but only lead to even serious oscillations [57][58][68]. On the other hand, increasing bandwidth by each of the proposed approaches compromises the system stability and optimum resonance damping. In order to limit the degradation in phase margin caused by the increase of K_p , ω_c tuning region is

defined and hence a stable system is ensured provided that ω_c reside within the region.

Table 5.9 illustrates the tuning procedure for a number of K_p values selected within the predetermined K_p tuning zone for this case study.

Table 5.9 K_p tuning regarding PM and BW (GCF).

K_p	$\zeta=0.707$			$\zeta=0.5$		
	PM (degree)	$f_c (\equiv \omega_c)$ (Hz)	BW (Hz)	PM (degree)	$f_c (\equiv \omega_c)$ (Hz)	BW (Hz)
0.3	54.9	188	320	59.2	191	307
0.35	55.2	216	384	60	221	371
0.4	54.9	245	454	60.2	251	453
0.45	54.2	273	529	60	282	576
0.5	53.2	301	602	59.3	314	744
0.55	52	330	671	58.4	347	859
0.6	50.6	358	731	57.1	381	932

As can be realized in Table 5.9, decreasing damping factor to 0.5 does not provide higher control bandwidth for the optimum K_p value ($K_p = 0.36$) even if the crossover frequency is increased. Thereby, tuning of K_p is also required to achieve higher bandwidth values when damping factor ζ is decreased. This result exactly overlaps with the findings in Section 4.4.5. Since, diminishing damping factor also diminishes the phase lag of the *LCL*-filter as depicted in Figure 4.32 and in return phase margin is increased as can be recognized in Table 5.9. By doing so, a margin is allocated to further increase the crossover frequency without degrading the phase margin significantly. Thus, increase in the crossover frequency in exchange nullifies the earnings supplied by the decrease in damping factor. Consequently, system has more or less the same phase margin with a higher crossover frequency and bandwidth at a lower resonance damping.

According to Table 5.9, increasing K_p value increases the control system bandwidth while compromising the phase margin of the system for each case. However, beyond

the optimum K_p value the increase in $\zeta=0.5$ case is much sharper compared to $\zeta=0.707$ case. Thereby, to reach higher bandwidth by decreasing the damping factor is confirmed by the results in Table 5.9. Besides, increasing only K_p value to enhance the bandwidth without changing the damping factor of the system is also verified. Note that resulting phase margins for all of the combinations in Table 5.9 ensures a stable closed-loop system because K_p is swept within its predefined tuning region and the damping factor is not decreased beyond 0.5 in the light of theoretical suggestions [57][68][69].

Figure 5.26 addresses the impact of K_p sweep both for $\zeta=0.707$ and $\zeta=0.5$ cases. As expected from the results in Table 5.9, increasing K_p degrades the closed-loop damping performance of the system substantially and likely to cause transient oscillations.

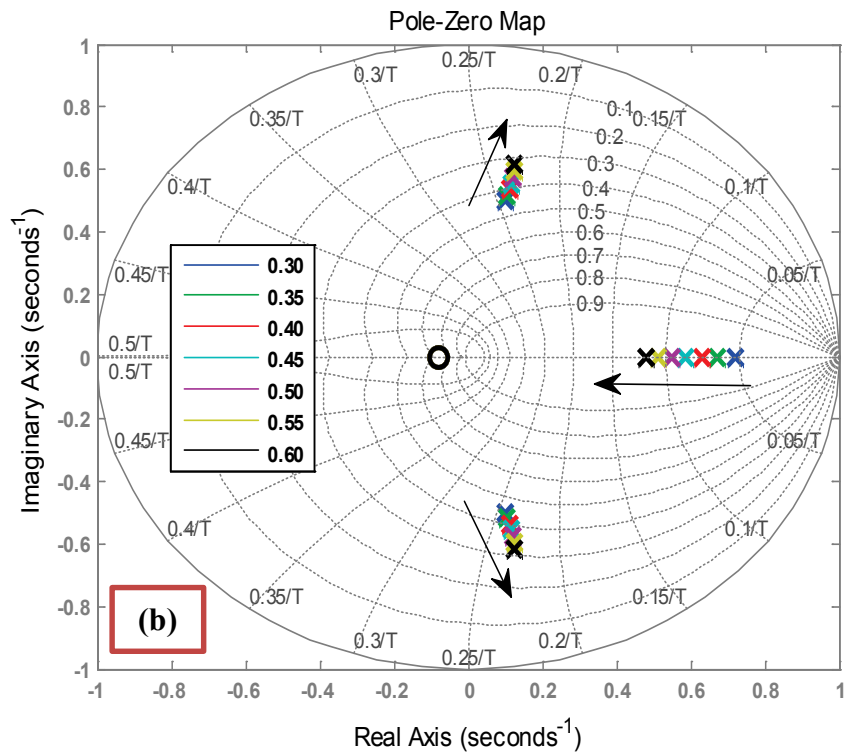
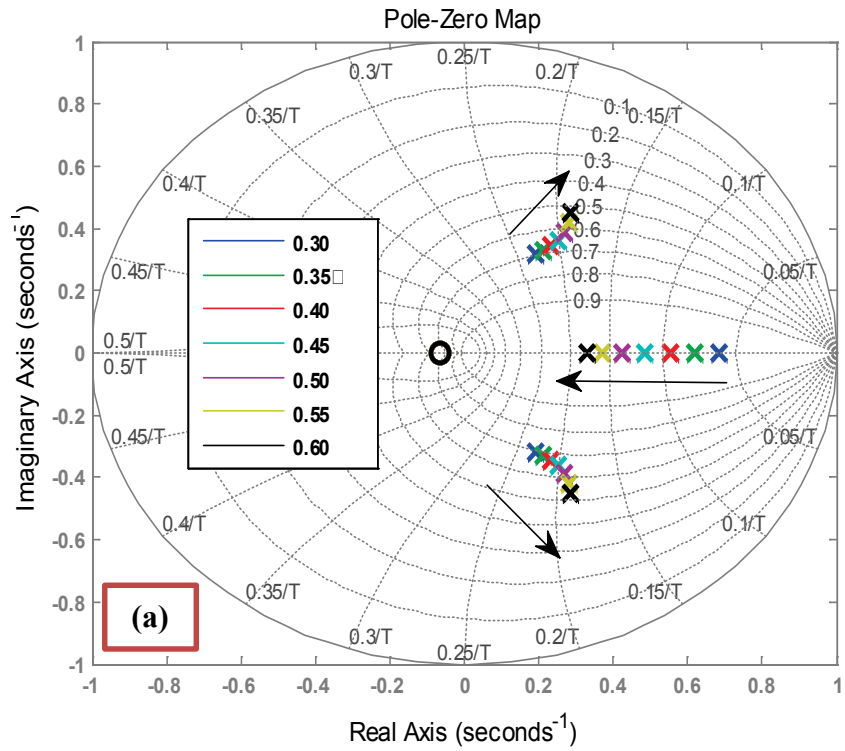


Figure 5.26 Pole-zero movements under GCF for (a) $\zeta=0.707$ (b) $\zeta=0.5$.

Besides, low frequency pole on the real axis tends to move away from the imaginary axis, hence attenuating its impact, and causing the system to gradually lose stability. As mentioned in the former chapter, real pole slows down of the overall step response, therefore resulting in a longer settling time. However, it damps transient oscillations more powerfully, leading to smaller overshoots [68]. All in all, lower K_p values keep the real pole close to the imaginary axis, in return, settling times are higher but oscillations are damped forcefully as can be seen in Figure 5.27(a). The numeric data of overshoot, settling time, and rise time characteristics in Figure 5.27 are tabulated in Table 5.10 for $\zeta=0.707$ case.

Table 5.10 Dynamic performance outputs (GCF– $\zeta=0.707$).

$\zeta=0.707$ K_p	Overshoot	Settling Time (s)	Rise Time (s)
0.3	23.6%	6.53m	0.859m
0.35	22.1%	6.19m	0.736m
0.4	21.1%	5.95m	0.645m
0.45	20.6%	5.74m	0.576m
0.5	21.1%	5.56m	0.523m
0.55	22.6%	5.38m	0.482m
0.6	24.7%	5.21m	0.449m
1	44.2%	4.01m	0.310m

According to the numerical performance values, $K_p=0.45$ provides the best dynamic response in terms of overshoot. Beyond 0.45, larger overshoots are observed. Since K_p is constrained in an interval warranting a satisfactory dynamic performance, outside of this tuning region should also be inspected to depict further deterioration in the dynamics. For this purpose, K_p value is increased to 1 and the step response under this value is obtained as shown in Figure 5.27(b). As anticipated, transient oscillations arise and overshoot almost doubles its value even if the settling time and rise are diminished substantially. To deduce, increased bandwidths in Table 5.9 lead to lower rise time and settling time while decreased phase margins result in worsened overshoots and transient oscillations.

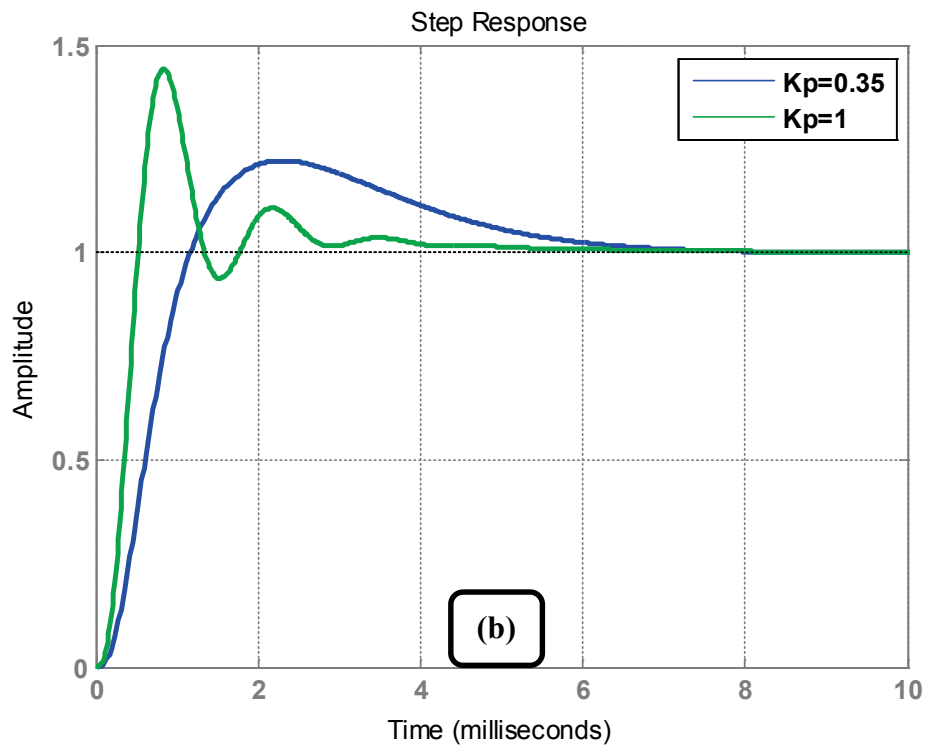
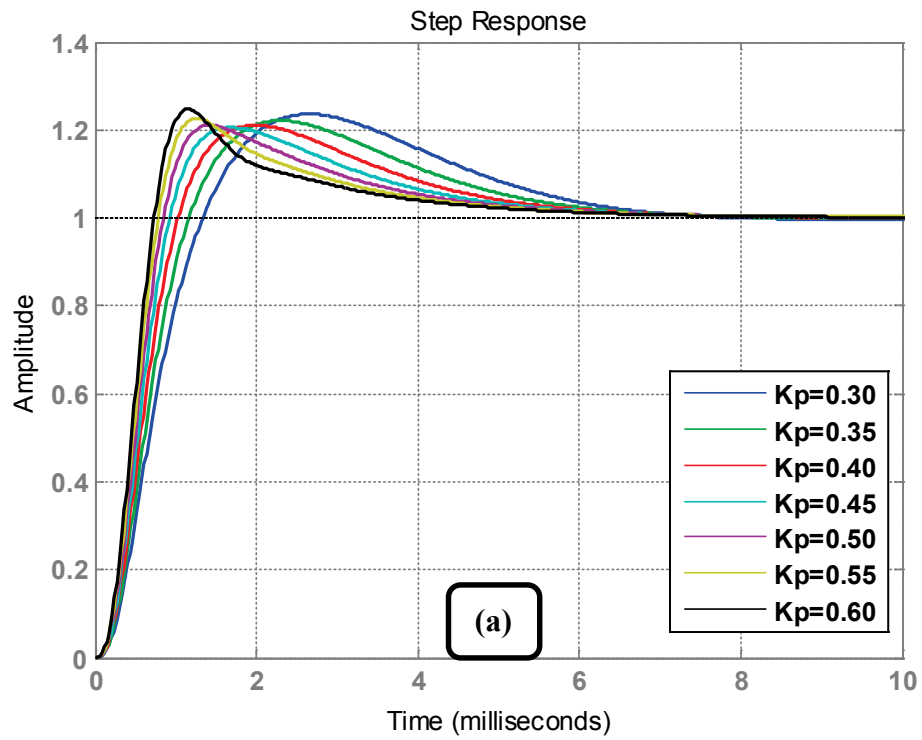


Figure 5.27 Step responses under GCF for $\zeta=0.707$ (a) $K_p=[0.3:0.6]$ (b) $K_p=[0.35, 1]$.

Last, in order to reveal worsened phase margin at $K_p=1$ under $\zeta=0.707$ case, open-loop and close-loop characteristics are acquired in Figure 5.28. Open-loop phase margin is shrunk from 55.2° to 36.1° leading to a very low closed-loop phase margin of 12.5° .

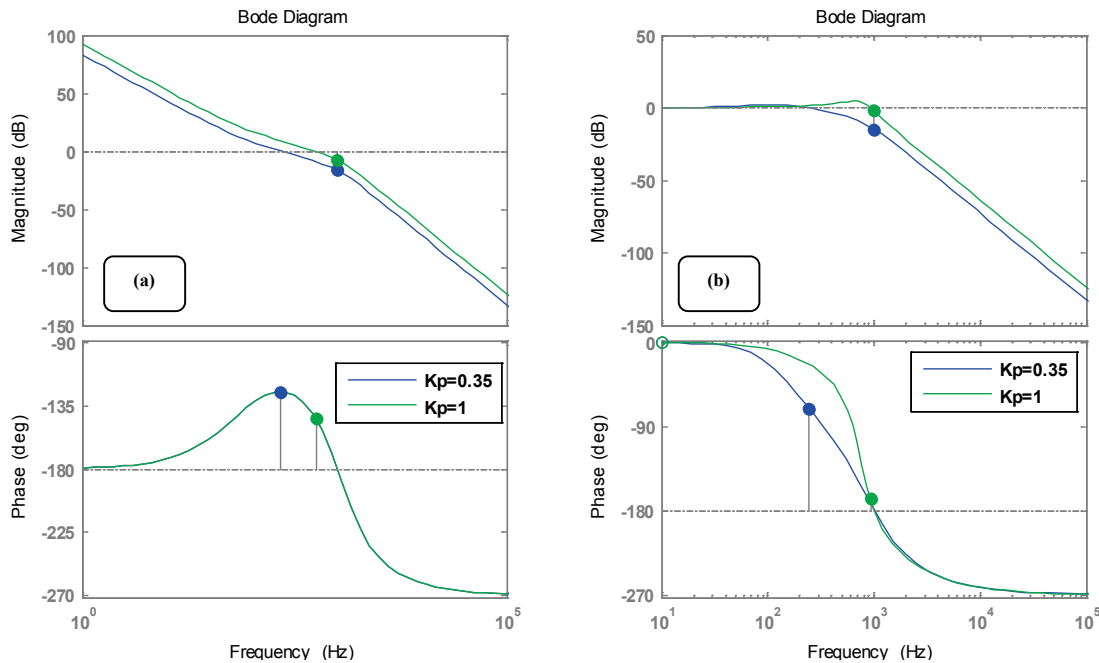


Figure 5.28 Bode plots for $\zeta=0.707$ (a) Open-loop (PM: 55.2° , 36.1°) (b) Closed-loop (PM: 110° , 12.5°).

Next, the same examinations are conducted for the case $\zeta=0.5$. Resulting dynamic performances are tabulated in Table 5.11. In this case, $K_p=0.55$ provides the best dynamic response in terms of overshoot. Beyond this value, larger overshoots are detected. The tendency of the dynamic properties are the same as the case for $\zeta=0.707$. Therefore, it is better to focus on the differences caused by the decreased damping factor.

Lower resonance damping due to the decreased damping factor 0.5 has resulted in more serious transient oscillations (Figure 5.29) and hence larger settling times compared to $\zeta=0.707$ case for all K_p values (Table 5.10). On the other hand, decreased damping factor 0.5 has led to lower rise times (owing to the increased

bandwidth) providing a faster current loop compared to $\zeta=0.707$ case for all K_p values. And in $\zeta=0.5$ case, better overshoot performance is achieved for all K_p values by the increased phase margins as highlighted in Table 5.10.

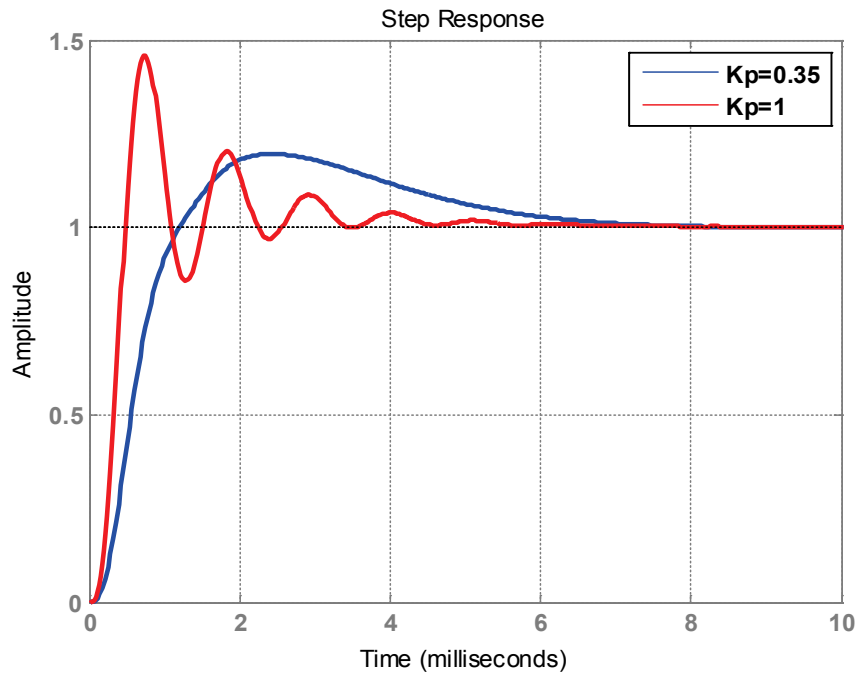


Figure 5.29 Step response under GCF at $\zeta=0.5$ for $K_p=[0.35,1]$.

Table 5.11 Dynamic performance outputs (GCF– $\zeta=0.5$).

$\zeta=0.5$ K_p	Overshoot	Settling Time (s)	Rise Time (s)
0.3	21.3%	6.75m	0.866m
0.35	19.6%	6.40m	0.710m
0.4	18.3%	6.13m	0.598m
0.45	17.2%	5.90m	0.521m
0.5	16.1%	5.69m	0.468m
0.55	15.1%	5.50m	0.429m
0.6	18.6%	5.32m	0.397m
1	45.6%	4.32m	0.276m

Likewise, $K_p=1$ under $\zeta=0.5$ case yields open-loop phase margin shrinking from 60° to 36.8° leading to an unstable closed-loop (phase margin is negative, -17.5°). Since open-loop and closed-loop attributes under $\zeta=0.5$ case very similar to $\zeta=0.707$ case (Figure 5.28), they are not shown for simplicity except for yielded margins above.

5.3.2.2. Detailed Analysis for 1 MVA Case under CCF Method

Aforementioned analyses in this study put a serious emphasis on different current feedback methods. Since, GCF and CCF requires different approaches on design and tuning phases. For instance, K_p has no considerable impact on resonance damping issue in GCF method; whereas, it is the only parameter that damps the resonant pole pair in CCF method without any additional damping scheme (i.e. inherent damping). Therefore, as this difference is reflected in the *LCL*-filter design algorithm, it should also be reflected in the procedure of fine-tuning of control parameters.

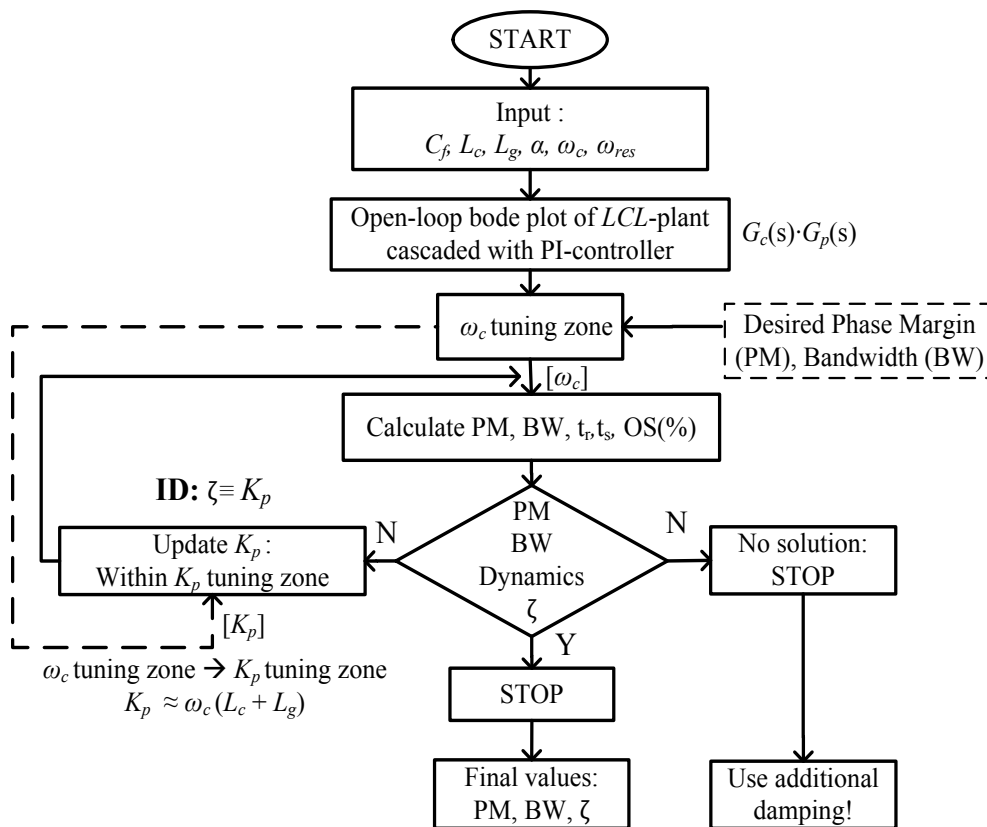


Figure 5.30 Proposed control algorithm for inherent damping (ID).

Figure 5.30 demonstrates the control algorithm modified for ID (CCF without additional damping). This algorithm lacks the explicit determination of the damping factor ζ unlike AD or PD methods. Therefore, it is computed inside the algorithm and returned as an outcome in the end. Then, according to the transient analyses ζ can be altered by varying K_p value within the boundaries of K_p tuning zone.

Table 5.12 illustrates the tuning procedure for a number of K_p values selected within the predetermined K_p tuning zone for ID method. According to Table 5.12, increasing K_p value increases the gain crossover frequency as expected. Besides, $K_p=0.45$ seems to provide slightly higher phase margin than $K_p=0.39$ (67.3°) that is calculated by the symmetrical optimum approach.

Table 5.12 PM and BW tuning for ID.

K_p	PM (degree)	$f_c (\equiv \omega_c)$ (Hz)	BW (Hz)	Stability Condition
0.3	65.1	178	249	Stable
0.35	66.7	205	291	Stable
0.4	67.5	233	339	Stable
0.45	67.7	262	406	Stable
0.5	67.3	291	533	Stable
0.55	66.5	321	N/A	Unstable
0.6	65.2	352	N/A	Unstable

Even though the resulting open-loop phase margins in Table 5.12 seem to provide stable closed-loop systems under increasing K_p , the underdamped resonance peak (as mentioned in Figure 5.21) prevents the closed-loop gain response from descending below -3dB (bandwidth frequency) as of a certain K_p value as shown in Figure 5.31. Hence, for high K_p values the gain response descends below -3dB at very high frequencies. It seems quite good to have such a high bandwidth for the closed-loop system unless the corresponding closed-loop phase margin is calculated.

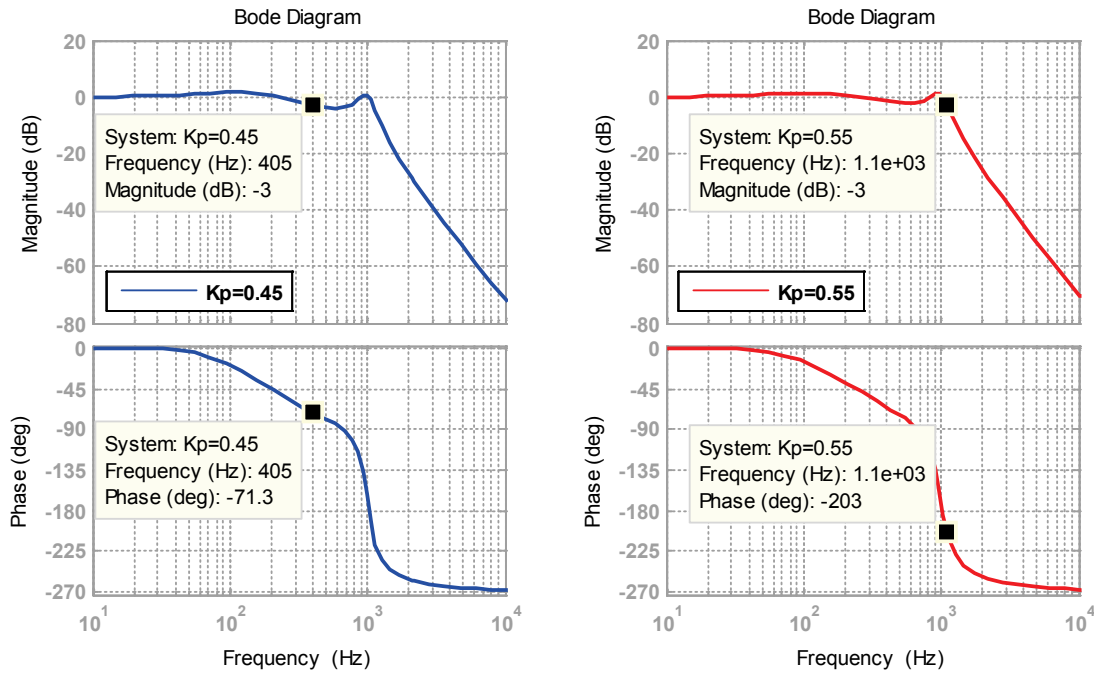


Figure 5.31 Closed-loop bode plot under CCF control ($L_c=145\mu\text{H}$, $\alpha=0.22$).

As can be seen in Figure 5.31, the weakly blunted resonance peak causes zero closed-loop phase margin leading to instability of the current controllers for $K_p=0.55$. Therefore, K_p should not exceed 0.5 in order to ensure a closed-loop stable system. If the desired dynamic response cannot be achieved by K_p values lower than 0.5, using additional damping is inevitable as described in Figure 5.30. Either active damping with capacitor current or passive damping with a simple damping resistor is a suitable solution to completely bring down the underdamped resonance peak. Note also that there is still underdamped resonance peak present in the magnitude response although the system is found to be closed-loop stable for K_p values smaller than 0.5. Nevertheless, it is very likely that unavoidable internal losses in practical systems would dampen this peak [60]. For a more reliable system, additional damping methods can also be implemented even if the stability is insured [57].

With the utilization of either AD or PD under CCF method, underdamped resonant peak in the magnitude response is dampened as depicted in Figure 5.32. In this case, damping is achieved in hybrid manner by adding additional damping (AD or PD) to

ID. For this reason, the required proportional gain constant K_d or damping resistor R_d is calculated by using the equalities below (exhibited in Chapter 4/Appendix A). Thus, in order to achieve the same damping factor under GCF and CCF methods, necessary K_d is always smaller in CCF compared to GCF. Same conclusion holds for R_d as can be seen in the below equality (derivation for PD is shown in Appendix A).

$$\mathbf{AD + ID: } 2\zeta\omega_{res} = \frac{K_p + K_d}{L_c}$$

$$\mathbf{PD + ID: } 2\zeta\omega_{res} = \frac{C_f R_d (L_c + L_g) + K_p [L_g C_f^2 \left(\frac{R_d}{T_i}\right) + L_g C_f]}{C_f L_c L_g + K_p L_g C_f^2 R_d}$$

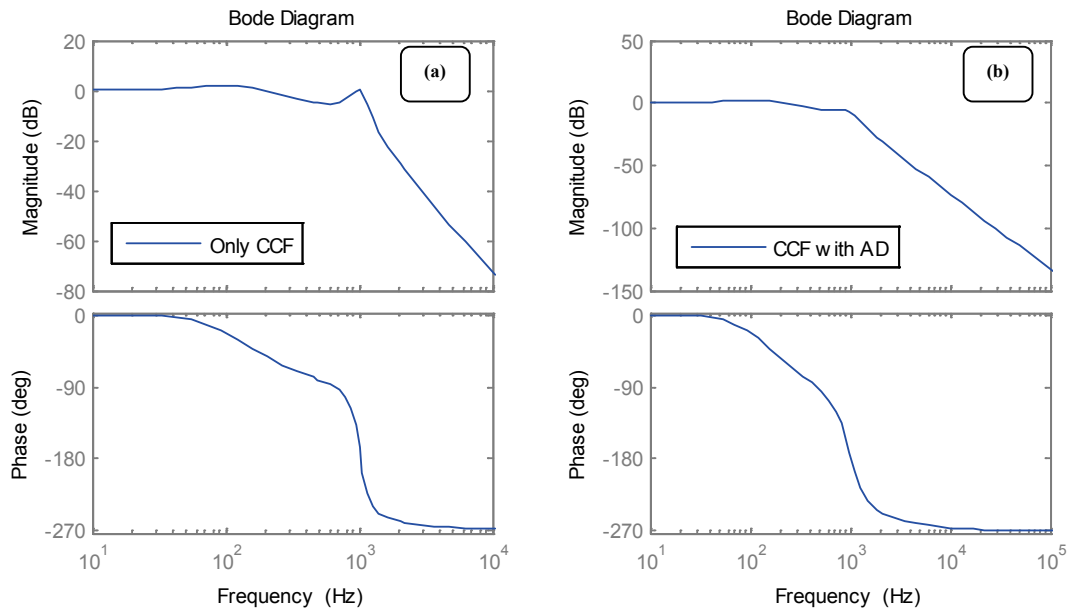


Figure 5.32 Closed-loop bode plots (a) $K_d=0$ (b) $K_d=0.93$.

Numeric values in Table 5.12 were recalculated for the case CCF with AD in Table 5.13. For all K_p values, phase margin and crossover frequency has slightly diminished owing to the introduction of AD block, as anticipated. On the other hand, the maximum achievable control bandwidth of the system has been improved in great extent thanks to the elimination of the underdamped resonant peak.

Table 5.13 K_p tuning regarding PM and BW for ID control with AD.

K_p	PM (degree)	$f_c (\equiv \omega_c)$ (Hz)	BW (Hz)	Stability Condition
0.3	61.7	177	264	Stable
0.35	62.7	204	313	Stable
0.4	62.9	230	374	Stable
0.45	62.6	258	459	Stable
0.5	61.8	285	628	Stable
0.55	60.6	312	809	Stable
0.6	59.0	339	862	Stable

Figure 5.33 and Figure 5.34 reveals the impact of the AD block that has blunted the resonance peak in Figure 5.32. For excessive K_p values, poles track outside the unit circle.

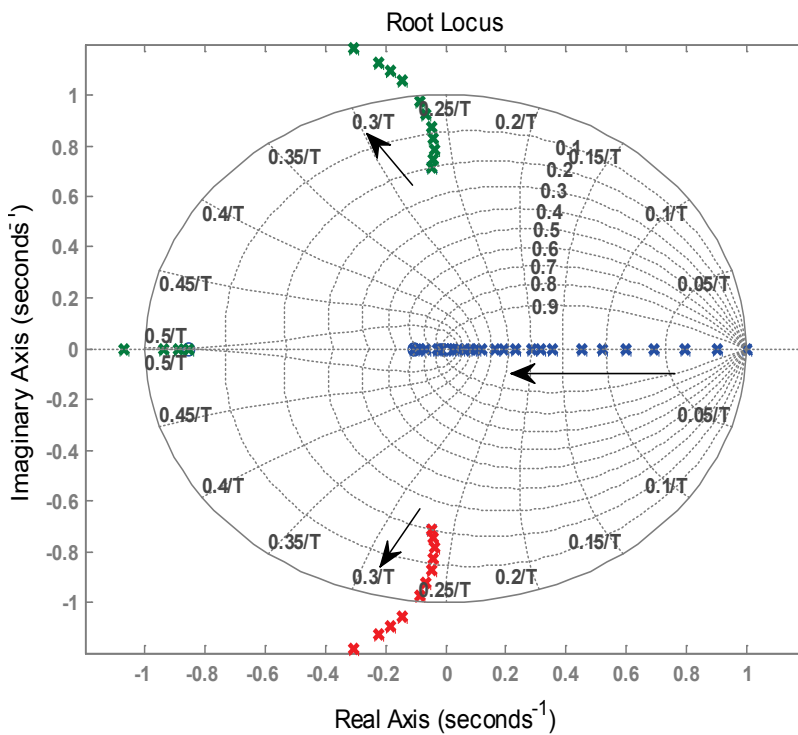


Figure 5.33 Pole movements under CCF control for $L_c=145\mu\text{H}$ (without AD).

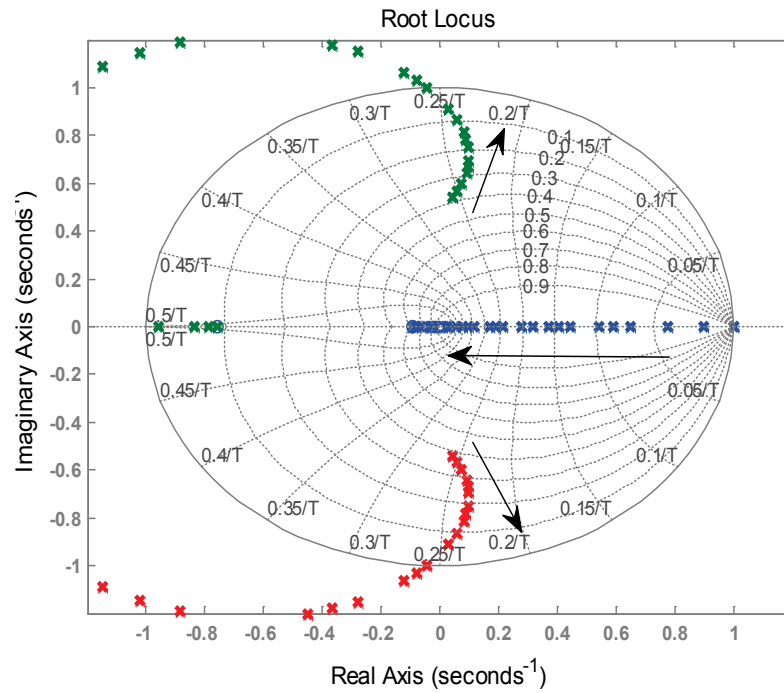


Figure 5.34 Pole movements under CCF control for $L_c=145 \mu\text{H}$ (with AD, $K_d=0.32$).

Proceeding analysis reveals the impact of AD on the step response. Relying on solely ID attribute provides a step response fluctuating at the resonant frequency (Figure 5.35) since the resonance peak is not flattened.

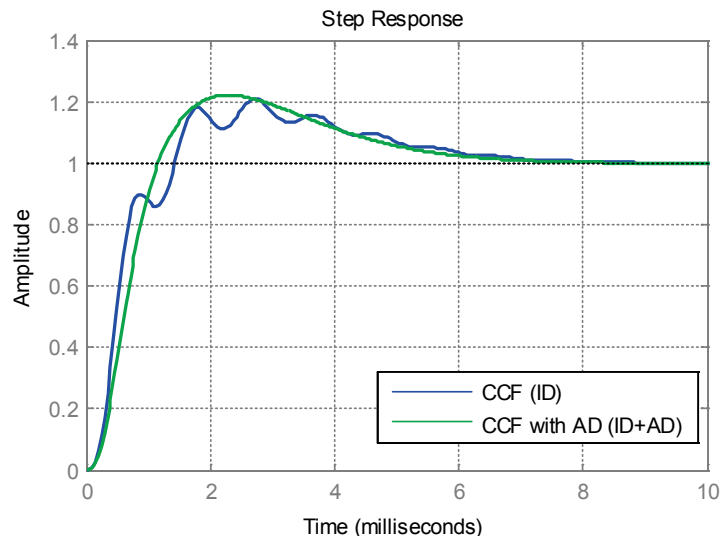


Figure 5.35 Step response under CCF control for $L_c=145 \mu\text{H}$ (with AD, $K_d=0.93$).

On the other hand, with the enabling of AD under CCF method, resonance peak is dampened and step response does not contain any fluctuations at all. Enabling AD feature; however, compromises transient-state performance as evident in Figure 5.35.

The last but the not least analysis to compare the performance of CCF and GCF methods is as follows. The thorough analyses in this section have shown that CCF (without damping and with damping) always provides higher phase margins compared to GCF method. Phase margin extent is calculated through open-loop data to comment on stability once the loop is closed. Nevertheless, checking only the open-loop phase margin of the systems employing CCF method might mislead the designer, particularly if the resonant peak in the magnitude response is underdamped. Therefore, it is always recommended to pay attention on the closed-loop characteristics as well.

Figure 5.36 and Figure 5.37 illustrates the abovementioned situation by depicting the open-loop and the closed-loop characteristics of the system controlled with GCF and CCF, respectively. As can be recognized in these figures, open-loop phase margins are equalized in each method by adjusting K_p value in CCF method. Nonetheless, the closed-loop phase margin becomes 0° for the adjusted value of $K_p=0.82$ in CCF method; whereas, it is found to be 55.2° in GCF method. It is an expected outcome in the light of above findings. Since, increasing K_p value above 0.5 would cause loss of stability unless additional damping is utilized.

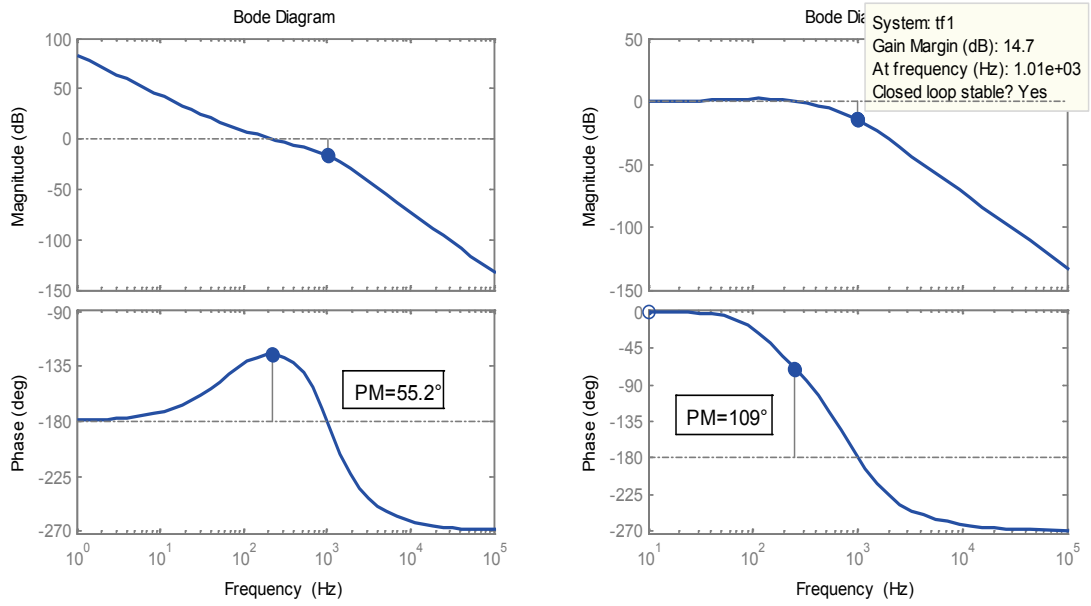


Figure 5.36 Bode plots under GCF control for $K_p=0.36$ (a) Open-loop (b) Closed-loop.

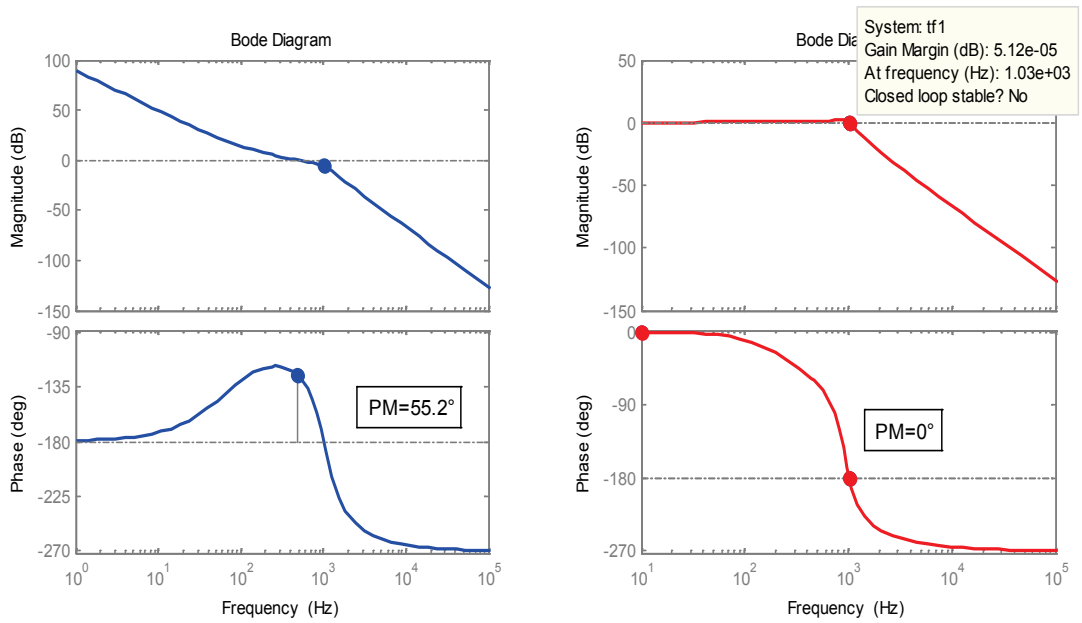


Figure 5.37 Bode plots under CCF control for $K_p=0.82$ (a) Open-loop (b) Closed-loop.

5.4. Summary and Conclusions

This chapter has been constructed upon the bases of Chapter 4. First of all, the importance of type of current feedback variable in filter design has been highlighted. Then, the widely-used conventional *LCL*-filter design has been presented. The design algorithm has proceeded with a case-study employing PD for dampening the resonance. In this case-study, a unique investigation aiming the same resonance damping under GCF and CCF has been provided. Nevertheless, critical damping resistor values have been found different for each of GCF and CCF cases owing to the distinct structure of the current loop. Reduced R_d value in CCF case has delivered both the same open-loop and closed-loop performance as R_d value in GCF method (Figure 5.6 and Figure 5.7). Thereby, passive damping losses have been almost halved under CCF method owing to the inherent damping nature of the current loop.

The stability and the dynamic response of the designed system have also been examined considering the sufficiency of resonant damping. In addition, grid code compatibility has also been investigated regarding the mentioned grid codes and standards. Design procedure has been followed by inspecting the impact of DPWM1 and SVPWM methods on efficiency under different loadings and switching frequencies.

In the second part of this chapter, a novel *LCL*-filter design algorithm has been proposed. This algorithm takes the control point of view of *LCL*-filters into account and provides probably one of the most detailed *LCL*-filter design methodologies in the literature. The prominent advantages of this design methodology are simply the capabilities to cover wide power scales and provide optimal filter elements minimizing size, cost and loss while affording a good filtering performance.

The *LCL*-filter design has been realized through three distinct case studies representing three different power converter designs involving 250 kVA, 1 MVA and 3 MVA VSCs. The steady-state and transient performance of the designed *LCL*-filters for these three distinct cases have been assessed. As a common conclusion,

transient performance is compromised as L_c increases. In other words, if α is set to higher values, phase margin starts to decrease and hence transient performance is degraded. However, resonant harmonics are eliminated better as higher inductance is employed; concluding the tradeoff between resonance damping and transient-state performance. On the other hand, α set value providing optimal filter components no longer converges around 0.3 as the switching frequency diminishes below 2-3 kHz. While $\alpha=0.28-0.34$ provides optimal filter values for 250 kW system, $\alpha=0.18-0.19$ delivers best suiting filter components for 3 MVA system. Thus, it has been proven that setting α around 0.3 is not suitable for every power scale, especially for high power applications. Particularly, converters switched at a few kHz generally suffer from the low controller bandwidth and low closed-loop phase margin and α set value should be kept low to limit the phase margin degradation. For instance, 3 MVA system could not be stabilized without PD for $\alpha > 0.19$ (for each of CCF and GCF control) because closed-loop phase margin decreases too much beyond that value.

Moreover, *LCL*-filter design algorithm has been supported by tuning of control parameters. For this purpose, two separate novel control tuning algorithms for GCF and CCF cases have been developed. These methodology have been exemplified and well-elaborated for 1 MVA case. The main differences in control point of view between CCF and GCF methods have been highlighted via root loci, step responses and bode diagrams. Thus, nuances about controller gain, active damping gain, damping ratio, bandwidth of the controllers, gain crossover frequency, resonance frequency, the relationship in between, and so on are well stated in this chapter.

It has been found that for the same α set point, filter design algorithm under GCF has provided slightly smaller filter components compared to CCF case. It is important to note that same α set point aims to provide filter elements that guarantee the same distance between resonance peak and gain crossover frequency, hence same margins for the control loop are provided. However, in order to obtain alike outcomes under GCF and CCF methods, resonant peak must be flattened properly; otherwise phase margin and dynamics are well degraded, leading to wrong assessment of GCF and CCF methods. For this reason, comparing CCF without additional damping case

with GCF case is not fair since GCF already uses additional damping otherwise system cannot be stabilized. Thus, comparison between GCF and CCF must be evaluated under equally damped resonance peak. The examination between GCF and CCF held in this chapter first concentrated on the comparison of GCF with AD case and CCF without additional damping case. Although the system under GCF employs lower filter inductance, it has provided better dynamic performance compared to the system under CCF since the system has suffered from underdamped resonance peak.

As inferred at the end of Chapter 4, CCF is superior to GCF on stabilization of the current loop if additional damping is not used. However, in practical applications inherent damping cannot be relied on, additional damping is always used regardless of the current control technique. For this reason, AD (if feasible) or PD must always be used to completely bring down the resonance peak. Once the same resonance damping is ensured, step response of the systems under GCF and CCF can be acquired as shown in Figure 5.38. Consequently, having same control loop hardware (AD is used in each method), same resonance damping and sensor count (2 sensors for each method) under the same VSC topology has yielded slightly smaller passive elements under GCF method. Additionally, being consistent with the conclusion drawn at the end of Chapter 4, GCF provides slightly faster and better transient response compared to CCF as revealed in Figure 5.38.

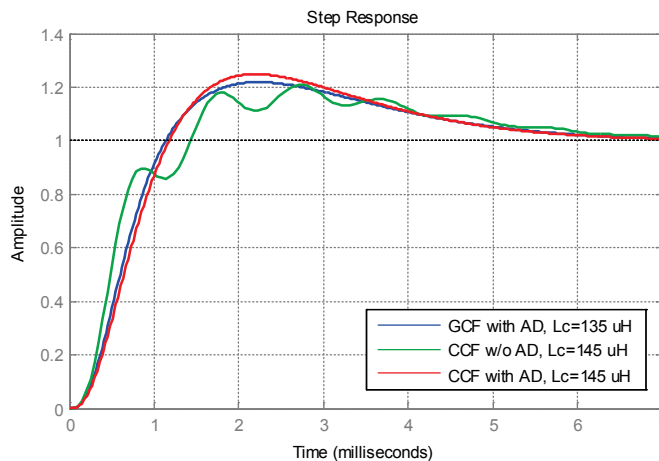


Figure 5.38 Step response comparison between CCF and GCF control.

Up until, converter efficiency specification, VSC topology, PWM method, switching frequency, *LCL*-filter design and tuning for optimal filter size and attenuation have been achieved in a step-by-step manner. As of this point, the VSC topologies to be considered in the eventual design algorithm must be studied well in order to gain experience on topological performance analysis. Thus, next chapter provides as a preliminary study providing detailed topological comparison involving the modeling of semiconductor loss, filter loss, as well as the efficiency, PWM and converter current ripple attributes of each topology.

CHAPTER 6

SEMICONDUCTOR MODULE AND MAGNETIC CIRCUIT LOSS CHARACTERIZATION CONSIDERING CONVERTER TOPOLOGIES AND PWM METHODS

This chapter provides power semiconductor module and magnetic circuit loss characterization considering converter topologies and PWM methods. Since the main focus of this dissertation is to devise a thorough converter design algorithm, this chapter can be deemed as a preliminary study providing a detailed topological comparison involving the modeling of semiconductor loss, filter loss, as well as the efficiency, PWM and converter current ripple attributes of each topology.

6.1. Introduction

As mentioned in the introduction chapter, three-phase two-level and three-phase three-level PWM VSC topologies are widely used in the grid-side converter of back-to-back converter topology. Grid-connected three-phase PWM VSC based wind power converters are generally designed for 500 kW-7 MW power scale nowadays. Hence, particularly for large wind turbine designs the two-level (2L) VSC topology reaches the design limits due to the restricted technology of power semiconductors that can be switched up to only a few kHz. In modern wind turbines utilizing 2L-VSC as the grid-side converter, the maximum rated power cannot exceed a few MW. Thus, for larger wind turbine designs that two-level is not feasible; utilization of higher level VSCs is favored. In the literature, three-level (3L) topologies and multi-level topologies are widely used beyond the power levels that the utilization of 2L-VSC is not viable. Nevertheless, apart from 2L-VSC the scope of this dissertation is only limited to two common 3L-VSC topologies, namely three-level

neutral point clamped converter (3L-NPC) and three-level T-type converter (3L-T). All in all, several analyses involving topological comparison between 2L, 3L-NPC and 3L-T VSCs are conducted as follows.

First of all, a general overview of three topologies will be provided. Then, a general methodology to calculate switching and conduction losses of semiconductors in a computer simulation environment will be delivered. The proposed scheme can be embedded in any design regardless of the simulator as long as the circuit employs ideal switches. Secondly, with the proposed loss calculator, topological semiconductor loss comparison will be made and verified by a design example by means of simulation outputs. Furthermore, *LCL*-filter loss modeling will also be provided regarding topological factors. Thirdly, a general topological efficiency comparison will be delivered by merging the semiconductor loss model and *LCL*-filter loss model.

After completing the loss modeling, formulation of the converter ripple under 2L and 3L-VSC topologies is discussed. Finally, the impact of the favored PWM pattern on output performance of 2L-VSC and 3L-VSC will be examined.

Throughout this chapter, required visual outputs for the performance analysis of the three VSC topologies are obtained using a 1 MVA grid-connected PWM-VSC employing space-vector PWM (SVPWM). For the PWM comparison section discontinuous PMW (DPWM1) pattern will also be employed. Simulation parameters are provided in Table 6.1 (selected from designed set of filter components, $\alpha=0.25$ in Table 5.6). Note that GCF control is favored throughout simulations.

Table 6.1 Simulation parameters for topological comparison analysis.

Converter	S_n	1 MVA	<i>LCL</i> <i>Filter</i>		
	f_{sw}	2 kHz			
	f_{samp}	4 kHz		L_c	173 μ H (11.2%)
	V_{DC}	1070 V		L_g	173 μ H (11.2%)
Grid	V_g	400 V _{rms-line}		C_f	332 μ F (5%)
	f_g	50 Hz			
	PF	0.95-1			

6.2. Overview of Proposed VSC Topologies

Figure 6.1 introduces one leg diagrams of 2L-VSC, 3L-NPC and 3L-T VSC topologies in (a), (b) and (c) respectively. All three converter legs of Figure 1.5 shall be replaced with the 3L leg modules of Figure 1.6, to obtain the full schemes of 3L-NPC and 3L-T type VSCs.

As briefly introduced in Chapter 1, the most promising power electronic converters approach for modern wind turbines are 2L and 3L converters. As also mentioned, decent individual wind turbines are generally designed for low-voltage connection (power of which is injected to the grid via step-up transformers connected to medium voltage), so there some certain power limits that the usage of 2L-VSC starts to lose its superiority. Beyond this level, usage of multilevel converters becomes a remedy. This dissertation contains the usage of only 3L-VSCs in place of 2L-VSC where the utilization of 2L is not feasible. Higher levels are beyond the scope of this thesis. Compared to 2L converters, 3L converters, which have various designs, embrace three voltage levels resulting in certain advantages over 2L-VSC. Firstly, lower total harmonic distortion (THD) of output waveforms is attained, compared to conventional 2L converters, leading to a better match to stringent grid connection standards [78]. Secondly, 3L-VSCs are totally appropriate for multi-megawatt scale wind turbines due to voltage sharing between levels [79]. Thus, 3L-VSCs are capable of supplying higher power even employing medium power semiconductor switches leading to reduction of switching losses. In return, switching frequency can be increased considerably compared to 2L-VSCs [78]-[81].

Three-level VSCs, particularly the 3L-NPC [79], are widely used in industrial medium voltage range applications such as rolling mills, fans, pumps, marine appliances, mining, tractions, and renewable energy [80][81]. On the other hand, NPC has become a favorable alternative for low-voltage wind energy applications recently [82][83]. Compared to 2L-VSC displayed in Figure 6.1(a), 3L-NPC contains two additional active switches and hence two extra isolated gate drivers, and four fast diodes per phase leg as evident in Figure 6.1(b) whereas the basic topology of the 3L-T (Figure 6.1(c)), is simply the extension of the conventional

two-level VSC topology with an active, bidirectional switch to the dc-link midpoint and thus eliminates two diodes per bridge leg [78]. The 3L-T mainly links the advantages of the 2L converter such as low conduction losses, small part count and a simple operation principle with the positive features of the three-level converter such as low switching losses and superior output voltage quality. Hence, 3L-T is regarded to be a perfect alternative to 2L converters for certain low-voltage applications [78].

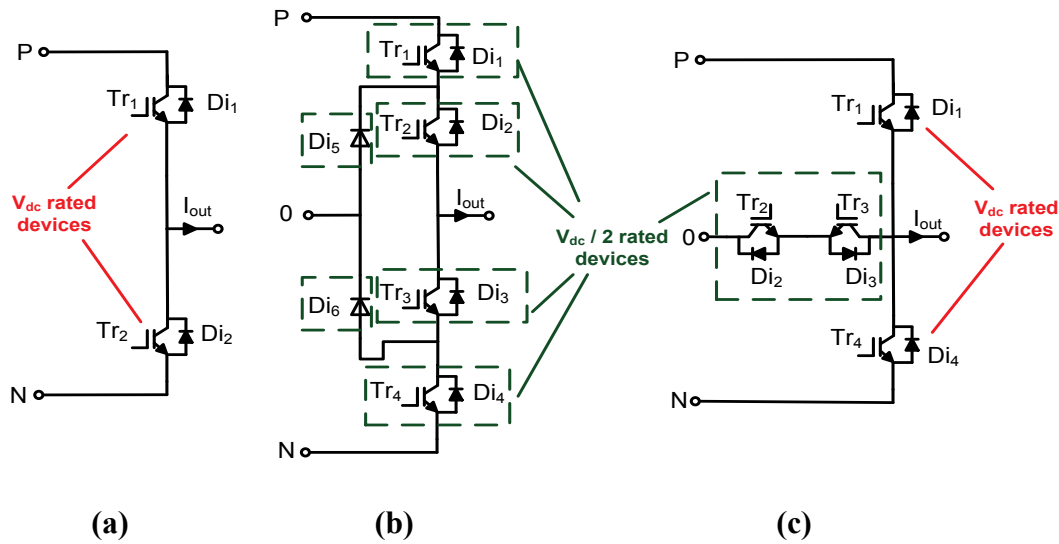


Figure 6.1 One converter leg (a) 2L (b) 3L-NPC (c) 3L-T.

6.2.1. Commutation Configuration

Generally, the formula depicted in (6.1) is valid for diverse converter switching states for all multilevel converters.

$$N_{sw} = n^m \quad (6.1)$$

where n is the number of voltage levels in the DC-link and m is the number of phases of the converter. Thus, the three-phase 3L-NPC and 3L-T involves 27 switch states in the modulation vector diagram, whereas 2L-VSC allows eight switch states only [81]. Thus, the control of phase currents and DC-link voltage is achieved in a

much superior way, being the most prominent feature of 3L-VSC over 2L converter [81]. Furthermore, if the switching frequency is high enough, 3L-NPC and T-type VSC can achieve lower losses than 2L converters [83]. However, the main disadvantage of the 3L-NPC is the necessary partial DC-link voltage balancing control and the commonly uneven loss distribution across the bridge-leg semiconductors [80] which is beyond the scope of this work.

The switching states of the 2L-VSC and 3L-VSC can be summarized as revealed in Table 6.2 and Table 6.3, respectively where a, b, and c are the phases and P, N, and 0 are dc-bus points highlighted in Figure 6.1. Note that the gate signals shown in tables below refer to the labels in the corresponding converter topologies revealed in Figure 1.6

Table 6.2 Switching states for 2L-VSC.

Switching State	Gate - (x) x=[a,b,c]		V(x) [Ph. voltage]
	Tr _{1x}	Tr _{2x}	
P	ON	OFF	+V _{dc} /2
N	OFF	ON	-V _{dc} /2

Table 6.3 Switching states for 3L-VSC

Switching State	Gate - (x) x=[a,b,c]				V(x) [Ph. voltage]
	Tr _{1x}	Tr _{2x}	Tr _{3x}	Tr _{4x}	
P	ON	ON	OFF	OFF	+V _{dc} /2
0	OFF	ON	ON	OFF	0
N	OFF	OFF	ON	ON	-V _{dc} /2

In principle, two semiconductor devices provide a conduction path for one direction at any state of a phase. So, once upper path positive current flows along active IGBT switches, inverse diodes provide negative direction of current flow [90]. On the other hand, lower current path provide positive current flow along the diodes, while negative current flows through IGBTs there. Contrary to ‘P’ and ‘N’ states common in 2L and 3L-VSC, zero state ‘0’ uses both upper and lower paths of neutral tap to provide bi-directional current flow [90].

The abovementioned switching states of converter topologies are provided to highlight that switching losses occur in different semiconductors depending on the switching transition and the direction of the output current. It is important to examine the commutation process in detail for every switching transition in order to find out which devices obtain turn-on and turn-off losses as well as diode reverse-recovery losses. Table 6.4 illustrates this case for 2L-VSC using the switching states depicted in Table 6.2. However, the commutation process for every switching transition for 3L-NPC and 3L-T topologies (refer to [78] and [91] for 3L-T and 3L-NPC, respectively) are not shown here for simplicity, since losses of individual semiconductors is beyond the objective of this chapter. Instead, total semiconductor losses are considered as to be done in the following sections.

Table 6.4 Switching loss energies.

Switching Transition	Switching Loss Energy
$I_{out} > 0$	
P → N	$E_{Tr1,off}, E_{Di2,on}$
N → P	$E_{Tr1,on}, E_{Di2,off}$
$I_{out} < 0$	
P → N	$E_{Tr2,off}, E_{Di1,on}$
N → P	$E_{Tr2,on}, E_{Di1,off}$

As a final point, 3L-T is a brand-new topology and its production volume is much lower than the NPC-type settled for years in industry [89]. As the area of utilization of 3L-T increases, not only initial cost of 3L-T will decrease in the long term but also innovative designs of active bidirectional switches will be present in the market.

For instance, Figure 6.2 depicts a brand-new solution to bidirectional switch configuration of 3L-T (RB-IGBT [92]), eliminating the body diodes Di_2 and Di_3 (Figure 6.1(c)), so is the diode losses. Thanks to this innovative design, the losses in 3L-T is lowered considerably. This special device will not be considered in this chapter whereas a detailed investigation on this innovative solution will be provided in next chapter involving financial aspects in long term in the field.

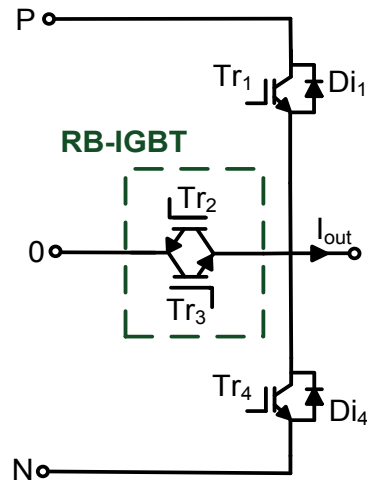


Figure 6.2 Brand new diode-less bidirectional switch for 3L-T.

6.2.2. A General Scheme for Calculation of Switching and Conduction Losses of Power Semiconductors in Computer Simulations

In this section, a general methodology to calculate switching and conduction losses of semiconductors in a computer simulation environment will be provided. The proposed scheme can be embedded in any design regardless of the simulator as long as the circuit employs ideal switches.

6.2.2.1. Conduction Losses

The conduction loss calculations are based on datasheet values and/or experimental measurements. The curve describing the relationship between voltage drop and U_{CE} and collector current I_C of the IGBTs is used to calculate conduction losses in a running simulation. Then, this curve must be approximated very accurately with high order polynomial fitting curves (2nd order or higher for more precision). For this purpose, MATLAB[®] and similar mathematical software can be benefited since they have curve fitting algorithms [77][93]. Then, the derived polynomial can be embedded in the circuit simulation in form of an equation that uses the current through the ideal switch as input value and gives the time behavior of the conduction loss of the IGBT as output during the simulation. In Figure 6.3 the implementation is

shown in a general form. The block in Figure 6.3 can be easily added to any ideal circuit simulation with no need to rebuild the power circuit or change the switch models.

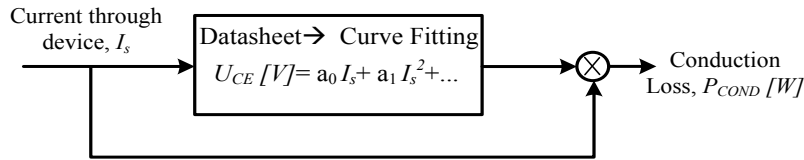


Figure 6.3 Conduction loss calculation block.

Note that this block should be established for each device in the circuit having conduction loss.

6.2.2.2. Switching Losses

Likewise, the switching loss calculations are based on datasheet values and/or experimental measurements. The curve describing the relationship between on loss E_{on} , off loss E_{off} and collector current I_C of the IGBTs is used to calculate switching loss in a running simulation. Then, these curves (E_{on} and E_{off}) must be approximated using curve fitting techniques as described in the former subsection. After obtaining the fitted curve coefficients, the general implementation of the scheme calculating the switching losses is shown in Figure 6.4. Whenever the switching signal detects a change of the state of the ideal switch from OFF to ON (rising-edge), a pulse of height 1.0 is generated with a defined pulse width ΔT . Dividing this pulse through its width ΔT creates a pulse signal with unit $[s^{-1}]$ that, multiplied with energy, represents a power.

The resulting time behavior of the switching losses $P_{SW}(t)$ will show pulses of physically correct magnitude and duration. If the blocking voltage V_{DC} is different from the one given in the datasheet ($V_{DC,N}$), it can be adjusted by a linear approximation employing the factor $V_{DC}/V_{DC,N}$.

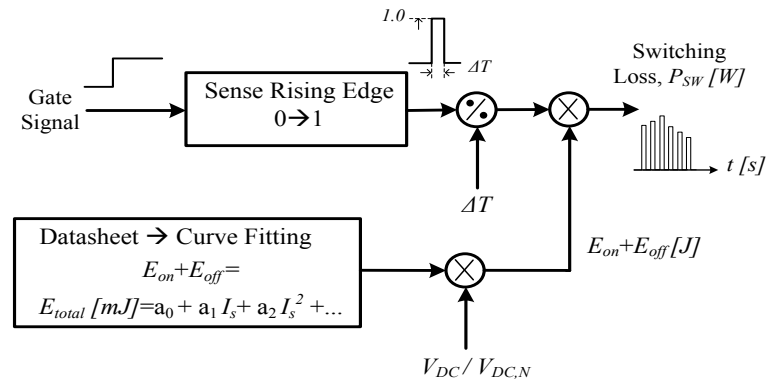


Figure 6.4 Switching loss calculation block.

As a remark, the loss calculation scheme is significantly simplified by counting on- and off-losses as a single event. If necessary, the scheme can easily be expanded by counting and weighting on- and off-losses separately. In the next section, this proposed loss calculation scheme will be benefitted to calculate individual semiconductor losses in each topology.

6.3. Topological Loss Comparison

For the first step of the topological loss comparison, suitable semiconductors are needed to be determined for each topology. Topological comparison will be held regarding the specifications in Table 6.1 Considering dc voltage ratings of each topology (in Figure 6.1), corresponding semiconductor switches and diodes are chosen as tabulated in Table 6.5.

Table 6.5 Selected semiconductors for topological comparison analysis.

	IGBT V / I	Fast diode	Active bidirectional switch
2L-VSC	1700 V / 1800 A	-	-
3L-NPC	1200 V / 1800 A	1200 V / 1800 A	-
3L-T	1700 V / 1800 A	-	1200V / 1800A

For 1700 V/1800 A switches IGBTs with product number CM1800HCB-34N [96] are used. For 1200 V/1800 A IGBTs, CM1800DY-24S [97] are utilized. For the fast diodes in NPC, the same series CM1800DY-24S [97] are used as diode modules. Last, for the active bidirectional switch in T-type CM1800HC-24NFM [98] switches are utilized. As a remark, the brand-new active bidirectional switch RB-IGBT [92] will be implemented later on.

6.3.1. Semiconductor Loss Calculated with Computer Simulation Loss Calculator

With the implemented loss calculation blocks in the computer simulator, switching and conduction losses of each semiconductor in each topology can easily be found.

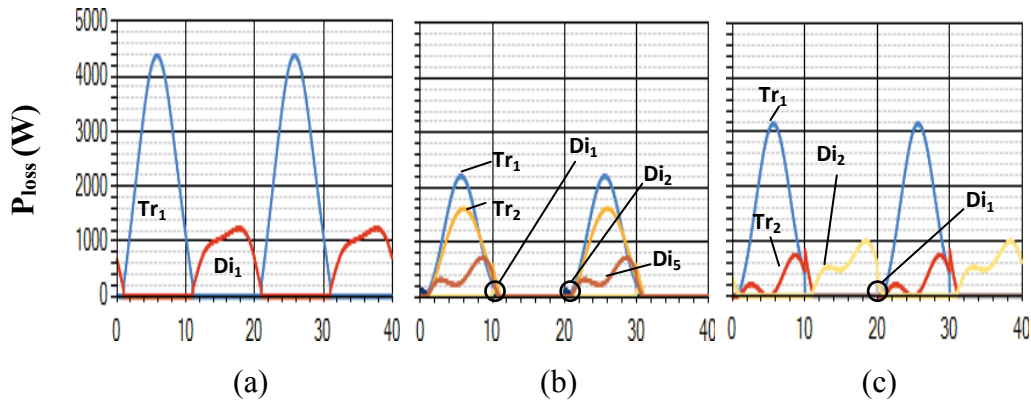


Figure 6.5 Semiconductor losses (W) vs. time (ms) at $f_{sw}=2$ kHz: (a) 2L-VSC (b) 3L-NPC (c) 3L-T.

The time behavior of total semiconductor losses of each semiconductor (symmetric components in each leg are omitted) for each topology are shown in Figure 6.5 (at $f_{sw}=2$ kHz). The characteristics of only one leg of the VSC are shown (with the same name labels in Figure 6.1), as the other two are identical. In Figure 6.5, the peak stress distributed on each semiconductor in 2L topology is higher than 3L topologies as the heat is concentrated in a few numbers of switches. Yet, in 3L topologies the peak stresses are distributed among more transistors and diodes resulting in reduction of the total stress on each component. Thus, better thermal performance is

realized (Figure 6.6). Besides, the peak stress on each semiconductor is the lowest in 3L-NPC topology providing the most stable thermal performance as shown in Figure 6.6. Consequently, volume and cost of the heat sink to be used in 3L-NPC and 3L-T will be less than that of 2L.

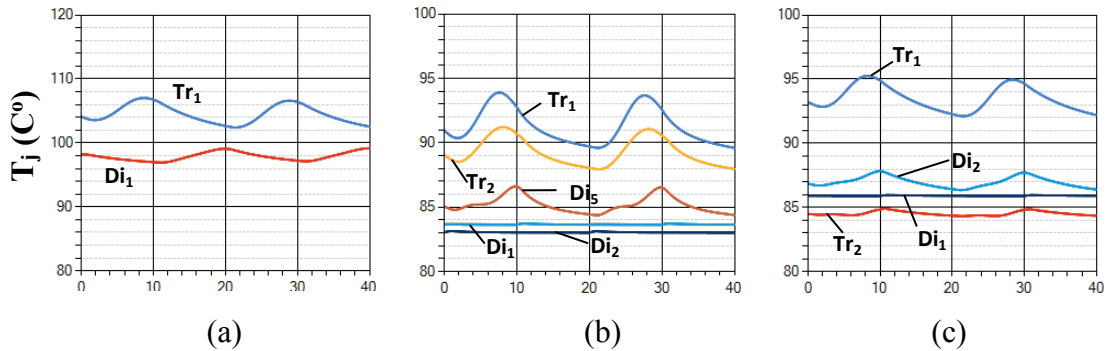


Figure 6.6 Junction temperature (T_j ($^{\circ}$ C)) vs. time (ms) at $f_{sw}=2$ kHz:(a) 2L-VSC (b) 3L-NPC (c) 3L-T.

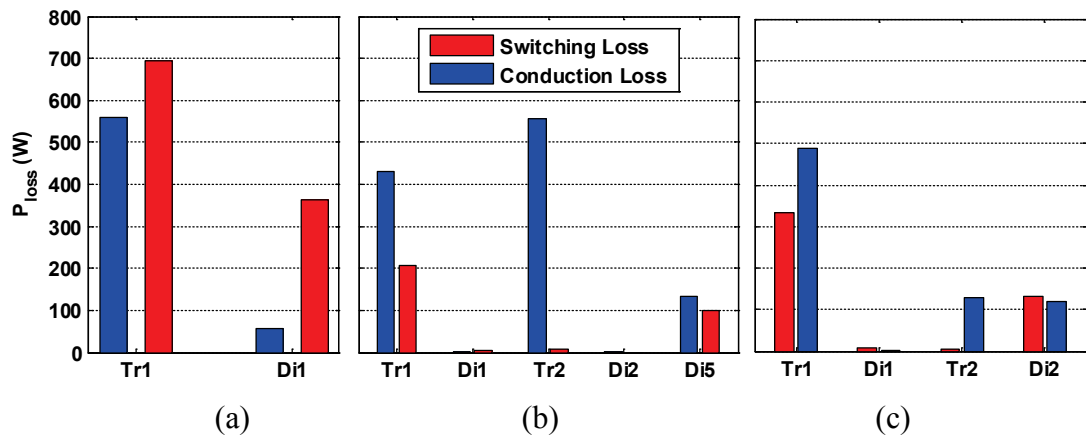


Figure 6.7 Semiconductor losses (W) at $f_{sw}=2$ kHz: (a) 2L (b) 3L-NPC (c) 3L-T.

3L-VSCs (T-type and NPC-type) are more favorable than 2L-VSCs in terms of reduced switching losses. The commutation voltage of all semiconductors in 3L-NPC is $V_{dc}/2$ rather than V_{dc} as in 2L-VSC (Figure 6.1). However, 3L-T is composed of both $V_{dc}/2$ (Tr2-3) and V_{dc} (Tr1-4) rated semiconductors. Hence, the total switching loss extent of 3L-T is lower than that of 2L-VSC; conversely, higher than that of 3L-NPC as can be seen in Figure 6.7.

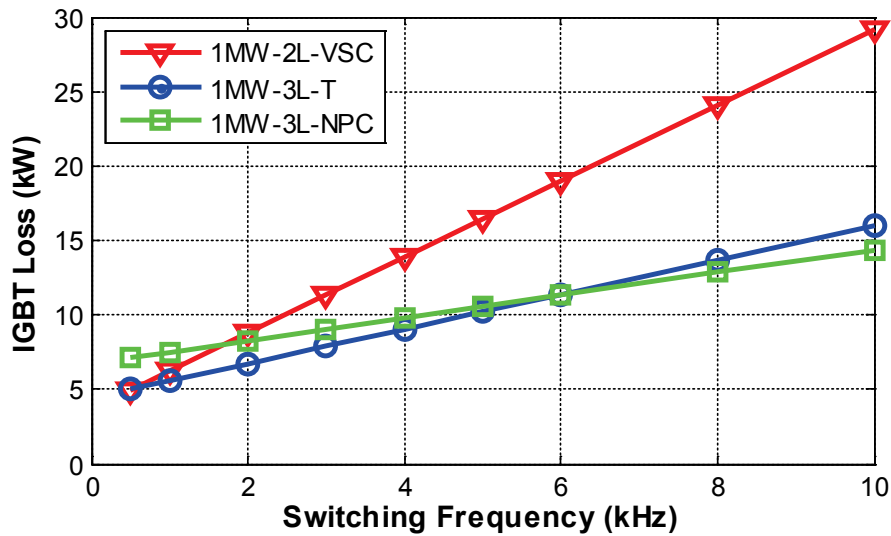


Figure 6.8 IGBT loss (kW) vs. f_{sw} (kHz) plot of three VSC topologies under SVPWM.

With the proposed loss calculation scheme in Section 6.2.2, total semiconductor losses are computed under varying switching frequency f_{sw} . As evident in Figure 6.8, 3L topologies deliver smaller IGBT losses compared to 2L-VSC under the same switching frequency, even though they employ higher number of semiconductors along the current path. Thus, the advantages brought by 3L topologies addressed in Section 6.2 are further proven.

Although the loss curves of NPC and T-type are very flat, nearly parallel and they would intersect at 6 kHz in Figure 6.8, this intersection point can move to the left by significant amount for higher V_{dc} values, making the NPC-type favorable over the T-type beyond the intersection point. In terms of conduction losses, with fewer elements along the current path yielding less losses, the 2L-VSC, T-type and NPC-type converters are ordered from the best to the worst in a sequence. Evaluating the total semiconductor losses, it becomes obvious at frequencies less than 6 kHz the T-type is more favorable. However, considering the efficiency constraint, f_{sw} cannot exceed 5-6 kHz which becomes a switching frequency constraint (as mentioned in detail in Chapter 3). Thus, in a more confined f_{sw} range, still the ordering from the

best to worst in terms of mitigated losses is T-type, NPC-type and 2L-VSC for the set of parameters in Table 6.1 and semiconductors in Table 6.5.

6.3.2. LCL-Filter Loss Model

LCL-filter loss is another significant loss mechanism in grid-connected converters apart from semiconductor loss. Therefore, a reasonable filter loss should be assumed according to power level of the design. For instance, applications higher than 300-400 kW presume less than 0.5% total filter loss at full load. As the power rating decreases, this percentage should be increased up to 1-2% to design feasible filters while keeping its size and cost moderate. Figure 6.9 displays possible filter loss extent as a percentage of rated power that can be assumed throughout modeling the filter losses.

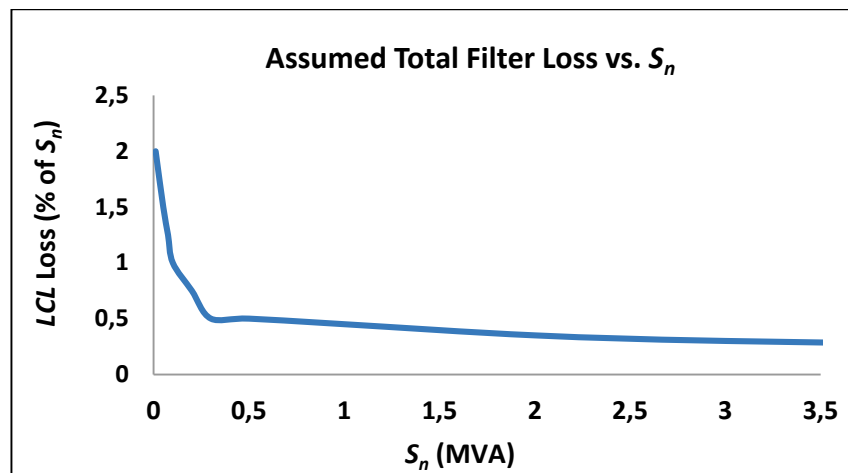


Figure 6.9 Assumed total filter loss vs. rated MVA (for full-load).

In the LCL-filter, the losses are predominantly inductor losses. The core losses mainly occur in converter-side inductor and the ohmic losses occur both in converter-side and grid-side inductors. Thus, in the design, only inductor losses are modeled for the filter loss calculations as in (6.2). LCL-filter loss (P_{filter}) contributes as an offset in efficiency attributes of 1MVA-VSC which accounts for a 0.5% decrease at full load.

$$P_{filter} = P_{fe} + P_{cu} = k_1 + k_2 * I_{load}^2 \quad (6.2)$$

where k_1 stands for core loss, P_{fe} (W), P_{cu} (W) is copper loss, and k_2 (W/A²) is a constant term. k_2 is calculated by subtracting predetermined P_{fe} (assumed at full load) from P_{filter} and the result is divided by the square of full load current. Afterwards, (6.2) can be employed under various load current (I_{load}) accordingly.

Core loss is calculated by the multiplication of core volume and core loss density as in (6.3) whereas core loss density formula is provided in (3.9).

$$P_{fe} = P_{core,dens} \cdot Volume \quad (6.3)$$

$$P_{core,dens} = K \cdot B^\alpha \cdot f^\beta \text{ (mW/cm}^3\text{)} \quad (6.4)$$

where B and f stand for magnetic flux density swing and operating frequency respectively and the terms marked as K , α , β are constants depending on the initial permeability of the core.

Since operating conditions (switching frequency and so on) and the filter is the same for 2L-VSC and 3L-VSC topologies during simulation studies in this chapter, P_{fe} can be deemed as constant constituting a certain extent in the assumed total filter loss. As a remark, if 2L-VSC and 3L-VSC were compared under distinct operating parameters such as switching frequency, then P_{fe} would be a nonlinear function of f_{sw} as evident in (6.4). Figure 6.10 reveals this nonlinear relationship between P_{fe} and f ($=f_{sw}$) assuming K , α , β constants determined by the core manufacturers. Magnetic flux density B can also be deemed as constant owing to the constant output current that magnetizes the core whereas α is determined within $1 < \alpha < 3$ typically [95]. Thus, P_{fe} variation against switching frequency can be modeled for a proper choice of β value. Investigation on manufacturer cores yields β within $2 < \beta < 3$ [94][95].

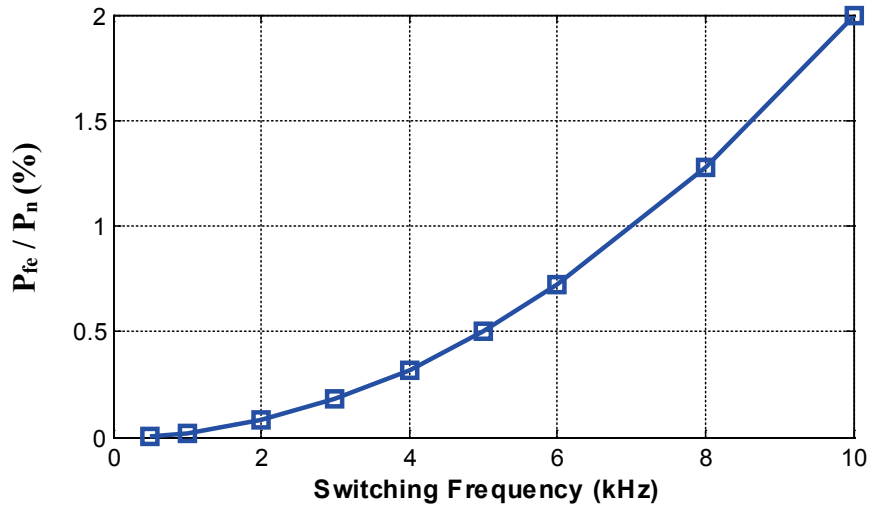


Figure 6.10 Core loss modeling against switching frequency (kHz).

Selecting $\beta=2$ yields $P_{fe} = \mathcal{C} \cdot f^2$ where \mathcal{C} is a constant representing the multiplication of $K \cdot B^\alpha \cdot Volume$. Thus, variation of P_{fe} under various switching frequencies is modeled as depicted in Figure 6.10. It should be noted that for switching frequencies higher than 4-5 kHz, core loss escalates too much; in return heating up the inductors significantly and such a design becomes infeasible. Therefore, P_{fe} must be limited in inductor design. Next, different core loss to total filter loss ratios will be inspected in order to draw a conclusion about feasibility of designed inductors.

In Figure 6.11, LCL -filter loss P_{filter} is plotted by means of (6.2) for three distinct filter designs against varying load current I_{load} including light load and overload conditions. As evident in all three cases in Figure 6.11, P_{filter} is assumed as constituting 0.5% of P_n at full load irrespective of the weight of P_{fe} and P_{cu} in P_{filter} . In the first design case, filter loss is evaluated by assuming P_{fe} constituting 25% of the total filter loss. For the other two cases, P_{fe} is increased with 25% steps while P_{cu} decreases with 25% decrement as highlighted in Figure 6.11.

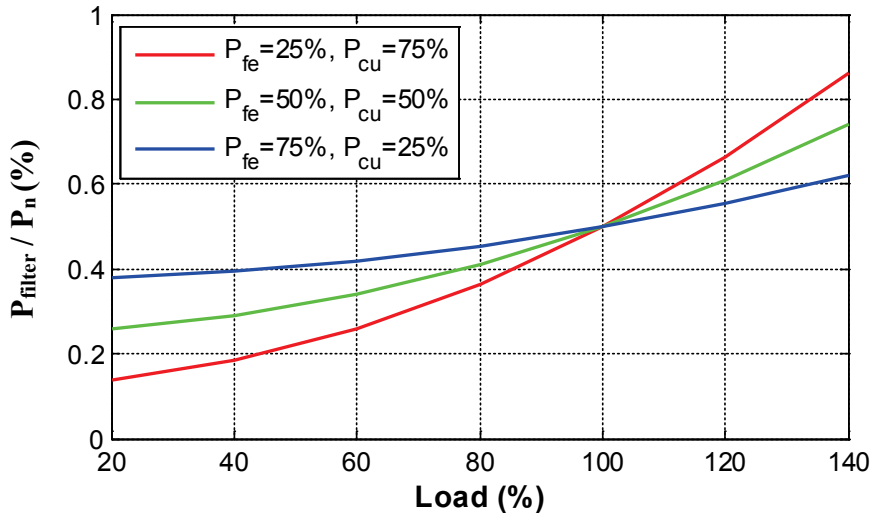


Figure 6.11 *LCL*-filter loss vs. load (%) characteristic.

As P_{fe} constitutes higher portion in P_{filter} , loss attributes become less sensitive to load variations as opposed to first design case. P_{fe} is constant regardless of I_{load} , whereas, P_{cu} is highly dependent on I_{load} due to its second order characteristics in (6.2). Therefore, in each three case a substantial increase in filter loss is inevitable as I_{load} increases. As expected, loss curve is much sensitive to variations of I_{load} in $P_{cu}=75\%$ case as can be seen in Figure 6.11. Conversely, I_{load} variation has the least impact on the shape of the loss curve in $P_{cu}=25\%$ case. It seems to contribute more like offset unlike the other two cases. Typically, the inductors are designed such that the core losses are about 25-40% of the total inductor losses, so that the light and no-load losses are maintained low [89][94].

It should be noted that 2L and 3L topologies are evaluated under identical system parameters (Table 6.1) so core loss and copper loss characteristics are identical for all.

6.4. Efficiency Comparison between Two-level and Three-level Topologies

Total semiconductor losses and *LCL*-filter losses comprises the biggest portion of the total losses in a grid-connected VSC, so they dominate the efficiency attributes.

Efficiency η (%) vs. switching frequency f_{sw} plot is obtained for each topology using the parameters provided in Table 6.1. Details of the *LCL*-filter loss model have also been investigated in Section 6.3.2. Thus, filter loss is reflected to the η curve which accounts for an increase of 0.5% of P_n in total losses at full load. For the selected switching frequency $f_{sw} = 2$ kHz, efficiency η (%) is higher than 98-98.5% for each topology which is compatible with the efficiencies of commercial products in wind turbine industry [84]. As evident in Figure 6.12, 3L topologies deliver even higher efficiencies than 2L-VSC at the same switching frequency, although they employ higher number of semiconductors along the current path. Thus, the advantages brought by 3L topologies addressed in Section 6.2 are further proven.

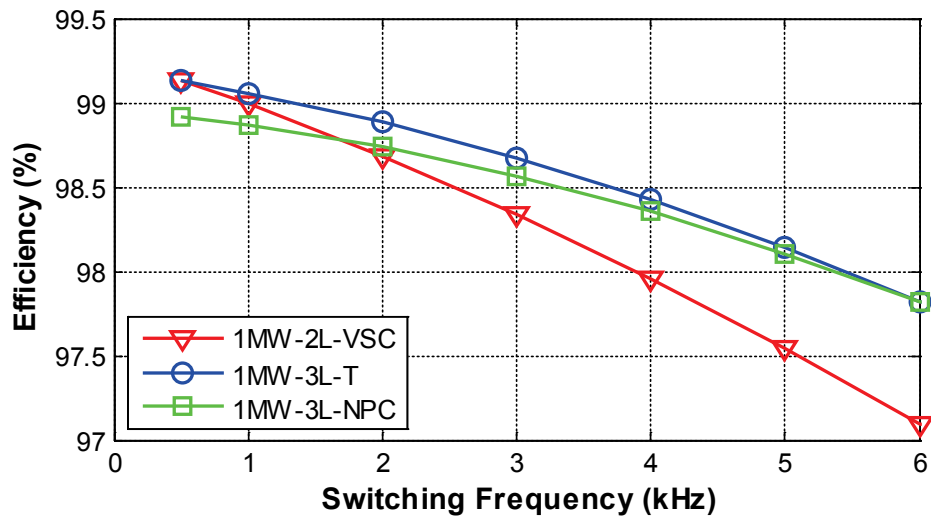


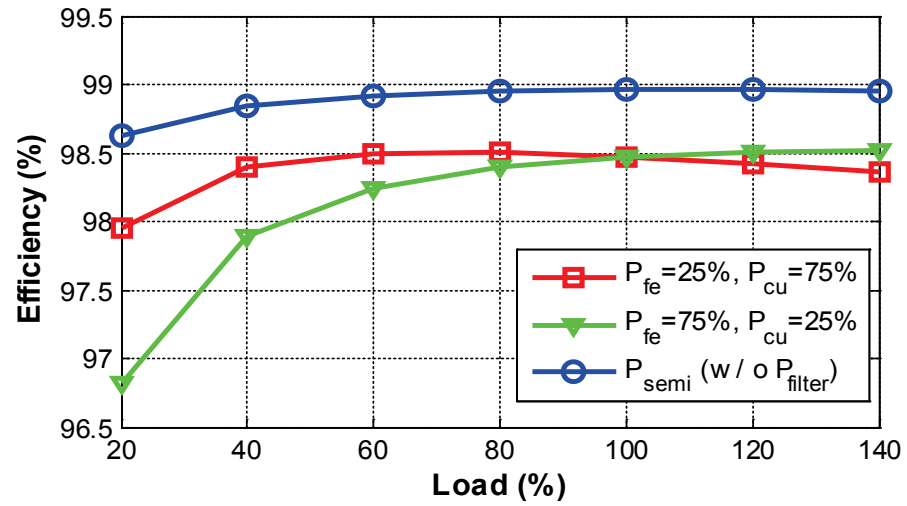
Figure 6.12. η (%) vs. f_{sw} plot of three VSC topologies under SVPWM.

Though the efficiency curves of NPC and T-type are very flat, nearly parallel and they would intersect at 6 kHz in Figure 6.12, this intersection point can move to the left hand side by major amount for higher V_{dc} values, making the NPC-type favorable over the T-type beyond the intersection point (right hand side of the point). In terms of conduction losses, with fewer elements along the current path yielding less losses, the 2L-VSC, T-type and NPC-type converters are ordered from the best

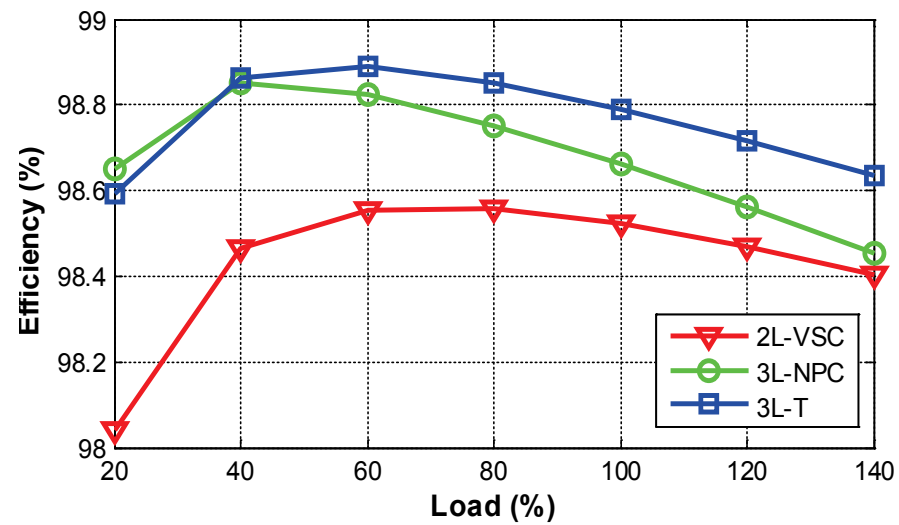
to the worst in a sequence. Evaluating the total semiconductor loss along with filter loss and determining the efficiency from here, it becomes obvious at frequencies less than 6 kHz T-type is more favorable. However, considering the efficiency constraint, f_{sw} cannot exceed 5-6 kHz which becomes a switching frequency constraint. Thus, in a more confined f_{sw} range, still the ordering from the best to worst in terms of efficiency is T-type, NPC-type and 2L-VSC for the set of parameters in Table 6.1 and semiconductors in Table 6.5.

In Figure 6.13(a), with the *LCL*-filter loss included, η (%) of 2L-VSC is plotted by means of (6.2) for two distinct filter designs against varying load current I_{load} including light load and overload conditions. In the first design case, efficiency degradation owing to the filter loss is evaluated by assuming P_{fe} constituting 25% of the total filter loss which was assumed as 0.5% of P_n at full load. Yet, the second design assesses the case that is less sensitive to load variations as opposed to first design case. Since P_{cu} is highly dependent on I_{load} , in both cases, a substantial degradation in efficiency compared to the case without filter losses is observed in Figure 6.13(a) as I_{load} increases. However, the deflection is much sensitive to increase in I_{load} in $P_{cu}=75\%$ case. Conversely, I_{load} increase does not affect the shape of the efficiency curve in $P_{cu}=25\%$ case significantly and it contributes more like offset. As a remark, Figure 6.13(a) shows efficiency curve for only 2L-VSC case when the two different filter loss modeling is implemented. However, efficiency attributes are alike for all topologies except for the numerical data, eliminating the need of highlighting efficiency vs. load curves for 3L-VSC. To conclude, as also mentioned in the former section, inductors are designed such that the core losses are about 25-40% of the total inductor losses typically. For this reason, efficiency η vs. load characteristics assuming P_{fe} constitutes 25% of P_{filter} for all topologies are depicted in Figure 6.13(b). Conduction losses increase faster (quadratic dependency) than switching losses (linear dependency) with increasing load current [82]. This impact can be realized in Figure 6.13(b), particularly as the load current passes beyond full load range. Up to 40-50% load, total losses of 3L-T and 3L-NPC are very close; however, beyond that point, the conduction losses of 3L-NPC rises considerably since four switches are present along the current path. Therefore, T-

type is more favorable at rated load while 2L-VSC has provided the lowest η (%) values among all topologies.



(a)



(b)

Figure 6.13 With the inclusion of *LCL*-filter loss, η (%) vs. load (%) characteristic

(a) 2L-VSC ($f_{sw}=2$ kHz) (b) All topologies under $P_{fe}=25\%$.

6.5. Converter Current Ripple Estimation of Two-level and Three-level Topologies

The power quality injected into the grid should comply with the stringent international grid standards as stated well in Chapter 2. Thus, necessary attributes of the grid-side current should be monitored carefully.

Except for holding the expectations reported by these standards, the internal design of the grid-side PWM VSC should also fulfill the design requirements addressed by many publications and know-how design rules in the literature. For instance, most of the articles in this field state that the worst case peak-to-peak converter side current ripple (Δi_{max}) should be confined into 10-25% of peak rated load current (\hat{I}_{rated}) [77]-[84]. Otherwise, very large stresses might be burdened to the semiconductors, ending up with overheating, aging and degradation of the devices even though the grid standards are met. Consequently, a thorough investigation both on internal design specifications and expectations of the corresponding grid standards is extremely necessary.

To suppress the ripple properly, the capability of converter-side inductance L_c must always be adequate to confine Δi_{max} within 10-25% under normal grid circumstances. However, current ripple is independent of the load so it does not deviate substantially under lighter or heavier loads. On the other hand, it is extremely sensitive to changes in grid voltage (V_g). Thus, the impact of grid voltage variation on converter current ripple must be explored. For this purpose, converter current ripple against modulation index (m_i) can be examined since m_i is defined as fraction of peak line-to-neutral grid voltage V_g to half of V_{dc} as depicted in (5.10) with a definition range of 0-1.15 for SVPWM [85]. Consequently, as the dc-link voltage controller (Chapter 4) controls V_{dc} and keeps its value constant, variation of grid voltage is inspected by practicing varying m_i .

$$m_i = \frac{\hat{V}_g}{V_{dc}/2} \quad (6.5)$$

To determine the worst case current ripple, the converter topology should be regarded together with the modulation algorithm. Thus, the worst case peak to peak ripple Δi_{max} expression should be derived as a function of m_i under the favored topology and PWM method. In our case SVPWM is preferred and Δi_{max} can be derived as a function of m_i under SVPWM for 2L-VSC as depicted in (6.6) [86].

$$\Delta i_{max} \cong \frac{V_{dc}}{3L_c f_{sw}} (1 - m_i) m_i \quad (6.6)$$

where L_c is the converter-side inductance. For the SVPWM implementation in 2L-VSC, the instantaneous phase-to-neutral voltage vector is simply the projection of the instantaneous reference voltage vector V^* onto the horizontal axis. The value of this instantaneous vector can vary from $-2/3 V_{DC}$ to $+2/3 V_{DC}$. Thus, modulator selects the proper vectors in the appropriate order to produce the desired fundamental waveform on average [88].

The voltage reference vector V^* is resolved into the three adjacent voltage vectors of V_0, V_1, V_2 such that they produce the desired voltage-second average as agreed in Figure 6.14.

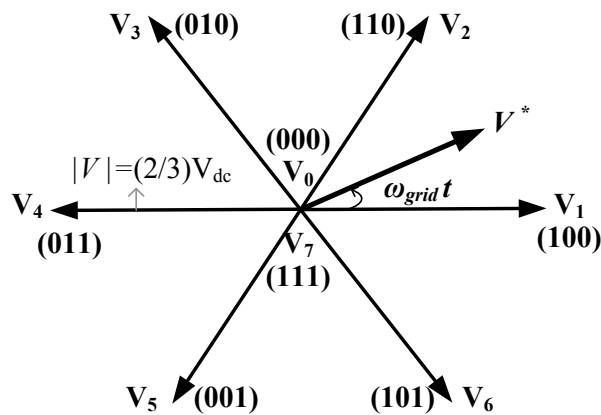


Figure 6.14 2L-VSC voltage vectors.

Over one switching period, the peak ripple current is defined by the difference between the peak volt-seconds and the average volt-seconds applied to the inductor [88]. The maximum ripple will occur when the reference voltage vector V^* is midway between phase vectors of V_1 and V_2 as illustrated in Figure 6.14, where $m_i=1/\sqrt{3}$ and phase a voltage is crossing through zero [88]. Thus, in SVPWM, the maximum ripple occurs when $m_i=1/\sqrt{3}$.

Figure 6.15 depicts the variation of converter-side current ripple of 2L-VSC against m_i for the simulated system. As can be seen in the figure, the maximum ripple of the simulated system is found as 21.3% at $m_i=1/\sqrt{3}$, further proving the theoretical findings. If L_c design were made by regarding only rated m_i (rated $m_i=1.05$ for the simulation case) L_c would be insufficient to suppress the ripple in case of V_g change during operation.

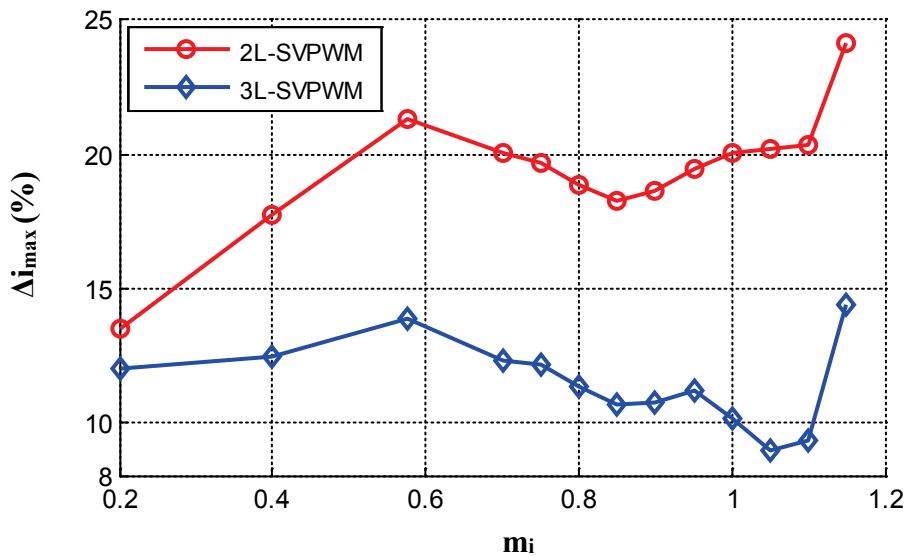


Figure 6.15 Δi_{max} (%) vs. m_i plot under SVPWM and DPWM1 (a) 2L-VSC (b) 3L-VSC.

Substituting $m_i=1/\sqrt{3}$ on (6.6) yields Δi_{max} formula in (6.7) that can be used to estimate the converter-side current ripple for 2L-VSC employing SVPWM:

$$\Delta i_{max}(\%) = \frac{V_{dc}}{12L_c f_{sw} \hat{I}_r} * 100 \quad (6.7)$$

As a remark, most of the PWM patterns involving zero sequence current injection have similar vector decomposition features with SVPWM, thus the formula in (6.6) applies for those schemes as well. Additionally, the corresponding converter parameters in Table 6.1 have been inserted in (6.7) and Δi_{max} was found as 20.9% (in high correlation with the simulations 21.3%).

Furthermore, the boundary region between linear-modulation region and over-modulation region in SVPWM is somewhat uncertain and probably unstable [88]. As a result, Δi_{max} rises substantially near 1.15 as demonstrated in Figure 6.15. Hence, maximum m_i should be limited to 1.05-1.1 to have enough margin for the control in SVPWM method.

According to simulation results in Figure 6.15, 2L and 3L-VSC topologies show very similar tendency against m_i variation. Nevertheless, converter current ripple extent of 3L-VSC is much lower compared to 2L-VSC for any m_i and the ripple variation in 3L-VSC was confined to 9-15% fluctuating in a narrower envelope. This is an anticipated outcome because the ripple declines substantially as the number of levels increase [78]. In order to derive Δi_{max} formula under SVPWM for 3L-VSC as well, applying inductor voltage-second balance yields Δi_{max} formula as displayed in (6.8) [88].

$$\Delta i_{max}(\%) = \frac{V_{dc}}{24L_c f_{sw} \hat{I}_r} * 100 \quad (6.8)$$

6.6. Impact of PWM Pattern on Output Performance of 2L and 3L Topologies

In this subsection it is intended to indicate that PWM modulation methods have an influence not only on THD_i and Δi_{max} performance of I_g , but also on total

semiconductor loss extent significantly. Thereby, the impact of the preferred PWM pattern is taken into account in this comparative chapter. In this dissertation, two of the most popular PWM methods containing zero sequence signal injection, namely SVPWM and DPWM1 are examined for 2L-VSC and 3L-VSC under “*equal switching loss*” principle. For this purpose, f_{sw} is increased by 50% in DPWM1 method so that the switching count and therefore the switching losses could remain the same while ripple of DPWM1 becomes less compared to SVPWM [86]. Further details have been given in Chapter 5 in Section 5.2.

The preferred PWM method influences η (%) vs. f_{sw} of 2L-VSC as depicted in Figure 6.16. Picking f_{sw} as 2 kHz for SVPWM and 3 kHz for DPWM1 verifies the theoretical approach and ensures “*equal switching loss*”.

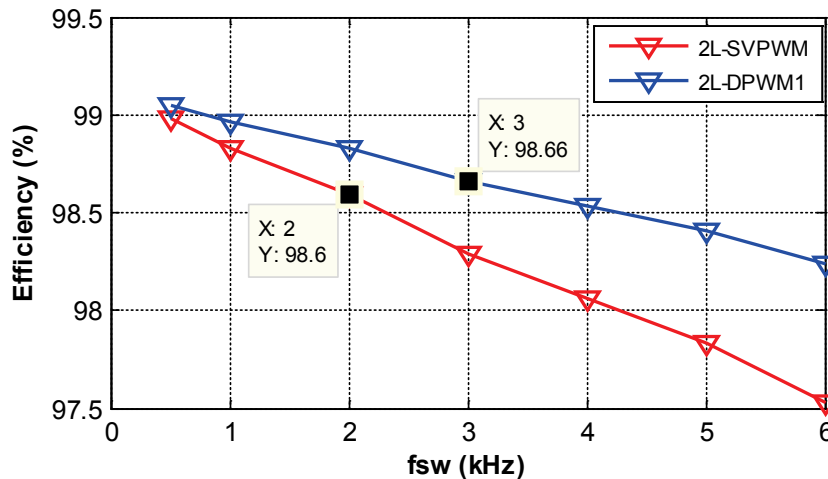


Figure 6.16. η (%) vs. f_{sw} (SVPWM and DPWM1).

Moreover, selected f_{sw} for 2L-VSC employing DPWM1 delivers slightly better THD_i performance against various L_c compared to SVPWM as shown in Figure 6.17(a). It should be noted that THD_i vs. L_c characteristics are derived under full load, thus THD_i and total current demand distortion (TDD_i) yield the same values. TDD can be calculated simply replacing the fundamental component in the denominator of (2.10) with maximum demand load current [52].

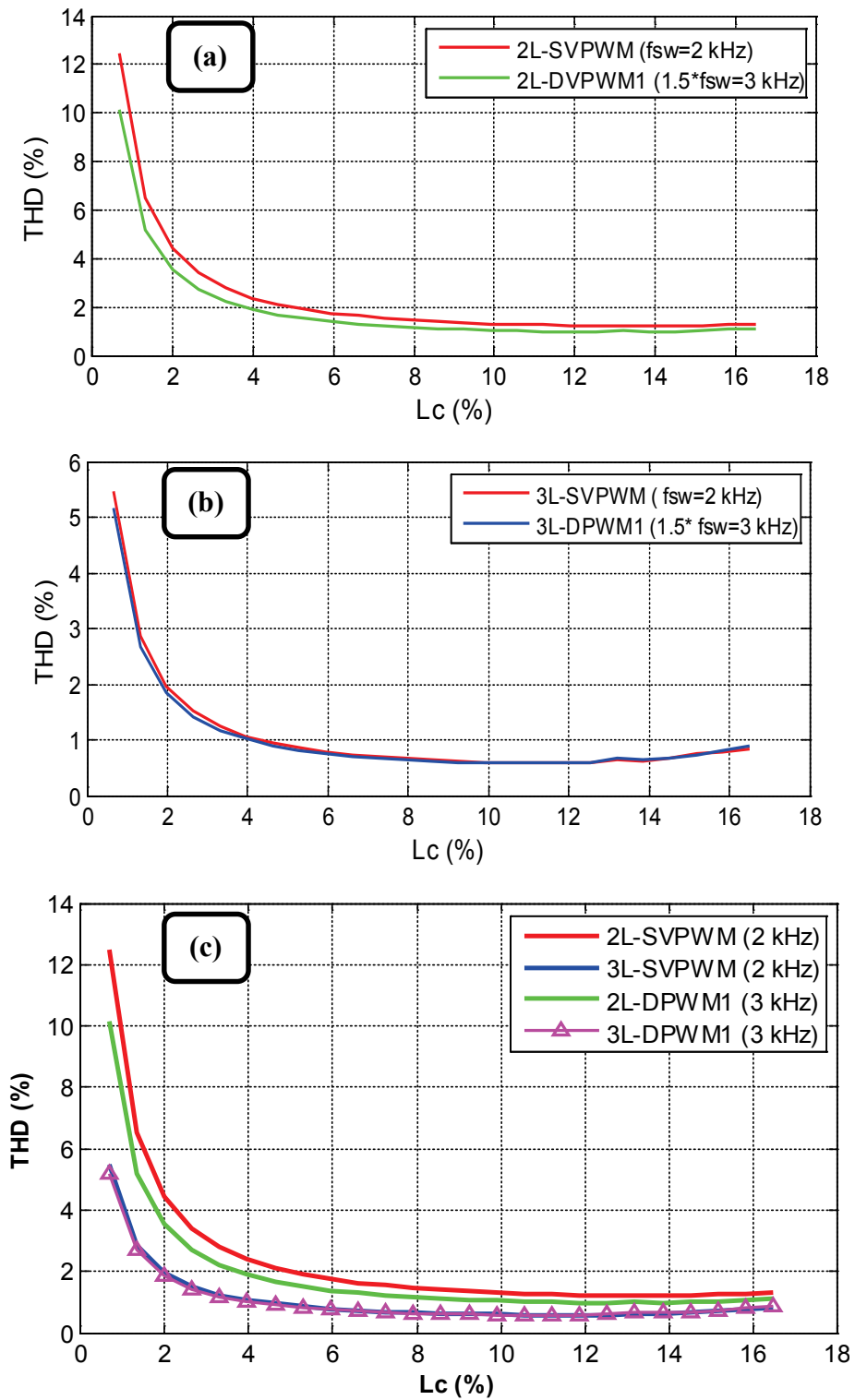


Figure 6.17. THD_i (%) vs. L_c (%) under SVPWM and DPWM1 (a) 2L (b) 3L (c) 2L&3L (Full load i.e. THD=TDD).

Not much changing in THD_i attributes but in value compared to 2L-VSC, designated f_{sw} for 3L-VSC under DPWM1 method supplies slightly better THD_i performance compared to SVPWM as shown in Figure 6.17(b), further validating the theoretical approach. Figure 6.17(c) gathers all the cases into a single plot and highlights that 3L-VSC provides better THD_i performance at the same f_{sw} compared to 2L-VSC and DPWM1 pattern delivers slightly better THD_i attributes compared to SVPWM for both topologies under “equal switching loss” [89].

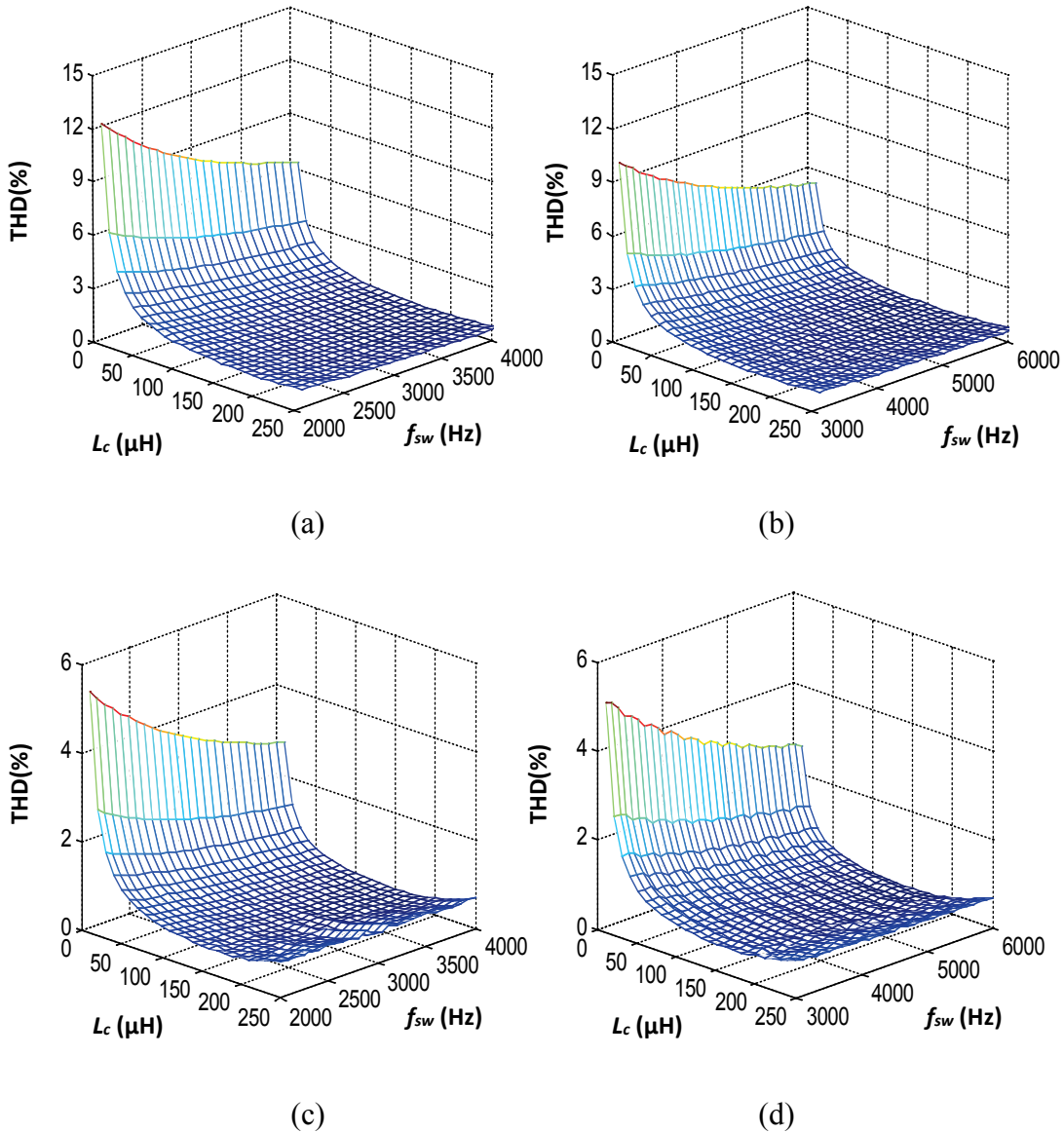


Figure 6.18 THD_i (%) vs. L_c and f_{sw} : (a) 2L-SVPWM (b) 2L-DPWM1 (c) 3L-SVPWM (d) 3L-DPWM1 (Full load i.e. $\text{THD}=\text{TDD}$).

THD_i vs. L_c (%) characteristics have been extended by including the impact of switching frequency f_{sw} as shown in Figure 6.18. To achieve “equal switching loss” principle, f_{sw} range was normalized in DPWM1 graphs as displayed. Under the same conditions, i.e. same L_c and f_{sw} , the improvement in THD_i performance owing to the increased level of the VSC topology can be recognized. Besides, DPWM1 offers a considerably better THD_i performance compared to SVPWM in 2L-VSC (Figure 6.18(a) and (b)) whereas this deviation is substantially reduced in 3L-VSC as evident in Figure 6.18(c) and (d).

SVPWM at low m_i and DPWM1 at high m_i have been widely used in industry. SVPWM loses its advantage around $m_i \approx 0.8$ since the ripple increases as m_i increases. On the contrary, ripple extent starts to decline considerably under DPWM1 around $m_i \approx 0.7-0.8$. Therefore; use of DPWM1 beyond $m_i > 0.8$ is suggested in [87]. This claim is further proven with the obtained attributes of ripple change against m_i in Figure 6.19(a). As can be seen in the response under 2L-VSC, DPWM1 exhibits worse ripple performance compared to SVPWM up to $m_i \approx 0.9$. However, a substantial improvement in DPWM1 is recognized beyond that point. Thus, DPWM1 is the optimum PWM pattern in ripple aspect for 2L-VSC for the rated $m_i=1.05$. If the nominal m_i value were lower than 0.8-0.9, use of SVPWM for 2L-VSC would be favored.

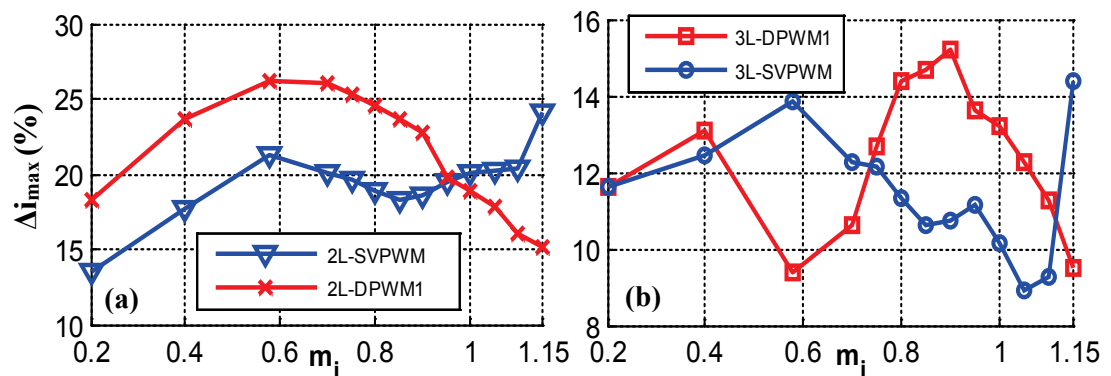


Figure 6.19 Δi_{max} (%) vs. m_i plot under SVPWM and DPWM1 (a) 2L-VSC (b) 3L-VSC ($f_{sw}=2$ kHz for SVPWM, $f_{sw}=3$ kHz for DPWM1).

However, 2L and 3L topologies shows opposite reactions to m_i variation under DPWM1 as can be seen in Figure 6.19(b). Under DPWM1, 3L-VSC yields the lowest Δi_{max} at $m_i = 1/\sqrt{3}$; whereas, 2L-VSC has its peak at $m_i = 1/\sqrt{3}$ as shown in Figure 6.19(b). However, the ripple variation under 3L-VSC is confined to 9-15% yielding much lower ripple compared to 2L-VSC varying in a narrower envelope.

The reason why 3L-VSC has shown different ripple pattern under DPWM1 compared to 2L-VSC should be analyzed in more detail. For this purpose, the attributes in Figure 6.19(b) have been derived once again by augmenting m_i samples that the peak to peak ripple is measured. Yet again, Δi_{max} tends to decrease around $m_i = 1/\sqrt{3}$, behaving more like a periodical waveform fluctuating in a narrow envelope.

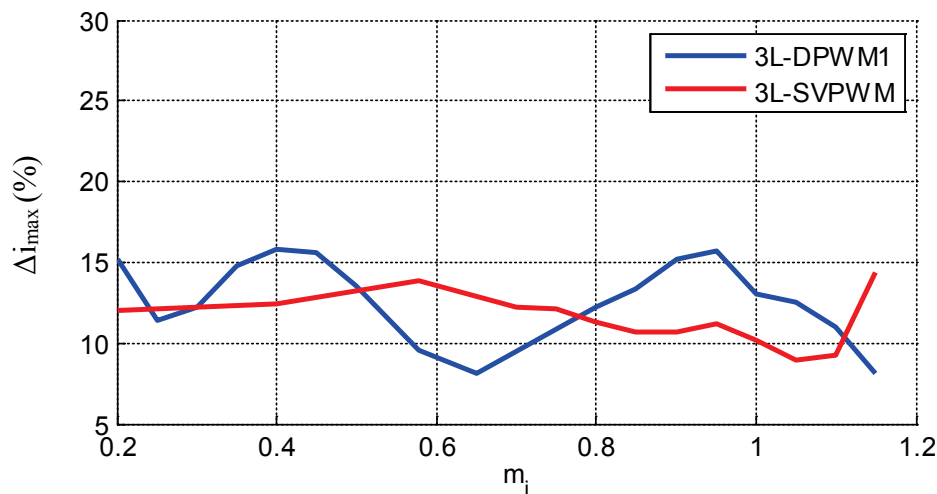


Figure 6.20 Δi_{max} (%) vs. m_i plot of 3L-VSC under SVPWM and DPWM1.

Since peak-to-peak current ripple measurement is somehow very likely to involve unexpected instantaneous variations, calculation of “*weighted total harmonic distortion (WTHD)*” values of converter voltage waveforms may yield more convenient results. It is different than classical THD calculation since output line voltage WTHD calculation contains the effect of orders of harmonics, not the

magnitudes of all harmonics as themselves. Thus, an outcome less sensitive to instantaneous variations can be obtained. WTHD is defined in percent as:

$$\text{WTHD (\%)} = \frac{\sqrt{\sum_{i=2}^n \left(\frac{V_{LLi}}{i}\right)^2}}{V_{LL1}} \times 100 \quad (6.9)$$

where i is the harmonic order and V_{LLi} is the amplitude of the i^{th} line-to-line harmonic voltage and n is the highest harmonic order to be involved. It is important to note that, V_n/n harmonics and WTHD values are irrespective from the parameters of the topology used, giving a general result [110].

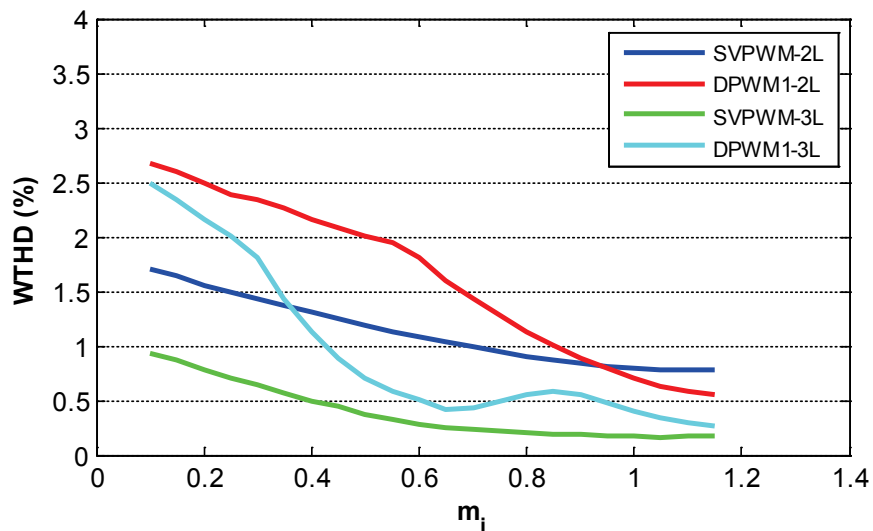


Figure 6.21 WTHD vs. m_i plot under SVPWM and DPWM1 ($f_{sw}=2$ kHz for SVPWM, $f_{sw}=3$ kHz for DPWM1).

For a number of different m_i 's, WTHD values of converter voltage have been computed using (6.9) accordingly. As can be seen in the figure, the sensitivity of WTHD characteristics under SVPWM against m_i variation decreases as the converter level increases. On the contrary, WTHD characteristics under DPWM1 are quite sensitive against m_i variation for both topologies. As evident in the figure, WTHD

characteristics roughly between $m_i = 0.4$ and $m_i = 0.6$ yields opposite responses under 2L and 3L topologies when DPWM1 is employed, which is similar with the case revealing peak to peak current ripple characteristics in Figure 6.19(b).

WTHD analysis further proves the fact that SVPWM at low m_i and DPWM1 at high m_i are favored for 2L-VSC. As can be seen, red curve starts to decline beyond a certain m_i and yields lower WTHD compared to SVPWM at high m_i . However, DPWM1 shows more unstable behavior under 3L-VSC against m_i change and also yields higher ripple/harmonic as highlighted both in Figure 6.20 and Figure 6.21, concluding that SVPWM is the favored pattern for the 3L-VSC topology.

6.7. Summary and Conclusions

In this chapter, a general overview of 2L, 3L-NPC and 3L-T topologies have been provided. Then, the methodology used to calculate switching and conduction losses of semiconductors in the computer simulation environment has been delivered. The employed scheme can be embedded in any design regardless of the simulator as long as the circuit employs ideal switches. Secondly, with the proposed loss calculator, topological semiconductor loss comparison has been made and verified by a design example by means of simulation outputs. Furthermore, *LCL*-filter loss modeling has also been provided regarding topological factors, operating conditions and type of design specifications. Apart from having revealed feasible filter loss against power level of the application, it has been also deduced that the inductors should be designed such that the core losses are about 25-40% of the total inductor losses, so that the light and no-load losses are maintained low. Thirdly, a general topological efficiency comparison has been delivered by merging the semiconductor loss model and *LCL*-filter loss model. After completing the loss modeling phase, formulation of the converter ripple under 2L and 3L-VSC topologies has been discussed. Finally, the impact of the favored PWM pattern on output performance of 2L-VSC and 3L-VSC has been examined in quite detail.

In the light of comparative study held in this chapter, THD_i and efficiency performances of 3L topologies were found to be superior to 2L topology under the

same f_{sw} . Thus, 3L-VSCs are economically feasible in low-voltage applications especially in high energy-cost markets. In addition, the reduction in the commutation voltage has provided lower temperature rises in 3L-VSCs in return reducing the cost and size of the heat sinks. Besides, 3L-T has been found to be the best choice for low-voltage applications if efficiency is the main concern.

For 2L-VSC, simulation results have depicted that DPWM1 is the optimum PWM pattern in ripple aspect for the modulation indices $m_i > 0.8$. 3L-VSC; on the other hand, has shown less dependency against m_i variation under SVPWM compared to DPWM1. However, both ripple and WTHD analyses have revealed that DPWM1 shows more unstable behavior under 3L-VSC against m_i change and also yields higher ripple/harmonic. To conclude, being less sensitive to m_i variation and yielding less ripple and harmonic, SVPWM can be deemed as the optimal PWM pattern for 3L-VSC.

To sum up, this chapter has supplied power semiconductor module and magnetic circuit loss characterization considering converter topologies and PWM methods, providing necessary modeling to realize a decent converter comparison study. The next chapter combines all of the information given by each chapter up until, in a successive order and merges them to yield a top to bottom converter design algorithm. Hence, a step by step method ending with optimized filter elements along with the best topological choice will be presented.

CHAPTER 7

DESIGN OF GRID CONNECTED PWM CONVERTERS CONSIDERING TOPOLOGY AND PWM METHODS FOR LOW-VOLTAGE WIND TURBINES

This chapter merges the content provided in each chapter and uses it as background and input to the targeted framework of this dissertation. The primary aim of this thesis is simply, to provide a top to bottom design methodology, that can span a wide power scale of grid connected PWM converters employed in wind turbine systems (under different PWM methods, VSC topologies, load conditions, modulation indices, and switching frequencies) and yield the optimum;

- Filtering including the design of *LCL*-parameters and control scheme,
- Topology among two-level (2L), three-level NPC (3L-NPC) and three-level T (3L-T) VSCs,
- PWM method;

that provide the lowest cost solution while fulfilling the design requirements. Thus design results for different systems with different performances can be evaluated and compared, allowing a better determination of a suitable system. To embody a head to toe converter design methodology based upon the abovementioned objectives, deep and extensive study in *LCL*-filter design, stability and controllability issues, wide-spread PWM VSC topologies and common PWM patterns favored in wind power industry are extremely required. For this purpose, up until this chapter, all of the mentioned topics are gone through with comprehensive theoretical background

supported with MATLAB[®] and simulation outputs (as further verification to the theory) which are far beyond the know-how design methods. In other words, in the former chapters, *LCL*-filter design, stability and optimal control tips, a comprehensive investigation on three-phase VSC topologies of 2L, 3L-NPC, and 3L-T under distinct PWM methods, filter elements, loadings, modulation indices, and switching frequencies are provided regarding the efficiency and grid-code requirements of the typical wind turbine applications. In this chapter, it is time to merge this advanced and thorough study into the converter design methodology. To conclude, each chapter in this dissertation can be deemed as a single block forming the entire converter design methodology in a successive order.

With the proposed design method in this chapter, the selection criterion for the best combination (topology and PWM pattern) is based essentially on pay-off time of total investment on the grid-side VSC. For each combination, pay-off time of the total investment cost is calculated and the one providing the shortest time period i.e. shortest pay-off time is highlighted as the optimum solution. Thus, a straightforward top to bottom converter design method is yielded. Note that to make a fair comparison between the yielded combinations, i.e. to select the optimal topology based only on pay-off time; output of all the topologies should afford a unique solution providing the same quality on the grid-side current (in THD_i and ripple aspect). Since, each topology ensures the same output quality under different efficiencies; then the assessment can be reduced to financial aspect. Consequently, the design methodology warrants the same quality grid-side current while differing in efficiencies.

To use financial terminology, ‘total investment’ term can be replaced with the term, ‘total cost of ownership (TCO)’ whereas ‘return on investment (ROI)’ term can be substituted on behalf of ‘pay-off time’ expression. Furthermore, a figure of merit defined as ‘operational efficiency’ is used to estimate ROI of each design’s TCO regarding the corresponding energy prices where the wind turbine is to be established. Thus, a well-elaborated but easy forward design method becomes possible.

The converter design process is divided into six main parts, namely designation of semiconductor and optimum switching frequency, design of *LCL*-filter and its control scheme, grid standards compatibility check for the designed *LCL*-filter, switching frequency adjustment for 3L-VSC, operational efficiency calculation and topological comparison based on operational efficiency and cost evaluation.

In the first part, suitable semiconductors are selected for 2L, 3L-NPC and 3L-T VSC topologies regarding the input parameters such as power rating of the VSC (S_n), DC bus voltage (V_{dc}), the grid frequency (f_g), grid voltage (V_g), power factor (PF). Then, the optimum switching frequency (f_{sw}) is designated with regard to the efficiency constraint under the favored PWM pattern. In the second part, *LCL*-filter design is provided based on 2L topology including filter stability analysis. Third, the grid-side current (and/or voltage with the estimation/calculation of grid impedance of the PCC where the turbine is connected) is examined whether it complies with the stringent grid requirements (as presented in Chapter 2). Fourth, switching frequency for 3L-NPC and 3L-T is optimized so that all topologies could afford a unique solution providing the same quality on the grid-side current (in THD_i and ripple aspect) using the same *LCL*-filter designed in the former step. However, each topology delivers the same quality output under different efficiencies. Therefore, operational efficiency is defined and calculated for each topology in the fifth part. Furthermore, TCO considers initial cost, operating cost, i.e. economic value of a product over a determined life time. Thus, in the final part, TCO of each topology is compared with the accumulated profit over the specified life time. Then, the topology having minimum ROI is selected as the optimum solution. Owing to this design algorithm, ROI becomes the only parameter to decide on the optimum topology providing the same unique solution. Following sections comprehensively examine the design algorithm and clarify all of the design steps with elaborated illustrations throughout a thorough case study and cost analysis.

7.1. Converter Design Methodology

Before descending into particulars of converter design steps, topological comparison involving financial aspects will be simplified by grouping the common and uncommon elements of three VSC topologies. Figure 7.1 summarizes the entire converter design procedure with a neat illustration. As evident in the upper side of figure, wind turbine system with full-scale converter is split into two regions by a dashed line where right hand side depicts the framework of this dissertation and left hand side shows the part beyond the scope. Therefore, left hand side is represented with a dc current source, modeling the output of generator-side AC/DC converter (bottom side of Figure 7.1). Accordingly, the converter design methodology represented in Figure 7.3 focuses on the right hand side with all its aspects. Converter design methodology not only involves the design of grid-side DC/AC converter and grid interface *LCL*-filter but also ensures the grid connection compatibility in the light of widely used international grid codes. In Figure 7.1, 2L-VSC is used to elaborate the structure of grid-side DC/AC converter, but all three converter legs of it shall be replaced with the 3L leg modules of Figure 7.2, to obtain the full schemes of 3L-NPC and 3L-T type VSCs. Consistent with Figure 7.1 and Figure 7.2, common parts can be grouped consisting of DC-link capacitor, current/voltage sensors, control hardware, common-mode filter (to suppress EMI) and dv/dt (at converter terminals to prevent overvoltage transients). On the other hand; IGBT, heat-sink, fast diode (NPC-type), bidirectional switch (T-type), and gate driver can be pooled as uncommon parts of the topologies. Additionally, *LCL*-filter is designed for once and it is identical in each topology; therefore it can also be deemed as a common element. If there are other components common in each topology, they should be omitted for simplicity since they would just contribute as offset to calculations. So, uncommon hardware elements can be named as power semiconductor main unit (PSMU) and one leg diagrams in Figure 7.2 represent PSMU revealing IGBTs/switches, fast diodes explicitly whereas unique heat sink designs and gate drivers in each topology are not shown. On the whole, topological comparison reduces to PSMU comparison.

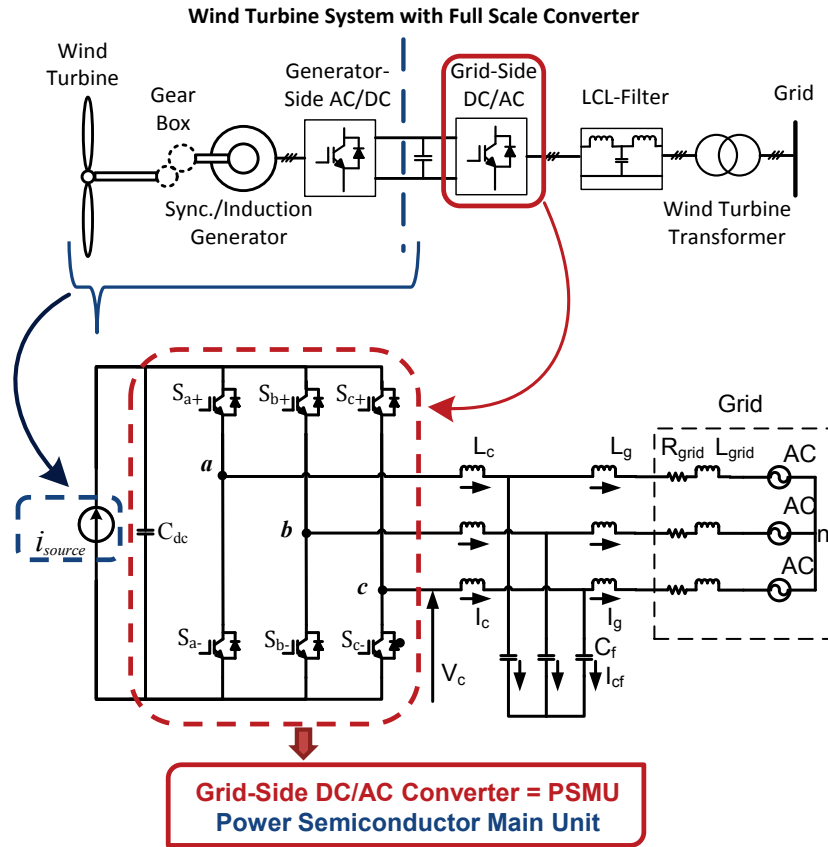


Figure 7.1 Simplification to topological comparison.

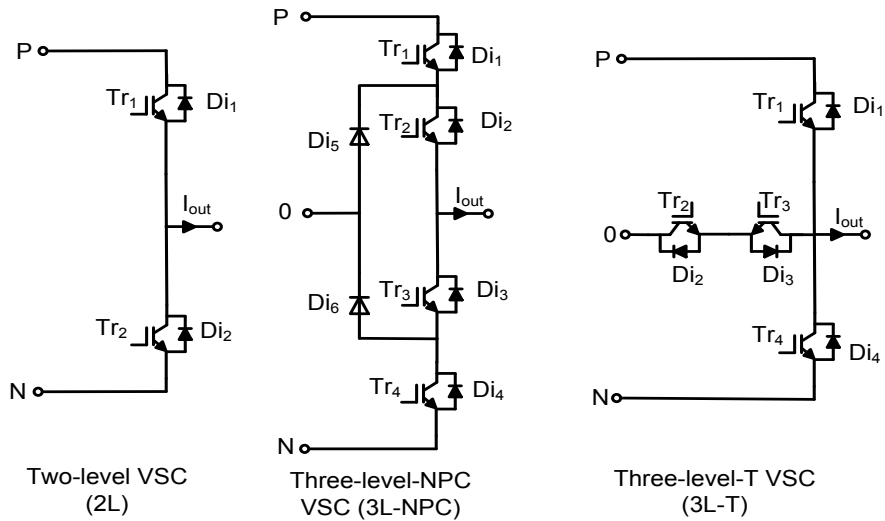


Figure 7.2 Simplified PSMU topologies.

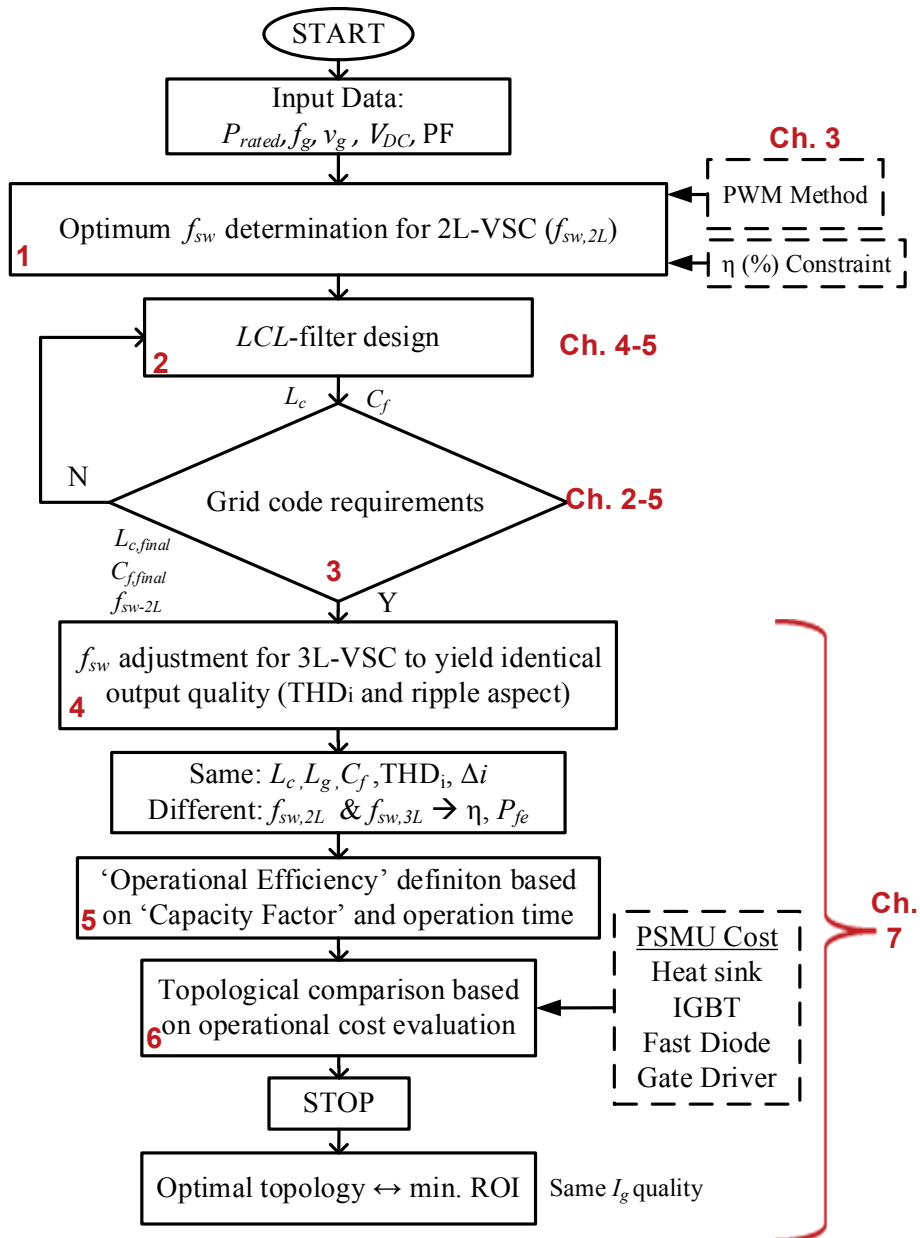


Figure 7.3 Complete design flow diagram (dashed boxes provide supplementary information for the related step).

As mentioned in the introduction, design methodology has been divided into six main steps. These steps are successively gone through in the following sections. Throughout this chapter, required outputs for the performance analysis of the three VSC topologies are obtained using a 1 MVA grid-connected PWM-VSC employing

space-vector PWM (SVPWM). Simulation parameters are provided in Table 7.1 (selected from designed set of filter components, $\alpha=0.25$ in Table 5.6). Note that GCF control will be favored throughout simulations and AD method will be used to stabilize the system.

Table 7.1 Simulation parameters to illustrate design steps.

Elements	Parameters	Values
Converter	S_n	1 MVA
	f_{sw}	2 kHz
	f_{samp}	4 kHz
	V_{DC}	1070 V
Grid	V_g	400 V _{rms-line}
	f_g	50 Hz
	PF	0.95-1

7.1.1. Optimum Switching Frequency Designation

Optimum switching frequency is designated in this step. As reference to the topological comparison section in Chapter 6, 3L-VSC is superior to 2L-VSC in terms of total semiconductor losses. Therefore, it is possible to achieve higher efficiencies using 3L-VSCs in place of 2L-VSCs at the same switching frequency. For this reason, maximum achievable efficiency is primarily limited by 2L-VSC. To further clarify this claim, an illustration of efficiency attributes of three VSC topologies versus various switching frequency is depicted in Figure 3.3. For a decent efficiency target around 98.5-99%, achievable f_{sw} interval has appeared to be within 1-2.5 kHz for 2L-VSC, posing a switching frequency constraint. For the same efficiency target, switching frequency is confined to 2.5-4.5 kHz interval for both 3L-VSC topologies as evident in Figure 3.3. Since the switching frequency constraint is primarily determined by the efficiency constraint of the design, the suitable switching frequency boundary should be designated regarding 2L-VSC

(Figure 3.3) in order to provide a comparative study that all the topologies comply with all of the design objectives and constraints.

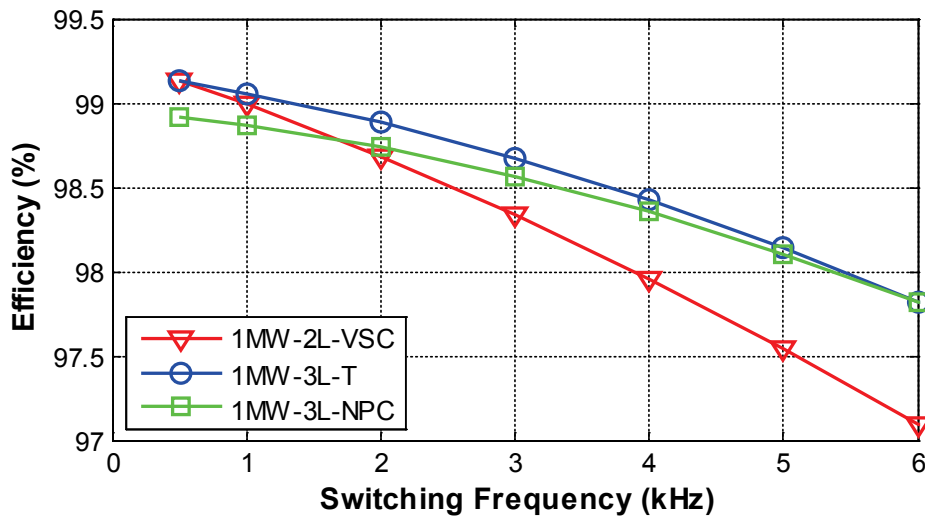


Figure 7.4 η (%) vs. f_{sw} plot of three VSC topologies under SVPWM.

7.1.2. LCL-Filter Design

In this step, LCL-filter design takes place with respect to the filter design algorithm provided in Chapter 5. As a reminder, this filter design algorithm depends primarily on the extensive control and stability analysis studied well in Chapter 4.

The filter design phase is only represented with a box in Figure 7.3 whereas its explicit notation is provided in Figure 7.5 (as reference to Section 5.3, Figure 5.18). Note that designed filter is identical for all VSC topologies to ensure same quality grid-side currents. For this purpose, filter design is done regarding the worst case scenario to provide satisfactory attenuation in any case; hence filter design is made considering the most limited topology in terms of the switching frequency, namely 2L-VSC. Then the switching frequency of 3L-VSC will be decreased in the 4th step to superpose the output characteristics of 3L-VSC with that of 2L-VSC since 3L-VSC provides better THD_i and ripple attributes on the grid-side at the same switching frequency as highlighted in the previous chapter. Since filter design procedure has already been presented elaborately in Chapter 5, the details are omitted in here and filter parameters are tabulated as in Table 7.2.

Table 7.2 Designed *LCL*-filter parameters.

Elements	Parameters	Values
<i>LCL</i> -Filter	L_c	173 μ H (11.4%)
	L_g	173 μ H (11.4 %)
	C_f	332 μ F (5%)

While designating the filter components, GCF control was favored throughout simulations and AD method was able to stabilize the system under 2L-VSC whereas the preferred PWM scheme was SVPWM. It must be noted that 2 kHz was sufficient to achieve AD. However, as mentioned in this section, filter design is made considering 2L-VSC, thus upgrading to 3L-VSC and decreasing the switching frequency to superpose the output attributes of 2L and 3L topologies may not hold the stability provided by AD for 3L-VSC any longer. In this case, use of PD for 3L-VSC become unavoidable and cause degradation in efficiency.

7.1.3. Grid Requirements Compatibility Test

The power quality injected into the grid should comply with the stringent international grid standards as stated well in Chapter 2. Thus, necessary attributes of the grid-side current should be monitored carefully.

Apart from holding the expectations reported by these standards, the internal design of the grid-side PWM VSC should also fulfill the design requirements addressed by many publications and know-how design rules in the literature. For instance, most of the articles in this field state that the worst case peak-to-peak converter-side current ripple (Δi_{max}) should be confined into 10-25% of peak rated load current (\hat{I}_{rated}) [54]-[70]. Otherwise, excessive stress might be burdened to the semiconductors, ending up with overheating, aging and degradation of the devices before its life-time even if the grid standards are met. Consequently, a thorough investigation both on internal design specifications and expectations of the corresponding grid standards is extremely necessary. For the internal design specifications, 10-25% worst case peak to peak current limit on the converter-side current is a good and sufficient design

requirement To suppress the ripple properly, the capability of converter-side inductance L_c must always be adequate to confine $\Delta i_{max(\%)}$ within 10-25% under normal grid circumstances. On the other hand, for the grid connection requirements, harmonics injected into the grid must be examined. By warranting these two requirements, the designed *LCL*-filter can be deemed as a decent, qualified and suitable filter for the grid connection. Note that magnitudes of the harmonic components injected into the grid depend not only on ripple extent on the converter-side inductance but also attenuation capability of the designed *LCL*-filter.

Figure 7.5 depicts the corresponding procedure of this step with a cascaded structure adjacent to *LCL*-filter design phase. After selecting a raw (untested) *LCL*-filter parameter set within the solution space, the corresponding system is simulated and examined under a special emphasis on the grid-side current. If simulation results reveal grid-side currents that cannot hold grid harmonic standards (weak design), a new set of filter parameters ought to be selected from the solution space by choosing a higher α set value, providing larger filter inductances. On the other hand, if the selected filter components provide harmonic attenuation more than enough, filter inductances should be decreased by choosing a lower α set value in order to prevent overdesign solution. If overdesign or weak design solutions cannot be overcome for none of the sets in the solution space, then a new solution space must be generated by assuming a new filter capacitance different than the one selected in the beginning of the algorithm. To sum up, for the selected value of filter capacitance C_f in the very beginning of the algorithm (within 1-5% of C_b), a unique solution space is generated. If no solution (and/or no optimal solution) case persist, C_f boundary may be extended beyond 1-5% interval; however; too much power factor deviation (reactive power absorption) is not desired in grid-connected converters. Thus, if altering C_f value and starting over the design phase does not work, then choosing a new switching frequency and starting over the *LCL*-design phase should be the ultimate remedy (Figure 7.5). In Chapter 5, this procedure is visualized in Figure 5.20.

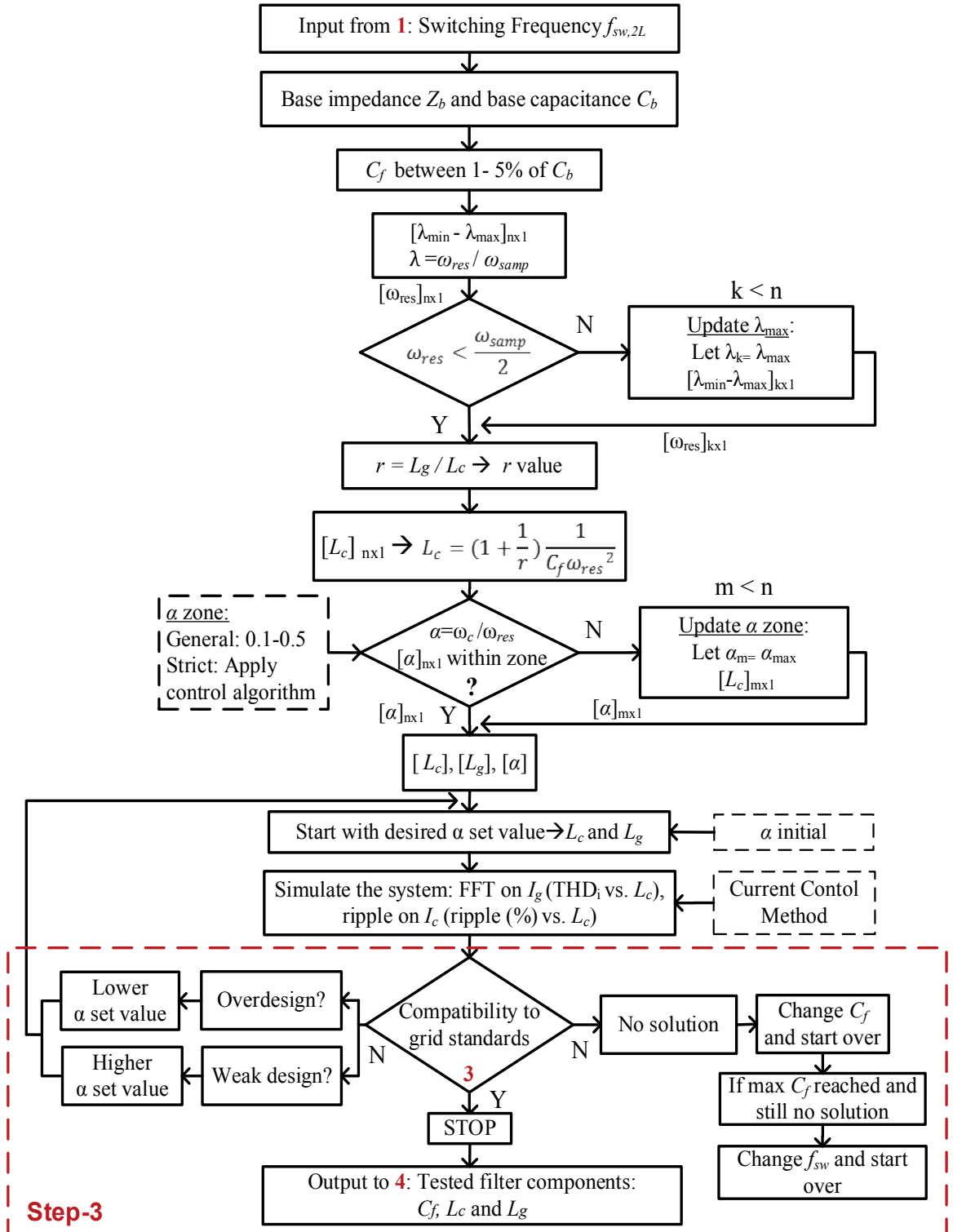
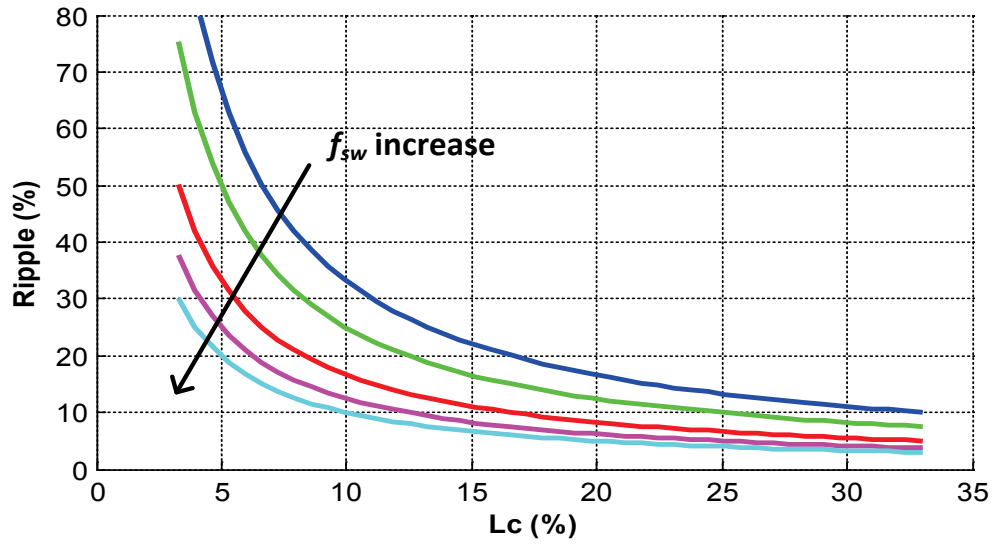
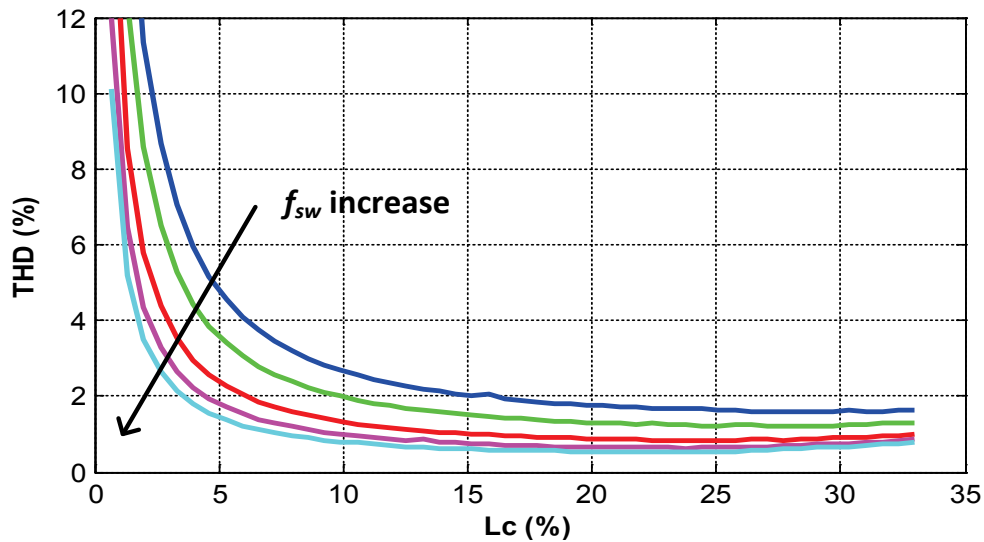


Figure 7.5 Proposed LCL-filter design algorithm.

Figure 7.6 reveals illustrations concerning the variation of converter current ripple and grid current THD_i against various converter side inductances (equals to grid-side inductance, $r=1$) within 0.03-0.32 p.u. These kinds of waveforms can be helpful attaining the desired specifications to hold grid standards on PCC before choosing a new α set point.



(a)



(b)

Figure 7.6 (a) Ripple (%) vs. L_c (%) (b) THD_i (%) vs. L_c (%).

For instance, if the optimal solution cannot be attained at the first trial for the initial α set point, it would guide the designer where the possible solution might be residing before setting a new α set point. Otherwise, trial-error process may take too much time and effort. In addition, Figure 7.6(a) and (b) depicts the shift of ripple and THD_i attributes against switching frequency change respectively to provide a better guidance on reaching the solution. To sum up, these characteristics can be deemed as feed-forward terms contracting the duration of design phase as suggested in the design algorithm in Figure 7.5.

As a remark, grid-side current THD_i attributes depends also on the ratio between converter-side inductance and grid-side inductance. Therefore, analysis of the current ripple attenuation (from converter side to grid side) should be monitored using (5.6). The primary objective of the LCL -filter is to confine the current ripple on L_c within 10-25%. Then, with the addition of $L_g C_f$ branch, minimum 80% additional current ripple attenuation (maximum 20% injection of the converter-side current ripple) with respect to the ripple on the converter side (10-25%) is aimed, confining the current ripple on the grid-side within 2-5% ($\equiv 0.02 \cdot 10\% - 0.02 \cdot 25\%$) of rated current in total [89].

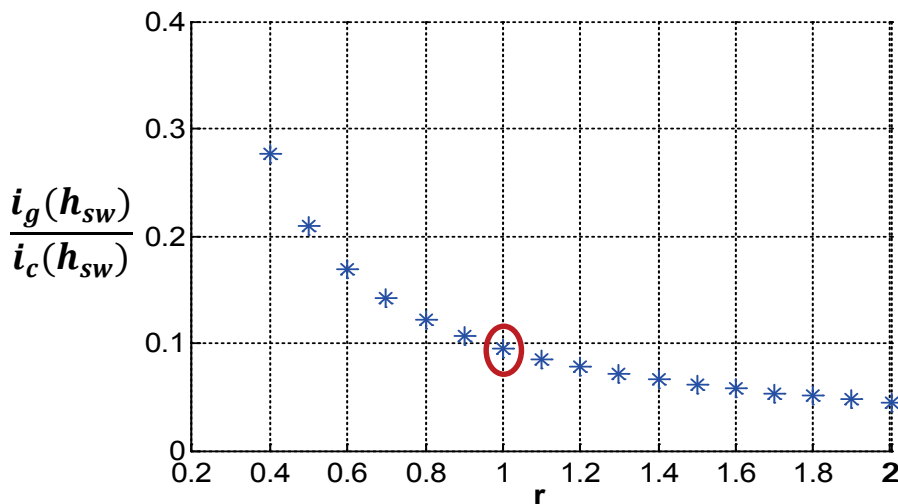


Figure 7.7 Harmonic attenuation vs. r .

Figure 7.7 illustrates the extent of converter-side current ripple injection to the grid for a number of grid-side inductance to converter-side inductance ratios. In general, this ratio is taken as unity to minimize the filter size and maximize the attenuation capability of the *LCL*-filter [89].

All things considered, it can be deduced that any converter-side inductance bigger than 0.1-0.15 p.u. does not enhance THD_i performance considerably as can be seen in Figure 7.6(b). Also, selecting $r > 1$ does not improve ripple attenuation considerably and *LCL*-filter become too bulky and costly [89].

7.1.4. Achieving Identical Output

After completing the filter design stage, analysis is extended by involving 3L-NPC and 3L-T type topologies. As a remark, the effective f_{sw} in 3L topologies is almost twice of f_{sw-2L} [77]-[83][89]. Therefore, THD_i performance of 3L topologies is expected to prevail over 2L topology under the same f_{sw} (Chapter 6). As mentioned previously, the target of the converter design algorithm is to provide the same output waveform quality (in THD_i and ripple aspect) under each topology by using the same *LCL*-filter parameters. Figure 7.8 illustrates the common and uncommon parts of the design that differ in each topology.

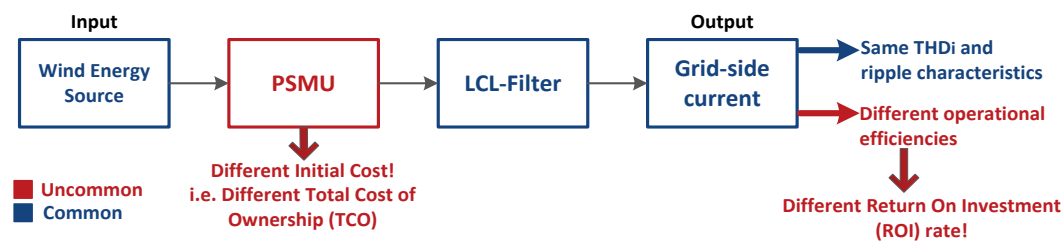


Figure 7.8 Achieving identical output.

As mentioned in Section 7.1, hardware based topological comparison is reduced to comparison of PSMU components, turning TCO analysis into PSMU cost calculation. As evident in Figure 7.8, distinct PSMU structures yield the same output at different efficiencies. Therefore, the cost savings owing to the saved losses by the

increased efficiencies will become of primary concern in ROI calculation. Further details about cost analysis will be provided in the cost evaluation section.

Switching frequency f_{sw} for 3L topologies (f_{sw-3L}) is varied with reasonable frequency steps to cover the set of f_{sw} values ($0.25f_{sw-2L} \div 1.5f_{sw-2L}$). Then, the optimum f_{sw-3L} is chosen providing the closest THD_i performance to that of 2L-VSC under varying L_c .

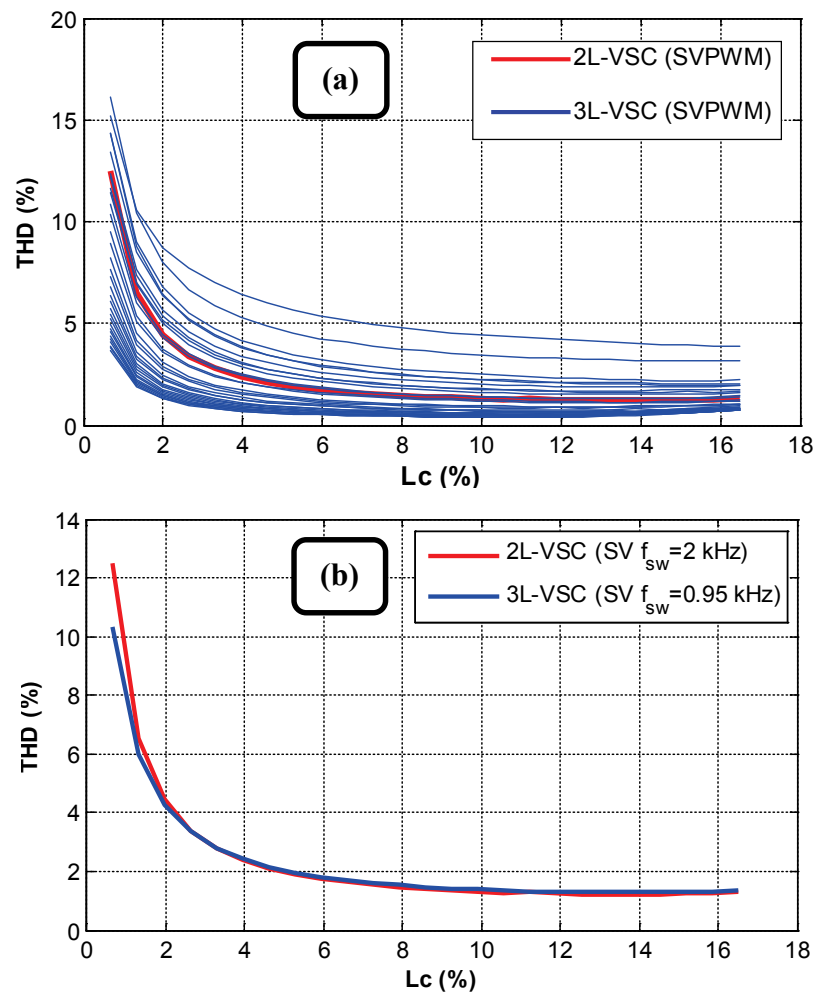


Figure 7.9 THD_i (%) vs. L_c under SVPWM (a) $f_{sw-2L}=2$ kHz, $f_{sw-3L}=0.25f_{sw-2L} \div 1.5f_{sw-2L}$ (b) $f_{sw-2L}=2$ kHz, $f_{sw-3L}=0.95$ kHz.

Figure 7.9(a) depicts THD_i vs. L_c (%) plots for 2L-VSC at f_{sw-2L} and 3L-VSC under the set of $0.25f_{sw-2L} \div 1.5f_{sw-2L}$. Then, f_{sw} iteration steps were adjusted sensitive enough to superpose the 2L and 3L plots. Figure 7.9 (b) shows the best fitting THD_i curve of

3L-VSC to the THD_i curve of 2L-VSC (at $f_{sw-3L}=0.95$ kHz). Consequently, f_{sw-3L} is found to be approximately half of the f_{sw-2L} as expected [89]. This can be further proven by the ripple attributes under the same conditions. Once the designated f_{sw-2L} and f_{sw-3L} values are substituted into the denominators of the formulas given in (6.7) and (6.8), same ripple values are yielded due to the relation of $24 \cdot f_{sw-3L} \equiv 12 \cdot f_{sw-2L}$. As a result, the ripple characteristic of 3L-VSC is found very close to that of 2L-VSC under the corresponding f_{sw-3L} , f_{sw-2L} values as depicted in Figure 7.10. Note that abovementioned formulas and THD_i and ripple analyses are determined based on SVPWM and DPWM1 methods, so for distinct switching patterns, these approximations may not hold. For simplicity, THD_i and ripple characteristics against converter side inductance are not revealed explicitly for DPWM1 scheme since the attributes of SVPWM and DPWM1 does not differ in shape but in magnitude slightly.

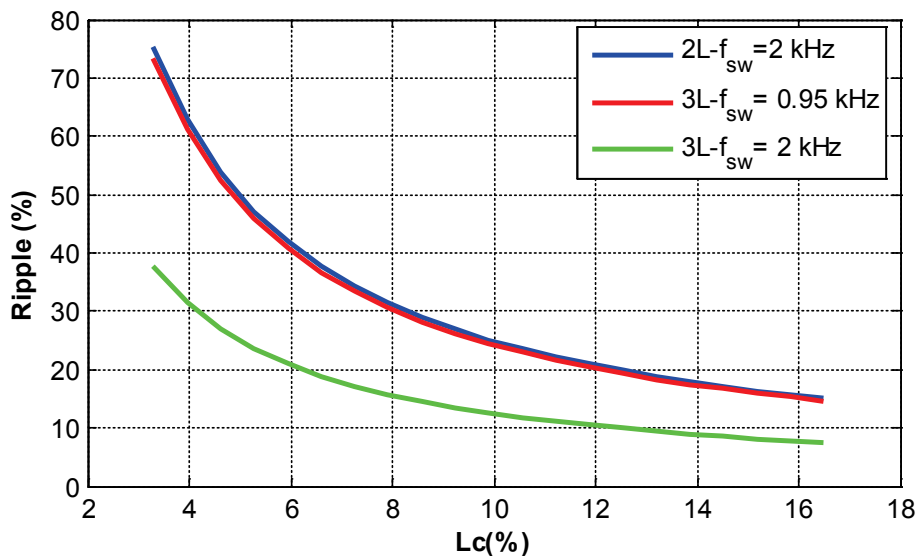


Figure 7.10 Ripple (%) vs. L_c under SVPWM.

All in all, THD_i and ripple performance of 3L-VSC is much better compared to 2L-VSC for the same f_{sw} (Figure 7.9 & Figure 7.10). However, with the arrangement of switching frequencies by means of the proposed methodology in this section, i.e. f_{sw} decrease in 3L-VSC, THD_i and ripple characteristics have been degraded, hence

improvements brought by 3L-VSC are nullified. For this reason, *LCL*-filter cannot detect any change in terms of stability and attenuation performance since PSMU blocks are arranged to perform alike.

7.1.5. Figure of Merit: Operational Efficiency

To calculate the operational efficiency, power output vs. wind speed characteristics is required as demonstrated in Section 2.4. MWT62/1.0 (Mitsubishi Wind Turbine Generator [84]) is selected as the reference wind turbine generator to illustrate the methodology. Its rated power is 1 MW and the grid-side DC/AC converter is designed considering connection to the low-voltage grid at 690 V line-to-line.

As mentioned in Chapter 2, wind turbine manufacturers assess their products regarding widely used term ‘capacity factor’ (*C.F*). Capacity factor is the actual output over a period of time as a proportion of a wind turbine or plant’s maximum capacity as depicted in (2.3). Capacity factor (i.e. power output in percentage) versus wind speed characteristic provided in MWT62/1.0 datasheet is shown in Figure 2.13. To highlight the power attributes of the selected wind generator, the first curve is elaborated as revealed in Figure 2.14 and then converted into rectangular boxes without changing the area under the curve to ease the numerical calculations.

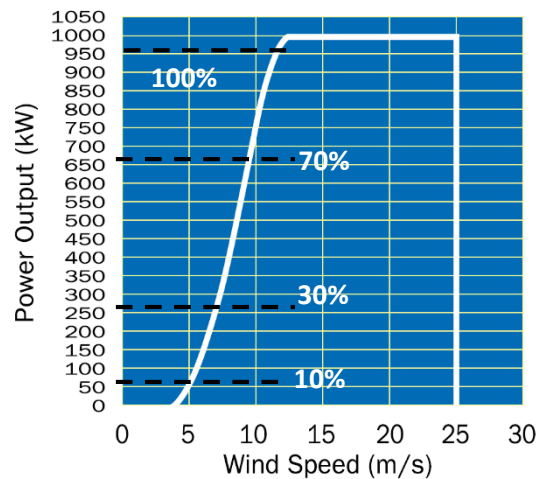


Figure 7.11 Power curve of MWT62/1.0.

The rectangular form assumes that the capacity factor is constant for the corresponding wind speed intervals. As evident in the power curve in Figure 2.14, wind speed is split into regions through which power output (P_{out}) is assumed as constant. The red-hatched slices referenced from c_1 to c_5 in Figure 2.14 depict the portions of each wind class benefited throughout the operation time (i.e. when wind speed is between 3.5-25 m/s). Depending on the width of these slices, the mean capacity factor is determined by weighing 5%, 20%, 50%, 85%, and 100% power outputs correspondingly as given in (2.4).

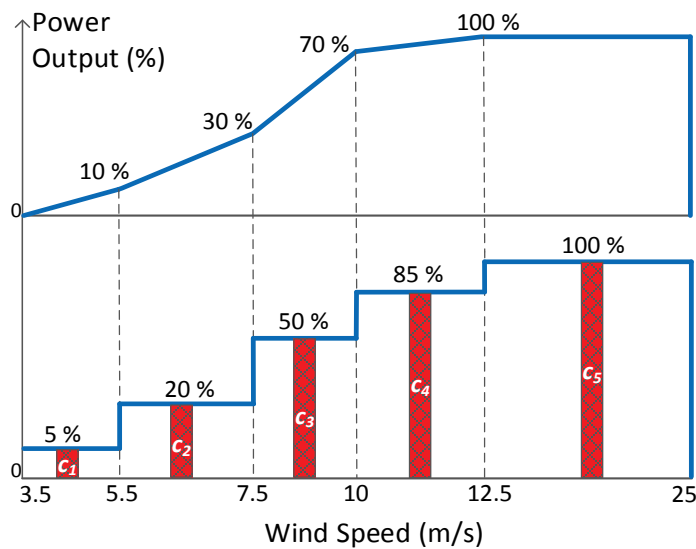


Figure 7.12 Modified MWT62/1.0 power curve.

The active operation time of a wind turbine per annum is represented with σ as revealed in (2.5). Since the power curve in Figure 2.14 represents the duration of active power generation, summation of weighing constants should be equal to the fraction σ as depicted in (2.6). In this chapter, maximum operation time for a wind turbine is assumed as 60% of the time annually ($\sigma=0.6$) [89]. Also, four distinct capacity factors, 20%, 30%, 40% and 50% will be considered through the analysis.

$$C.F(\%) = c_1 * 5 + c_2 * 20 + c_3 * 50 + c_4 * 85 + c_5 * 100 \quad (7.1)$$

$$\sigma = \frac{\text{Duration of active power generation per annum [hour]}}{\text{One year [hour]}} \quad (7.2)$$

$$\sum_{m=1}^5 c_m = \sigma \quad (7.3)$$

The classified wind speed intervals according to possible wind strengths in Figure 2.14 are tabulated in Table 2.4. Then, occurrence frequency of each wind strength is weighed so that corresponding 5%, 20%, 50%, 85% and 100% power outputs provide the mean capacity factors depicted in the first column of Table 2.4. ϕ_1 - ϕ_5 coefficients represent the weight of each wind strength benefited during $\sigma=60\%$ operation time. The sum of the wind speed coefficients is unity as revealed in (2.7). Thus, c_1 - c_5 and ϕ_1 - ϕ_5 represent the coefficients of the same weigh function; however, $\sum c_m = \sigma$ whereas $\sum \phi_n = 1$. So, in order to reflect 40% idle time period (no power generation) c_1 - c_5 constants should be normalized by multiplying ϕ_1 - ϕ_5 with $\sigma=0.6$ as shown in (2.8). Consequently, equivalent capacity factors representing 60% operation time per annum are embodied.

$$\sum_{n=1}^5 \phi_n = 1 \quad (7.4)$$

$$\sum_{m=1}^5 c_m = \sigma * \sum_{n=1}^5 \phi_n \quad (7.5)$$

Operational efficiency η_{op} can be calculated by using (2.9) where $\eta_{5\%}$, $\eta_{20\%}$, $\eta_{50\%}$, $\eta_{85\%}$, and $\eta_{100\%}$ are the efficiencies at 5%, 20%, 50%, 85%, and 100% load, respectively. As a remark, operation at 20% *C.F* means that the converter employed in the wind turbine provides 20% of its rated power to the load (devices connected to the PCC).

Table 7.3 Wind speed classification.

<i>C.F</i> (%)	Wind Speed Coefficients (ϕ_n)				
	ϕ_1 3.5-5.5 m/s	ϕ_2 5.5-7.5 m/s	ϕ_3 7.5-10 m/s	ϕ_4 10-12.5 m/s	ϕ_5 12.5-25 m/s
20 %	0.30	0.30	0.20	0.10	0.10
30 %	0.20	0.25	0.15	0.15	0.25
40 %	0.10	0.10	0.20	0.25	0.35
50 %	0.05	0.05	0.05	0.30	0.55

Operational efficiency η_{op} can be calculated using (2.9):

$$\eta_{op} = \phi_1 \cdot \eta_{5\%} + \phi_2 \cdot \eta_{20\%} + \phi_3 \cdot \eta_{50\%} + \phi_4 \cdot \eta_{85\%} + \phi_5 \cdot \eta_{100\%} \quad (7.6)$$

where $\eta_{5\%}$, $\eta_{20\%}$, $\eta_{50\%}$, $\eta_{85\%}$, and $\eta_{100\%}$ are the efficiencies at 5%, 20%, 50%, 85%, and 100% load (power output), respectively. As a remark, η_{op} definition uses coefficients ϕ_1 - ϕ_5 since efficiency can be discussed only when power is generated. Wind speed classification as given in Table 2.4, and an efficiency curve against load variation to calculate necessary efficiency values ($\eta_{5\%}$, $\eta_{20\%}$, $\eta_{50\%}$, $\eta_{85\%}$, $\eta_{100\%}$) are necessary to compute the operational efficiency (η_{op}) of the wind turbine. The wind data provided in [101] was benefited to determine ϕ_1 - ϕ_5 in Table 2.4. Figure 6.13 reveals the efficiency curves of 2L, 3L-NPC and 3L-T type VSCs under various loading conditions including light load and overload circumstances. Thus, corresponding efficiency of the grid-connected VSC under the loading conditions between 20-140% can be obtained.

Calculated operational efficiencies of each topology under 20%, 30%, 40% and 50% *C.F* are tabulated in Table 7.4. At all capacity factors, 3L-T topology prevailed over the other topologies; whereas, 2L-VSC delivered the worst efficiency performance.

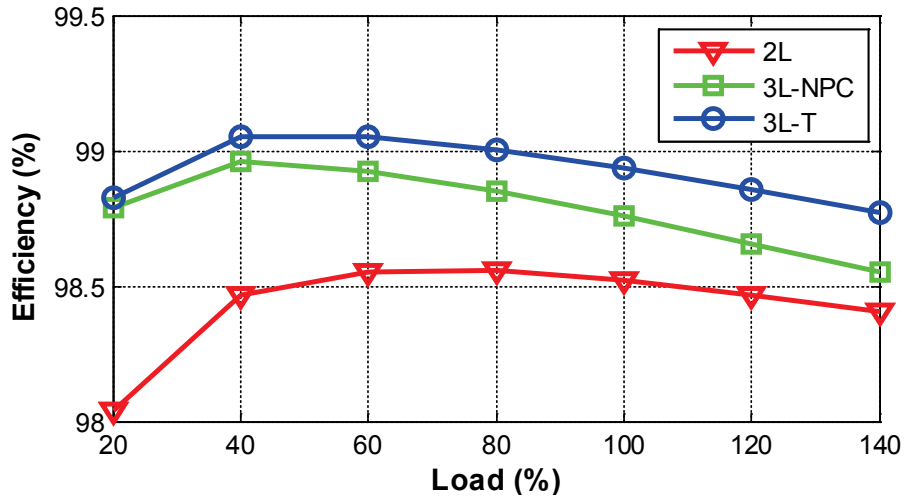


Figure 7.13 η (%) vs. load (%) characteristic for all topologies.

Table 7.4 Comparison of η_{op} (%) under $C.F$.

$C.F$ (%)	η_{2L} (%)	η_{3L-NPC} (%)	η_{3L-T} (%)
20 %	97.36	98.30	98.33
30 %	97.73	98.46	98.53
40 %	98.14	98.65	98.76
50 %	98.34	98.70	98.85

In the upcoming section, ROI (i.e. pay-off time) of each topology regarding $C.F$ and the energy price in major energy markets will be investigated.

7.1.6. Operational Cost Evaluation

TCO contains initial cost and operating cost, thus TCO is economic value of a plant over a determined life time. Operation schedule of a plant is the key point in ROI analysis. To calculate ROI, TCO is proportioned to the overall profit gained along the life time of the plant as depicted in (7.7). Then, topological comparison is made in terms of ROI of each design regarding the corresponding energy prices where the wind turbine is to be established. The topology providing minimum ROI is selected as the optimum solution.

$$\text{ROI [hour]} = \frac{\text{TCO [\$]}}{\text{Saved losses [kW]} \cdot \text{Electricity price [$/kWh]}} \quad (7.7)$$

7.1.6.1. Initial Cost Analysis

In this section, current market quotations for the components and energy prices (all in \$) to perform cost calculations are considered. IGBTs with 600V, 1200V, and 1700V were priced as 9ct/A, 17ct/A, and 23ct/A per IGBT, respectively. Furthermore, 1200V fast diodes employed in 3L-NPC were determined as 5 ct/A per diode, respectively. Gate drive units were accounted for \$10 per channel. The heat sink design has been achieved by following the steps revealed in [103]. Then, required minimum sink to ambient resistance value ($R_{th(s-a)}$) is found by means of the detailed temperature analysis provided in Chapter 6. The semiconductors in each leg (phase) were mounted on the same heat-sink resulting in three heat-sinks for each of 3L-NPC and 3L-T topologies. However, heat sinks in 2L-VSC had to be placed separately for each of the six IGBT modules since the stress on each module is excessive and cooling of these components become an issue.

Cost of system components common in each topology is omitted for simplicity since it would just contribute as offset to calculations. Thus, cost calculation of *LCL*-filter is redundant since it is identical in each topology.

The resulting cost for the individual converter components that are not common in each VSC topology, i.e. PSMU cost is summarized in Table 7.5 .

Table 7.5 TCO of PSMU.

1MW System	2L-VSC	3L-NPC	3L-T
IGBTs	\$2484	\$3672	\$4320
Fast Diodes	\$0	\$540	\$0
Gate Driver	\$60	\$120	\$120
Heat Sink	\$2551	\$1275	\$1275
TOTAL	\$5095	\$5607	\$5715

Initial PSMU costs of 3L topologies are slightly higher compared to 2L due to the higher semiconductor and gate driver cost. Savings in the heat sink cost has reduced the gap between the PSMU costs of 2L and 3L topologies. Besides, initial PSMU cost of NPC-type is marginally cheaper than that of T-type.

7.1.6.2. Accumulated Cost Savings Using Capacity Factor

In this section, instead of calculating the overall TCO of each topology, the cost savings (difference in TCOs) owing to the improved efficiency (saved losses) in 3L-NPC and 3L-T topologies in comparison to 2L topology will be determined. For this purpose, the operational efficiency of each topology under 20%, 30%, 40% and 50% *C.F* is made use of (Table 7.4) considering 1 year, 5 years, and 10 years of operation time. Then, the resulting kWh difference is utilized to calculate the cost savings in low, medium and high price energy markets, such as the USA, France and Japan, respectively. The net cost paid per kWh in industry was 17.9ct/kWh, 12.2ct/kWh, and 7ct/kWh in Japan, France, and the USA, respectively in 2013 [101]. The overall cost savings including a possible annual interest rate in electricity can be calculated by employing (9).

$$s_0 = \sum_{i=1}^{12n} \frac{s_i}{12(1 + \frac{k}{12})^i} \quad (7.8)$$

where s_0 is the cost savings in present, s_i is cost savings in month i , k is annual interest rate, and n is number of years. A 2L grid-connected VSC operating at 20% *C.F* (1752h annually) has 9640 W more losses than 3L-T as computed from operational efficiency results in Table 7.4. Thus, 16889 kWh less energy losses in 3L-T achieves a cost saving of s_i =\$3023, s_i =\$2061, s_i =\$1182 in each single year in the major markets, namely Japan, France, and the USA, respectively. Then, by means of calculated s_i , the overall energy cost savings at present value, s_0 was calculated regarding the operation time of 1 year, 5 years, and 10 years. The annual interest rate is taken as 3% ($k=0.03$). Eventually, the resulting s_0 was tabulated in

Table V. Likewise, the same approach was adopted for the comparison between 2L-VSC and 3L-NPC and resulting outcomes are presented in the Table V as well. Similarly, the cost savings of the systems operating at 30%, 40% and 50% C.F were also considered.

Table 7.6 s_0 vs. operation time in Japan, France and the USA.

(a) $C.F=20\%$

$C.F=20\%$	2L vs. T			2L vs. NPC		
	1 year	5 years	10 years	1 year	5 years	10 years
Japan	\$2975	\$14021	\$26090	\$2879	\$13568	\$25249
France	\$2028	\$9556	\$17782	\$1962	\$9248	\$17209
USA	\$1163	\$5483	\$10203	\$1126	\$5306	\$9874

(b) $C.F=30\%$

$C.F=30\%$	2L vs. T			2L vs. NPC		
	1 year	5 years	10 years	1 year	5 years	10 years
Japan	\$3717	\$17521	\$32604	\$3389	\$15974	\$29725
France	\$2534	\$11941	\$22221	\$2310	\$10887	\$20260
USA	\$1454	\$6852	\$12750	\$1325	\$6247	\$11624

(c) $C.F=40\%$

$C.F=40\%$	2L vs. T			2L vs. NPC		
	1 year	5 years	10 years	1 year	5 years	10 years
Japan	\$3815	\$17982	\$33463	\$3096	\$14594	\$27157
France	\$2600	\$12256	\$22807	\$2110	\$9947	\$18509
USA	\$1492	\$7032	\$13086	\$1211	\$5707	\$10620

(d) $C.F=50\%$

$C.F=50\%$	2L vs. T			2L vs. NPC		
	1 year	5 years	10 years	1 year	5 years	10 years
Japan	\$3961	\$18667	\$34738	\$2817	\$13275	\$24703
France	\$2699	\$12723	\$23676	\$1920	\$9048	\$16837
USA	\$1549	\$7300	\$13585	\$1102	\$5191	\$9661

Although TCO of 3L topologies are \$500-600 more than 2L topology, 3L topologies pay-off the initial PSMU cost difference just in one year even in low energy price markets like the USA. However, $C.F$ and total operation time influence ROI substantially. For instance, if the system were operating under 40% $C.F$ for ten years, 3L-T would save \$33463 over 2L; whereas, 3L-NPC would save \$27157 over 2L in Japan. Thus, T-type would become the most optimum solution for the implied conditions. Conversely, ROI of NPC and T-type is nearly one year over 2L-VSC under low $C.F$ (20%) in low energy price markets such as the USA (7ct/kWh [101]).

The initial PSMU cost of 3L-T is expected to be lower than 3L-NPC because 3L-NPC has a higher total volt-ampere (VA) per volume index due to additional diodes. However, T-type has become popular recently and its production volume is much lower than the NPC-type settled for years in industry. As the area of utilization of 3L-T increases, TCO of PSMU for 3L-T will decrease in the long term and the advantages brought by 3L-T over NPC will become more evident.

As mentioned in Chapter 6, the brand-new active bidirectional switch designed by *Fuji* [100] eliminates the diodes and diminishes total semiconductor losses in a great extent. The enhancement brought by this new switch in terms of efficiency is revealed in Figure 7.14. Also, resulting operational efficiency outcomes are computed using the curve and the corresponding coefficients in Table 7.3. With the operational efficiency outcomes of NPC and $T_{RB-IGBT}$ (Table 7.7), differential TCO comparison is provided below in Table 7.8.

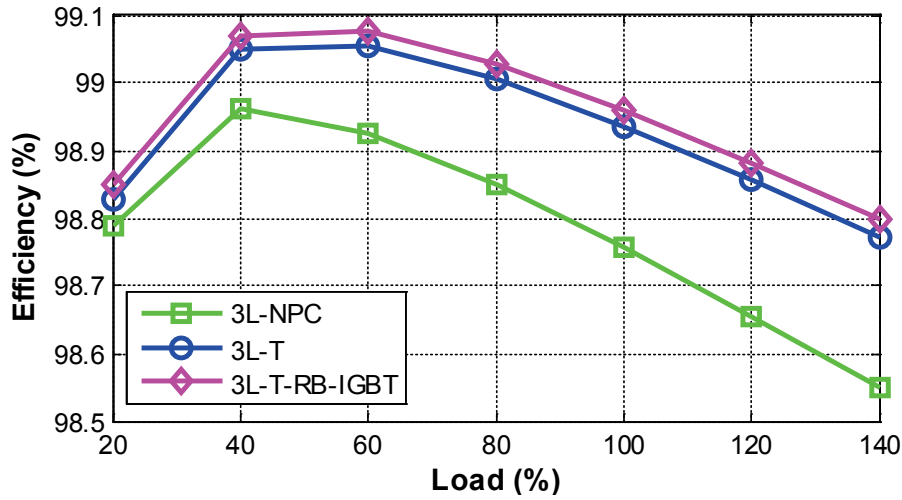


Figure 7.14 Improvement brought by 3L- $T_{RB-IGBT}$ in η (%) vs. load (%) characteristic under $P_{fe}=25\%$.

Table 7.7 Comparison of η_{op} (%) under $C.F.$

$C.F$ (%)	η_{3L-NPC} (%)	η_{3L-T} (%)	$\eta_{3L-T RB-IGBT}$ (%)
20 %	98.30	98.33	98.35
30 %	98.46	98.53	98.56
40 %	98.65	98.76	98.79
50 %	98.70	98.85	98.88

Table 7.8 Differential TCO comparison between NPC and $T_{RB-IGBT}$.

NPC vs. T_{RB_IGBT}	$C.F=20\%$			$C.F=50\%$		
	1 year	5 years	10 years	1 year	5 years	10 years
Japan	\$169	\$797	\$1483	\$1330	\$6269	\$11665
France	\$115	\$543	\$1011	\$907	\$4272	\$7950
USA	\$67	\$312	\$580	\$520	\$2451	\$4562

For the turbines generate energy at low capacity factor, contribution of $T_{RB-IGBT}$ is not considerable in short term even in high energy price markets. For longer operation time, cost difference becomes prominent. Nevertheless, $T_{RB-IGBT}$ becomes

quite favorable over NPC-type particularly for turbines operating at higher capacity factor even in short-term.

7.2. Case Study: 3 MVA VSC Design

In this section, a higher power VSC design case will be provided. However, details will not be shown for simplicity, only the outcomes will be tabulated. Then, a brief comparison regarding 1 MVA (given in Section 7.1) and 3 MVA designs will be made at the end. The design procedure up to Step-4 has been completed and corresponding outcomes together with the input parameters are merged and tabulated in Table 7.9.

Table 7.9 Simulation parameters for 3 MVA system.

Elements	Parameters	Values
Converter	S_n	3 MVA
	f_{sw}	1 kHz
	f_{samp}	2 kHz
	V_{DC}	1070 V
Grid	$V_{g,line-line}$	690 V _{rms}
	f_g	50 Hz
	PF	0.95-1
LCL-Filter	L_c	110 μ H (21.8%)
	L_g	110 μ H (21.8 %)
	C_f	1000 μ F (5%)

Frankly, low-voltage grid-connected 3 MVA system is not technically feasible without paralleling converters or power modules since there are not any semiconductors yet that is capable of switching nearly 3.6 kA at 1070 V_{DC}. So, a parallel structure of multiple power components is a widely used solution for multi-megawatt wind turbines nowadays [8].

Since I_r is 2511 A_{rms} for 3 MVA VSC, a suitable IGBT must have a minimum current rating of 1.5 times the peak rated current i.e. $1.5 * 2511 * \sqrt{2} = 5.33$ kA

whereas the appropriate voltage level should be 1700 V_{DC} regarding 1070 V_{DC} dc-link voltage. Recalling that 1.7 kV / 1.8 kA power device was selected for the 1 MVA 2L-VSC in Chapter 6, three paralleled modules or converters can barely supply (5.33 kA / 3= 1.78 kA) the design of 3 MVA for 2L-VSC topology. Likewise, for 3L-NPC topology three paralleled 1.2 kV/ 1.8 kA modules or converters are suitable. For the main switches in 3L-T, three paralleled 1.7 kV / 1.8 kA modules or converters while for the middle bidirectional switch 1.2 kV / 1.8 kA switches are appropriate.

It should be noted that previous chapters have solely analyzed the theoretical feasibility of 3 MVA design, so they have not sought the practical feasibility particularly. That is the reason why the switching frequency is selected as 1 kHz and the *LCL*-filter design is made correspondingly. If the practical viability were sought, three modules or converters would be paralleled for the 3 MVA VSC. Then, the switching frequency needn't have been decreased to 1 kHz and filter size needn't have been kept larger to compensate for the low switching frequency. For instance, each of paralleled module or converter could be deemed as 1 MVA system, hence the switching frequency could be increased to 2 kHz. But, the converter design methodology will proceed using the parameters in Table 7.9 in order to keep the link between former chapters illustrating 3 MVA system.

It should be noted that 1 kHz is too low to achieve AD especially when the filter inductance values get higher. This situation has been mentioned well in detail in Section 5.3.1.3. Besides, it is further decreased in 3L-VSC topologies, compelling the use of PD. Thus, for both 2L and 3L topologies PD is used to ensure stability. It should also be noted that PD can be used simultaneously with AD in order to minimize the need of damping resistor. It is evident that either AD or ID provides a degree of damping in the control loop even under low switching frequencies. But, usually this damping extent is not adequate to stabilize the system. The idea here is simply inserting the missing part of the damping to reach stability. In this way, a hybrid damping is employed and PD losses are minimized. Since AD is implemented within the Digital Signal Processor (DSP) chips and in physical

systems there are always current sensors measuring the currents on both converter-side (for over-current protection) and grid-side (for unity power factor), then usage of AD does not bring a significant complexity. With the proposed scheme, critical R_d value should be 0.23Ω under GCF control. It should be lower under CCF control as reference to the findings in Section 5.2. Nevertheless, GCF is preferred in this case study since PD losses will contribute to all topologies in the same amount, so there will be no considerable impact except for the offset. After sorting all the things out up until this step and superposing the output attributes of both topologies, resulting operational efficiency outcomes are computed using the individual efficiency values of 5%, 20%, 50%, 85% and 100% and the corresponding coefficients in Table 7.3. With the operational efficiency outcomes of NPC and $T_{RB-IGBT}$ (Table 7.10), differential TCO comparison is provided in Table 7.11.

Table 7.10 Comparison of η_{op} (%) under $C.F$ (3 MVA).

$C.F$ (%)	η_{2L} (%)	η_{3L-NPC} (%)	η_{3L-T} (%)	$\eta_{3L-T RB-IGBT}$ (%)
20 %	98.08	98.55	98.61	98.63
30 %	98.32	98.69	98.76	98.78
40 %	98.59	98.85	98.93	98.95
50 %	98.71	98.91	98.99	99.02

Table 7.11 Differential TCO comparison between NPC and $T_{RB-IGBT}$ (3 MVA).

NPC vs. $T_{RB-IGBT}$	$C.F=20\%$			$C.F=50\%$		
	1 year	5 years	10 years	1 year	5 years	10 years
Japan	\$257	\$1215	\$2260	\$854	\$4022	\$7484
France	\$175	\$828	\$1541	\$582	\$2741	\$5101
USA	\$100	\$475	\$884	\$334	\$1573	\$2927

Similar to 1 MVA case, the efficiency of 3L topologies are far much superior to that of 2L-VSC. Evaluating 3L topologies and determining the highest efficiency from there, it become obvious that contribution of $T_{RB-IGBT}$ is not considerable in short term even in high energy price markets for the turbines generate energy at low

capacity factor. On the other hand, for longer operation time, cost difference becomes considerable and $T_{RB-IGBT}$ becomes quite favorable over NPC-type particularly for turbines operating at higher capacity factor even in short-term.

7.3. Conclusions

This chapter has provided a complete design analysis for grid-connected PWM converters by combining the *LCL*-filter design procedure with topological comparison. As summarized in Figure 7.1, this chapter has benefitted from the former six chapters. First two chapters have determined the type of system and application area, constraints, requirements and so on. Third chapter has provided efficiency target, PWM method and eventually switching frequency constraint for the design. Fourth and fifth chapters have delivered required background for *LCL*-filter stability and design. Sixth chapter has supplied power semiconductor module and magnetic circuit loss characterization considering converter topologies and PWM methods, providing necessary modeling to realize a decent converter comparison study. And finally, seventh chapter has combined all of the information given by each chapter in a successive order and merges them to yield a top to bottom converter design algorithm. Hence, a step by step method ending with optimized filter elements along with the best topological choice based on the minimum ROI has been achieved.

THD_i and efficiency performances of 3L topologies were found to be superior to 2L topology under the same f_{sw} . Thus, 3L-VSCs are economically feasible in low-voltage applications especially in high energy-cost markets. In addition, the reduction in the commutation voltage has provided lower temperature rises in 3L-VSCs in return reducing the cost and size of the heat sinks. Besides, the 3L-T was found to be the better choice for low-voltage applications if efficiency and costs are the main concern. Finally, it has been shown that any improvement in the bidirectional middle switch in T-type poses a great impact on saved losses, making T-type much more favorable over 2L and NPC topologies in low-voltage wind turbine systems.

It must be noted that 2 kHz was sufficient to achieve AD. However, as mentioned in this chapter, filter design has been made considering 2L-VSC, thus upgrading to 3L-VSC and decreasing the switching frequency to superpose the output attributes of 2L and 3L topologies may not hold the stability provided by AD for 3L-VSC any longer. In this case, use of PD for 3L-VSC become unavoidable and cause degradation in efficiency. Finally, additional operational efficiency analysis (and hence ROI calculations) did not have to be done since DPWM1 and SVPWM were compared under equal semiconductor loss criterion. Thus, PWM method comparison has been conducted considering ripple, THD and WTHD performance of the topologies.

To sum up, after merging the laborious study held in each chapter and yielding a complete converter design algorithm, next section visualizes the performance of a designed converter under ideal, distorted and unbalanced grid conditions.

CHAPTER 8

THE PERFORMANCE ANALYSIS OF THREE-PHASE TWO-LEVEL VSC VIA COMPUTER SIMULATIONS

In this chapter, simulation study of 1 MVA three-phase two-level VSC is realized and the compatibility of the outcomes and expected results in the light of former chapters is examined. To achieve a proper simulation model, an input current source is inserted to model wind energy. In addition, device and controller parameters are modeled in accordance with the designed circuit models in the former chapters.

Computer simulations are carried out to guide the implementation step. SIMPLORER[®], which is a simulation program designed especially for power electronics applications [21], has been used. This chapter starts with a brief description of phase locked loop configuration. Since, this configuration (Figure 8.1) is vital for abc to dq -frame transformations (and vice-versa) throughout the simulations. The converter scheme for the simulation procedure is depicted in Figure 8.2. Besides, modeled control loop, PWM signal generation unit, PLL implementation unit, the emulation of distorted grid and semiconductor loss calculator unit are revealed in Figure 8.3-Figure 8.7, respectively.

Simulation results such as steady state measurements, input and output characteristics, dynamic responses are listed under three distinct operation cases, namely balanced grid operation, distorted grid operation and unbalanced grid-operation. Finally, the performance comparison of three different cases is carried out and the compatibility with the expected results is discussed. As a final remark, the exact control structure shown in this chapter is also used for 3L-VSCs, expect for the simple modification done in the PWM block (the more switches, the more gate

signals to be produced). Thus, one can simply replace 2L-VSC and modify PWM block to achieve a functioning 3L-VSC in accordance with 2L-VSC shown in here.

8.1. Phase Locked Loop

Before proceeding to simulation study part, phase locked-loop (PLL) configuration is mentioned briefly. PLL systems have been used in several equipment applications such as, UPS systems, active power filters, PWM rectifiers, etc., in which phase angle information of utility voltage is necessary. Since VSCs are designed to be grid-connected, grid synchronization with high power factor is important because of the requirements stated in the standards. As a result, determining amplitude, frequency and phase angle (θ_g) of the grid is necessary. Synchronous reference frame PLL (SRF-PLL) generates these information via Park transformation given in (4.9) with fast dynamic response and noise free operation by means of low pass filter characteristic for grid connected three-phase applications [109]. Note that i and θ are replaced in (4.9) by V and θ_{PLL} respectively and (8.1) is yielded:

$$\begin{bmatrix} V_d \\ V_q \end{bmatrix} = \begin{bmatrix} \cos\theta_{PLL} & -\sin\theta_{PLL} \\ \sin\theta_{PLL} & \cos\theta_{PLL} \end{bmatrix} \begin{bmatrix} V_\alpha \\ V_\beta \end{bmatrix} \quad (8.1)$$

where θ_{PLL} represents the phase angle output of the PLL block. SRF-PLL operation for three phase systems can be easily implemented since direct and quadrature axis of the dq -transformation block can be produced from the phase voltages as it is shown in Figure 8.1. Sampled stationary reference frame line to line voltages are converted to DC quantities by means of $\alpha\beta$ -transformation and Park (dq) transformation, respectively. In order to determine frequency and phase information, the DC quantity (V_q) is used in a control loop. V_q is controlled to be zero via a PI-controller with a reference signal V_q^* and the controller gives the result as a compensated line frequency in radian ($\Delta\omega$).

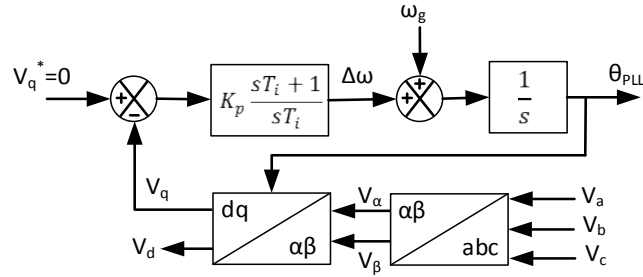


Figure 8.1 PLL structures for three phase grid synchronization.

Grid frequency is added to the result and an integral operator gives the phase angle of the utility grid which is also used as a feedback parameter in Park transformation block (Chapter 4). Thus, grid voltages V_a , V_b and V_c are inputted to the block as revealed in Figure 8.1 and the phase angle is extracted. As a remark, PI parameters of PLL block is computed using the formulas provided in [109] and for further details, aid of [109] can be applied.

8.2. Simulation Studies

The circuit parameters are stated in accordance with the calculated values in Chapter 5 as it is listed in Table 8.1. The converter circuit for the simulation studies is depicted in Figure 8.2. Besides, modeled control loop, PWM signal generation unit, PLL implementation unit, the emulation of distorted grid and semiconductor loss calculator unit are revealed in Figure 8.3-Figure 8.7, respectively.

Modeled_Wind_Source function block represents the wind energy attributes shown above. DC link voltage is measured via a voltmeter through the terminals of DC-link capacitors (Figure 8.2). As a remark, damping resistors are also present however; they are set to zero while active damping or inherent damping is employed. It should also be noted that grid-side inductance is arranged such that it contains the assumed grid inductance value; hence only resistor is inserted to model the utility grid. The voltage control block in Figure 8.3 uses the measured voltage and regulates the DC-link voltage as mentioned in Chapter 4. The output of this block, namely IC_dq_ref

block conducts the sinusoidal current reference generation and grid synchronization by generating proper dq -reference values. These reference values are inserted to the current PI controllers as the set values. The output these PI controllers (voltage reference vectors) are back transformed to three-phase abc signals (Figure 8.3). However, if active damping is utilized, the reference voltage vectors generated by the PI controllers are modified as can be seen in Figure 8.3. These voltage reference vectors are used by PWM block (Figure 8.4) to generate gate signals for IGBT switching. Vzero block in Figure 8.4 computes the zero sequence signals to be injected on the abc -output waveforms of current control loop (voltage reference vectors). Different means of zero sequence component computations (i.e. SVPWM and DPWM1) are involved in this block. The procedure addressed in [112] has been implemented to realize these two modulation methods. Furthermore, TRIANG1 block provides the carrier signal. Finally, COMP1, COMP2 and COMP3 blocks provide gate drive signals to the IGBTs by comparing the carrier signal with the resulting voltage reference vectors after zero sequence component injection. The PLL structure revealed in Figure 8.1 is accurately implemented in the simulation as depicted in Figure 8.5 where Vq_zero represents the zero reference input, CONST2 stands for ω_g and GS1 models $1/s$. Figure 8.6 depicts the modeling of distorted grid by injecting suitable magnitudes of 5th, 7th, 11th and 13th voltage harmonic components as percentage to the fundamental voltage component. Finally, Figure 8.7 shows the semiconductor loss calculation modeling presented in Chapter 6.

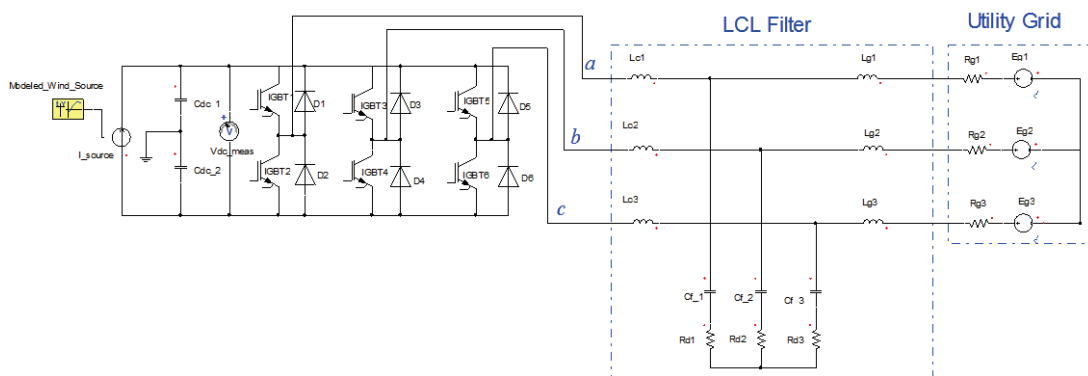


Figure 8.2 Simulation screen for three-phase 2L-VSC (Main body).

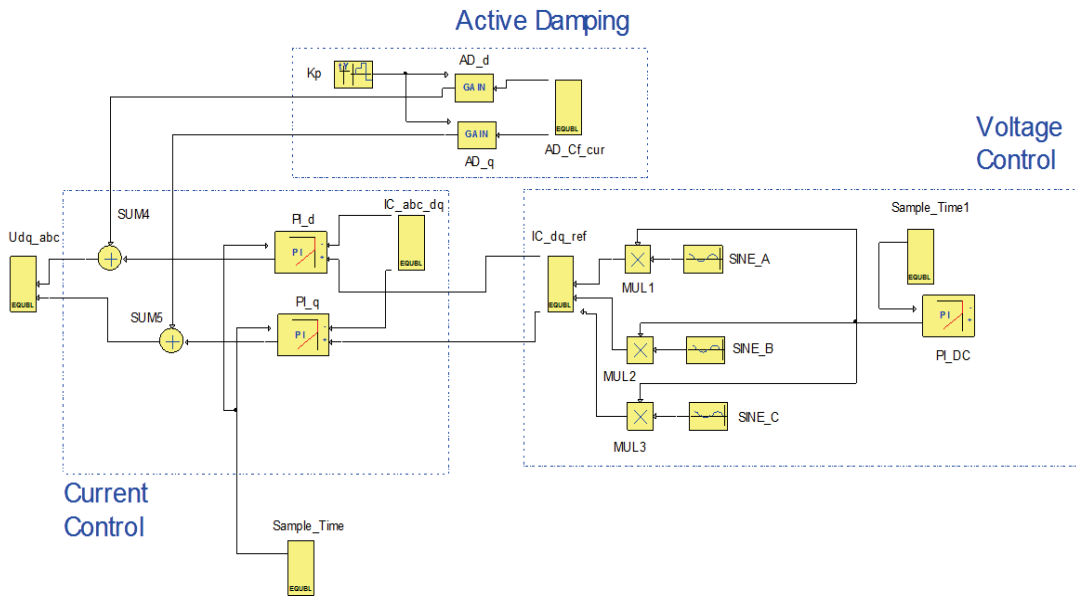


Figure 8.3 The circuit model of the control loops.

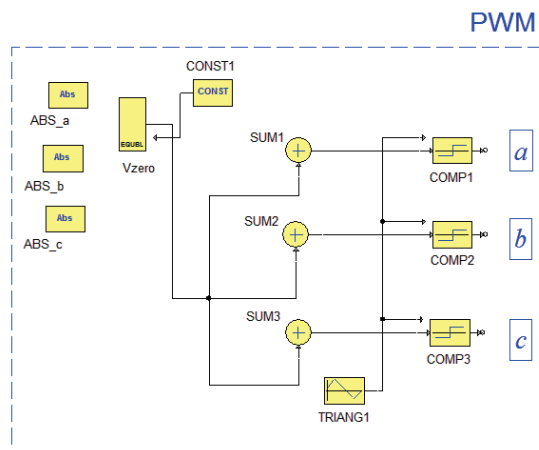


Figure 8.4 The circuit model of the PWM signal generation unit.

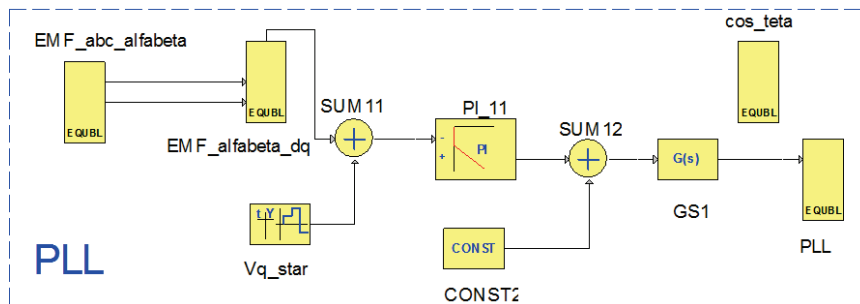


Figure 8.5 The circuit model of the PLL implementation.

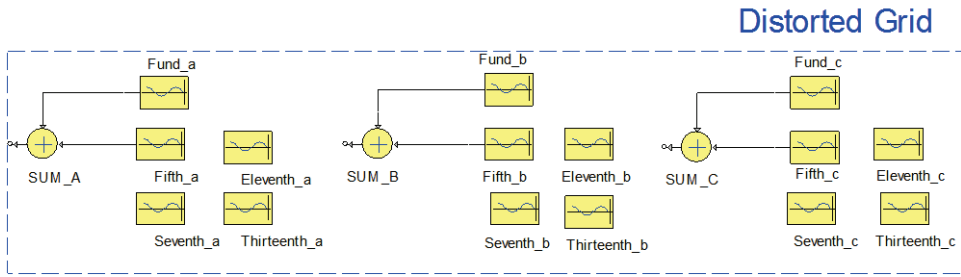


Figure 8.6 The circuit model of the distorted grid voltage.

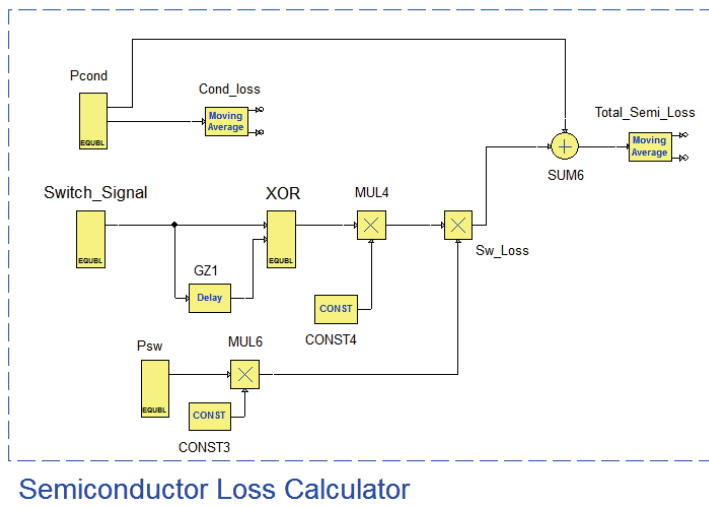


Figure 8.7 Implementation of the semiconductor loss calculator block.

Table 8.1 2L-VSC simulation parameters.

Elements	Parameters	Values
Converter	S_n	1 MVA
	f_{sw}	2 kHz
	f_{samp}	4 kHz
	V_{DC}	1070 V
	C_{DC}	8 mF
Grid	V_g	690V _{rms}
	f_g	50 Hz
	PF	0.95-1
LCL-filter	L_c	173 μ H (11.2%)
	L_g	173 μ H(11.2%)
	C_f	332 μ F (5%)
Damping method	GCF	AD
	CCF	ID
PI-current controller	K_p	0.51
	T_i	1.8ms
	$AD-K_d$	0.4
AD controller (P-controller)	K_d	0.98
PI-voltage controller	K_{DC}	5
	T_{DC}	7.2ms
PI-PLL controller	K_{PLL}	0.24
	T_{PLL}	1.8ms

8.2.1. Modeled Wind Energy Characteristics

A conventional wind turbine is modeled as a DC current source and its characteristics are modeled according to the intermittent nature of wind as shown in Figure 8.8.

As it can be seen in the figure, the maximum power of the wind turbine is 1 MW. In addition, current and voltage are measured to be 1183 A and 1070 \pm 5 V respectively. In the following sections the simulation outputs of 2L-VSC are realized under ideal, distorted and unbalanced grid conditions, respectively.

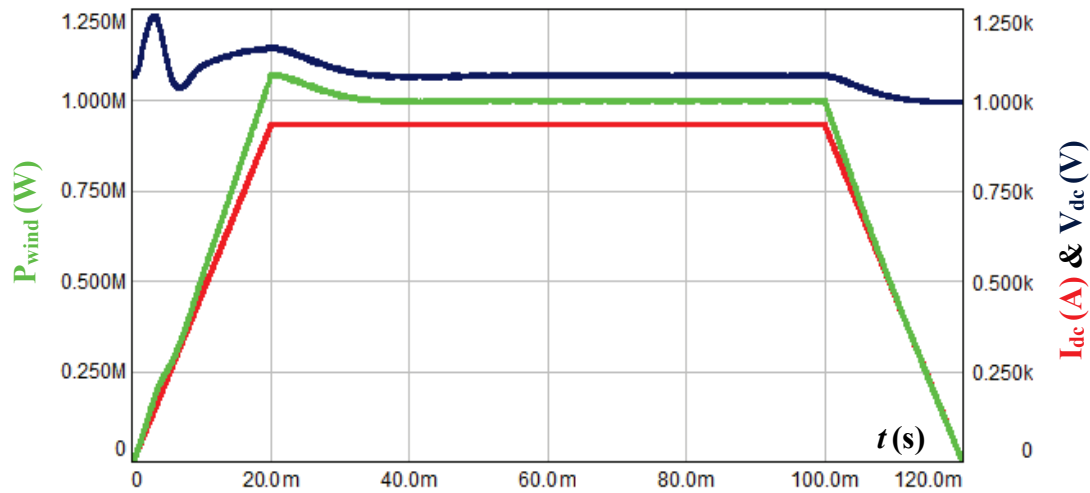


Figure 8.8 Modeled wind power (green) and I-V (red-blue) characteristics.

8.2.2. Simulation Results under Balanced Grid Conditions

In this section, a comprehensive simulation study is conducted to model normal grid operation and corresponding outputs are revealed and supported with reasonable comments.

8.2.2.1. Input Characteristics

DC-link capacitors are calculated as 8 mF in order to limit the input voltage ripple under 5%. In accordance with the calculated results, the measured voltage ripple is shown in Figure 8.9 where it is equal to 5V at 1 MW which corresponds to 1.47%.

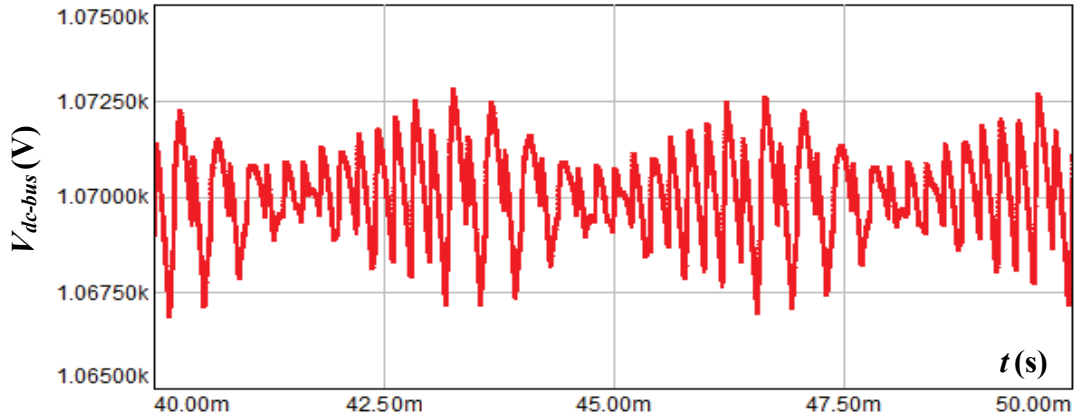


Figure 8.9 DC bus voltage ripple.

8.2.2.2. Output Characteristics

In this section, grid-side currents injected to the grid, filter capacitor currents, grid-voltage and grid current inspection for power factor (PF) and the performance of PLL block are revealed. Besides, $\alpha\beta$ -waveform of grid-side currents is also depicted in order to check the PWM operation region, i.e. whether the VSC operates in the linear modulation region or enters in the saturation region.

Figure 8.10 shows the grid-side currents. They are well-regulated under balanced grid and a very low THD_i of 0.75% is achieved due to the ideal grid-modeling.

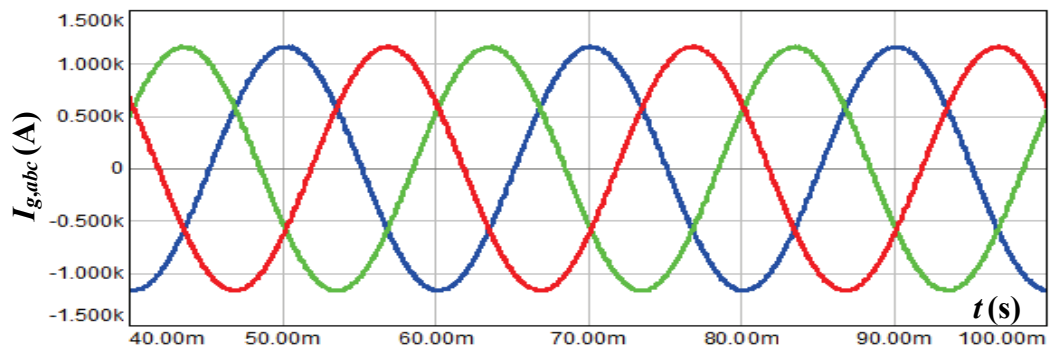


Figure 8.10 Grid-side currents (blue I_{ga} , red I_{gb} , green I_{gc}).

Besides, Figure 8.11 depicts that filter capacitor branch absorbs high frequency harmonic components as well as a small portion of fundamental component.

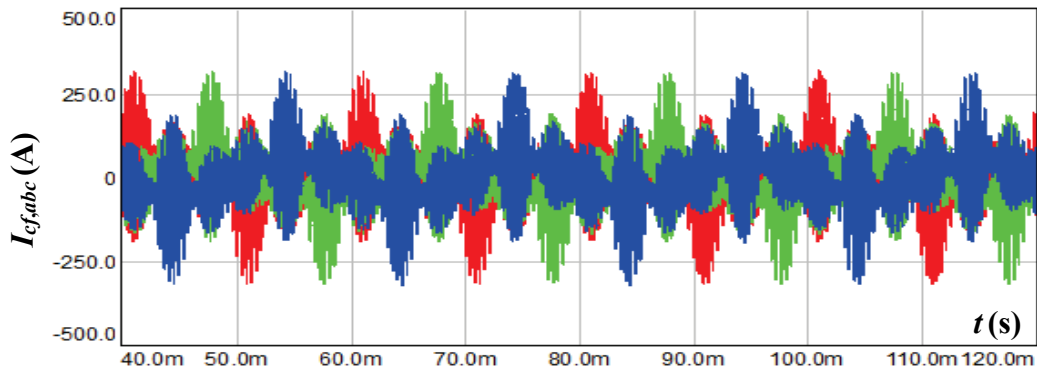


Figure 8.11 Capacitor currents (blue I_{cfa} , red I_{cfb} , green I_{cfc}).

Figure 8.12 shows one phase grid voltage and grid current waveforms. It is evident that unity power factor is achieved. Besides, Figure 8.13 and Figure 8.14 demonstrate related PLL outputs, concluding that PLL functions perfectly fine.

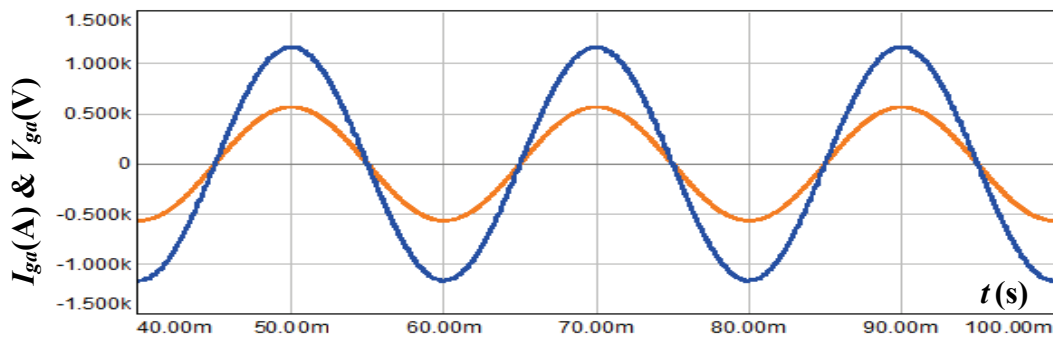


Figure 8.12 Phase a grid-side voltage and current (blue I_{ga} , orange V_{ga}).

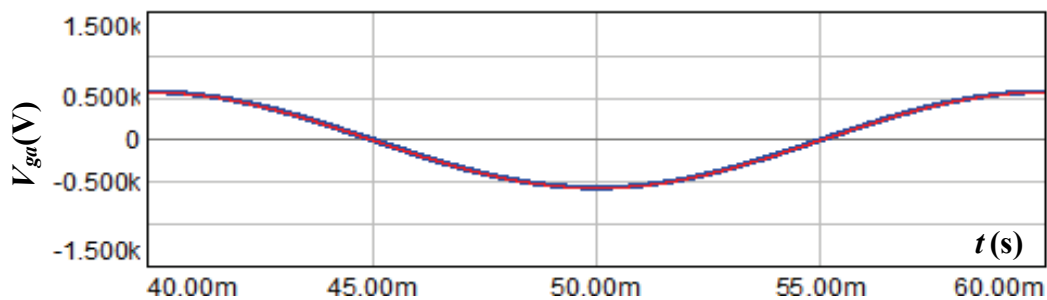


Figure 8.13 Phase a grid-side voltage and PLL output (blue V_{ga} , red $V_g \cdot \cos\theta$).

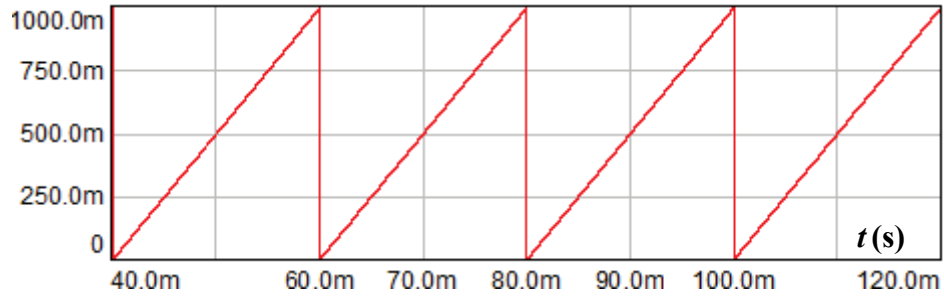


Figure 8.14 PLL vs. time.

Finally, Figure 8.18 reveals α vs. β frame components of grid-side current, concluding that PWM unit operates in linear modulation region. It is also evident in the grid-side currents containing no low-order harmonics.

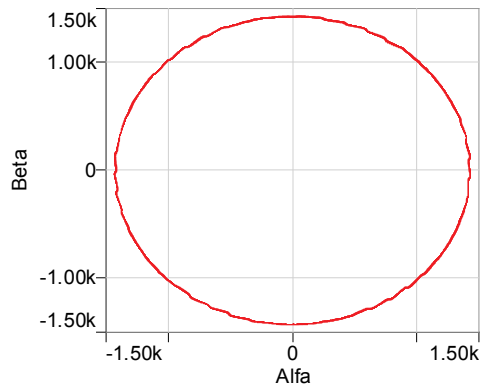


Figure 8.15 α vs. β frame components of grid-side current.

8.2.2.3. Steady-state measurements

The numerical data derived at rated power in the light of the steady-state attributes of 1 MW VSC shown above are summarized in Table 8.2.

Besides, THD_i of the output current is measured as 0.75% which is under the 5% limit stated in the IEC standards [48]. On the other hand PF is also higher than 0.95 which is quite satisfactory.

Table 8.2 2L-VSC steady-state measurements.

Parameters	Values
Input power P_{in} (kW)	1000
Grid power P_{grid} (kW)	987
Power loss P_{loss} (kW)	13
Efficiency η (%)	98.7
Power factor (PF)	0.996
Grid current THD _i (%)	0.75%
Peak grid current (A)	1168.6

8.2.2.4. Dynamic Response under Rapidly Changing Conditions

In addition to the steady-state characteristics, the performance of the VSC under rapidly changing conditions is also measured. For a 1MW WT system, there is always possibility of a sudden change of wind speed caused by the intermittent attributes of the nature. The designed control block should have the ability to adapt the rapidly changing conditions.

In Figure 8.16, a sudden power reduction of 250 kW (rated power to 75% of rated power) on input power is realized simulating a sudden decrease of input DC current source at 100th millisecond and it is observed that the control algorithm moves the rated power to the new maximum power operating point (750 kW) where the elapsed time to reach the new operating point is measured to be 15.1 milliseconds.

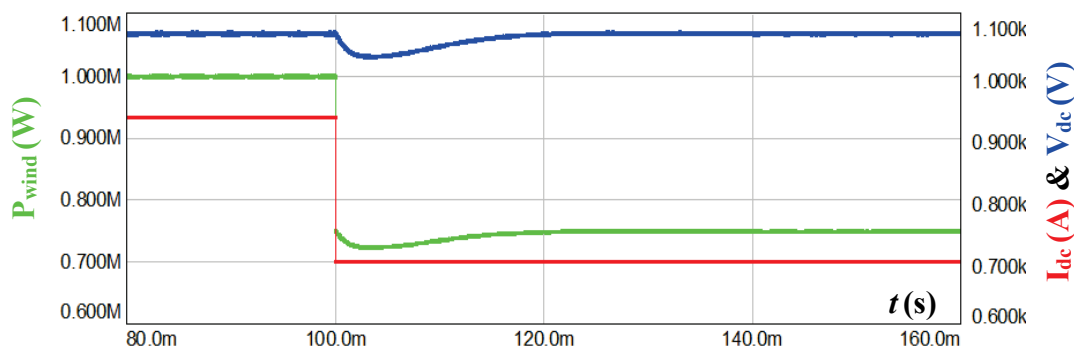


Figure 8.16 Dynamic response of DC-link voltage (blue), input power (green).

The adaptation to the new operating point is achieved by changing the reference input values inputted to current controllers and corresponding grid currents are produced as depicted in Figure 8.18.

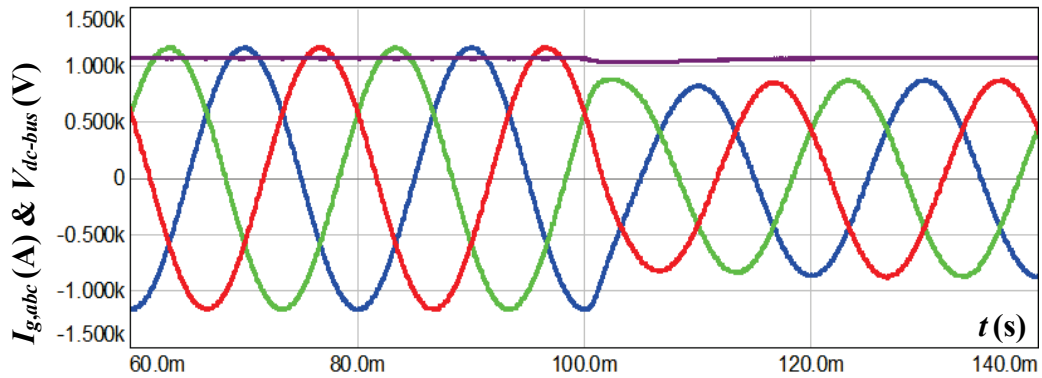


Figure 8.17 Dynamic response of DC-link voltage (purple) and grid currents (blue I_{ga} , red I_{gb} , green I_{gc}).

8.2.3. Simulation Results under Distorted Grid Conditions

In this section, a comprehensive simulation study is conducted to model distorted grid operation and corresponding outputs are revealed and supported with reasonable comments. Figure 8.6 depicts the modeling of distorted grid by injecting suitable magnitudes of 5th, 7th, 11th and 13th voltage harmonic components as percentage to the fundamental voltage component (3.08%, 2.21%, 1.41% and 1.21%, respectively).

8.2.3.1. Input Characteristics

In accordance with the calculated results, the measured voltage ripple is shown in Figure 8.18 where it is equal to 10 V at 1 MW which corresponds to 2.81%.

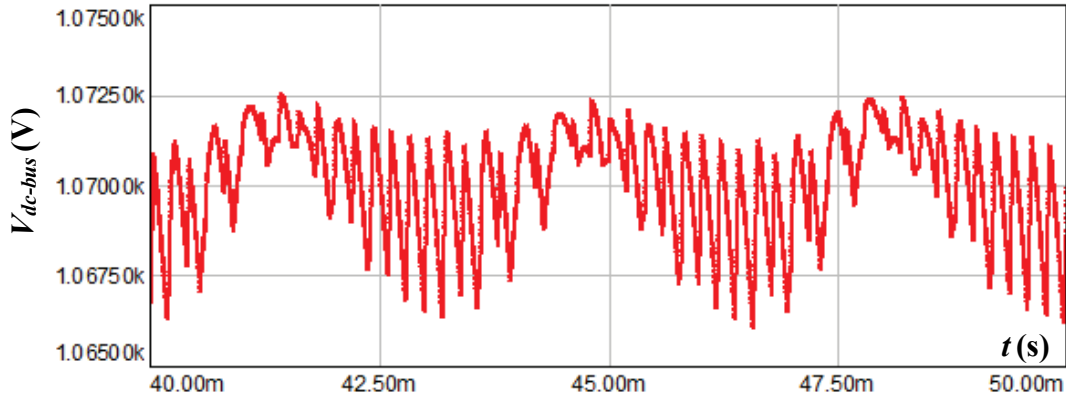


Figure 8.18 DC bus voltage ripple.

8.2.3.2. Output Characteristics

In this section, grid-side currents injected to the grid, filter capacitor currents, grid-voltage and grid current inspection for power factor (PF) and the performance of PLL block are revealed. Besides, $\alpha\beta$ -waveform of grid-side currents is also depicted in order to check the PWM operation region, i.e. whether the VSC operates in the linear modulation region or enters in the saturation region.

Figure 8.19 shows the grid-side currents. They contain low order harmonics due to the distorted grid voltage and a high THD_i of 6.29% is obtained due to the injected 5th, 7th, 11th and 13th components. The magnitudes of these components are selected very high on purpose in order to simulate the worst case scenario.

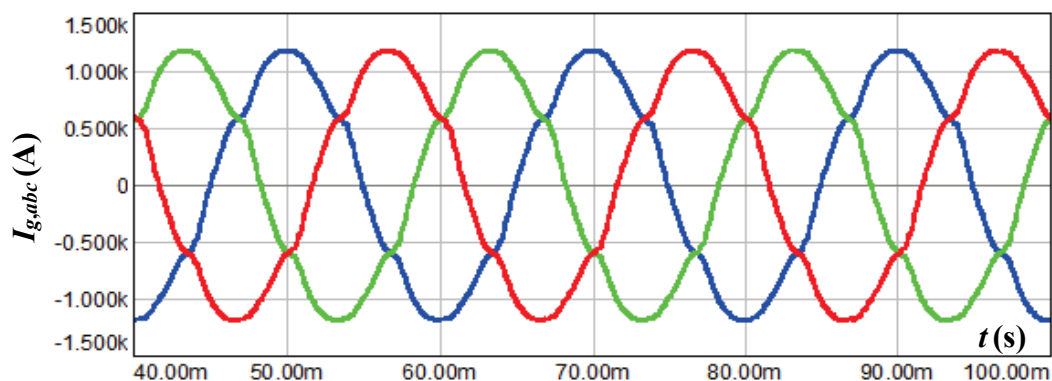


Figure 8.19 Grid-side currents (blue I_{ga} , red I_{gb} , green I_{gc}).

In addition, Figure 8.20 depicts that filter capacitor branch absorbs high frequency harmonic components as well as a small portion of fundamental component. They seem similar to the ones in balanced grid case, since filter capacitors show very high impedance to the low order harmonic components.

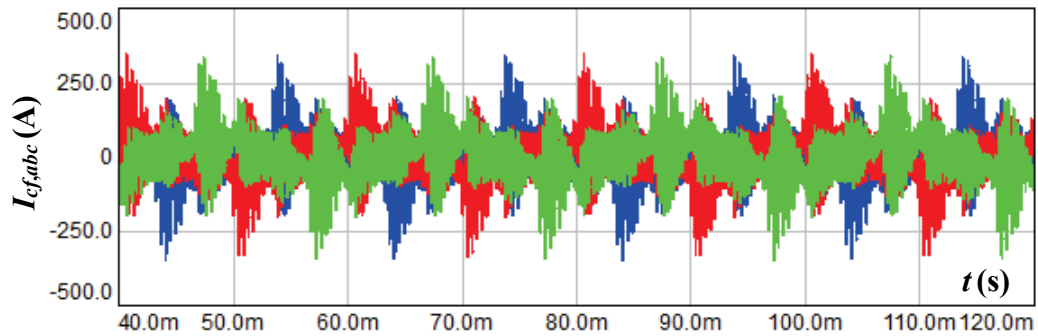


Figure 8.20 Capacitor currents (blue I_{cfa} , red I_{cfb} , green I_{cfc}).

Figure 8.21 shows one phase grid voltage and grid current waveforms. It is evident that unity power factor is still achieved even under distorted grid. Besides, Figure 8.22 and Figure 8.23 demonstrates related PLL outputs, concluding that PLL functions properly but contains slight fluctuations.

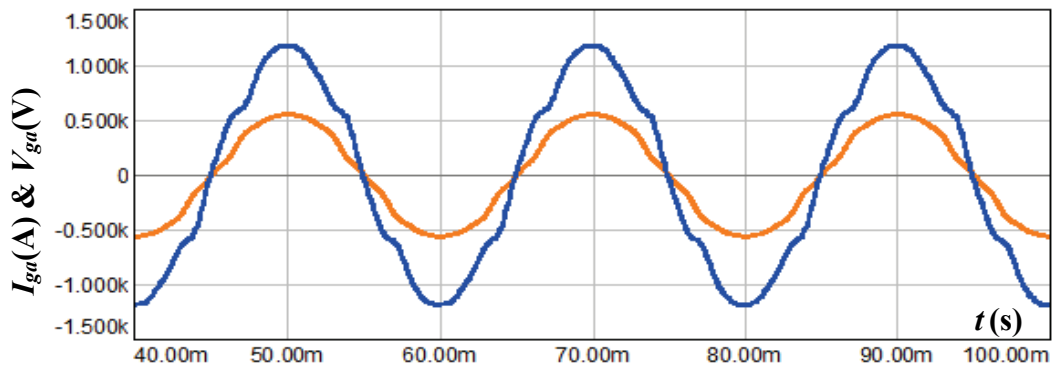


Figure 8.21 Phase a grid-side voltage and current (blue I_{ga} , orange V_{ga}).

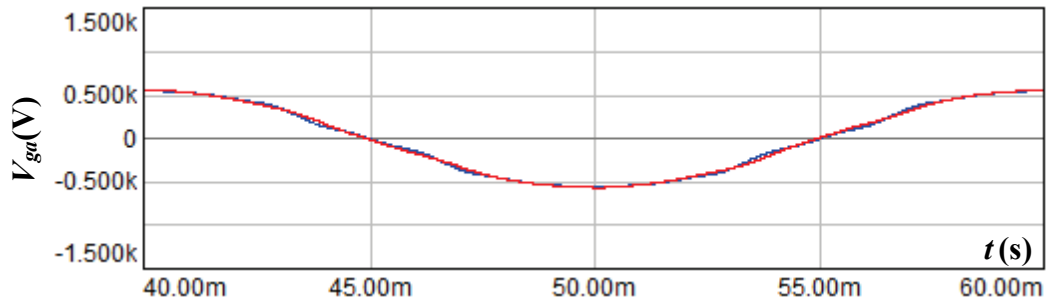


Figure 8.22 Phase a grid-side voltage and PLL output (blue V_{ga} , red $V_g \cdot \cos\theta$).

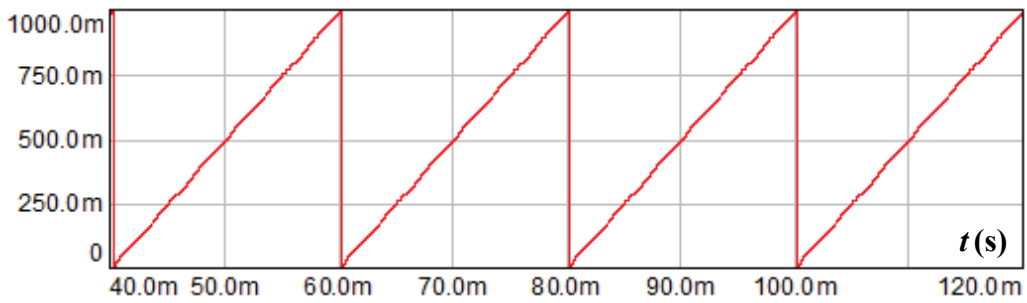


Figure 8.23 PLL vs. time (s).

Finally, Figure 8.24 reveals α vs. β frame components of grid-side current. PWM unit operates in linear modulation region; however, circular shape is slightly distorted due to the distorted grid operation.

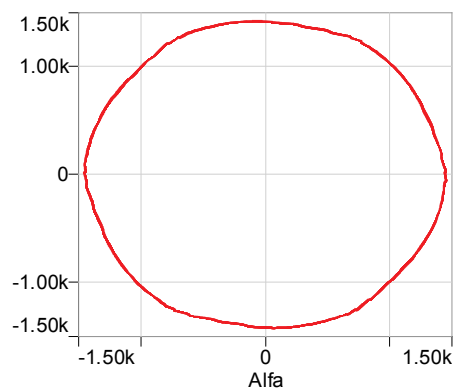


Figure 8.24 α vs. β frame components of grid-side current.

8.2.3.3. Steady-state measurements

The numerical data derived at rated power in the light of the steady-state attributes of 1 MW VSC under distorted grid operation are summarized in Table 8.3.

Table 8.3 2L-VSC steady-state measurements (distorted grid).

Parameters	Values
Input power P_{in} (kW)	1000
Grid power P_{grid} (kW)	975
Power loss P_{loss} (kW)	25
Efficiency η (%)	97.5
Power factor (PF)	0.994
Grid current THD _i (%)	6.29%
Peak grid current (A)	1185

Moreover, THD_i of the output current is measured to be 6.29% where THD_v is 4.22%. On the other hand PF is found to be higher than 0.95 which can be stated as satisfactory. It should be noted that peak grid current has been increased under distorted grid case compared to the normal grid case, leading to higher semiconductor and filter losses; hence lower efficiency is attained.

8.2.3.4. Dynamic Response under Rapidly Changing Conditions

In Figure 8.25, a sudden power reduction of 250 kW (rated power to 75% of rated power) on input power is realized simulating a sudden decrease of input DC current source at 100th millisecond. It is observed that the control algorithm moves the rated power to the new maximum power operating point (750 kW) where the elapsed time to reach the new operating point is measured to be 16.3 milliseconds.

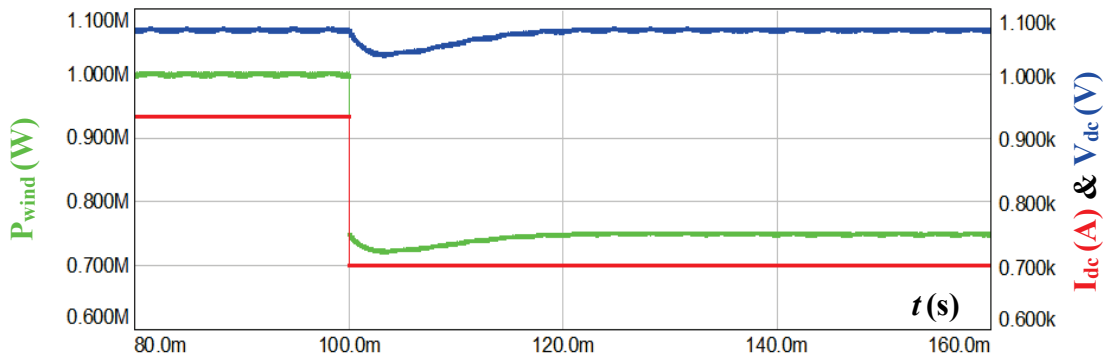


Figure 8.25 Dynamic response of DC-link voltage (blue), input power (green).

The adaptation to the new operating point is achieved by changing the reference input values inputted to current controllers and corresponding grid currents are produced as depicted in Figure 8.26.

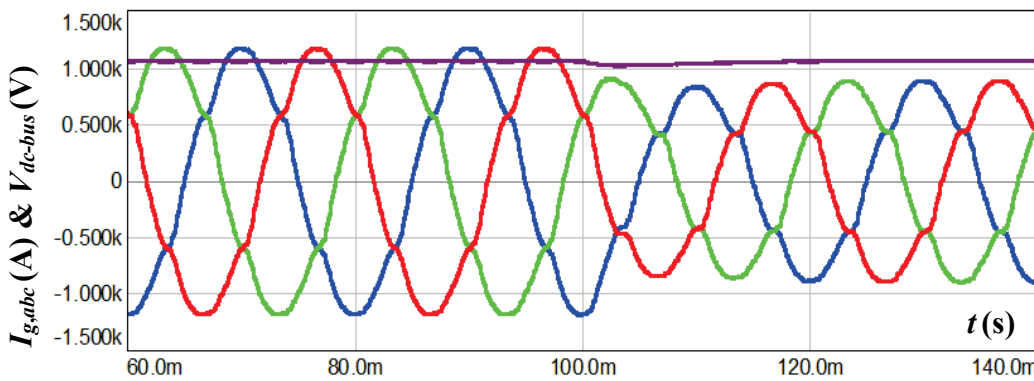


Figure 8.26 Dynamic response of DC-link voltage (purple) and grid currents (blue I_{ga} , red I_{gb} , green I_{gc}).

8.2.4. Simulation Results under Unbalanced Grid Conditions

In this section, a comprehensive simulation study is conducted to model unbalanced grid operation where phase c is faulted and corresponding outputs are revealed and supported with reasonable comments. Figure 8.28 depicts the unbalanced grid voltage component (phase c -200 V_{rms}).

8.2.4.1. Input Characteristics

In accordance with the calculated results, the measured voltage ripple is shown in Figure 8.27 where it is equal to 50 V at 1 MW which corresponds to 4.67%.

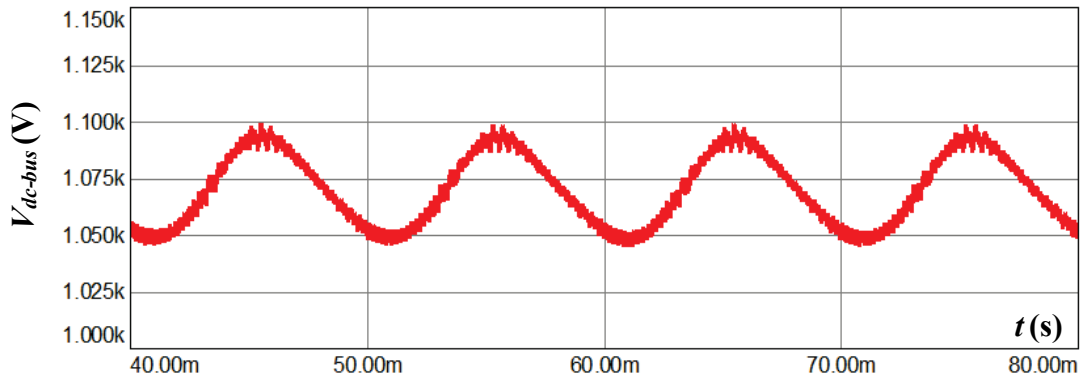


Figure 8.27 DC bus voltage ripple.

8.2.4.2. Output Characteristics

In this section, unbalanced grid-voltages, grid-side currents injected to the grid, filter capacitor currents, grid-voltage and grid current inspection for power factor (PF) and the performance of PLL block are revealed. Besides, $\alpha\beta$ -waveform of grid-side currents is also depicted in order to check the PWM operation region, i.e. whether the VSC operates in the linear modulation region or enters in the saturation region.

Figure 8.28 shows the distorted grid voltages. Thus, grid-side currents are distorted in a great extent as shown in Figure 8.29.

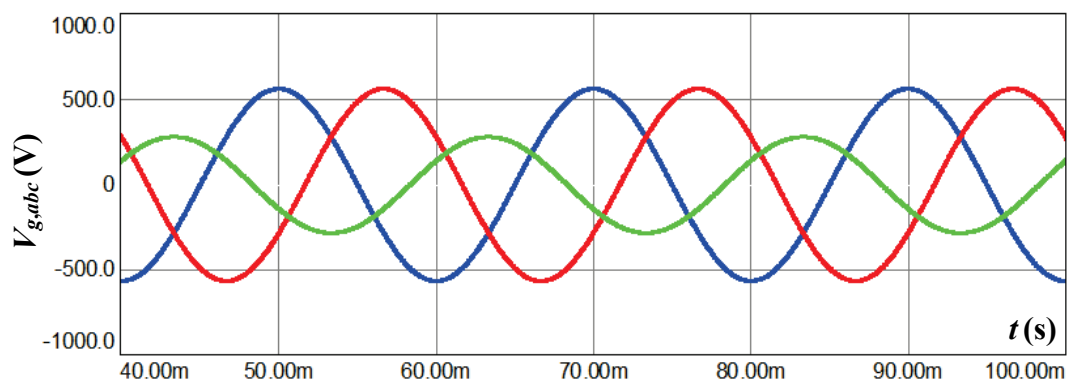


Figure 8.28 Grid voltages (blue V_{ga} , red V_{gb} , green V_{gc}).

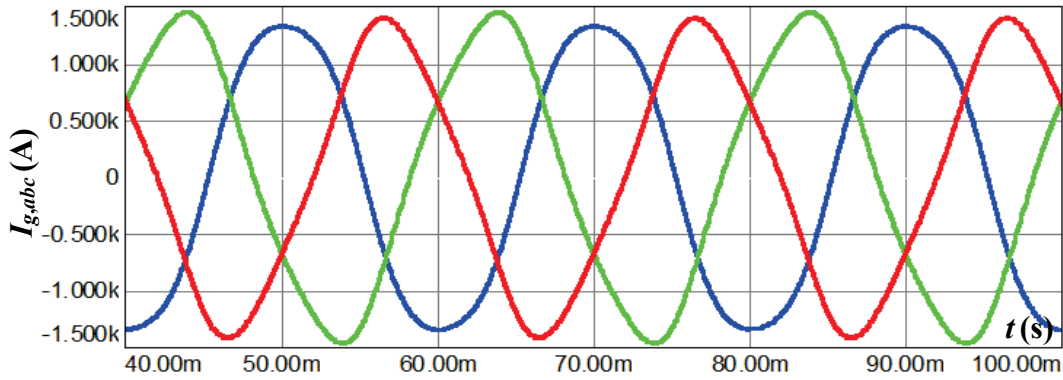


Figure 8.29 Grid-side currents (blue I_{ga} , red I_{gb} , green I_{gc}).

In addition, Figure 8.30 depicts that filter capacitor branch absorbs high frequency harmonic components as well as a small portion of fundamental component. They seem similar to the ones in balanced grid case and distorted grid case expect for the phase c component.

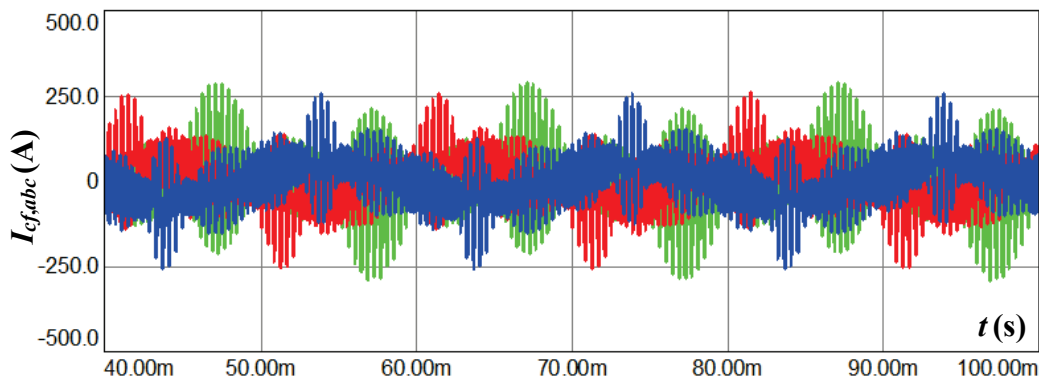


Figure 8.30 Capacitor currents (blue I_{cfa} , red I_{cfb} , green I_{cfc}).

Figure 8.31 shows one phase grid voltage and grid current waveforms. It is evident that PF close to unity power factor is still achieved even under unbalanced grid. Besides, Figure 8.32 and Figure 8.33 demonstrates related PLL outputs, concluding that PLL functions properly but this time a slight phase shift has been occurred due to the unbalanced grid voltages..

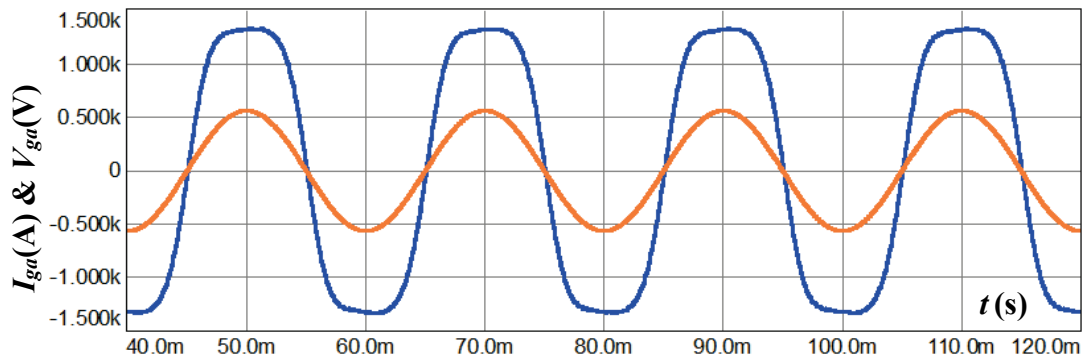


Figure 8.31 Phase a grid-side voltage and current (blue I_{ga} , orange V_{ga}).

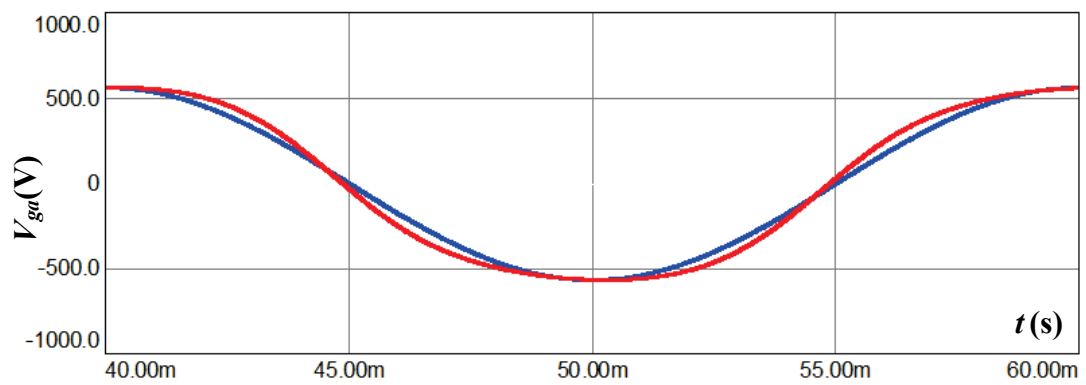


Figure 8.32 Phase a grid-side voltage and PLL output (blue V_{ga} , red $V_g \cdot \cos\theta$).

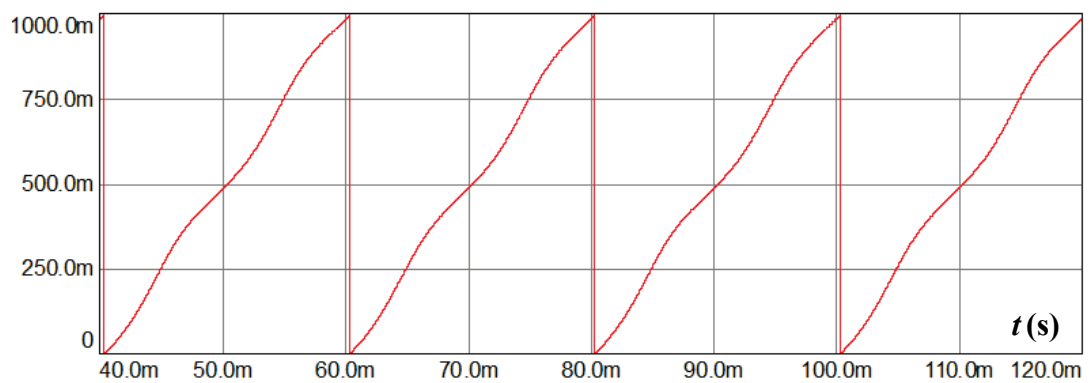


Figure 8.33 PLL vs. time.

Finally, Figure 8.34 reveals α vs. β frame components of grid-side current. PWM unit overflows in saturation modulation region as depicted in Figure 8.34(a). The shape of the circular arc is shown in Figure 8.34(b). Consequently, distorted grid-currents containing low order harmonics becomes more evident. Since the designed VSC already operates at high modulation index in linear modulation region ($1.057 < 1.15$) under normal grid conditions; however, under unbalanced grid condition, VSC cannot compensate the desired output and enters into the saturation modulation region.

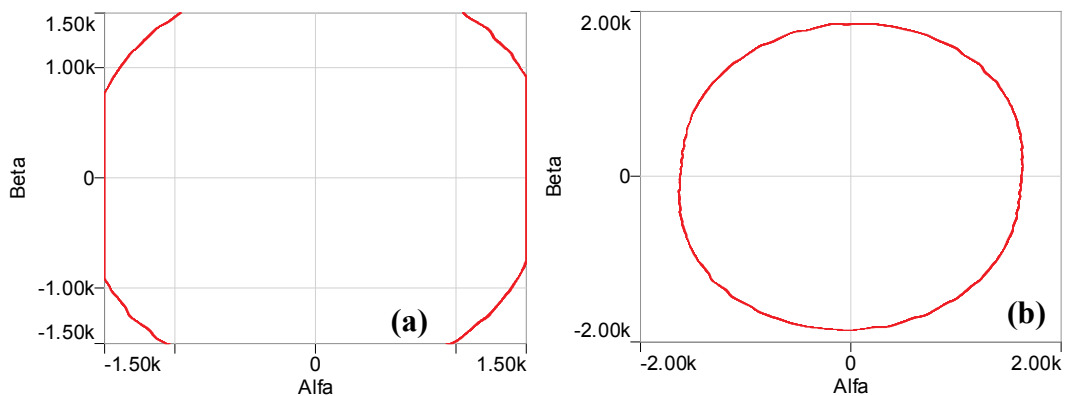


Figure 8.34 α vs. β frame components of grid-side current.

In order to elaborate the saturation region impact on grid-side currents, FFT analysis has been conducted. Figure 8.35 and Figure 8.36 reveals the individual current harmonics residing inside the grid currents.

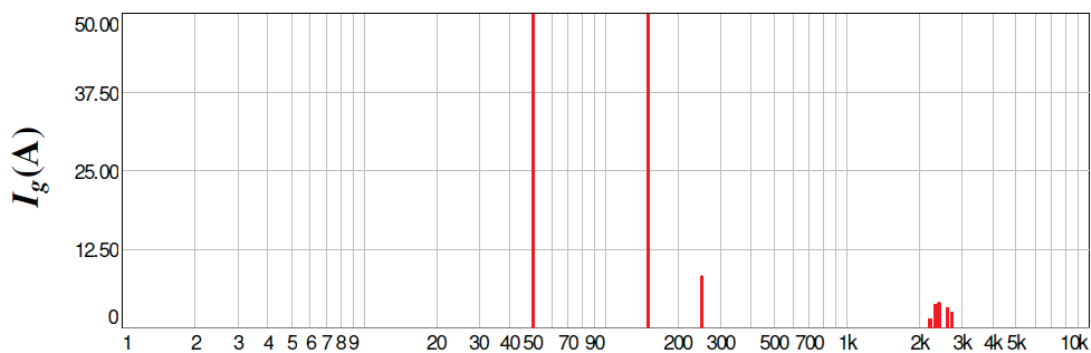


Figure 8.35 FFT analysis of I_g (2D-Graph).

	f [Hz]	I _{g1.i} [a]	Phi [rad]	Phi [deg]	%(Max)
Minimum	50.00000	1.37456	677.19277m	38.80029	102.80215m
Maximum	2.70000k	1.33709k	5.60403	321.08711	100.00000
0	50.00000	1.33709k	4.70274	269.44731	100.00000
1	150.00000	107.82072	1.62670	93.20294	8.06382
2	250.00000	8.13815	4.52470	259.24623	608.64509m
3	2.20000k	1.37456	3.80697	218.12349	102.80215m
4	2.30000k	3.64789	2.10969	120.87655	272.82286m
5	2.40000k	3.86781	5.60403	321.08711	289.27046m
6	2.60000k	3.11242	677.19277m	38.80029	232.77492m
7	2.70000k	2.34181	4.16501	238.63736	175.14222m

Figure 8.36 FFT analysis of I_g (Table).

As evident in these figures, saturated grid currents contain very high 3rd harmonic component (8.07%).

8.2.4.3. Steady-state measurements

The numerical data derived at rated power in the light of the steady-state attributes of 1 MW VSC under unbalanced grid operation are summarized in Table 8.4.

Table 8.4 2L-VSC steady-state measurements (unbalanced grid).

Parameters	Values
Input power P_{in} (kW)	1000
Grid power P_{grid} (kW)	961
Power loss P_{loss} (kW)	39
Efficiency η (%)	96.1
Power factor (PF)	0.994
Grid current THD _i (%)	15.92%
Peak grid current (A)	1338

THD_i of the output current is measured to be 15.92%. On the other hand PF is found as higher than 0.95 (0.994) which can be stated as satisfactory. In any case, even under unbalanced grid circumstances, system is kept steady-state stable. It should be noted that peak grid current has been increased under unbalanced grid case compared to the other cases, leading to higher semiconductor and filter losses; hence the lowest efficiency is attained.

8.2.4.4. Dynamic Response under Rapidly Changing Conditions

In Figure 8.25, a sudden power reduction of 250 kW (rated power to 75% of rated power) on input power is realized simulating a sudden decrease of input DC current source at 100th millisecond. It is observed that the control algorithm moves the rated power to the new maximum power operating point (750 kW) where the elapsed time to reach the new operating point is measured to be 17.1 milliseconds.

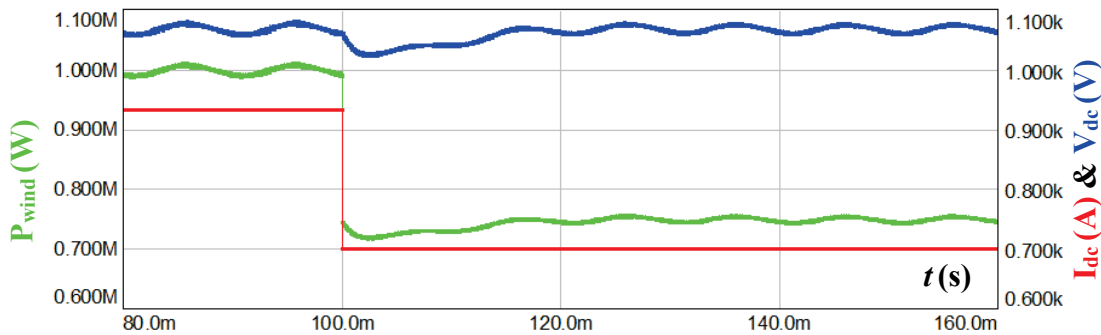


Figure 8.37 Dynamic response of DC-link voltage (blue), input power (green).

The adaptation to the new operating point is achieved by changing the reference input values inputted to current controllers and corresponding grid currents are produced as depicted in Figure 8.38.

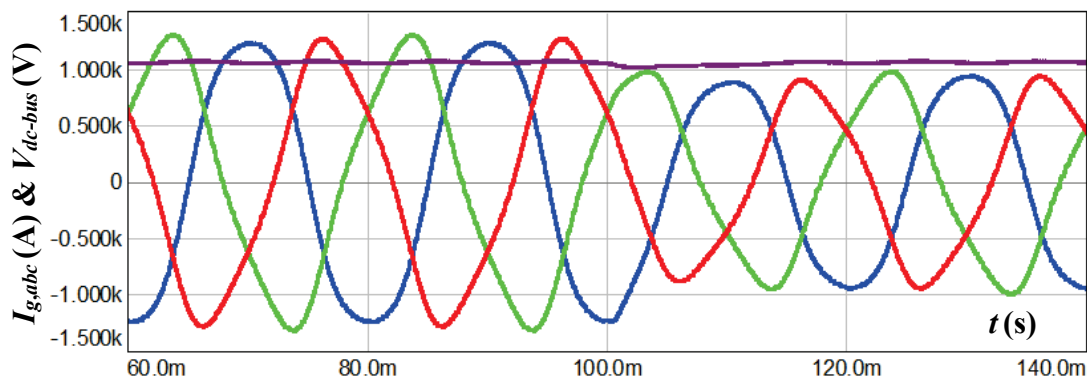


Figure 8.38 Dynamic response of DC-link voltage (purple) and grid currents (blue I_{ga} , red I_{gb} , green I_{gc}).

8.3. Summary

In this chapter, the constructed simulation system has been described step by step in accordance with the proposed techniques within the former chapters. Only 2L-VSC has been examined since the outcomes of 3L-VSC would differ only in numbers. The primary target of this chapter is not to compare the outputs of VSC topologies, since it has already been done in the previous chapters. On the contrary, it is to depict the simulation circuit that has been used throughout the laborious dissertation study.

The simulated results of 2L-VSC topology have been investigated under normal, distorted and unbalanced grid conditions according to the steady state and dynamic performances. It has been inferred that VSC operates well under balanced grid, delivers grid currents compatible to standards and provides efficiency very close to the calculated/expected efficiency value. On the other hand, under distorted and unbalanced grid operation, efficiency has been degraded due to the higher output peak currents. Besides, unbalanced grid realization has caused the saturation of the converter therefore very high magnitude low order harmonics have appeared on grid-side current waveforms. Also, almost unity PF has been provided under each case. Dynamic response has been satisfactory for each case and system could be kept stable under all circumstances.

CHAPTER 9

CONCLUSION

The installation of the large amount of wind turbines at both onshore and offshore are rapidly increasing by quality of the recent improvements in wind turbine technology and the incentives provided by the governments. Consistent with the wind integration studies performed by the TSOs and organizations from academy and industry, the grid code requirements have been revised, wind turbine manufacturers have been implementing new developments to the market, and the wind power plant developers have been conducting the connection studies considering grid codes and wind turbine technology.

The framework of this thesis is design of three-phase PWM-VSC widely used for grid-interface of renewable energy systems, particularly of wind turbine systems. The design procedure also involves devising the optimal *LCL*-filter parameters, determining the switching frequency, the PWM method, the VSC topology (two-level, three-level NPC, three-level T), the cost-effective feedback controlled algorithm, etc. for the VSC. Then, the design is verified by means of detailed computer simulations and computer based mathematical tool outputs. The study takes into account the balanced and unbalanced grid conditions, which may occur in the grid operating conditions. Several power ratings, operating conditions and financial aspects are considered to provide a thorough performance evaluation of the designed system.

To elaborate, the primary focus of this thesis is to provide a top to bottom design methodology that can span a wide power scale of grid connected PWM converters employed in wind turbine systems (under different PWM methods, VSC topologies, load conditions, modulation indices, switching frequencies) and yield the optimum:

- i. Filtering including the design of *LCL*-parameters and control scheme,
- ii. Topology among two-level (2L), three-level NPC (3L-NPC) and three-level T (3L-T) VSCs,
- iii. PWM method;

that provide the lowest cost solution while fulfilling the design requirements.

In the first chapter, an overview of recent wind turbine technologies and typical wind turbine configurations has been provided. WT configurations together with VSC topologies have been presented with their prominent advantages. Thus, WT systems with full-scale power converters have been favored. Also, for the grid-side converter of back-to-back VSC, 2L-VSC, 3L-NPC and 3L-T topologies have been found superior due to their simplicity, mass production volume and prosperous literature background. Finally, brief information about the preferred type of grid interface and PWM methods has been given.

In the second chapter, the types of renewable energy systems according to their output power level and intermittency characteristics have been elaborated. A number of statistical data concerning the proportion that wind turbine (WT) applications constitute in the total installed capacity both in domestic and worldwide aspects have been provided. Additionally, the insights on WT applications have been broadened in terms of capacity factor, power quality i.e. grid code requirements regarding the type and location (country, geographical conditions, etc.) of the application, fault conditions and transformer structures on PCC connection in the light of individual and farm applications. Besides, IEC 61400-21 has found to be the most convenient grid standard for wind turbine converters. Plus, VDEW gives the most elaborate study concerning individual current harmonics.

Third chapter has stated determination of switching frequency constraint for the converter design procedure using efficiency constraint by taking the type of VSC topology and PWM pattern into account. Thus, efficiency target, PWM method and eventually switching frequency constraint for the design have been addressed respectively.

Fourth chapter has provided extensive control background of the grid-connected PWM VSCs utilizing *LCL*-type filters. Optimum damping hints have been provided regarding active damping, passive damping and inherent damping techniques. The importance of the location of resonant frequency has also been studied and exemplified via comprehensive case studies. Additionally, the main differences between grid-side feedback and converter-side feedback, which are not mentioned in the literature in such a clear way, have been well-explained based on thorough MATLAB[®] and simulation outputs. Thus, a unique, extensive, well-detailed and top to bottom study has been unveiled enabling one to be able to comment on the steady-state and transient-state behavior of the *LCL*-filters according to the location of the resonant frequency in the frequency spectrum. Assessment of the steady-state and transient performance of the *LCL*-filter with respect to the location of the resonant frequency is one of the merits of this dissertation. Important deductions made concerning *LCL*-filter control and stability can be summarized as follows.

- i. The grid and converter-side inductances should be equal so as to maximize the filtering capability of inductors.
- ii. This study has comprehensively explored the inherent damping (ID) characteristic of an *LCL*-filter, which so far has not yet been discussed much in the literature. It specifically shows that the current control loop has an inherent damping term embedded when the converter current is employed for current feedback (CCF). This inherent damping term can be used for optimal damping of the *LCL* resonance without demanding additional PD or AD, only if the filter components are designed suitably. Such inherent damping unfortunately does not exist when the grid current is measured for feedback control (GCF); hence leading to the general conclusion that CCF is more stable than GCF as long as additional damping is not used under each method.
- iii. CCF control has yielded lower damping factor when only ID is benefitted. To compensate for this, detailed examination for tuning the damping factor is proposed, which would preserve the advantage of using only CCF (without

damping), but at the expense of a more compromised transient response compared to GCF case.

- iv. In the light of extensive analysis in case studies, GCF with AD has provided faster transient performance compared to CCF without damping case without compromising resonance damping. On the other hand, CCF without AD case has provided a degree of resonance damping, with a tradeoff of transient performance. Further damping has been obtained by using AD with the capacitor current. However, this has further reduced dynamic performance of CCF.
- v. It has been found that additional filtering improvement of *LCL*-filter is compromised as the resonant frequency moves to high resonant frequency region. This is due to the fact that *LCL*-filter behaves very similar to a single *L*-filter as demonstrated by the simulation outputs and root loci. Thus, the benefits introduced by *LCL*-filter are almost nullified if the resonant frequency passes beyond critical resonant frequency.
- vi. Apart from the critical resonant frequency region, there is also a critical ratio λ (resonant frequency to sampling frequency ratio) in high resonant frequency region determining the effectiveness of AD for the systems using GCF method. This critical ratio identification is inherent to this thesis work, so it can be deemed as a novel approach on commenting on the effectiveness of the AD methods in high resonant frequency regions.

Fifth chapter has discussed the *LCL*-filter design methods by comparing the conventional methods presented in literature with the novel design algorithm intrinsic to this thesis work. The design algorithm puts special emphasis on the controllability and stability issues of *LCL*-filters and involves them into the design phase. Thereby, optimum filter components in terms of size, cost, filtering performance and reliability are delivered. In the final part, a novel tuning methodology for controller and active damping gain constants are provided for each

of grid-side current control and converter-side current control. Important conclusions can be summarized as follows.

- i. A unique investigation aiming the same resonance damping under GCF and CCF has been provided. Nevertheless, critical damping resistor values have been found different for each of GCF and CCF cases owing to the distinct structure of the current loop. Reduced R_d value in CCF case has delivered both the same open-loop and closed-loop performance as R_d value in GCF method. Consequently, passive damping losses have been almost halved under CCF method owing to the inherent damping nature of the current loop.
- ii. The novel *LCL*-filter design algorithm takes the control point of view of *LCL*-filters into account and provides probably one of the most detailed *LCL*-filter design methodologies in the literature. The prominent advantages of this design methodology are simply the capabilities to cover wide power scales and provide optimal filter elements minimizing size, cost and loss while affording a good filtering performance.
- iii. With the comprehensive analyses in this chapter, it has been proven that setting α around 0.3 is not suitable for every power scale, especially for high power applications. Particularly, converters switched at a few kHz generally suffer from the low controller bandwidth and low closed-loop phase margin and α set value should be kept low to limit the phase margin degradation. For instance, 3 MVA system could not be stabilized without PD for $\alpha > 0.19$ (for each of CCF and GCF control) because closed-loop phase margin decreases too much beyond that value.
- iv. It has been found that for the same α set point, filter design algorithm under GCF has provided slightly smaller filter components compared to CCF case. It is important to note that same α set point aims to provide filter elements that guarantee the same distance between resonance peak and gain crossover frequency, hence same margins for the control loop are provided. However, in order to obtain alike outcomes under GCF and CCF methods, resonant

peak must be flattened properly; otherwise phase margin and dynamics are well degraded, leading to wrong assessment of GCF and CCF methods. For this reason, comparing CCF without additional damping case with GCF case is not fair since GCF already uses additional damping otherwise system cannot be stabilized. Thus, comparison between GCF and CCF must be evaluated under equally damped resonance peak. Although the system under GCF employs lower filter inductance, it has provided better dynamic performance compared to the system under CCF since the system has suffered from underdamped resonance peak.

- v. CCF has been found superior to GCF on stabilization of the current loop if additional damping is not used. However, in practical applications inherent damping cannot be relied on, additional damping is always used regardless of the current control technique. Consequently, having same control loop hardware (AD is used in each method), same resonance damping and sensor count (2 sensors for each method) under the same VSC topology has yielded slightly smaller passive elements under GCF method. Additionally, being consistent with the conclusion drawn at the end of Chapter 4, GCF provides slightly faster and better transient response compared to CCF control.

Sixth chapter has afforded a brief topological comparison of two-level and three-level VSC regarding differences in hardware components and semiconductor losses. Besides, a general scheme for calculation of switching and conduction losses of power semiconductors in computer simulations has been provided. By merging these two, a detailed comparative study between 2L-VSC and 3L-VSC has been conducted considering semiconductor loss, *LCL*-filter loss model, converter efficiency, converter-side current ripple and PWM pattern. Prominent differences between 3L-NPC and 3L-T have also been mentioned.

In the light of comparative study held in the sixth chapter, THD_i and efficiency performances of 3L topologies have been found to be superior to 2L topology under the same f_{sw} . In addition, the reduction in the commutation voltage has provided lower temperature rises in 3L-VSCs in return reducing the cost and size of the heat

sinks. Besides, 3L-T has been found to be the best choice for low-voltage applications if efficiency is the main concern. For 2L-VSC, simulation results have depicted that DPWM1 is the optimum PWM pattern in ripple aspect for the modulation indices $m_i > 0.8$. 3L-VSC; on the other hand, has shown less dependency against m_i variation under SVPWM compared to DPWM1. However, both ripple and WTHD analyses have revealed that DPWM1 shows more unstable behavior against m_i change under 3L-VSC and also yields higher ripple/harmonic. To conclude, being less sensitive to m_i variation and yielding less ripple and harmonic, SVPWM can be deemed as the optimal PWM pattern for 3L-VSC.

Seventh chapter has merged the content studied in the previous chapters and has used it as background and input to the analyses conducted. In this chapter, the extended top to bottom converter design algorithm, which is mentioned as the focus of the thesis work, has been constructed. The algorithm enables various system designs operating under distinct PWM method, *LCL*-filter parameter set, load, modulation index, and switching frequency. With the proposed design method, selection criterion for the best combination (VSC topology and PWM pattern) is reduced to economic assessment. For each combination, the pay-off time of the total initial cost is calculated and the one providing the shortest time period i.e. shortest pay-off time is highlighted as the optimum solution. Thus, a straightforward top to bottom converter design method becomes possible.

Apart from the converter design algorithm, another contribution of this dissertation is the figure of merit called operational efficiency. Literature lacks an operational efficiency definition that involves large scale of power converters employed in large scale wind turbine generators. Thereby, a simple definition has been proposed which takes into account the wind characteristics and capacity factor and then yields coefficients for the operational efficiency formula for the specific application based on the capacity factor and wind speed. In other words, the proposed definition affords distinct coefficients for each design case according to capacity factor and power output vs. wind speed characteristics of the application. Hence, a fair calculation of the operational efficiency can be achieved.

THD_i and efficiency performances of 3L topologies were found to be superior to 2L topology under the same f_{sw} . Thus, 3L-VSCs are economically feasible in low-voltage applications especially in high energy-cost markets. Since DPWM1 and SVPWM were compared under equal semiconductor loss criterion, additional operational efficiency analysis (and hence ROI calculations) did not have to be done. Thus, PWM method comparison has been conducted considering ripple, THD and WTHD performance of the topologies. In addition, the reduction in the commutation voltage has provided lower temperature rises in 3L-VSCs in return reducing the cost and size of the heat sinks. Besides, the 3L-T was found to be the better choice for low-voltage applications if efficiency and costs are the main concern. Finally, it has been shown that any improvement in the bidirectional middle switch in T-type poses a great impact on saved losses, making T-type much more favorable over 2L and NPC topologies in low-voltage wind turbine systems.

It must be noted that 2 kHz was sufficient to achieve AD. However, filter design has been made considering 2L-VSC, thus upgrading to 3L-VSC and decreasing the switching frequency to superpose the output attributes of 2L and 3L topologies may not hold the stability provided by AD for 3L-VSC any longer. In this case, use of PD for 3L-VSC become unavoidable and cause degradation in efficiency.

Finally, in eighth chapter, detailed performance analysis of three-phase 2L-VSC are conducted via the computer simulations. The simulated results of 2L-VSC topology have been investigated under normal, distorted and unbalanced grid conditions according to the steady-state and dynamic performances. It has been inferred that VSC operates well under balanced grid, delivers grid currents compatible to standards and provides efficiency very close to the calculated/expected efficiency value. On the other hand, under distorted and unbalanced grid operation, efficiency has been degraded due to the higher output peak currents. Besides, unbalanced grid realization has caused the saturation of the converter therefore very high magnitude low order harmonics have appeared on grid-side current waveforms. Also, almost unity PF has been provided under each case. Dynamic response has been satisfactory for each case and system could be kept stable under all circumstances.

To sum up, Figure 9.1 summarizes the approach how the focus of this dissertation is narrowed down step-by-step. Also, the favored topologies, PWM techniques, resonance damping techniques and current feedback control techniques are depicted based on the deductions given in this conclusion chapter.

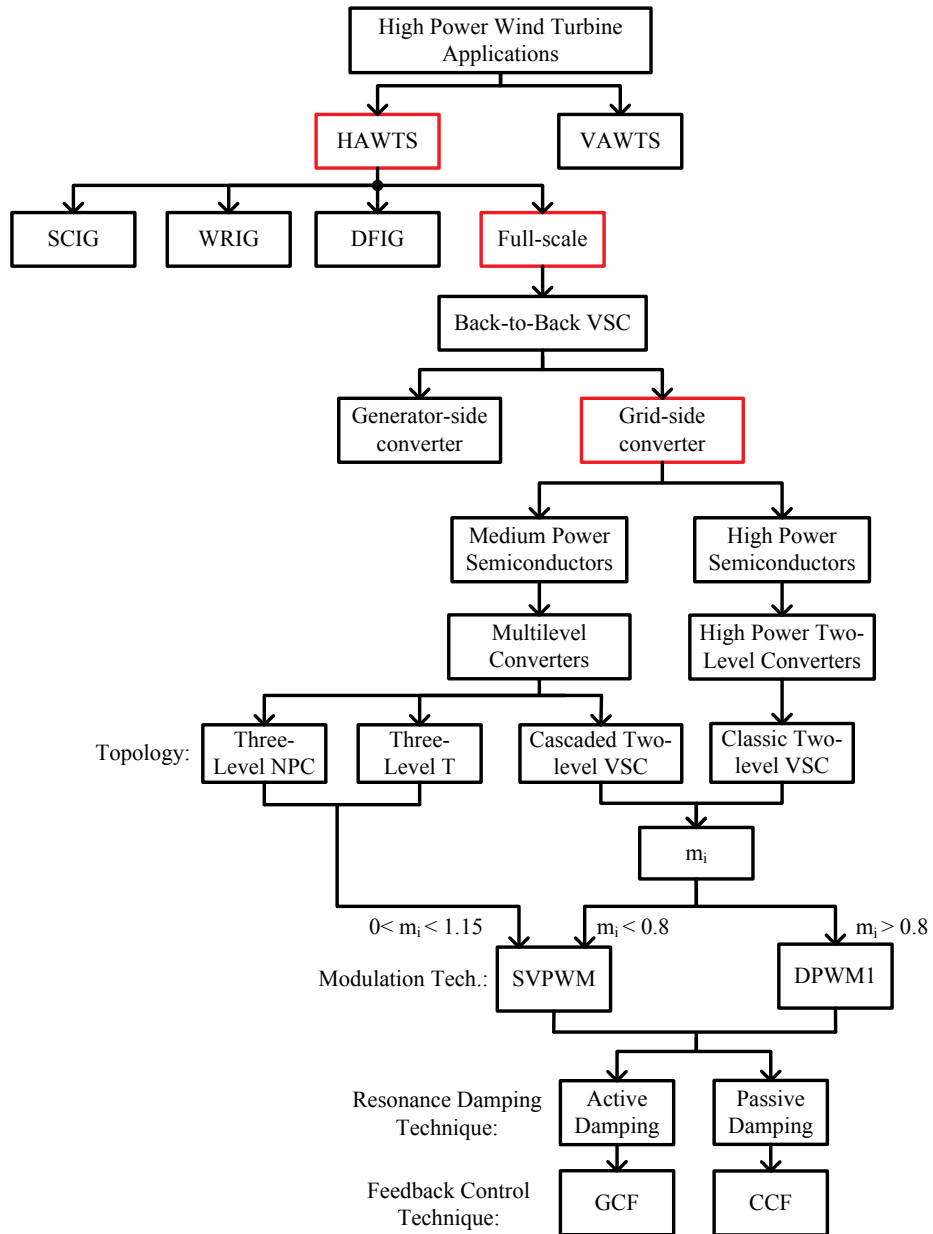


Figure 9.1 Overview of the study together with the favored methods under considered topologies.

As future work, the number of inspected voltage source converter topologies might be increased. Furthermore, a simple algorithm can be devised to assume the maintenance cost roughly for each topology. Thus, a more realistic design can be afforded by including this model to the main algorithm. Besides, faults occurred at the grid-side converters of wind turbines can be inspected and a simple model can also be devised in order to reflect the loss of power generation caused by each topology.

REFERENCES

- [1] U.S. Energy Information Administration, “Annual Energy Outlook 2013, Early Release Overview”.
- [2] A.Pullen, L. Qiao and S. Sawyer, “Global Wind Report 2013”, Global Wind Energy Council GWEC, Brussels, Belgium, March 2013.
- [3] A.Pullen, L. Qiao and S. Sawyer, “Global Wind Report 2013– Market Forecast 2014-2018”, Global Wind Energy Council GWEC, Brussels, Belgium, March 2013.
- [4] Schwabe, P.; Lensink, S.; Hand, M. (2011). IEA Wind Task 26 - Multi-national Case Study of the Financial Cost of Wind Energy; Work Package 1 Final Report. 122 pp.; NREL Report No. TP-6A20-48155 http://www.osti.gov/greenenergy/rddetail?osti_id=1009268.
- [5] Kocewiak, Lukasz Hubert, “Harmonics in large offshore wind farms”, Department of Energy Technology, Aalborg University, 2012. 332 p. Ph.D. thesis.
- [6] Sudipta Chakraborty, Marcelo G. Simões and William E. Kramer, “Power Electronics for Renewable and Distributed Energy Systems: A Sourcebook of Topologies, Control and Integration”, Springer, 2013.
- [7] Kantar, Emre; Hava, Ahmet M., "Design of grid connected PWM converters considering topology and PWM methods for low-voltage renewable energy applications, "*Power Electronics Conference (IPEC-Hiroshima 2014 - ECCE-ASIA), 2014 International*, vol., no., pp.2034, 2041, 18-21 May 2014.

- [8] Zhou, D, Lau, M, Blaabjerg, F & Tonnes, M 2013, 'Thermal Cycling Overview of Multi-Megawatt Two-Level Wind Power Converter at Full Grid Code Operation' *Denki Gakkai Ronbunshi. D, Sangyo Oyo Bumonshi*, vol 2, no. 4, pp. 173-182., 10.1541/ieejia.2.173.
- [9] N. Mohan, T. M. Undeland, and W. P. Robbins, "Power Electronics: Converters, Applications, and Design." 3rd Edition, John Wiley & Sons, Inc., 2002.
- [10] Ahmed, K.H.; Finney, S.J.; Williams, B.W., "Passive Filter Design for Three-Phase Inverter Interfacing in Distributed Generation," *Compatibility in Power Electronics, 2007. CPE '07*, vol., no., pp.1,9, May 29 2007-June 1 2007.
- [11] M. Liserre, F. Blaabjerg, and S. Hansen, "Design and control of an LCL-filter-based three-phase active rectifier," *IEEE. Trans. Industrial Applications*, vol. 41, pp. 1281-1291, 2005.
- [12] J. Dannehl, F.W. Fuchs, S. Hansen, and P.B. Thogersen, "Investigation of Active Damping Approaches for PI-Based Current Control of Grid-Connected Pulse Width Modulation Converters with LCL Filters," *IEEE. Trans. Industrial Applications*, vol. 46, pp. 1509-1517, 2010.
- [13] S. G. Parker, B. P. McGrath, and D. G. Holmes, "Regions of Active Damping Control for LCL Filters" *IEEE Trans. Ind. App.*, 2012-IPCC-463.
- [14] Y. Tang, P. C. Loh, P. Wang, F. H. Choo and F. Gao, "Exploring inherent damping characteristics of LCL-filters for three-phase grid-connected VSI," *IEEE Trans. Power Elec.*, vol. 27, no. 3, pp. 1433-1443, Mar. 2012.
- [15] M. Schweizer and J. W. Kolar, "Design and implementation of a hybrid efficient three-level T-type converter for low-voltage applications," *IEEE Trans. Power Electron.*, vol. 28, no. 2, pp. 899-907, Feb. 2013.

- [16] A. Nabae, I. Takahashi, and H. Akagi, "A new neutral-point-clamped PWM inverter," *IEEE Trans. Ind. Appl.*, vol. 17, no. 5, pp. 518-523, Sept./Oct. 1981.
- [17] T. Soeiro, M. Schweizer, J. Linner, P. Ranstad, and J. W. Kolar, "Comparison of 2- and 3-level active filters with enhanced bridge-leg loss distribution," in *Proc. 8th International Conf. on Power Electronics (ECCE Asia)*, 2011.
- [18] T. Brückner, S. Bernet, and H. Güldner, "The active NPC converter and its loss-balancing control," *IEEE Trans. Ind. Electron.*, vol. 52, no. 5, pp. 855-868, June 2005.
- [19] R. Teichmann and S. Bernet, "A comparison of three-level converters versus two-level converters for low voltage drives, traction, and utility applications," *IEEE Trans. Ind. Appl.*, vol. 41, May 2005.
- [20] M. Schweizer, I. Lizama, T. Friedli, and J. W. Kolar, "Comparison of the chip area usage of 2-level and 3-level voltage source converter topologies," in *Proc. 36th Annual Conf. of IEEE Industrial Electronics (IECON)*, 2010.
- [21] Ansoft-Simplorer V7.0. A power electronics simulation software, Ansoft Corporation, 2004.
- [22] A. Pullen, L. Qiao and S. Sawyer, "Global Wind Report 2013", Global Wind Energy Council GWEC, Brussels, Belgium, March 2013.
- [23] I. Martinez de Alegria, J. Andreu, J.L. Martin, P. Ibanez, J.L. Villate and H. Camblong, "Connection requirements for wind farms: a survey on technical requirements and regulation", *ScienceDirect Renewable and Sustainable Energy Reviews* 11, pp.1858-1872, January 2006.
- [24] "*Türkiye Rüzgar Potansiyeli Atlası*", <http://www.eie.gov.tr/>, last accessed date: 23/06/2014.

- [25] T. Ackermann, Ed., "Wind Power in Power Systems", Chichester: John Wiley & Sons Ltd, 2005.
- [26] O. A. Lara, N. Jenkins, J. Ekanayake, P. Cartwright and M. Hughes, "Wind Energy Generation, Modelling and Control", Chichester: John Wiley & Sons, 2009.
- [27] Hansen L, Madsen P, Blaabjerg F et al (2001) Generators and power electronics technology for wind turbines. The 27th annual conference of the IEEE industrial electronics society (IECON).
- [28] Baroudi J, Dinavahi V, Knight A (2005) A review of power converter topologies for wind generators. In: IEEE international conference on electric machines and drives.
- [29] Sudipta Chakraborty, Marcelo G. Simões and William E. Kramer, "Power Electronics for Renewable and Distributed Energy Systems: A Sourcebook of Topologies, Control and Integration", Springer, 2013.
- [30] Winkel, M. (2012, Sept). Offshore Wind Energy Factbook. Retrieved May 29, 2014, from <http://www.eon.com>.
- [31] Muljadi E, Butterfield CP, Ellis A et al (2006) Equivalencing the collector system of a large wind power plant. In: IEEE power engineering society general meeting.
- [32] Wind Turbine Grid Connection and Interaction Deutsches Windenergie-Institut GmbH.
- [33] Tsili, M.; Papathanassiou, S., "A review of grid code technical requirements for wind farms," Renewable Power Generation, IET , vol.3, no.3, pp.308,332, Sept. 2009.
- [34] Jauch C, Matevosyan J, Ackermann T et al. (2005) International comparison of requirements for connection of wind turbines to power systems. Wind Energy 8:295.

- [35] M. Altin, O. Goksu, R. Teodorescu, P. Rodriguez, B. Bak-Jensen, L. Helle, "Overview of recent grid codes for wind power integration," Proc. of OPTIM'2010, pp.1152-1160, 2010.
- [36] Transmission Code 2007. Networks and System Rules of the German Transmission System operators, VDN-e.v. beim VDEW, August 2007, www.vdn-berlin.de.
- [37] "Requirements for Offshore Grid Connections in the E.ON Netz Network" by E.ON, 2008, www.eon-netz.com.
- [38] E. H. Camm, M. R. Behnke, O. Bolado, M. Bollen, M. Bradt, C. Brooks, W. Dilling, M. Edds, W. J. Hejduk, D. Houseman, S. Klein, F. Li, J. Li, P. Maibach, T. Nicolai, J. Patino, S. V. Pasupulati, N. Samaan, S. Saylor, T. Siebert, T. Smith, M. Starke, and R. Walling, "Wind Power Plant Grounding, Overvoltage Protection, and Insulation Coordination: IEEE PES wind plant collector system design working group," in Proc. IEEE Power Energy Soc. Gen. Meet., 2009, pp. 1–8.
- [39] Mahmood, H.; Jin Jiang, "Modeling and Control System Design of a Grid Connected VSC Considering the Effect of the Interface Transformer Type," Smart Grid, IEEE Transactions on , vol.3, no.1, pp.122,134, March 2012.
- [40] Shuhui Li; Haskew, T.A; Williams, K.A; Swatloski, R.P., "Control of DFIG Wind Turbine With Direct-Current Vector Control Configuration," Sustainable Energy, IEEE Transactions on , vol.3, no.1, pp.1,11, Jan. 2012.
- [41] Grid connection of wind turbines to networks with voltages above 100 kV, Regulation TF 3.2.5, Eltra and Elkraft System, December 2004.
- [42] NGET, "The Grid Code", Issue 4, National Grid Electricity Transmission Plc, June 2009.
- [43] Red Electrica, "Resolution-P.O.12.3-Response requirements against voltage dip in wind installations", March 2006.

- [44] J.C. Smith, M.R. Milligan, E.A. De Meo and B. Parsons, "Utility wind integration and operating impact state of the art", IEEE Transactions on Power Systems, Vol. 22, No. 3, pp. 900-908, August 2007.
- [45] EWEA, "Generic grid code format for wind power plants", The European Wind Energy Association EWEA, Brussels, Belgium, November 2009.
- [46] C.H.Chienand, R.W.G.Bucknall,"Theoretical Aspects of the Harmonic Performance of Subsea AC Transmission Systems for Offshore Power Generation Schemes," in Proc. Generation Transmission and Distribution, 2006, pp.599-609.
- [47] Kocewiak, Lukasz Hubert, "Harmonics in large offshore wind farms", Department of Energy Technology, Aalborg University, 2012. 332 p. Ph.D. thesis.
- [48] IEC 61400-21, "Wind turbine generator system - Part 21: Measurement and assessment of power quality characteristics of grid connected wind turbines", 2008.
- [49] EN 50160 ed. 2 - "Voltage characteristics of electricity supplied by public distribution networks," English version 2007.
- [50] S. Grunau, F.W. Fuchs," Effect of Wind-Energy Power Injection into Weak Grids," in Proc. Generation Transmission and Distribution, 2006, pp.599-609.
- [51] IEC 61000-2-2, Part 2-2: Environment - Compatibility Levels for Low Frequency Conducted Disturbances and Signaling in Public Low Voltage Power Supply Systems, IEC 61000-2-2 Standard, 2004.
- [52] "IEEE Std. 519-1992", IEEE Recommended Practices and Requirements for Harmonic Control in Electric Power Systems, 1993.

- [53] VDEW Eigenerzeugungsanlagen am Mittelspannungsnetz-Richtlinie für Anschluss und Parallelbetrieb von Eigenerzeugungsanlagen am Mittelspannungsnetz.
- [54] M. Liserre, F. Blaabjerg, and S. Hansen, "Design and control of an LCL-filter-based three-phase active rectifier," *IEEE Trans. Industrial Applications*, vol. 41, pp. 1281-1291, 2005.
- [55] J. Dannehl, F.W. Fuchs, S. Hansen, and P.B. Thogersen, "Investigation of Active Damping Approaches for PI-Based Current Control of Grid-Connected Pulse Width Modulation Converters with LCL Filters," *IEEE Trans. Industrial Applications*, vol. 46, pp. 1509-1517, 2010.
- [56] E. Kantar, S. N. Usluer, and A. M. Hava, "Design and Performance Analysis of a Grid Connected PWM-VSI System," *Electrical and Electronics Engineering (ELECO), 2013 8th International Conf.*, pp. 220-224, Nov. 2013.
- [57] Y. Tang, P. C. Loh, P. Wang, F. H. Choo and F. Gao, "Exploring inherent damping characteristics of LCL-filters for three-phase grid-connected VSI," *IEEE Trans. Power Elec.*, vol. 27, no. 3, pp. 1433-1443, Mar. 2012.
- [58] S. G. Parker, B. P. McGrath, and D. G. Holmes, "Regions of Active Damping Control for LCL Filters" *IEEE Trans. Ind. App.*, 2012-IPCC-463.
- [59] E. Kantar, S. N. Usluer, and A. M. Hava, "Control Strategies for Grid Connected PWM-VSI Systems," *Electrical and Electronics Engineering (ELECO), 2013 8th International Conf.*, pp. 157-161, Nov. 2013.
- [60] B.G. Cho, S.K. Sul, "LCL Filter Design for Grid-connected Voltage-source Converters in High Power Systems," *IEEE Trans. Industrial Applications*, pp. 1548 – 1555, 2012.

- [61] J. Dannehl, C.Wessels, and F.W. Fuchs, "Limitations of voltage-oriented PI current control of grid-connected PWM rectifiers with LCL-filters," *IEEE Trans. Ind. Electron.*, vol. 56, no. 2, pp. 380–388, Feb. 2009.
- [62] Blasko, V.; Kaura, V., "A novel control to actively damp resonance in input LC filter of a three-phase voltage source converter," *Industry Applications, IEEE Transactions on*, vol.33, no.2, pp.542,550, Mar/Apr 1997.
- [63] S. N. Usluer, E. Kantar, and A. M. Hava, "Evaluation of PWM-VSI Systems Connected to the Grid through LCL Filters," presented at YEKSEM, Kyrenia, Cyprus 2013.
- [64] N. Hoffman, F. W. Fuchs and J. Dannehl, "Models and effects of different updating and sampling concepts to the control of grid connected PWM converters - A study based on discrete time domain analysis," in *Proc. IEEE European Conference on Power Electronics (EPE)*, Birmingham, UK, 2011.
- [65] B. Terzic, G. Majic, A. Slutej, "Stability Analysis of Three-Phase PWM Converter with LCL Filter by Means of Nonlinear Model," in *Automatika* vol.51, no.3, pp.221-232, 2010.
- [66] Peña-Alzola, R.; Liserre, M.; Blaabjerg, F.; Sebastián, R.; Dannehl, J.; Fuchs, F.W., "Analysis of the Passive Damping Losses in LCL-Filter-Based Grid Converters," *Power Electronics, IEEE Transactions on*, vol.28, no.6, pp.2642,2646, June 2013.
- [67] Liserre, M.; Dell'Aquila, A; Blaabjerg, F., "Stability improvements of an LCL-filter based three-phase active rectifier," *Power Electronics Specialists Conference, 2002. pesc 02. 2002 IEEE 33rd Annual*, vol.3, no., pp.1195, 1201 vol.3, 2002.
- [68] Yi Tang; Poh Chiang Loh; Peng Wang; Fook Hoong Choo; Feng Gao; Blaabjerg, F., "Generalized Design of High Performance Shunt Active Power Filter With Output LCL Filter," *Industrial Electronics, IEEE Transactions on*, vol.59, no.3, pp.1443,1452, March 2012.

- [69] Kantar, Emre; Hava, Ahmet M., "Design of grid connected PWM converters considering topology and PWM methods for low-voltage renewable energy applications, " *Power Electronics Conference (IPEC-Hiroshima 2014 - ECCE-ASIA), 2014 International*, vol., no., pp.2034, 2041, 18-21 May 2014.
- [70] Parker, S.G.; McGrath, B.P.; Holmes, D.G., "A general discrete time model to evaluate active damping of grid converters with LCL filters, " *Power Electronics Conference (IPEC-Hiroshima 2014 - ECCE-ASIA), 2014 International*, vol., no., pp.2019,2026, 18-21 May 2014.
- [71] Terciyanlı, A; Ermis, M.; Cadirci, I, "A Selective Harmonic Amplification Method for Reduction of kVA Rating of Current Source Converters in Shunt Active Power Filters," *Power Delivery, IEEE Transactions on*, vol.26, no.1, pp.65,78, Jan. 2011.
- [72] M. Liserre, F. Blaabjerg, and A. Dell'Aquila, "Step-by-step design procedure for a grid-connected three-phase PWM voltage source converter," *International Journal of Electronics*, vol. 91, no. 8, pp. 441–460, Aug 2004.
- [73] Dannehl, J.; Fuchs, F.W.; Hansen, S., "PWM rectifier with LCL-filter using different current control structures," *Power Electronics and Applications, 2007 European Conference on*, vol., no., pp.1, 10, 2-5 Sept. 2007.
- [74] Teodorescu, R.; Blaabjerg, F.; Liserre, M.; Dell'Aquila, A, "A stable three-phase LCL-filter based active rectifier without damping," *Industry Applications Conference, 2003. 38th IAS Annual Meeting. Conference Record of the*, vol.3, no., pp.1552, 1557 vol.3, 12-16 Oct. 2003.
- [75] Araujo, S.V.; Engler, A; Sahan, B.; Antunes, F., "LCL filter design for grid-connected NPC inverters in offshore wind turbines, " *Power Electronics, 2007. ICPE '07. 7th International Conference on*, vol., no., pp.1133, 1138, 22-26 Oct. 2007.

- [76] Meyer, R.; Mertens, A, "Design of LCL filters in consideration of parameter variations for grid-connected converters, "*Energy Conversion Congress and Exposition (ECCE), 2012 IEEE*, vol., no., pp.557,564, 15-20 Sept. 2012.
- [77] U. Drofenik, J. W. Kolar, "A General Scheme for Calculating Switching- and Conduction-Losses of Power Semiconductors in Numerical Circuit Simulations of Power Electronic Systems", *Proceedings of the International Power Electronics Conference (IPEC 2005)*, Niigata, Japan, April 4-8, CD-ROM, ISBN: 4-88686-065-6, 2005.
- [78] Schweizer, M.; Kolar, J.W., "Design and Implementation of a Highly Efficient Three-Level T-Type Converter for Low-Voltage Applications,"*Power Electronics, IEEE Transactions on*, vol.28, no.2, pp.899,907, Feb. 2013.
- [79] A. Nabae, I. Takahashi, and H. Akagi, "A new neutral-point-clamped PWM inverter," *IEEE Trans. Ind. Appl.*, vol. 17, no. 5, pp. 518-523, Sept./Oct. 1981.
- [80] T. Soeiro, M. Schweizer, J. Linner, P. Ranstad, and J. W. Kolar, "Comparison of 2- and 3-level active filters with enhanced bridge-leg loss distribution," in *Proc. 8th International Conf. on Power Electronics (ECCE Asia)*, 2011.
- [81] T. Brückner, S. Bernet, and H. Güldner, "The active NPC converter and its loss-balancing control," *IEEE Trans. Ind. Electron.*, vol. 52, no. 5, pp. 855-868, June 2005.
- [82] R. Teichmann and S. Bernet, "A comparison of three-level converters versus two-level converters for low voltage drives, traction, and utility applications," *IEEE Trans. Ind. Appl.*, vol. 41, May 2005.
- [83] M. Schweizer, I. Lizama, T. Friedli, and J. W. Kolar, "Comparison of the chip area usage of 2-level and 3-level voltage source converter topologies," in *Proc. 36th Annual Conf. of IEEE Industrial Electronics (IECON)*, 2010.

- [84] Mitsubishi Heavy Industries, "Mitsubishi Wind Turbine Generator," MWT62/1.0 datasheet, last access on [May 2014].
- [85] A. A. Rockhill, M. Liserre, R. Teodorescu, and P. Rodriguez, "Grid filter design for a multi-megawatt medium-voltage voltage source inverter," *IEEE Trans. Ind. Electron.*, vol. 58, no. 4, pp. 1205–1217, Apr. 2011.
- [86] Prasad, V H, "Analysis and comparison of space vector modulation schemes for three-leg and four-leg voltage source inverters", Master dissertation, 1997, Virginia Polytechnic Institute and State University, Blacksburg, VA.
- [87] Hava, A.M.; Çetin, N.O., "A Generalized Scalar PWM Approach With Easy Implementation Features for Three-Phase, Three-Wire Voltage-Source Inverters," *Power Electronics, IEEE Transactions on*, vol.26, no.5, pp.1385,1395, May 2011.
- [88] Rockhill, AA; Liserre, M.; Teodorescu, R.; Rodriguez, P., "Grid-Filter Design for a Multimegawatt Medium-Voltage Voltage-Source Inverter," *Industrial Electronics, IEEE Transactions on*, vol.58, no.4, pp.1205,1217, April 2011.
- [89] Kantar, Emre; Hava, Ahmet M., "Design of grid connected PWM converters considering topology and PWM methods for low-voltage renewable energy applications, " *Power Electronics Conference (IPEC-Hiroshima 2014 - ECCE-ASIA), 2014 International*, vol., no., pp.2034, 2041, 18-21 May 2014.
- [90] Zhukov S., "Loss Modelling of Three-Level Inverters controlled with Space Vector Modulation Technique", Master dissertation, 2012, Lappeenranta University of Technology, Lappeenranta Finland.
- [91] Schweizer, M.; Friedli, T.; Kolar, J.W., "Comparison and implementation of a 3-level NPC voltage link back-to-back converter with SiC and Si diodes," *Applied Power Electronics Conference and Exposition (APEC), 2010 Twenty-Fifth Annual IEEE*, vol., no., pp.1527,1533, 21-25 Feb. 2010.

- [92] Fuji Electric Semiconductors, "4MBI300VG-1800R-50R," datasheet, last access on [July 2014].
- [93] Drofenik, U.; Kolar, J.W., "Thermal analysis of a multi-chip Si/SiC-power module for realization of a bridge leg of a 10 kW Vienna rectifier," *Telecommunications Energy Conference, 2003. INTELEC '03. The 25th International*, vol., no., pp.826, 833, 23-23 Oct. 2003.
- [94] Muhlethaler, J.; Biela, J.; Kolar, J.W.; Ecklebe, A, "Core Losses Under the DC Bias Condition Based on Steinmetz Parameters," *Power Electronics, IEEE Transactions on*, vol.27, no.2, pp.953,963, Feb. 2012.
- [95] Reinert, J.; Brockmeyer, A.; De Doncker, R.W.; "Calculation of losses in ferro- and ferrimagnetic materials based on the modified Steinmetz equation," *Industry Applications Conference, 1999. Thirty-Fourth IAS Annual Meeting. Conference Record of the 1999 IEEE* , vol.3, no., pp.2087-2092 vol.3, 1999.
- [96] Mitsubishi IGBT Modules, "CM1800HCB-34N," datasheet, last access on [July 2014].
- [97] Mitsubishi IGBT Modules, "CM1800DY-24S," datasheet, last access on [July 2014].
- [98] Mitsubishi IGBT Modules, "CM1800HC-24NFM," datasheet, last access on [July 2014].
- [99] National Wind Watch "Presenting the Facts about Industrial Wind Power," *National Wind Watch Inc.*, 2007. [Online]. Available: <http://www.etsi.org>. [Accessed: May. 12, 2014].
- [100] Fuji Electric Semiconductors, "4MBI500VG-1800R-50R," datasheet, last access on [July 2014].

- [101] European Renewable Energy Council, 2004 [online] Available: <http://www.erecrenewables.org/documents/targets-2040/EREC-Scenario%202040.pdf>
- [102] California Energy Commission, 2006 [online] Available: <http://www.energy.ca.gov/efficiency> [Accessed: May. 12, 2014].
- [103] S. Lee, "How to select a heat sink", Aavid Thermalloy Application Note, <https://www.aavid.com/sites/default/files/technical/papers/how-to-select-heatsink.pdf>, [Accessed: April 16, 2014].
- [104] S. M. Muyeen (ed.), Wind Energy Conversion Systems, Green Energy and Technology, DOI: 10.1007/978-1-4471-2201-2_2, Springer-Verlag London Limited 2012.
- [105] "ABB low voltage wind turbine converters ACS 800" by ABB, 2013, www.abb.com.
- [106] "PCS 6000 for large wind turbines medium voltage, full power converters up to 9 MVA" *PCS6000Wind_3BHS351272_E01_RevA.pdf* by ABB, 2012, www.abb.com.
- [107] "Vacon ac drives and power converters" *Vacon-8000-Wind-Brochure-BC00424B-EN.pdf* by Vacon, 2013, www.vacon.com.
- [108] Klug, R.-D.; Klaassen, N., "High power medium voltage drives - innovations, portfolio, trends," *Power Electronics and Applications, 2005 European Conference on*, vol., no., pp.10.
- [109] V. Kaura, V. Blasko, "Operation of a phase locked loop under distorted utility conditions," *IEEE Transactions on Industry Applications*, Vol. 33, No. 1, pp. 58-63, January/February 1997.

- [110] Ciftci, Baris; Erturk, Feyzullah; Hava, Ahmet M., "Selection of suitable carrier-based PWM method for Modular Multilevel Converter," *Power Electronics Conference (IPEC-Hiroshima 2014 - ECCE-ASIA), 2014 International*, vol., no., pp.3734, 3741, 18-21 May 2014.
- [111] Matlab R2013a. A numerical computation software, Mathworks Inc., September 2013.
- [112] Hava, A.M.; Kerkman, R.J.; Lipo, T.A, "Simple analytical and graphical methods for carrier-based PWM-VSI drives," *Power Electronics, IEEE Transactions on* , vol.14, no.1, pp.49,61, Jan 1999.

APPENDIX A

LCL-FILTER TRANSFER FUNCTION UNDER PASSIVE DAMPING AND CAPACITOR CURRENT FEEDBACK CONTROL

Section 4.4.3 has provided some valuable information about PD method. However, in that section, the *LCL*-filter transfer function has been derived by proportioning grid current I_g to converter voltage V_c that neglects the PI-controller transfer function. As provided in active damping method, transfer functions including PI-controller can also be derived for PD method as well. In this case, transfer function derived in (4.24) should be modified by proportioning I_g to I_e as in (4.29) and (4.32) for GCF method and CCF method, respectively. Thus, resulting admittance transfer functions represent cascaded $G_c(s) \cdot G_p(s)$ for PD method under GCF and CCF methods, respectively.

$$Y_{LCL,GCF}(s) = \frac{I_g(s)}{I_e(s)} = \frac{K_p \left\{ s^2 C_f R_d + s \left(C_f \left(\frac{R_d}{T_i} \right) + 1 \right) + \frac{1}{T_i} \right\}}{s^4 C_f L_c L_g + s^3 C_f R_d (L_c + L_g) + s^2 (L_c + L_g)} \quad (\text{A.1})$$

$$\begin{aligned} Y_{LCL,CCF}(s) &= \frac{I_g(s)}{I_e(s)} \\ &= \frac{K_p \left\{ s^2 C_f R_d + s \left(C_f \left(\frac{R_d}{T_i} \right) + 1 \right) + \frac{1}{T_i} \right\}}{s^4 (C_f L_c L_g + K_p L_g C_f^2 R_d) + s^3 \left(C_f R_d (L_c + L_g) + K_p L_g C_f^2 \frac{R_d}{T_i} + K_p L_g C_f \right) + s^2 \left(L_c + L_g + K_p L_g \frac{C_f}{T_i} \right)} \end{aligned} \quad (\text{A.2})$$